THESES

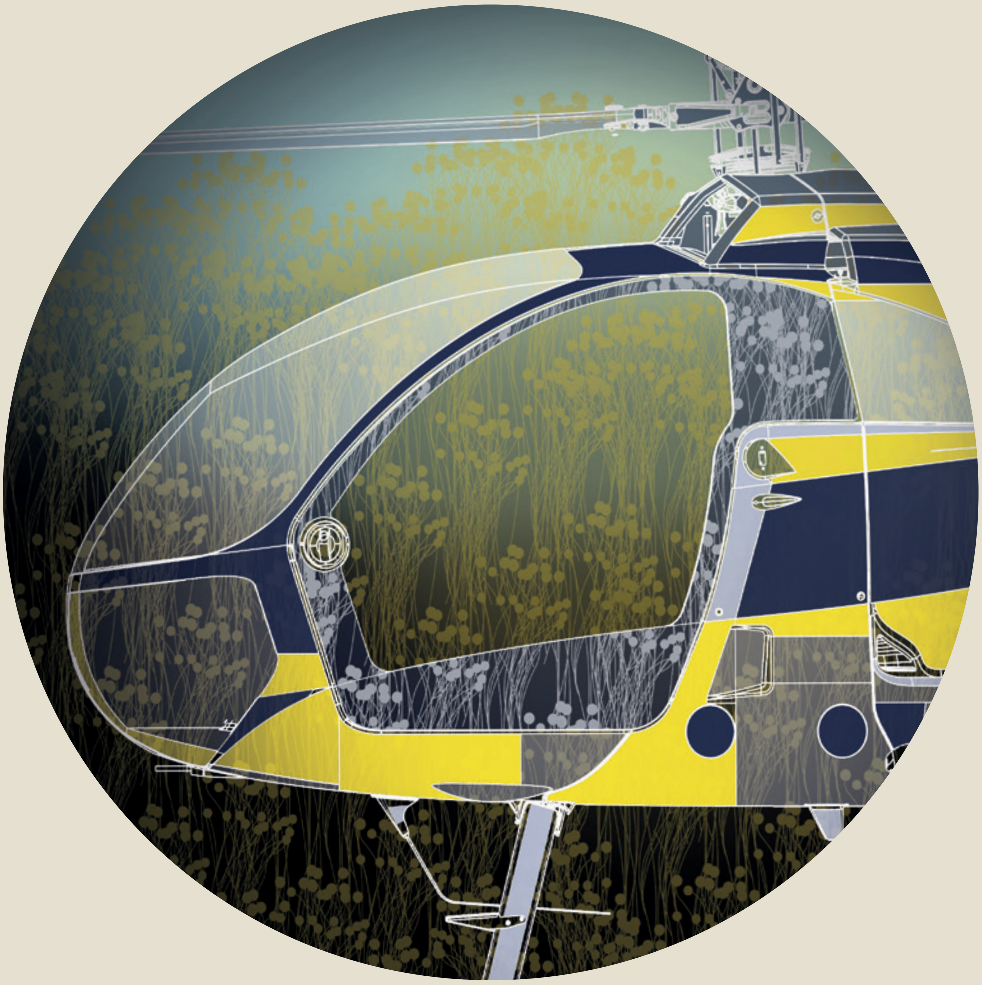

Maschinenbau

Katharina Andrea Henschel

Biocomposites in Aviation Structures on the Example of Flax and its Hybrids

TUM.University Press

Lehrstuhl für Hubschraubertechnologie
Fakultät für Maschinenwesen
Technische Universität München

Katharina Andrea Henschel

Biocomposites in Aviation Structures on the Example of Flax and its Hybrids

Vollständiger Abdruck der von der Fakultät für Maschinenwesen
der Technischen Universität München zur Erlangung des akademischen
Grades eines Doktor-Ingenieurs (Dr.-Ing.) genehmigten Dissertation.

Vorsitzender:

Prof. Dr.-Ing. Hartmut Spliethoff

Prüfer der Dissertation:

1. Prof. Dr.-Ing. Manfred Hajek
2. Prof. Dr.-Ing. Horst Baier

Die Dissertation wurde am 15.07.2019 bei der Technischen
Universität München eingereicht und durch die Fakultät für Maschinenwesen
am 25.11.2019 angenommen.

The German National Library has registered this publication in the German National Bibliography. Detailed bibliographic data are available on the Internet at https://portal.dnb.de.

Imprint

1. Edition

Layout design and typesetting: Katharina Andrea Henschel
Layoutguidelines for cover design: Designbuero Josef Grillmeier, Munich
Cover design: Caroline Ennemoser
Cover illustration: Caroline Ennemoser, partially using graphic
material by Katharina Andrea Henschel

TUM.University Press
Technical University of Munich
Arcisstrasse 21
80333 Munich

DOI: 10.14459/2019md1488689
ISBN printed edition: 978-3-95884-047-8

www.tum.de

Abstract

This work deals with the application potential of natural fiber composites in aviation structures as the overriding goal, and in helicopter structures in particular. This goal will be approached using various empirical investigations with flax fiber composites as epoxy prepreg material. Tests for the analysis of structural mechanics are carried out and evaluated, including tensile, bending, impact, and crash tests. Existing material models are further developed and applied within the framework of a finite element method, whereby a tailplane and a cabin door of an ultralight helicopter were investigated on their mechanical performance in a highly bio-based hybrid design. Iterative verifications on element, sub-component, and component level supported the hybridization and development of the parts.

The tensile tests showed a nonlinear stress-strain behavior of the flax fiber composites, which was described as bilinear. This finding was incorporated into the design in the form of a failure criterion. Furthermore, the structural-mechanical properties of fabric weaves were compared to continuous unidirectional fiber composites. Woven flax composites showed mechanical performance below the expectations and the application of unidirectionally reinforced laminates was identified to be preferable.

The finally manufactured parts were empirically analyzed as well, whereas their simulations and derived material models could be validated. Additional investigations concerned the hygroscopy of the flax fiber composites, as well as the suitability for non-destructive test methods. The widely promoted superior damping properties of flax could be verified as well. With regard to the motivation of using natural fiber composites, the eco-efficiency of the designed parts was evaluated by comparing the embodied energy of production and end-of-life with incorporated mass-related emissions in the operational life. It could be shown that savings in primary material production can compensate for small additional mass penalties and still lead to an overall beneficial eco-efficiency.

All in all, several properties of flax fiber composites compared to conventional fiber composites were analyzed. Findings and identified tendencies provide a basis for further detailed investigations in research and recommendations for the application in aviation and related industries.

Zusammenfassung

Die Arbeit befasst sich mit dem Anwendungspotenzial von Naturfaserverbundwerkstoffen in Luftfahrtstrukturen als übergeordnetes Ziel. Dieses Ziel wird anhand verschiedener empirischer Untersuchungen mit Flachsfaserverbunden als Epoxid-Prepreg-Material untersucht. Dabei wurden Versuche zur Analyse der Strukturmechanik durchgeführt und bewertet, unter anderem Zug-, Biege-, Impact und Crash Versuche. Hiermit wurden bestehende Materialmodelle weiterentwickelt und im Rahmen einer Finite Elemente Methode angewandt, wodurch ein Höhenleitwerk und eine Kabinentür eines Ultraleichthubschraubers in hybrider Bauweise ausgelegt werden konnten. Iterative Verifikationen auf Element, Subkomponenten und Komponenten Ebene dienten der Entwicklung der Bauteile.

Die Zugversuche zeigten ein nichtlineares Spannungs-Dehnungsverhalten der Flachsfaserverbunde, welches als bilinear beschrieben wurde. Diese Erkenntnis wurde in Form eines Versagenskriteriums in die Auslegung miteinbezogen. Weiterhin wurden die strukturmechanischen Eigenschaften von unidirektional verstärkten Laminaten und Geweben aufgezeigt. Dabei zeigte sich, dass die Notwendigkeit gesponnener Fasern (nur in Geweben) zu mechanischen Eigenschaften unter den Erwartungen führt und die Nutzung von unidirektionalen Lagen zu bevorzugen ist.

Abschließend wurden die beiden Bauteile gefertigt und ebenfalls experimentell charakterisiert, wodurch deren Finite Elemente Analysen und Materialmodelle validiert werden konnten. Zusätzliche Untersuchungen betrafen die Hygroskopie der Flachsfaserverbunde, sowie die Eignung zu Untersuchungen mittels zerstörungsfreier Prüfmethoden. Die überlegenen Dämpfungseigenschaften von Flachs konnten bestätigt werden, wie in einschlägiger Literatur gezeigt. Im Hinblick auf die Motivation zur Verwendung von Naturfaserverbunden, wurde die Ökoeffizienz dieser neuartigen Werkstoffe bewertet, indem die massenbasierte Energiebilanz der Fertigung und Entsorgung, der des Betriebslebens gegenübergestellt wurde. Dabei zeigte sich, dass Energieeinsparungen in der Faserherstellung ein zuätzliches Gewicht in geringem Maße ausgleichen können und zu einer energieschonenderen Gesamtbilanz führen kann.

Alles in Allem konnten verschiedene Eigenschaften von Flachsfaserverbunden im Vergleich zu konventionellen Faserverbunden in ihrer Tendenz identifiziert werden. Die gewonnenen Erkenntnisse und Tendenzen bieten eine Grundlage für weitere, detaillierte Untersuchungen in der Forschung und geben Empfehlungen für die Anwendung in der Luftfahrt und verwandten Industriezweigen.

Contents

List of Figures

List of Tables

Acronyms, Symbols, Sub-, and Superscripts

1, 2, 3	local coordinates used for fiber orientations
C	carbon
F	flax
$()_f$	fiber
$()_H$	hybrid
$()_m$	matrix
$()_{abs}$	absorbed
AC	aircraft
ACP	ANSYS Composite PrepPost
α	angle of attack
am	areal mass
ASTM	American Society for Testing and Materials
BD	bidirectional
BVID	barely visible impact damage
CAD	computer-aided design
CFRP	carbon fiber reinforced polymers
CHS	coefficient of hygroscopic swelling
CLT	Classical Laminate Theory
CMP	carbon mass penalty
CoAX 2D	coaxial ultralight helicopter made by edm aerotec GmbH
Con	consumption
CoV	coefficient of variation
$()_{CP}$	center of pressure
CT	computer tomographic
$()_D$	drag
$\Delta\kappa$	work hardening increment
DIC	digital image correlation
E-CO_2	embodied CO_2
E-E	embodied energy
$()_{eff}$	efficient
EMA	experimental modal analysis
EMP	energy mass penalty
η	efficiency
FCC	fuel carbon consumption

FEA	Finite Element Analysis
FED	fuel energy density
FFRP	flax fiber reinforced polymers
FIR	finite-duration impulse response
FRF	frequency response function
GFRP	glass fiber reinforced polymers
HSH	University of Applied Sciences Hanover
$()_{ini}$	initial
K	yield point
$()_{L}$	lift
$()_{LB}$	lower bound
LCA	life-cycle assessment
LTF-ULH	Lufttüchtigkeitsforderungen für Ultraleichthubschrauber, German national certification specifications for ultralight helicopters
MAC	Modal Assurance Criterion
MC	moisture content
MTOW	maximum take-off weight
NDI	non-destructive inspection
NDT	non-destructive testing
$()_{NE}$	never exceed
NFRP	natural fiber reinforced polymers
ν	Poisson's ratio
ω	frequency
PEK	parallel exponential kinetics
Φ	mode shape vector
φ_f	fiber volume fraction
$()^{pl}$	plastic
PP	polypropylene
prepreg	prepreg manufacturing with autoclave curing
Re	Reynolds Number
ROM	Rule of Mixtures
s	stroke
S_F	safety factor
$()_{spec}$	specific
TDI	turbocharged diesel injection
TDS	technical data sheet
θ	twist angle
TRL	Technology Readiness Level
TSI	turbocharged stratified injection

TUM	Technical University of Munich
$()_{UB}$	upper bound
UD	unidirectional
UL	ultralight
$()^{ult}$	ultimate
UV	ultra violet
VI	vacuum assisted resin infusion
w	deflection
w'	distortion
x, y, z	global coordinates used for parts and coupons
ζ	viscous damping ratio

1 Introduction

Composite structures are used in aviation since the 1940s [142]. Starting then, the application range was increasing rapidly. Helicopter blades for the Alouette II (a French serial production helicopter) were made out of fiberglass-polyester composite in 1958 [127]. In the following centuries, aramid, and carbon fibers were also used in aviation structures, leading to the state-of-the-art aviation, and in particular helicopter structures, which are typically manufactured from preimpregnated composites with a high content of carbon fiber reinforced polymers (CFRP).

CFRP are beneficial in many ways for aerospace applications, but there are drawbacks in terms of brittleness, dynamic behavior, cost, and environmental pollution. Carbon and glass composites fail, due to their inherent brittle failure of the fibers, often catastrophically, without prior indication for the operator [127]. Additionally, the use of CFRP in helicopters raised new issues in structural dynamics, as rivets were highly contributing to structural damping in metallic joints, composite appropriate joining technologies show less inherent damping and resonance problems increased. Furthermore, the cost for the production of carbon fibers is high, which is due to and along with a high energy consumption in production [173], but regarding the weight savings due to tremendously high specific strength and stiffness, it is still superior to metallic structural parts; as thereby, in the overall life-cycle of the aviation systems, costs and energy consumption can be reduced [172].

A new approach, evolved by the increasing environmental awareness, politically and scientifically, is addressing these issues inherent with the use of CFRP: Biocomposites. Biocomposites are defined in [146] and referenced in ScienceDirect by the following definition:

A biocomposite is a material composed of two or more distinct constituent materials (one being naturally derived) which are combined to yield a new material with improved performance over individual constituent materials.

Biocomposites are having a comeback. Soybean resin and paper as natural reinforcement was already used by Henry Ford in automotive applications starting from the 1940s [26]; but were then completely displaced by nowadays conventional reinforcement fibers: glass and carbon. There are also specifications by the British Standards Institution for flax as lacing cord or sewing thread in aviation applications from 1975, compare [35, 33, 34]. Back then, the motivation of using flax was not driven by the environmental footprint, but by the high mechanical performance regarding its weight.

Recent research studies state that biocomposites could reduce the environmental footprint of structural parts due to the significantly lower energy input in the production process.

The energy consumption for the production of flax sliver can be estimated between 10–60 MJ kg^{-1} and for a yarn by 86 MJ kg^{-1} [50, 51, 112], while CFRP-production consumes 450–770 MJ kg^{-1} [10, 185]. Additionally, it is expected that a preferably high bio-based mass content would conclude to a better recyclability of the part. Recent studies also highlight the mechanical and lightweight potential of flax fiber reinforcements in modern composite structures [29, 68]. The purposeful application of modern flax composites is already demonstrated in the automotive industry [89]. Here the applications focus in door panels and boot liners as the acoustic and vibratory insulation properties are considered superior.

For structures in aviation, typically stricter certification standards must be applied. But the low density in combination with high inherent damping offer a high potential especially in helicopter structures. The question we want to answer within this work is, which special considerations and problems arise from the aviation side for the structural use of natural fiber reinforced polymers (NFRP). Therefore, considerations on system environment, inspection methods and failure mechanisms are performed as well as investigations on the beneficial properties, which support the use of NFRP, such as damping, eco-efficiency, low cost, and low density.

While there is several ongoing research investigating this applicability [85], there is still no state-of-the-art deployment of NFRP in serial aviation products. Several studies are focusing on detailed problems, such as hygroscopy and fire resistance, while this work is pursuing a holistic approach in order to differentiate between other industries and give guidance for future scrutinies. In order to achieve this goal, this work was using the natural fiber "flax" in combination with synthetic epoxy matrices on two parts of a technology demonstrator the coaxial ultralight helicopter made by edm aerotec GmbH (CoAX 2D). Flax offers mechanically superior properties compared to other fibers [29]; and as certification requirements are included in the evaluation, a synthetic matrix, which is already widely used in aviation vehicles, was considered target-oriented. While other research on whole aviation structural components is often hypothetical, as its based on estimations and simulations, this work was actually manufacturing and testing whole parts made from FFRP.

Even though flax offers high mechanical properties compared to other natural fibers, the weight-specific performance is multiple times lower than the one of state-of-the-art applied CFRP. A detailed overview on the flax specific properties is given in Section 1.1.

In this work, we focus on semi-structural parts, where one function of the part is structural integrity, but it is not considered primary structure of which any catastrophic failure would lead to a loss of the aviation system. In the aimed applications, the lower strength and stiffness of flax fiber composites is aimed to be compensated by a hybridization, where the use of carbon fiber is reduced significantly but the structural performance is retained. In the result, this is leading to the optimization target of a high bio-based mass content with a high damping capability, under consideration of certification specifications on structural performance.

The good energy dissipating properties of FFRP are emphasized in different sources, including very good vibrational damping, crash absorbing and impact resistance properties [6, 189, 148, 120]. However, the main motivational aspect of this study is to reduce greenhouse emissions, which is evidently comprehensible considering the universal presence of climate change. To give a short overview of energy consumption in the whole life cycle of a helicopter, we did mass-based considerations in Section 1.3. As a conclusion, with an assumed life-cycle of 20 000 h, the break even in terms of embodied energy would be reached when the hybrid cabin is approx. 5% heavier than the reference. Eventually, the high energy demand in the operational life is strongly influencing the overall eco-efficiency, but minor drawbacks in weight (between 1–2%) could still be beneficial when significant reductions of the embodied energy in the primary production can be achieved. Furthermore, the costs of flax are only 2% of the costs of carbon, when comparing the raw fibers' primary production in [10]. This enormous difference can lead to significant cost savings in the system manufacturing. If we consider processed prepreg materials with epoxy coating, the prices will converge, but a remaining benefit is expected.

The named motivational drivers for this investigations lead to detailed empirical studies on the structural performance. One significant outcome was the consideration of the non-linear stress-strain behavior of FFRP, and according to related work of NFRP in general. This was included in FEA modeling and regarded in the part design as yield failure mechanism. Furthermore, the performance of UD reinforced material was proven significantly beneficial in structural-mechanical and dynamical performance, while the production of weaves includes necessary spinning processes, which lead to detrimental weave densities, low fiber volume contents and thereby, poorer mechanical performance. Additionally, environmental influences need to be investigated in more detail, especially combinations with fluids as FFRP show strong hygroscopic behavior, attributed to the natural fibers.

Unfortunately, not all material properties could be investigated within this work. Specifically, aviation-relevant properties were identified and focused. Properties which are considered relevant but could not be covered within this work, such as fatigue, are briefly summarized as literature reviews.

This thesis is constructed as follows, Chapter 1 includes the motivational aspects and the methodology applied in this work. Next, the details on the used material combined with derived FEA material modeling are explained in Chapter 2. These models are then applied and verified by the components tailplane and cabin door ot the CoAX 2D in Chapter 3, which also covers further investigations, giving empirically determined tendencies of material properties. All findings contribute to the final potential evaluation and are summarized in Chapter 4, where the findings also yield to application recommendations in aviation.

1.1 Flax Fibers — From Plant to Laminate

Flax is a natural plant, which is primarily grown in Europe, but also in other temperate regions [24, 29, 89]. The fibers are extracted from the stem, which is shown in Figure 1.1, by a multistage process: planting, harvesting, drying/rotting, scutching, hackling, and partly spinning and weaving.

The extracted fibers measure a diameter of averaged 19 µm and a length of 25–120 cm [192]. Figure 1.2 a) shows the flax plant after harvesting a tuft off the field, and b) a twill weave made from extracted flax fibers. As the fibers are neither synthetically produced nor endless, the production process of a weave requires yarning by spinning, while UD reinforced mats can be aligned without yarning. The woven fabrics nowadays available are limited in smaller scales to an areal density of about 100 g m^{-2}. Just as a side note, the biological name of flax is *Linum usitatissimum*, which is part of the bast plant family *Linaceae*, the scientific name is *Linum.*

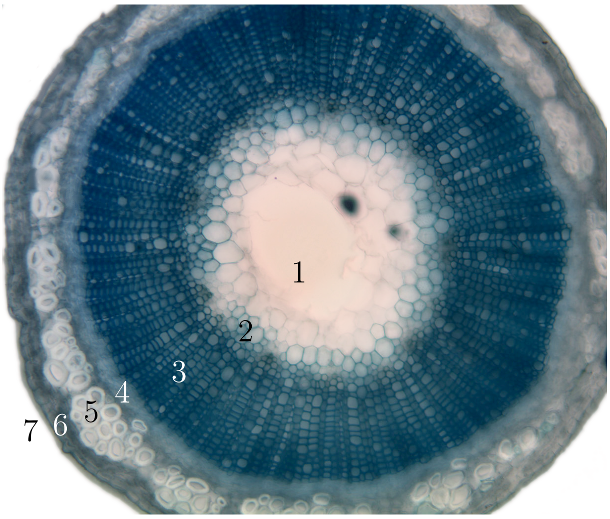

Legend:

1 - Pith
2 - Protoxylem
3 - Xylem II
4 - Phloem I
5 - Sclerenchyma (Bast Fiber)
6 - Cortex
7 - Epidermis

Figure 1.1: Cross-Sectional View of Flax Stem, Fibers are in Position 5 [59]

a) b)

Figure 1.2: Photographic Images of Flax, a) Harvested Plant [18], b) Flax Woven Fabric [43]

The use of NFRP is supported by the political and ecological interest of greener aviation. The weight-saving potential and the better carbon footprint as well as energy efficiency compared to carbon are supportive arguments [164]. In previous studies the flax fiber was found to be the most promising natural fiber for an application of high demands in specific strength and stiffness, compared to other natural fibers [64]. The material choice for structures in aviation is often driven by high specific mechanical characteristics, which also regard the material density. In this aspect, the lightweight potential of flax is high, as the fibers have a lower density than conventional fibers (such as glass and carbon) [141]; combined with a stiffness comparable to glass fiber composites and a strength in the same range as aluminum alloys.

Table 1.1 lists selected properties of the currently in aviation composites applied fibers (glass and carbon) in comparison to the herein analyzed flax fibers. Only the damping ratio is determined from the cured laminate, the other values refer to pure fibers. The fiber values are taken from [10] and do not cover all results in relevant scientific publications, this one-source-principle was deployed in order to maintain comparability.

Table 1.1: Mechanical and Primary Production Related Properties of Carbon, Glass, and Flax Fibers [10, 181]

Property	Unit	Glass	Carbon	Flax
Density	$[\mathrm{g\,cm^{-3}}]$	2.55–2.60	1.80–1.84	1.42–1.52
Tensile Strength	$[\mathrm{N\,mm^{-2}}]$	1 900–2 050	4 400–4 800	750–940
Tensile Modulus	$[\mathrm{N\,mm^{-2}}]$	72 000–85 000	225 000–260 000	75 000–90 000
Specific Strength	$[\mathrm{kN{\cdot}m\,kg^{-1}}]$	731–804	2 391–2 667	493–662
Specific Stiffness	$[\mathrm{kN{\cdot}m\,kg^{-1}}]$	27 692–33 333	122 282–144 444	49 342–63 380
Embodied Energy	$[\mathrm{MJ\,kg^{-1}}]$	62–69	380–420	10–12
Embodied CO_2	$[\mathrm{CO_2\text{-}kg\,kg^{-1}}]$	3.34–3.69	23.90–26.40	0.37–0.41
Water Usage	$[\mathrm{L\,kg^{-1}}]$	89–99	399–441	3 900–3 250
Damping Ratio*	[%]	0.15	0.18	1.47
Costs	$[\mathrm{USD\,kg^{-1}}]$	1.63–3.26	124.00–166.00	2.10–4.20

*value not related to the pure fiber, but to the cured fiber-reinforced laminate

We can see that the density is significantly lower for the flax composites, but in specific strength and stiffness, the carbon fiber is showing the best properties. Nevertheless, flax fibers show higher specific stiffness than glass fibers and as the design of some aviation structures, such as aerodynamic surfaces, is typically stiffness constrained, this is considered a supportive property. Additionally, a superior energy dissipation of FFRP compared to CFRP and GFRP is emphasized in different sources, observing very good vibrational damping, crash absorbing, and impact resistance properties [181, 138, 105, 93, 21].

Another significant difference can be seen when comparing embodied energy and embodied CO_2. Flax fibers need only a small fraction of the in primary production embodied values of the conventional fibers. On the other hand, when comparing water usage, but also area or space requirements, flax fibers are inferior to conventional, synthesized fibers. In terms of costs, flax fibers are also multiply superior to carbon fibers. But the composites differ less in energy consumption and costs as the added epoxy also requires resources and further manufacturing steps add up equally to both fiber types and thereby reduce the relative discrepancy. The actually paid prices per square meter differed in approx. 30%, still a significant benefit. As flax prepregs are not very common yet and production batches are small, we expect costs of flax prepregs to decrease.

All in all, flax was chosen as representative fiber in NFRP due to its high availability and its superior stiffness and strength values compared to other natural fibers [85, 29]. GFRP were added in this overview for comparison, but are not used in this work. It is aimed to find an advantageous combination of high-performance CFRP in a small proportion, with a high proportion of eco-efficient FFRP, which then should embody beneficial aspects of both materials.

1.2 Hybrid Composites — A Smart Combination

Hybrid composites mean the incorporation of typically different fiber materials consolidated by a matrix into one material. Hybrid composites are motivated by the combination of favorable properties inherent to each individual fiber material, to a beneficial combination of both. Hybrid composites are often using short and non-oriented fibers, where higher productivity manufacturing can be applied and thereby a significant cost reduction is possible [129]. In this work, long, oriented fibers are used, which are typically accompanied with higher costs, but enable tailored, high-performance structures, as used in aviation.

Thereby, three types of hybridizations can be distinguished: the hybridization of the weave fabric, which is called intra-laminar hybridization (I), where the different types of fibers are regularly alternated in the fabric. Next, inter-laminar hybridization (II), where each layer in a stack-up is reinforced by one type of fiber and in the whole stack-up the layers are varied. And lastly, separate reinforcing elements (III), where local reinforcements from different materials are serving as straps or stiffening ribs [129].

Typically, by the use of hybrid composites, the following benefits are envisaged: multi functionality, a benefit in cost, weight, or technical performance. The properties of a hybrid composite is mainly dependent on the fiber content, their orientation, the fiber to matrix bonding, and the arrangement of both [83]. Thereby, a smart design is inevitable in order to achieve the envisaged benefits.

Hybrids including metals and other non-polymeric or fibrous materials are not regarded in this study, but are matter of research and offer multi-functional potentials [177]. This work focuses on the use of bio-based composites in a high proportion with local, design-driven hybridization to maintain mass and technical performance of a mainly CFRP containing reference.

In doing so, the inter-laminar hybridization (II) and separate reinforcements (III) were used, in two kinds of manufacturing techniques. Either using a single epoxy matrix in vacuum assisted resin infusion technique or different epoxy matrices in prepreg manufacturing with autoclave curing (prepreg). Details on all used matrices are summarized in Section 2.9.

One major research interest is to investigate on the hybridization capabilities of these two fiber materials and also to analyze multi-functionality regarding the counterparts stiffness and damping [12]. Another research interest is, whether CFRP material in low loaded areas could be replaced by FFRP and to which extent this is not accompanied by performance reductions.

Generally, the performance of a composite is highly depending on the design, by the use of multiple materials, the design variable "kind of material" adds variability to the stack-up order. Regarding thermal coefficients and discrete stiffness transitions, there are new criteria to be regarded, as well as combined failure mechanisms need to be verified. Conventional methods of FEA modeling should be investigated for this endeavor and design principles will be identified so that an eco-efficiently beneficial application can be facilitated.

1.3 Greener Aviation — Increasing the Eco-Efficiency

As already presented before, one crucial motivational aspect is to reduce greenhouse emissions in the rapidly increasing aviation industry. In order to show proportionality between resource demand in production and use-life of aviation systems, we want to compare different transportation systems. Thereby, we want to expound the choice of the ultralight helicopter as technology demonstrator.

Increasing the eco-efficiency of a transportation system can typically be achieved by a weight reduction, as transportation systems require energy per transported mass in the operational life. While the approach within this work is focusing on a reduction of required resources in the production phase, the inherent possibility of a weight increase should be evaluated. In order to pursue a holistic approach, we want to consider all three life-cycle phases: production, operational life, and end-of-life. Figure 1.3 is schematically showing energy and CO_2-demand of two cars, two passenger aircraft, and two helicopters, where several assumptions are applied and only materials' primary production is considered. We compare the energy and CO_2 demand of 1 kg CFRP structure in production and consider combustion at the end-of-life. In combustion we consider the heat release as energy recovery, while the CO_2 release is adding up to the overall CO_2 consumption. For 1 kg of CFRP we considered 554 MJ kg^{-1} and 40 CO_2-kg kg^{-1}, which should be replaced by 1.05 kg of FFRP (5% heavier), which is consuming 104.70 MJ kg^{-1} and 6.08 CO_2-kg kg^{-1}. Values account for the whole composite in production and end of life, calculated from data in [10]. Additionally, a factor of 1.5 was applied to the material mass, as in the whole life-cycle, i.e. during maintenance and in manufacturing, more material is needed than the parts built-in weight.

The additional 5% of mass are contributing to the use life, where the different transportation systems are modeled with an energy and CO_2 penalty per kg, which is assessed as in Table 1.2. The values of the transportation systems represent approximations and are achieved from the following references [2, 3, 4, 5, 10, 44, 55, 184]. The energy and CO_2 savings from production, maintenance replacement, and end-of-life are summarized and result in the initial reduction, compared to the CFRP part (Benchmark in Figure 1.3). As soon as the respective line of the technology is crossing the benchmark line, there is no energy or CO_2 benefit left of using the 5% heavier FFRP structure compared to the 1 kg-CFRP structure.

Table 1.2: Eco-Efficiency Data for 1 kg Structural Mass in Different Transportation Systems [2, 3, 4, 5, 10, 44, 55, 184]

Technology – Specification	MTOW $[kg]$	Con $[\frac{L}{h}]$	FED $[\frac{MJ}{L}]$	EMP $[\frac{MJ}{kg \cdot h}]$	FCC $[\frac{kg_{CO_2}}{L}]$	CMP $[\frac{kg_{CO_2}}{kg \cdot h}]$	Usage $[\frac{h}{year}]$
Diesel Car – VW Golf 1.6 TDI	1 337	4	38	0.11	3.1	0.009	250
Gasoline Car – VW Golf 1.2 TSI	1 260	5	35	0.14	2.9	0.012	200
Short-haul AC – Airbus A320	87 000	2 700	35	1.09	3.0	0.093	2 500
Long-haul AC – Airbus A380	575 000	12 000	35	0.73	3.0	0.062	3 000
Helicopter – Airbus H135	2 910	240	35	2.89	3.0	0.247	400
UL Helicopter – CoAX 2D	450	19	35	1.48	2.9	0.122	300

A linear development of additional fuel consumption is a simplification, as well as the purely mass-based calculations of energy savings per kg in production and recycling. The values should not be considered reliable, this is a simplified approach with several approximations and is only sufficient to identify trends and proportionality, which we intend to show by this estimation.

The left-side graphs of Figure 1.3 show that the most energy-per-mass consuming technology is the conventional helicopter, as its additional energy demand per extra weight is the highest. Next, the ultralight gasoline helicopter (CoAX 2D), which will serve as technology demonstrator within this work, and then the fixed wing aircraft, followed by the cars. This order is more or less what we would expect from consumption rates, the differences between energy and CO_2-consumption are small, but there is a slight shift to earlier break-evens in the CO_2 contemplation. However, if we do not compare 20 000 h usage, but 20 years and the operational hours per year are taken into consideration, the helicopters and aircraft switch in their order. This is because fixed wing passenger aircraft are operated at higher rates per year, estimated at approximately ten times as much as helicopters or private-use aircraft.

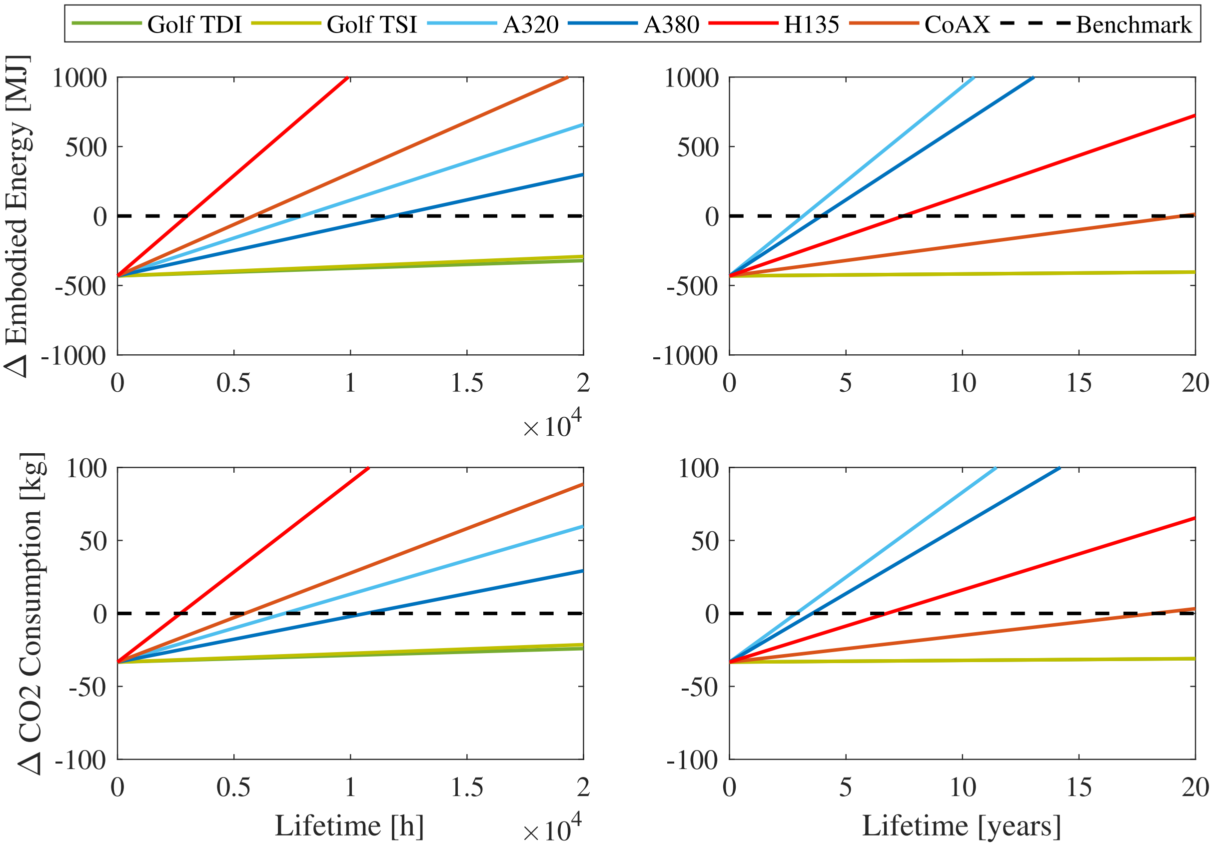

Figure 1.3: Comparison of Exemplary Transportation Systems when 1 kg of CFRP Structure is Replaced by 1.05 kg of FFRP in Terms of Embodied Energy and CO_2 Emissions

Naturally, this proportion is not applicable for each individual aviation system, but nevertheless, the yearly energy-mass-penalty is contributing strongly in the passenger-aircraft

system. Concluding to the choice of sport and leisure systems to be the most promising aviation technology, either aircraft or helicopter, as the low yearly operational hours shift the proportionality of production and operation to more advantageous levels.
As a conclusion, we can say that an additional mass of 5% can still be beneficial in terms of eco-efficiency over the whole life, but the application of private use ultralight helicopters or small aircraft, with few operational hours per year, are the aviation technologies we should focus on, if we anticipate extra weight. Additionally, ground vehicles, such as cars, rail transport, or trucks are identified as proper testbed for this endeavor, but are also state-of-the-art applications already [89].

1.4 Helicopter Structures — Performance and Certification

The choice of the technology demonstrator, the CoAX 2D, serving as representative aviation structure, should be retraced in this section. The helicopter is shown in Figure 1.4, where most modules are well visible. The CoAX 2D consists of the following modules:

- Rotor
- Rotor Mast Assembly
- Engine
- Frame Structure
- Cabin
- Tail Boom
- Landing Gear

Figure 1.4: Photographic Image of the Technology Demonstrator: The Coaxial Ultralight Helicopter by edm aerotec GmbH (CoAX 2D) [55]

There is a high demand of new innovative technologies in aviation industries, but the inherent risk due to the operation off-ground is resulting in strict airworthiness regulations and certification specifications. If these are not considered entirely since the beginning of a new technology, it is likely to result in delays or even failure of projects and disruptive technologies. Therefore, a special focus is given to material certification standards for aviation industries; including German, European, and US standards for helicopters and fixed wing aircraft.

There are significant certification differences between load-bearing primary structures, secondary structures, and among certain applications. While passenger airlines require quantitatively and qualitatively the most extensive tests, smaller aircraft standards reduce qualification efforts in some areas, e.g. regarding fire resistance.

Therefore, a sports and recreational aviation system was also considered beneficial in this point of view. The helicopter identified for this research was the CoAX 2D. It was considered a good fit in terms of embodied energy proportionality during the life cycle as described in Section 1.3 and in terms of more fundamental certification specifications.

Ultralight helicopter structures are, like other aircraft structures, typically weight-optimized structures. In the technology demonstrator of this study, most of the cabin structures are built from only two layers of carbon weave. Therefore, the structures of investigation are very thin and mass is a very important parameter, besides strength and stiffness. Another demand in the mechanical context is the dynamic behavior of the structures. Helicopter structures are highly exposed to vibrations, which are induced mechanically, acoustically, and aerodynamically. These vibrations result in high-cycle stresses, which shall not reduce the structures' life-time due to fatigue. Furthermore, it is aimed to reduce discomfort for the passengers regarding noise and vibrations. Especially for these demands, NFRP seem to be a perfect fit.

Further important aspects for aviation are the safety requirements, which include: crash behavior, impact, fire resistance, etc. Also, environmental influences should be identified, which are wearing and tearing the structures. For NFRP this aspect is regarded critically. Additionally, there are manufacturing and handling requirements, this aspect is taken into account secondarily, as the laboratory conditions of the investigations differ from industrial standards in manufacturing.

This overview on aviation-specific demands is given as background information. Certain evaluation in terms of aviation needs and (empirical) findings are summarized in Chapter 4. While the next section is presenting the applied methodology.

1.5 Methodology — Empirical and Numerical Design

Generally, this research is based on experimental investigations, which are either analyzed standalone or used for validation of the FEA simulation. The superordinate goal is to identify beneficial applications for flax fiber composites and to unveil drawbacks in terms of aerospace certification needs. Therefore, two trial parts were chosen to serve as application models, a tailplane and a cockpit door. Both built-in components of the CoAX 2D and as today consisting majorly of CFRP. The parts were chosen as they fulfilled the demands: representative for aviation, not primary structure, rather stiffness than strength constrained, vibratory loaded, and of acceptable handling size. The tailplane has a simple geometry, with only one-dimensional curvatures, this allows the application of UD material. The cabin door has a more complex geometrical shape, where woven material will be needed. Both parts will be designed regarding the benchmark performance, which is their respective carbon reference version. Constraints are regarded in terms of weight, cost, mechanical properties, and eco-efficiency. While investigations on mechanical properties are addressing strength, stiffness and damping performance. The design methodology of both parts as well as preliminary and final results are explained in Section 3.1 and Section 3.2. The general approach can be compared to a top-down methodology from the requirements side. The reference parts were analyzed and broken down to certain material requirements by a specifications book. But in experimental view, a bottom-up methodology would describe the general procedure, as there were several tests on coupon and element level done for the FEA material models.

In summary, the iterative requirement verification, based on design, FEA simulations and experiments, is done following the V-model approach [183]; while the empirical investigations are following the sampling methodology according to Rouchon [143]. Here, low level samples such as coupons or elements are tested in a high quantity and by increasing model fidelity the quantity reduces. Both models are adapted to the contents of this work, shown in Figure 1.5.

Schematic pictographs in Figure 1.5 are labeled regarding their test level, e.g. A1. An overview of test and sampling scopes is given in Table 1.3, with respect to the labels as in the graphic. The two components of investigation are on top, tailplane and cockpit door, and their respective subordinate experimental work orders below. The levels themselves are ordered alphabetically, beginning with C for the low level coupon tests and ending with A for the high level component tests. Category C parts were mainly investigated empirically, the results were then used for either the material model or understanding of the material's specific behavior. Level B specimens, Elements, were already predicted by FEA calculations, and the results were used for model and design validations and possible improvements, which also applies to the sub-component "A3". Level A components, the final parts, were predicted and designed using the built-up FEA model and tests were only used for design validation. Finally, the overall performance was verified to accordance with the requirements, more precisely the certification specifications.

Table 1.3: Overview of Empirical Investigations Performed within this Thesis as Schematically Drawn in Figure 1.5

ID	Description	Group	Amount	Tests	Investigations
A1	Cockpit Door	Door	1	EMA, Static	Damp., Stiff.
A2	Tailplane	Tailplane	1	EMA, Static	Damp., Stiff., Fail.
A3	Double-T Beam	Tailplane	1	Static	Stiff., Fail.
B1	Omega Beams	Door	3 x 1	EMA, Static	Damp., Stiff., Fail.
B2	Sandwich	Tailplane	3 x 3	Static	Stiff., Fail.
B3	Hybrid Coupons	Door	1 x 8	Static	Stiff., Fail.
C1	UD Coupons	Tailplane	3 x 8	Static	Stiff., Fail.
C2	BD Coupons	Door	2 x 8	Static	Stiff., Fail.
C3	Bistable Plates	Hydro	3 x 3	Hydro-Swelling	Deformation, Mass
C4	Impact Plates	Impact	10 x 4	Impact	Impact, NDI
C5	Crash Cylinders	Crash	4 x 3	Static & Dynamic	Crashworthiness

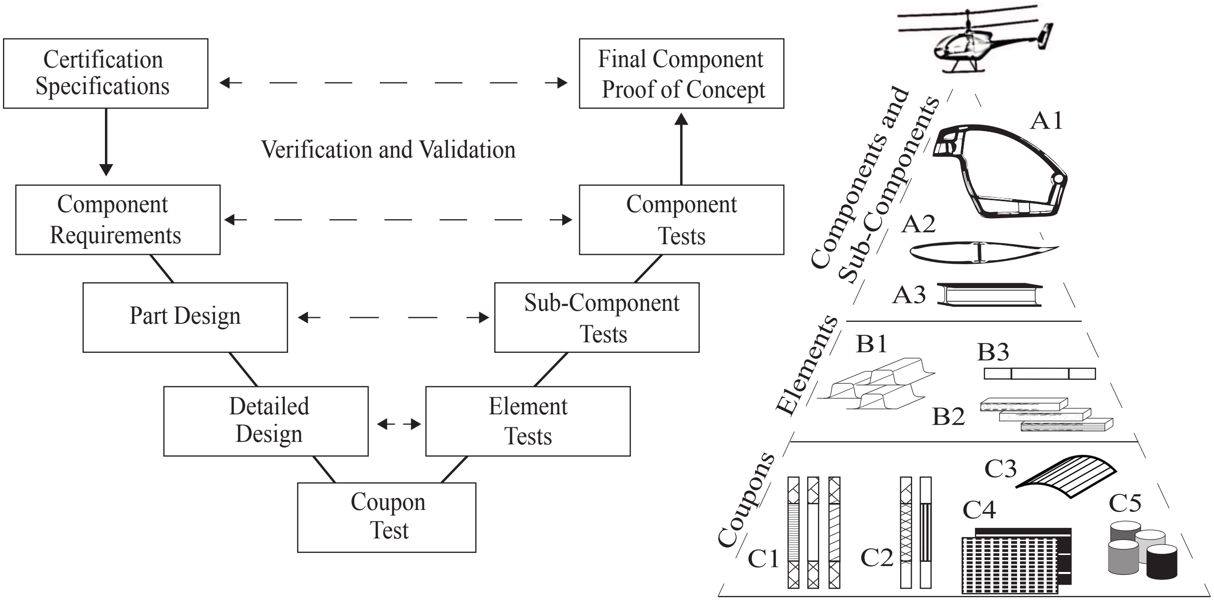

Figure 1.5: Methodology Adapted from the V-Model Approach and the Test Pyramid after Rouchon

Some investigations of the Category C are analyzed by themselves, as they did not contribute directly to the FEA model and the parts' design. These address mainly pretests in order to identify beneficial material properties of flax and its interaction with CFRP as an inter-laminar hybrid. The coupon tests C1, C2, and their derived material models are described in Chapter 2, while the details on the part design and other experimental results are included in Chapter 3.

2 Flax Composite Material — Structural-Mechanical Analysis and FEA Modeling

In this chapter, we focus on material choice of the flax fiber prepregs and describe the applied material analysis techniques. Furthermore, we want to emphasize the differences between natural and conventional fibers, as the intuitive handling, as known from conventional composites, can lead to malfunction. A special regard is put on the material modeling and failure analysis using FEA simulations, precisely the special intend on the flax fiber inherent nonlinear stress-strain relation. Overall, each used material is introduced shortly.

The concluding results contribute to the design and testing of the whole parts in Chapter 3, which then also contribute to the summarizing Chapter 4, where the applicability and the potential of flax composites in aviation structures will be evaluated.

2.1 Flax Fiber Material Choice

The material choice was driven by the primary goal of using bio-based composites. Because flax fibers show superior mechanical properties compared to other natural fibers, the use of flax was determined quickly. The choice of a thermoset matrix was decided in order to simplify the certification proofs, as the current state-of-the-art is barely using thermoplastic matrices for structural aerospace composites. With natural fibers being already new to aerospace applications, this decision was taken in order to avoid multiple modifications and keep the matter of research focused on the new fibers. However, flax fibers pre-impregnated in thermoset matrices are available in manifold configurations such as different thicknesses, manufacturers, weave-style, and fiber grammage. Our research focused on finding the ideal configurations of UD and BD material, to yield the best possible results for the composite application.

Therefore, different flax-epoxy composite suppliers and configurations were analyzed at University of Applied Sciences Hanover (HSH) using VI manufacturing. A summary of the experimentally determined tensile properties is shown in Table 2.1, all tested in $[0]_n$ lay-up. The fibers were combined with four different VI epoxy systems, one purely synthetic epoxy system, Araldite® LY 5052 / Aradur 5052 from Huntsman and three partly bio-sourced matrices, SuperSap (19% bio-based), Resoltech 1800 (33% bio-sourced) and Greenpoxy (56% bio-sourced).

These pretests gave guidance to the chosen flax material. As this work focuses on prepreg manufacturing, the matrix system is not freely selectable and was not matter of investigation. By using prepreg systems, there is typically a higher fiber volume fraction (φ_f) achievable. Thus, the herein summarized VI specimens showed considerably low φ_f, calculated values of these kinds of specimens range from 25 to 37% for the weaves.

Table 2.1: Tensile Properties of Flax Fiber Webs and Weaves from Several Suppliers, Manufactured in a Vacuum Assisted Resin Infusion Technique

Supplier	Type -	Grammage [g m^{-2}]	Thickness [mm]	E-Modulus [GPa]	Strength [MPa]
(UD) Unidirectionally Reinforced					
Bcomp	UD	120	0.282	18.0–21.4	139–185
Lineo	UD	150	0.286	18.7–22.0	187–206
Time-Out	UD	190	0.334	18.3–22.5	159–198
(BD) Bidirectionally Reinforced					
Lineo	twill 2/2	150	0.296	6.9–8.7	90–106
Lineo	twill 2/2	200	0.549	8.5	66
Composites Evolution	twill 2/2	100	0.287	8.4–8.8	76–97
Composites Evolution	twill 2/2	200	0.464	7.1–9.1	70–89
Composites Evolution	twill 2/2	300	0.835	8.9	77
Composites Evolution	twill 2/2	400	0.860	7.9	62
Heger	plain 1/1	220	0.319	6.5–8.9	69–76
Coex	plain 1/1	112	0.315	5.4	36

For the flax fiber material choice, the thickness, strength, and stiffness were evaluated. The thicknesses were considered beneficial, when values were small, because a higher design variation in amount of plies, and thereby variability of angles within the ply, can be achieved. Stiffness and strength values were evaluated beneficial when higher values could be achieved. Two kinds of fabrics were resulting from the selection, one UD sheet and one BD (weave) material.

Comparing the UD results, the highest stiffness values were achieved by the supplier Time-Out, with the 190 g m^{-2} material, but the highest strength values by the Lineo 150 g m^{-2}, with comparable stiffness properties. As a result, the chosen material for the prepreg manufacturing was of the supplier Lineo, namely the FlaxPreg T-UD 110, of even lower thickness.

By comparison of the BD materials, the highest stiffness was achieved by the Composite Evolutions material of 200 g m^{-2}, but again, the highest strength by the Lineo 150 g m^{-2} material. As the proportional difference in strength was higher and again small thickness was taken into account, the chosen material for prepreg manufacturing was also produced by Lineo, namely the FlaxPreg BL150.

The results of prepreg materials, pre-empt here, were up to 32 GPa stiffness and 275 MPa for UD laminates, while 8.70 GPa in stiffness and 92 MPa in strength were achieved with the weave material. These results will be described in detail in Section 2.4. For material inspection, NDI, and impact tests, the Composite Evolution material of $100\,\mathrm{g\,m^{-2}}$ was also tested.

As a remark, tensile and compressive modulus is likely to be unequal for FFRP [115]. It is conspicuous that the $150\,\mathrm{g\,m^{-2}}$ weave is performing better in tensile strength and modulus than the thinner $100\,\mathrm{g\,m^{-2}}$ weave and the thicker $200\,\mathrm{g\,m^{-2}}$ weave. A similar trend was discovered in the impact load tests. The influence of the spinning and weaving on the mesh size and induced twist-angle is itemized in Section 2.6.2.

2.2 Material Processing Methods

There are several manufacturing techniques for composite materials. In this work, specimens were either made by vacuum assisted resin infusion (VI) or by prepreg manufacturing with autoclave curing (prepreg). As most of the used materials are state-of-the-art technology, both procedures are only explained shortly with a focus on the FFRP-specific parameters.

2.2.1 Vacuum Assisted Resin Infusion

This manufacturing method works with dry fabrics laid on a release waxed surface. A flow aid and the resin feed as well as the vacuum connection are then sealed with a seal tape and foil. The injection of resin is supported by the applied vacuum and gravity. The injection speed and the vacuum tightness are important variables to fiber matrix bonding and the amount of voids. A cross-linking reaction is then initiated by temperature and/or time, while the vacuum is maintained. The curing time is defined by the respective resin curing cycle. Due to the high cycle times, this method is only suitable for low batch sizes and rather large structures [28].

One advantage of injection molding is that weave and matrix are variable, the combinations of diverse bio-based epoxy resins and weaves can be tailored, compared to prepregs, where the material combination is set. Also, the amount of epoxy can be regulated in a certain range.

Disadvantages are the typically long processing duration, as the matrix flows slowly and can take hours for large structures. Furthermore, there is typically a lower φ_f and inherent lower mechanical performance, compared to prepreg processing.

By the analysis using CT imaging, there were more voids visible within the FFRP, than for the reference CFRP. A possible explanation is the rougher surface of flax fibers compared to carbon fibers, which adheres voids within the fluid to some extent. Also, significantly better results were achieved with additional pressure applied in the curing cycle, instead of only temperature. The external pressure increases φ_f, and might also reduce voids.

Nevertheless, the more common processing method in aviation structures is the prepreg technique. Consequently, most specimens and experimental investigations in this work were also based on the prepreg process, which is described in more detail in the following.

2.2.2 Prepreg Processing and Autoclave Curing

Using prepreg processing, the primary material is already pre-impregnated with a specific thermoset matrix. These pre-impregnated UD-layers or weaves are applied to the waxed mold surface and sealed in a vacuum with additional external pressure while curing. The curing cycle is again dependent on the resin material and its cross-linking properties.

The prepreg process is shown in Figure 2.2, schematically. In order to determine the input and output based eco-efficiency, the material masses used in production and recycling are included. As the lamination and curing process is similar for carbon and flax prepreg processing, the energy footprint is estimated to be the same.

This process was applied to both, the UD and the BD material. The consolidation of the UD sheets worked well, when the curing cycle from its TDS was applied [181]. In contrast, for the BD material, the inter-laminar adhesion of the woven flax prepreg did not show satisfying results with the curing cycle from its TDS [151]. Two cured layers, which is a considerably thin laminate, could be ripped apart easily. Therefore, different cycles were tested under a variation of time, temperature, and pressure (vacuum pressure as well as external pressure), which are plotted in Figure 2.1.

It was observed, that the matrix bonded more evenly when temperature was risen quickly, but preheating was not feasible with the large molds of the cabin door. Therefore, a quick heating cycle up tp 140°C was applied, in Figure 2.1 Cycle 7. Cycle 0 was only applied for manufacturing the reference door, as its molds did not allow temperatures above 85°C. Cycle 1 was the cycle given in the FlaxPreg BL150 TDS.

Furthermore, strong vacuum was decreasing the contained epoxy and not considered beneficial. It appeared as if the prepreg was lacking epoxy. In other tests, enormously high external pressure ($>$250 bar) resulted in a better laminate quality, but would be too high for the foam molds with rather low compressive resistance. Still, the consolidated material surface still appeared porous. As a result, a moderate external pressure of $+2$ bar was considered sufficient showed the best results in terms of inter-laminar adhesion and surface smoothness.

The unidirectionally reinforced prepreg layers were manufactured with this curing cycle successfully. The woven layers still bonded weakly and manually pulling the layers apart was still possible with low effort. As this phenomenon was explained by a lack of epoxy, additional epoxy film layers were applied. Two ratios of epoxy film to flax prepreg were

tested 1:1 and 1:2. The 1:1 ratio was considered sufficient. As a result, for the development of the cockpit door, each layer of flax prepreg was combined with an epoxy film layer of the type Henkel LOCTITE Aero 7000 EA (TDS [75]).
The process as pictured in Figure 2.2 is exemplary and represents the manufacturing steps of the Aerospace Institute workshop at TUM. The processing steps were generally the same for FFRP and CFRP and their hybridization composites. Therefore, this process was not included in the LCA comparison.

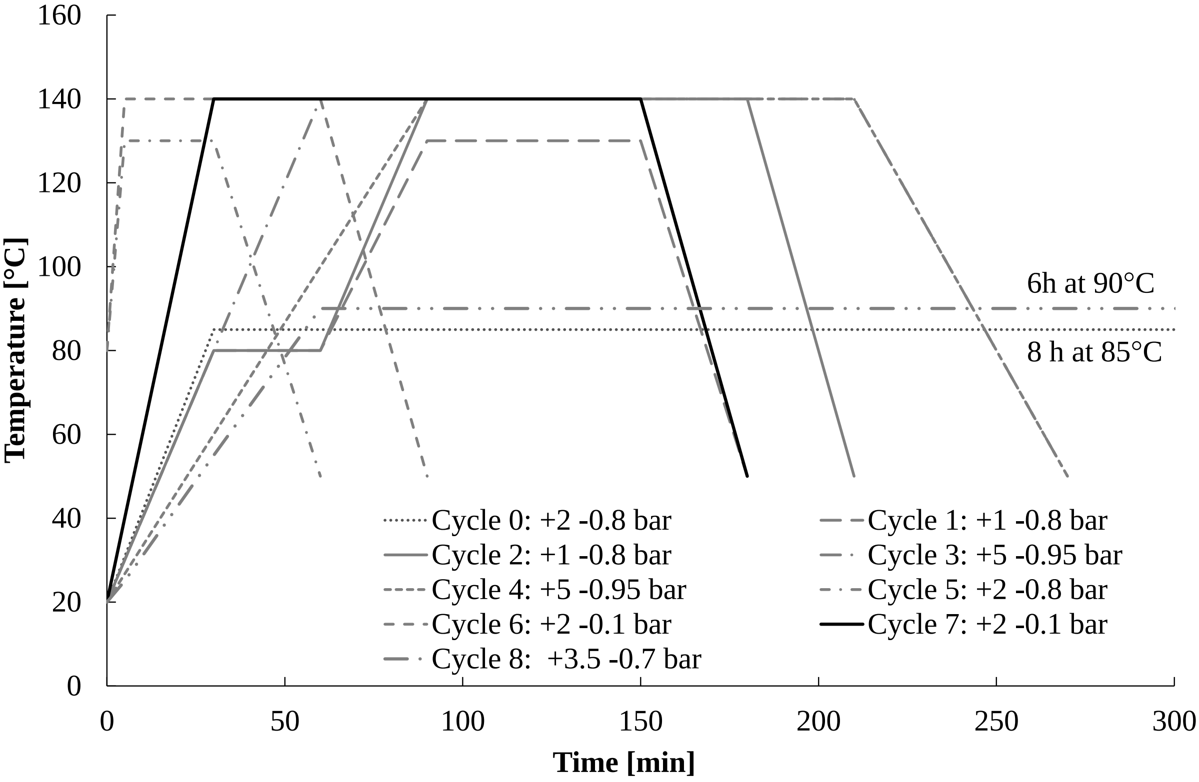

Figure 2.1: Overview of all Tested Curing Cycles for Weave Manufacturing, used Curing Cycle for Flax Prepreg Manufacturing Shown in Black, Other in Gray

2.3 Material Imaging Analysis

In terms of material analysis we want to separate two inspection methods: the destructive material analysis, which is done for quality inspections and in order to analyze the material in more detail; and NDI methods, which are performed in order to identify necessary maintenance or perform quality assurance. Within this section destructive analysis inspection methods are described, including computer tomographic (CT) scans and microscopic imaging. The NDI methods ultrasonic echo analysis and vibration induced thermographic inspection are applied to impact-damaged specimen. These are be described and analyzed within the experimental investigations chapter, Chapter 3.

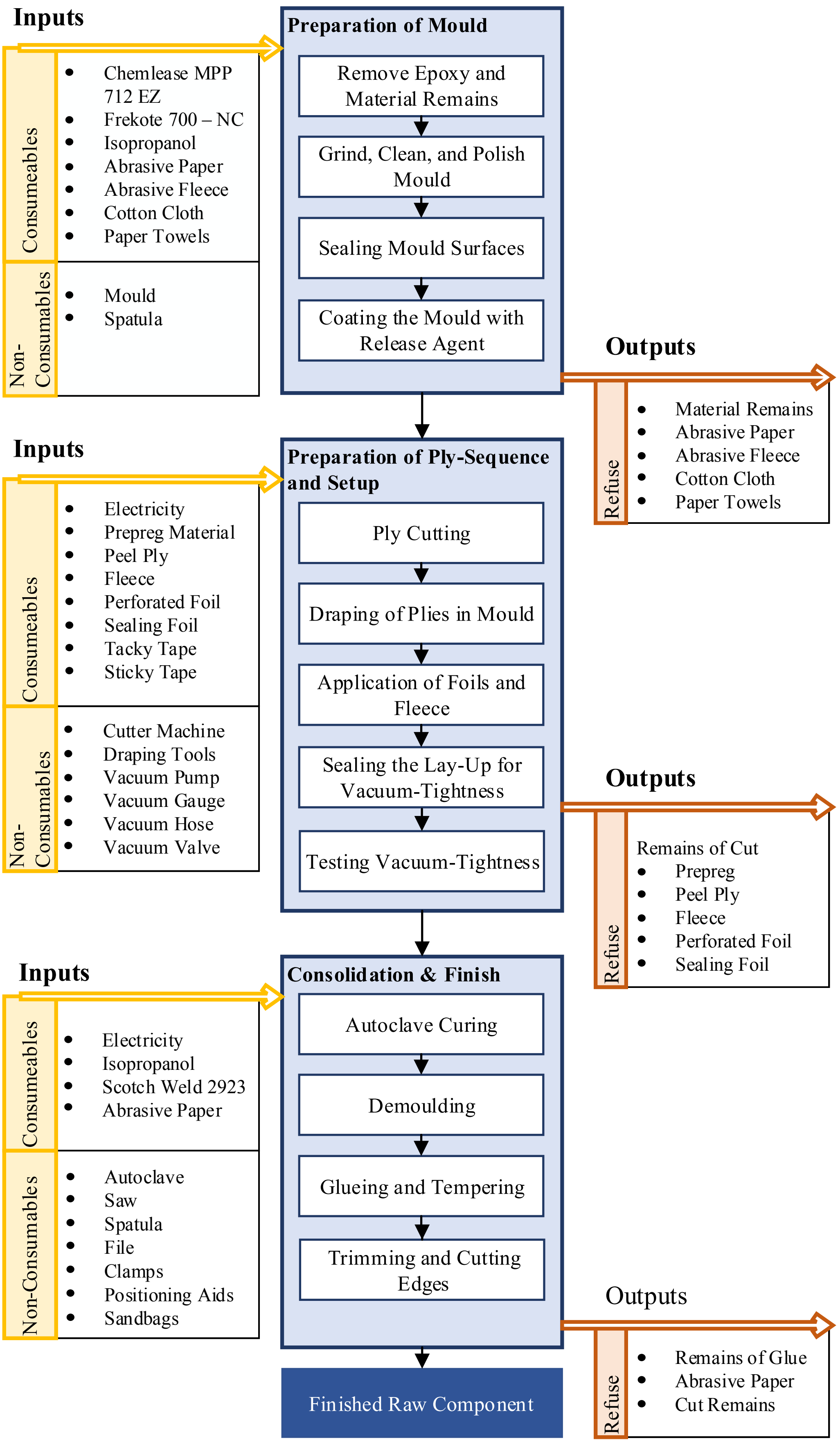

Figure 2.2: Schematic Process of Prepreg Processing, Including Inputs and Outputs

2.3.1 Computer Tomographic Scans

Parts of this section were already published in DLRK2017.

CT scans are used to find out about the fiber matrix adhesion, void contents, and the inter- and intra-laminar composite quality. Additionally, it is possible to measure the φ_f based on contrasts in CT images. The CT images were provided by HSH.

In Figure 2.3 we can see the transversal and cross-sectional view of carbon and flax laminates. The green colored areas are marking the fibers for a φ_f calculation. The computer tomographic scans show clearly the weave pattern in different gray scales of fibers and matrix. When comparing the materials, the different φ_f can be retraced. It is visible, that the mesh and yarn size of the $200\,\mathrm{g\,m^{-2}}$ flax weave is large and show dark gray areas which represent epoxy, while the fiber density looks higher for the $150\,\mathrm{g\,m^{-2}}$ material. Additionally, air voids within the twisted yarn can be seen in the out-of-plane view of flax $200\,\mathrm{g\,m^{-2}}$ and the UD material.

The neater weave in the $150\,\mathrm{g\,m^{-2}}$ scan could explain the better mechanical values, see Table 2.1. Still, the carbon weave shows the highest φ_f. This is also explained in Section 2.6.2, where the 3D-weave-geometry of flax is reproduced and compared to carbon weave. The carbon weave barely shows matrix spaces or voids and the fiber bundles are neatly compacted, which explains the highest fiber volume content of this material.

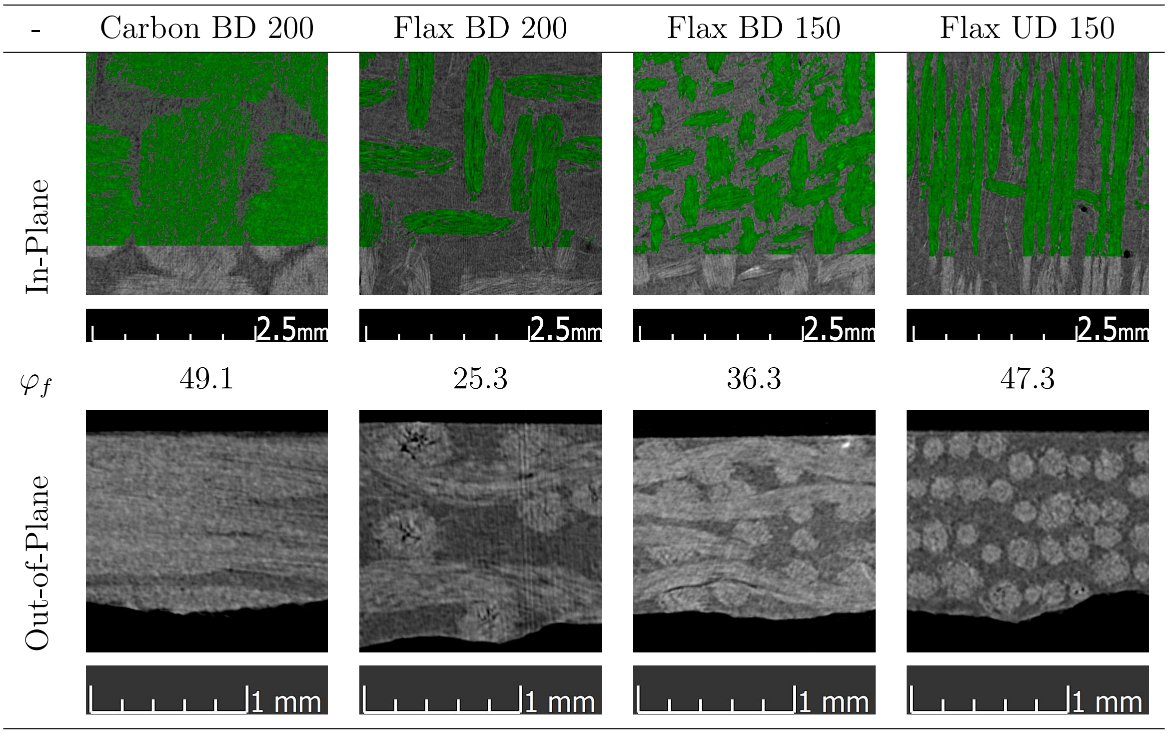

Figure 2.3: CT Scans of VI-Manufactured Carbon and Flax Laminates of Various Fiber Grammage in Perpendicular Cross Sectional Views [166]

As a result, CT scans work well on flax composites and a significant difference between different fiber grammage, and between UD and BD material could be identified. Furthermore, the FFRP weave density is considerably smaller than the CFRP weave density.
The given φ_f values in Figure 2.3 were calculated by Equation (2.1), where m_F and ρ_F account for mass and density of the respective fiber. When hybrids were analyzed, Equation (2.2) was applied, with $i = 1, ..., n$, while n represents the number of different materials used in the hybrid and their areal mass (am). Further subscripts are fiber $()_f$, matrix $()_m$, and hybrid $()_H$.

$$\varphi_f = \frac{\frac{m_f}{\rho_f}}{\frac{m_f}{\rho_f} + \frac{m-m_f}{\rho_m}} \tag{2.1}$$

$$\rho_{f,H} = \sum_i \frac{am_i}{am_H} \cdot \rho_i \tag{2.2}$$

2.3.2 Microscopic Imaging

Parts of this section were already published in ECCM2018.
By the use of microscopic imaging, prepreg laminates of the following stack-ups were analyzed: $[C]_8, [C_2/F_2]_S, [F_2/C_2]_S$, and $[F]_8$, where the pure carbon and flax laminates served as references, and the others were matter of investigation for the capability of inter-laminar hybridization in a sandwich stacking sequence. The flax material used in this inspection was supplied by Lineo, with the identification: FlaxPly BL150, and the carbon weave (identification: CW200-TW2/2-E503-45%) was produced by the SGL Group. Both were chosen due to same thicknesses and comparable meshing sizes. Additionally, as described before in Table 2.1, the $150\,\mathrm{g\,m^{-2}}$ showed better mechanical behavior than the $200\,\mathrm{g\,m^{-2}}$ flax material. All laminates were produced with woven fabrics of the lay-up $[0/90]_8$. The specimens were prepared using prepreg manufacturing with curing parameters as Cycle 3 shows in Figure 2.1.
Flax fibers are not endless, they need to be spun into a yarn for the weave fabrication. The diameter of a yarn is about 5 to 10 times the diameter of a fiber, which can be seen in Figure 2.4. The resulting large bundles lead to a large spacing in the weave between the yarns, as well as a certain void content inside each bundle, which was already visible in the CT scan in Figure 2.3. Some yarns seem to be hollow, which is assessed from the longitudinally cut in the microscopic pictures of FF and FC in 4–20x magnifications. Fiber-matrix bonding showed partly good results in the higher magnifications of 50x where the cross-section is perpendicular to the fiber yarns, but the FF-100x picture shows an intra-laminar fiber-matrix interface crack. Therefore, the flax-fiber-matrix bonding is not consequently evaluated to be good. On the other hand, the hybrid inter-laminar bonding appears better, despite different epoxy systems.
The laminates' φ_f with respective standard deviations, as well as fiber mass fractions and bio-based masses are shown in Table 2.2. The volume content was calculated by

previously presented Equation (2.1), using weight and size measurements combined with data of the respective TDS.

Table 2.2: Averaged Fiber Mass, Fiber Volume, and Bio-Based Mass Fractions with Respective Standard Deviations

[Unit]	φ_f [vol.-%]	s [vol.-%]	Fiber Mass [mass.-%]	s [mass.-%]	Bio-Based Mass [mass.-%]
$[C]_8$	46.2	4.05	56.8	4.02	0.0
$[C_2/F_2]_S$	50.4	2.56	58.6	2.47	24.2
$[F_2/C_2]_S$	50.0	2.72	58.2	2.66	24.0
$[F]_8$	46.3	3.73	51.5	3.74	51.5

Regarding the pure materials, we achieved comparable values for φ_f with the flax weave and the carbon weave. The fiber mass contents diverge, as the density of carbon fibers is higher, but the increase of bio-based mass is evident, even for the hybrid laminates, where the inter- and intra-laminar bonding was considered superior. Therefore, we conclude at this point, that the hybridization was sufficiently increasing the performance in three perspectives: the void content and overall stiffness/strength compared to the flax, and the eco-efficiency compared to the carbon.

We can also see that the φ_f of both hybrid laminates do not order linearly between the φ_f of pure carbon and pure flax laminates, but are significantly higher. In order to verify this calculation, the microscopic inspection was analyzed in the contact area of both laminates. It was observed that a more compact packing due to different fiber diameters of flax and carbon could be a possible explanation. Both laminates were pressed in between each other (Figure 2.4 CF and FC columns, where carbon fibers appear light colored and flax fibers dark). This effect of a denser volumetric packing, when combining two differently sized circular shaped elements can be widely observed in chemistry and physics. Still, the standard deviations of the measured data was high, and this statement needs further verification.

As a conclusion, the hybridization of different fibers and epoxy systems worked well. The choice of the $150\,\mathrm{g\,m^{-2}}$ flax weave could be confirmed, but the flax material showed voids within its yarns and the high fiber volume content was not satisfactorily as epoxy was lacking.

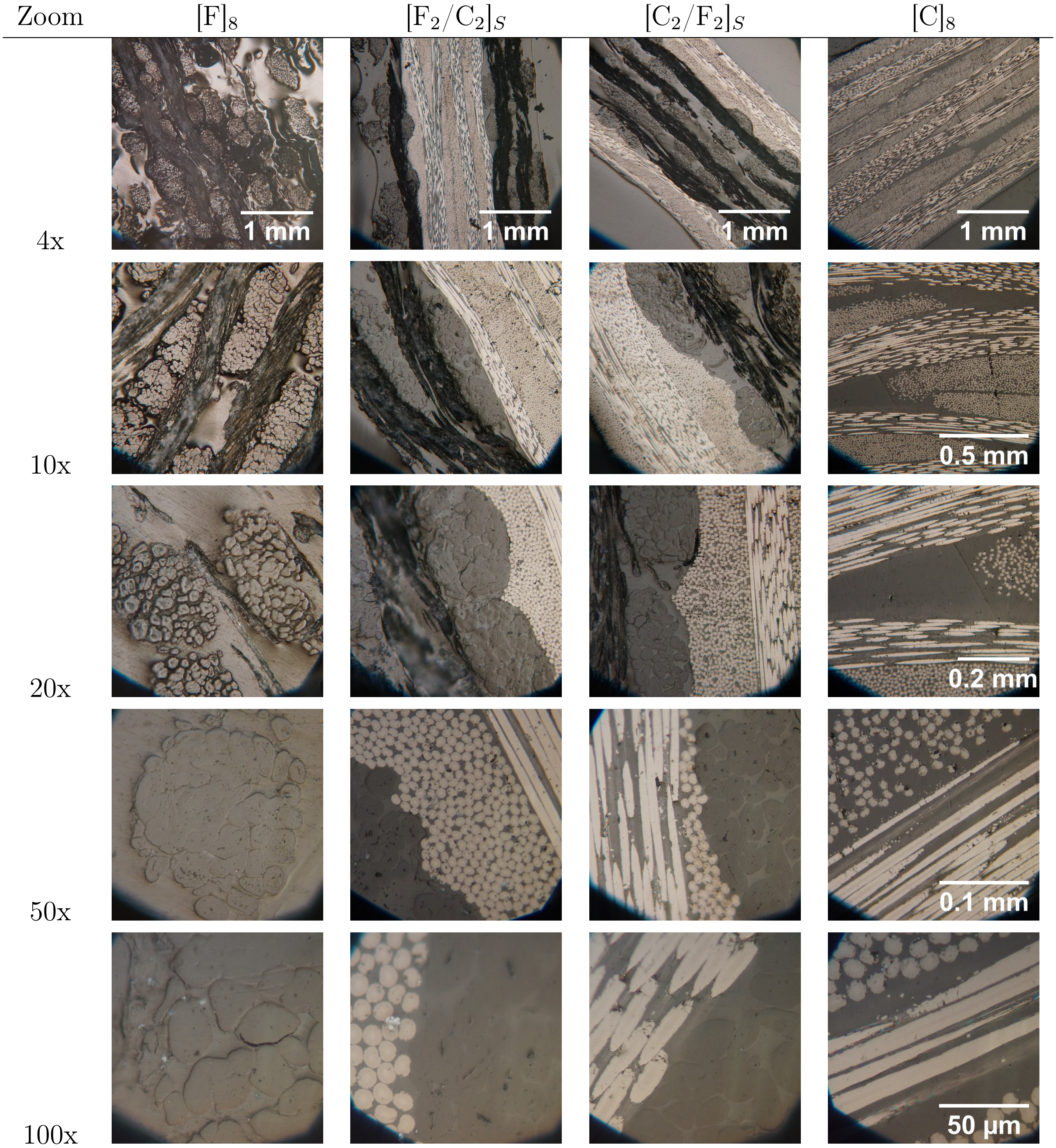

Figure 2.4: Microscopic Inspection with Different Magnifications of Eight-Layered Woven Prepreg Materials: Pure Flax, Pure Carbon, and Hybrid Laminates

2.4 Tensile Test Scope and Experimental Setup

Parts of this section were already published in JMSC2018.

In this section, the experimental setup of all tensile tests, which were used for parameter identification of the material models, are explained. Both composite materials of investigation, flax and carbon, were tested as UD and woven (BD) reinforced laminate.

Elasticity and failure properties were matter of investigation, where each laminate was characterized with lay-ups of $[0]_n$, $[\pm 45]_n$ and $[90]_n$. The results are analyzed and discussed along the applied material models in the next section.

The experiments for characterization of the UD material were performed according to the European Standards DIN EN 2561:1995 [125], for parallel testing, DIN EN 2597:1998 [126], for perpendicular testing, and EN 6031:2015 [60] for characterizing shear properties with tensile tests. The respective standards for the weave characterization were: DIN EN 6031:2015 [60], DIN EN ISO 527-4:1997-07 [49].

The mean values of the specimens' dimensions and respective standard deviations are shown in Figure 2.5 and listed in Table 2.4. The fiber volume content φ_f was calculated by geometry and mass measurements. The letters d-f in 2.5 are used for the measurement evaluation and represent the applied digital extensometers. These were aiming to reduce scatter by application of a high measurement length to the analysis. Further details on the respective experimental procedure are contained in the students theses Steigenb.2018, Huber2018 and [131].

The manufacturing method of the specimens was the prepreg process, where autoclave curing was applied with curing Cycle 7 for the flax specimens and Cycle 8 for the carbon specimens, as defined in Figure 2.1. The prepreg-material was laid down on a polished steel plate and was covered with a same-sized, polished aluminum plate. Then a porous non-woven was applied and a film sheet with sealing strips was used to close the gasket. Thereby, both sides of the plates became even and shiny, which were considered apparently well impregnated surfaces.

For cutting the specimens, a sheet metal cutter was used, which resulted in proper cutting edges, unlike when other methods were applied, such as metal scissors, box cutters and saws. A dry-cutting method was favored to avoid impairing the cured laminate with its hygroscopic and swelling fibers. This was not possible for cutting the tailplane and the crash specimens, due to the included, moderately thick carbon material.

A summary of the geometrical, manufacturing, and weight-based data for each kind of specimens is listed in Table 2.4, where $\bar{x}$ represents the arithmetic mean of the measured specimens and s indicates the standard deviation.

Generally, a low batch-size of 6 to 8 specimens is prone to outliers and the values can not be considered statistically significant. The geometrical data was not analyzed in further detail and only the thickness c is considered to be material dependent in combination with the amount of layers. The density of all flax specimens was significantly lower than the density of the carbon specimens. As carbon fibers are of higher density (approx. $1.80\,\mathrm{kg\,m^{-3}}$) than flax fibers (approx. $1.40\,\mathrm{kg\,m^{-3}}$) this was expected, additionally, the low density of epoxy (approx. $1.10\,\mathrm{kg\,m^{-3}}$) resulted in a reduced density when the fiber volume content was low.

Overall, fiber volume ratios of weaves are typically lower than the ones of unidirectional layers and the fiber volume ratios of flax material were typically lower than the ones of

carbon. Additionally, the UD-cross-ply laminates of flax ([±45]) show lower fiber volume contents than the respective $[0]_n$ and $[90]_n$ specimens. This is explained to eventuate from less compact packing, since perpendicular-aligned fibers do not push in between each other as easily as parallel-aligned fibers. This effect was only observed for the flax-UD samples.
The applied deformation measurement method for the tensile testing was the digital image correlation (DIC) method with the two-camera system ARAMIS. The DIC system measures displacements over the entire specimen area, thereby the fracture and Poisson's ratios can be determined continuously until fracture. As strain gages can influence the measurement when its inherent stiffness is considerably high, this non-contact method was considered suitable. Two references [46, 109] showed that this technique is applicable for epoxy and its reinforced composites.

The used DIC system works with a stochastic pattern, which is applied to the specimens' surface. The cameras have a resolution of 5 MPixels and the free clamping length of the specimens was 150 mm, with the respective widths as listed in Table 2.4. Both resulted in a measurement resolution of 15.3 pixels mm^{-2}. The stochastic contrast pattern was created by dots in the size of 0.30–0.60 mm, aiming 50% black dots and 50% white parts.

The pattern was applied using a compressed-air spray gun. First, the matte white color was applied to the specimens in three layers with fine spray. Next, matte black dots were applied, where the size and density could be adjusted with air pressure, distance, and amount of color, manually. Figure 2.6 shows the pattern on the specimens exemplary on the background layer.

During the test, the two cameras were photographing with rates according to the testing speed, with the overall amount of measurement points aiming approx. 200 images. These are imported as stages into GOM Correlate, a DIC analysis software. Facets of unique patterns are laid over the measurement area; their sizing was 19 x 16 pixels. When the coupon deforms, the facets deformation can be analyzed within this tool.

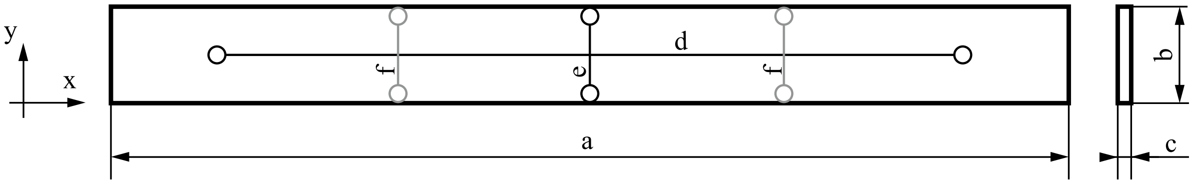

Figure 2.5: Test Specimen Geometry (a, b, and c) and Applied Digital Extensometers (d,e, and f), Coupon-Respective Geometric Values are Listed in Table 2.4

Table 2.3: Coupon Specimen Specifications in Terms of: Geometry, Density, Fiber Volume and Mass Fraction, Amount of Specimens and of Layers, with Arithmetic Mean Values per Specimen Configuration and Respective Standard Deviations

		Mean Dev.	a [mm]	b [mm]	c [mm]	Density [kg cm^{-3}]	φ_{vol} [%]	φ_{mass} [%]	Lay. [-]	No. [-]
F_{UD}	0°	$\bar{x}$	150	15.24	0.89	1.20	55	61	7	10
		s	0.851	0.055	0.013	0.014	0.71	0.69	-	-
	90°	$\bar{x}$	150	16.24	0.80	1.18	56	61	6	8
		s	-	0.315	0.006	0.006	0.36	0.34	-	-
	±45°	$\bar{x}$	150	16.11	1.14	1.16	53	58	8	10
		s	-	0.091	0.025	0.018	0.78	0.76	-	-
C_{UD}	0°	$\bar{x}$	150	15.01	1.13	1.52	59	70	2	6
		s	-	0.020	0.037	0.013	1.84	1.62	-	-
	90°	$\bar{x}$	150	25.01	2.15	1.54	62	73	4	6
		s	-	0.027	0.046	0.009	1.32	1.11	-	-
	±45°	$\bar{x}$	150	25.01	4.45	1.54	62	73	8	6
		s	-	0.014	0.279	0.006	0.81	0.68	-	-
F_W	0°	$\bar{x}$	150	25.74	2.45	1.17	32	39	8	8
		s	-	0.111	0.022	0.008	0.20	0.21	-	-
	±45°	$\bar{x}$	150	25.56	2.44	1.18	32	38	8	8
		s		0.692	0.016	0.008	0.13	0.14	-	-
C_W	0°	$\bar{x}$	150	25.00	1.66	1.48	54	65	8	6
		s	-	0.014	0.028	0.014	0.89	0.81	-	-
	±45°	$\bar{x}$	150	25.00	1.65	1.48	53	65	8	6
		s	-	0.018	0.008	0.004	0.45	0.42	-	-
H_W	±45°	$\bar{x}$	150	25.75	2.14	1.22	37	43	8	8
$([C_1/F_3]_S)$		s	-	0.016	0.025	0.008	0.33	0.47	-	-

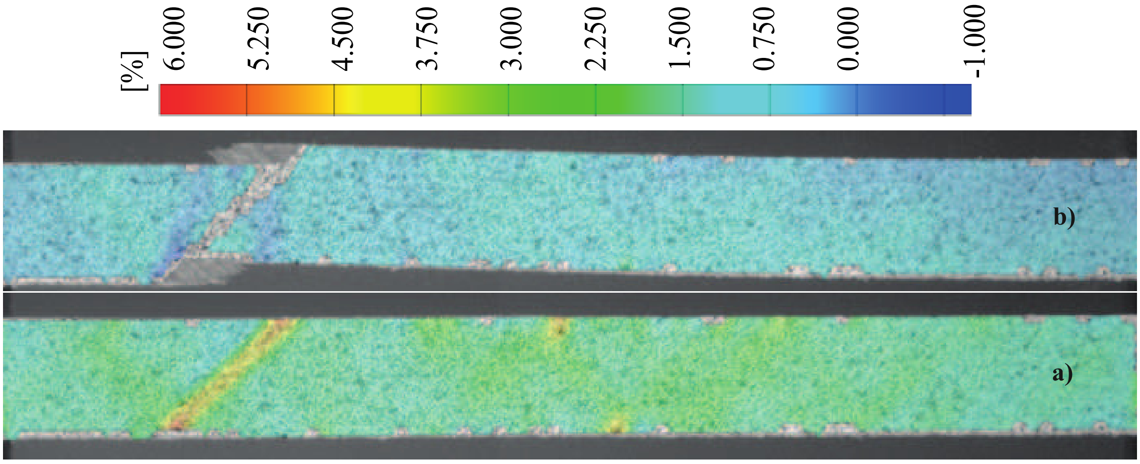

Figure 2.6: Color Plot of Strain [%] in Longitudinal Direction of a [±45] Specimen a) before and b) after Fracture b)

Figure 2.6 shows a [±45] specimen before and after fracture, the color bar indicates the strain in x-direction in [%]. The intra-laminar fracture in 45° shows high strains before fracture, in red and yellow in a), as well as the elastic contraction in terms of a different elastic strain (green and blue), when comparing both measurements of the same color scale. Furthermore, longitudinal plastic deformation is visible after fracture, which is light blue in b) instead of mid-blue as 0% would be.

The noise of facet-strain values was approx. ±0.02%, which was reduced by applying digital extensometers in the results interpretation. The lines within the specimen in Figure 2.5 d, e, and f, represent the extensometers. In transversal direction of the specimen, the initially applied extensometer (e) was limited to the width of the respective specimen (b), which was significantly lower than d and thus resulting in a higher scatter of these measurements. This effect added to the fact that transversal strains were very low within the [90] specimens and thereby the relative scatter considerably high. For these specimens, scatter was reduced by adding two more digital extensometers (f) in 20 mm longitudinal distance. Forces were measured with load cells, where the suitable load cell size was determined from pretests and TDS-values, load cells with maximum forces between 1 and 5 kN were used for the flax specimens, up to 100 kN for the carbon specimens.

The tests were performed on an Instron tension and compression machine. The load introduction in the material was supported by glass-fiber doublers, which were stuck to both ends of all specimens, but the [90] UD-flax specimens. Here, the inherent stiffness was expected to be significantly lower than the stiffness of the glass doublers, so in this case they were replaced by sand paper.

The results of tensile tests and the derived material models for the FEA are described in the next section. In order to distinguish between fiber and specimen coordinates, fiber-oriented directions will be numbered by $i = 1, 2, 3$ and the coordinates $i = x, y, z$ will be used for specimen orientations.

2.5 Stress-Strain Relations and Material Models of Composites

In this section, the results of the performed tensile tests on the used composite materials are described, respective to their material combination. Furthermore, the derived and applied material models are introduced and evaluated. The materials are grouped by their fabric type, first all UD reinforced materials are listed, next all woven composites. Resulting material characteristics and modeling data are applied to the design problems in Chapter 3, an tailplane and a cockpit door of an ultralight helicopter.

Nowadays, modeling composite materials can be done using different approaches. First, there are micro-scale models, where each fiber and the bonding matrix is modeled with several solid elements [1]. Ongoing research is often using micro-scaled models to develop accurate prediction of failure mechanisms. Next, there are models using multiple solid elements per layer with smeared properties, thereby computational cost can be reduced, these models are considered meso-scale [100]. But, as details are diminished, some physical material behavior is typically not modeled properly, such as fiber kinking. Furthermore, as composite layers and respective structures are rather thin, the elements' aspect ratio is prone to locking phenomena. For reasons of computational cost, structures or larger parts are often modeled using shell elements containing properties of all layers, the macro-scale approach (including solid-shell approaches and layered shells). These are capable of proper bending and buckling simulation, which is often the occurring stress state, but are typically not capable of modeling intra-layer failure or detailed inter-laminar behavior.

In terms of stiffness, most of conventional laminates show linear elastic behavior, which results in the fact that most of the macro-scale composite models are using linear stress-strain approaches. Also metallic structures are typically designed within their linear range and the beginning of nonlinearity is considered the yield stress or stress limit.

In this work, the FEA tool ANSYS was used, including its ACP environment for composite pre- and post processing. Mesoscale layered solid elements and macro-scale shell element approaches were used. Either to understand the material behavior and analyze the nonlinear stress-strain relation of flax or for designing the structural parts. The layered solid elements were considering nonlinearities, while for the design of structures shell element approaches within the linear elastic range were considered sufficient.

The next sections describe the behavior of the conventional material CFRP followed by the differences of FFRP to CFRP. First, UD coupons and results are described, introducing a bilinear mesoscale approach to modeling the flax' specific nonlinear behavior. Next, woven coupons are evaluated, where again the conventional CFRP material is discussed first. The bilinear approach is applied to the weaves by additional angles which are determined from the weaves' geometrical data. Finally, an additional failure criterion after Hashin is described, which will be used in the part design in Chapter 3. The derived material specific properties were then applied to the analysis of hybrid, woven coupons.

2.5.1 Tensile Stress-Strain Relation of UD Carbon Composites

Test results of the CFRP coupons will not be described in detail, as CFRP is a state-of-the-art material in aviation industry. Simply, the stress-strain curves of all tested samples and the material modeling data used in the FEA simulation are included.
The tensile stress-strain relations of the $[0]_2$ samples of this material should be kept in mind for the further on described bilinear behavior of UD reinforced FFRP. This plot should underline that conventional materials, such as CFRP, do not show a considerable nonlinear behavior when loaded in fiber direction.
The stress-strain relation of $[\pm 45]_8$ specimens is also nonlinear, which is explained by the progressive damage regarding the cross-ply delamination. Therefore, the further on described model could also be used as a simple approach to modeling cross-ply CFRP laminates. Figure 2.7 shows exemplary stress-strain relations, derived from tensile tests of CFRP-UD samples, performed within [131].

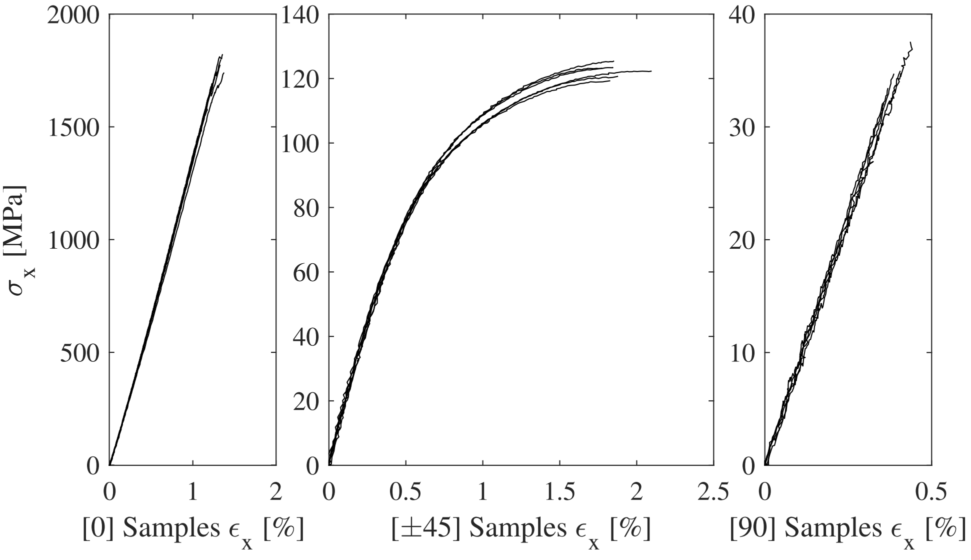

Figure 2.7: Tensile Stress-Strain Relation of Unidirectionally Reinforced CFRP Samples

The experimental results show scatter to some extent, which results from the load cell signal on the one hand and from scatter within deformation analysis by DIC on the other hand. Considering the overall progress, scatter is in an acceptable range.
These curves should serve as reference for evaluating the qualitative progress of the stress-strain relation in conventional laminates and also serve as a benchmark to the performance of the applied measurement technique.
Table 2.4 lists the experimental data derived from the tensile tests of the material "C UD-600-E501-53" by SGL group. Data which was not experimentally determined, but needed in the FEA material model, was obtained from the material's TDS or other related research.

Table 2.4: Experimentally Determined Values from Tensile Tests of UD-Carbon Coupons used in FEA Material Model

Parameter	Unit	Value
Stiffness		
E_1	[GPa]	134.20
$E_2 = E_3$	[GPa]	9.17
$\nu_{12} = \nu_{13}$	[-]	0.30
ν_{23}	[-]	0.42
$G_{12} = G_{13}$	[GPa]	4.96
G_{23}	[GPa]	3.08
Strength		
σ_1	[MPa]	1793.50
$\sigma_2 = \sigma_3$	[MPa]	35.90
$\tau_{12} = \tau_{13}$	[MPa]	62.00
τ_{23}	[MPa]	45.00

2.5.2 Tensile Stress-Strain Relation of UD Flax Composites

Referring to the tensile behavior of the tested UD CFRP coupons, we can see that the typical behavior of conventional composites is purely linear and typically purely elastic. The load induced deformations are reversible when loaded in the fiber-reinforced directions. In flax composites, and other NFRP, there is a reduction in their elastic modulus of approx. 30% beginning at low strains measurable.

Related work also shows a nonlinear tensile response of flax fibers and composites, but also other NFRP [79, 157, 39, 40, 90, 69, 108, 115]. In [132] Pitarresi et al. described a nonlinear stress-strain behavior of flax fibers with the fabrication methods: hand lay-up, vacuum bagging, and resin infusion. The same behavior was observed within this work, where epoxy pre-impregnated fibers and an autoclave-curing process was applied. We conclude that this nonlinearity is inherent in natural and specifically flax fibers and not dependent on the processing.

A decrease in stiffness can be observed when longitudinal strains exceed approximately 0.15%. The plastic elongation was also shown by [114] under cyclic loading. After this "yield" point, the modulus is reduced by about 30%, from approx. initial 32 MPa to 23 MPa. We describe this nonlinearity as bilinear behavior. In [57] cellulose composites are also described in a bilinear approach.

We want to explain this nonlinear behavior by showing an exemplary stress-strain curve of UD FFRP in Figure 2.8. We can see an initial steep inclination up to a yield point K and a less steep inclination to fracture S11 with a reduction of the applied stress to 0 and the respective strain to 0.33%. The initial E$_{ini}$ is plotted besides the reduction in order to show the similarity to the unloading elasticity.

Regarding the exemplary tensile response in Figure 2.8 there are two regions describing the stress-strain relation, one part before the yield point K and another part between K and failure (point S11). These regions are also distinguished by [134]. Furthermore, the plastic elongation after failure $\epsilon^{pl,ult}$ is noticeable. It is assumed that in the first part of the stress-strain curve (between 0 and K), the material behaves elastic. At the yield point K, it starts to yield and deforms plastically. Both parts are almost linear, with the respective moduli E_{ini} and E_{tan}.

The assumption of plasticity after the yield point is likely to be an approximation to the real behavior. In [132] it is shown, that the material still shows thermoelastic behavior after the yield point, which is typically related with an elastic change of volume in the material, but the thermal irradiation is dropping quickly from the beginning on. Regarding the elongation after fracture $\epsilon^{pl,ult}$, and the behavior under cyclic loading, which is experimentally investigated in related research [114, 134, 79, 15, 157], we conclude that the tensile response after the yield point can be described rather plastic than elastic.

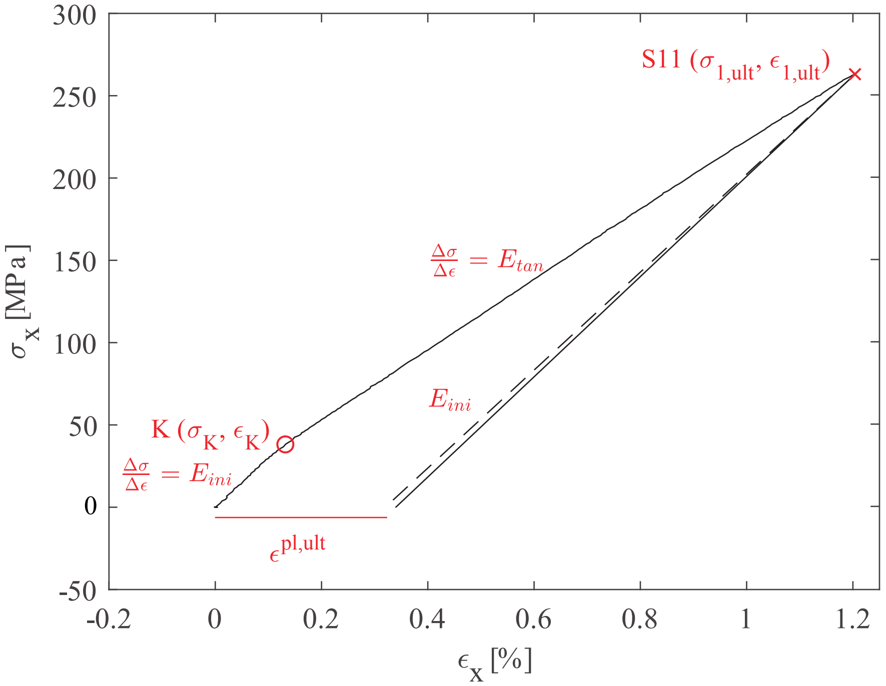

Figure 2.8: Schematic Stress-Strain Curve of Uniaxial Loading on a [0]-UD-FFRP Sample (Curve from Experimental Data of UD0-1 Specimen)

The elongation after fracture $\epsilon^{pl,ult}$ in the $[0]_7$ specimen is significant ($\approx 0.3\%$). The contraction shows a $\frac{\Delta\sigma}{\Delta\epsilon}$ ratio of about the same as in the initial elastic modulus E_{ini}, which supports the described assumptions. Shah et al. [156] also describe the stiffness after the yield point as fairly constant. State-of-the-art linear approaches for flax composites show either a large discrepancy at very high strains, when using a linear approach with the initial elastic modulus. Or, when using an averaged modulus, the values in the area of the yield point differ from measurements [128, 195]. This led to the motivation to model this phenomenon in a simple FEA approach. Other nonlinear modeling approaches are exemplary done by [7, 134, 114, 41], but as yet have not been implemented in an accessible FEA code.

2.5.3 Generalized Hill Potential Theory as Bilinear Orthotropic Material Model

Contents of this section were previously published in JMSC2018.

Motivated by the bilinear behavior of flax fibers themselves, a bilinear elastic-plastic approach was applied, which is based on the generalized Hill potential theory. This theory was primarily developed for metallic plastification, but is easily applicable to composite materials. The method was used to model the nonlinear stress-strain behavior under quasi-static tensile loading of UD FFRP laminates and was found to be sufficient for modeling the progressive damage induced plastification of both, UD flax composites in [0] and in [±45] cross-ply stacking.

For further needs, the Hashin failure mechanisms using the stress strain data of the bilinear model were applied as well. These are also applied to predict the beginning of plastification in the linear shell element models.

The special demand, eliminating several FEA-implemented nonlinear material models, is the need of an orthotropic yield criterion. Most of the implemented nonlinear models use isotropic formulations. The finite element solver ANSYS was used, which contains a bilinear anisotropic model for elastic-plastic deformations based on the generalized Hill potential theory. This was adapted to layered solid elements of different axis orientations.

The generalized Hill potential theory can be understood as an extension to the von Mises yield criterion being able to describe orthotropic yielding, the von Mises yield criterion assumes isotropic material behavior. The following description summarizes contents of the methodology from [9]. The generalized Hill potential theory can describe different material properties and yield strengths in tension, compression, and shear for all three orthotropic directions [159]. It is based on work hardening, which is used to update the yield criterion [179]. Additionally, plastic incompressibility is assumed, which makes the uniaxial yield strengths dependent among each other.

The material is assumed to have three orthogonal planes of symmetry. Thereby, the plastic behavior can be described by the stress-strain response in the three coordinate directions and the corresponding shear stress-strain behavior. For a single composite layer, either woven or unidirectionally reinforced, this assumption is considered valid. From descriptions in [9], the yielding stress in the generalized Hill potential theory is expressed in

Equation (2.3).

$$\sigma_K = (\frac{1}{3}\{\sigma\}^T[\boldsymbol{M}]\{\sigma\} - \frac{1}{3}\{\sigma\}^T\{\boldsymbol{L}\})^{-\frac{1}{2}} \tag{2.3}$$

$[\boldsymbol{M}]$ is a matrix containing the yield stresses and respective orientations. Matrix $[\boldsymbol{M}]$ is a symmetric 6 x 6 matrix with values in the diagonal and in the three top left entries. Vector $\{\boldsymbol{L}\}$ accounts for the delta between tensile and compressive yield strengths. $\{\boldsymbol{L}\}$ can be related to a yield surface translation and the equivalent stress function can be interpreted as shifted by an initial translation [9]. Vector $\{\boldsymbol{L}\}$ has the form of $L_i \neq 0$ for $i = 1, 2, 3$ and $L_i = 0$ for $i = 4, 5, 6$. When σ_K in the FEA model equals the material yield stress K, the material is assumed to yield. The yield criterion equation is then Equation (2.4):

$$\{\sigma\}^T[\boldsymbol{M}]\{\sigma\} - \{\sigma\}^T\{\boldsymbol{L}\} - K = 0 \tag{2.4}$$

Assuming plastic incompressibility, the off-diagonals of [M] can be calculated by the Equations (2.5) and (2.6) leading to Equation (2.7), as similarly explained in [9].

$$\sum_1^3 M_{ji} = 0 \qquad for \qquad j = 1, 2, 3 \tag{2.5}$$

$$\sum_1^3 L_i = 0 \tag{2.6}$$

$$\begin{aligned} M_{12} = M_{21} &= -\frac{1}{2}(M_{11} + M_{22} - M_{33}) \\ M_{13} = M_{31} &= -\frac{1}{2}(M_{11} - M_{22} + M_{33}) \\ M_{23} = M_{23} &= -\frac{1}{2}(-M_{11} + M_{22} + M_{33}) \end{aligned} \tag{2.7}$$

UD reinforced structures show transversal isotropy instead of orthotropy, this difference can easily be adapted with the assumption that the fiber-transversal properties in the second and third direction equal each other. Therefore, in our case, it can be assumed that $M_{22} = M_{33}$ and respectively $M_{12} = M_{13}$.

Plastic incompressibility and the mentioned equations lead to the consistency Equation (2.8), which shows compression and tensile yield strengths being dependent amongst each other, further outlined in [159].

For the specific case of transversal isotropic material, the consistency Equation (2.8) reduces to Equation (2.9). Assuming that the yield stresses in both transversal directions equal each other: $\sigma_{2,t} = \sigma_{3,t}$ and $\sigma_{2,c} = \sigma_{3,c}$.

$$\frac{\sigma_{1,t} - \sigma_{1,c}}{\sigma_{1,t}\sigma_{1,c}} + \frac{\sigma_{2,t} - \sigma_{2,c}}{\sigma_{2,t}\sigma_{2,c}} + \frac{\sigma_{3,t} - \sigma_{3,c}}{\sigma_{3,t}\sigma_{3,c}} = 0 \tag{2.8}$$

$$\frac{\sigma_{1,t} - \sigma_{1,c}}{\sigma_{1,t}\sigma_{1,c}} + 2\frac{\sigma_{2,t} - \sigma_{2,c}}{\sigma_{2,t}\sigma_{2,c}} = 0 \tag{2.9}$$

For shear loads, it is assumed that tensile and compressive yield stresses are the same. Defined shear yield stresses do not influence uniaxial yield stresses, neither tensile nor compressive.

Furthermore, the yield strengths must result in a closed, elliptical yield surface, which is defined when the following criterion is met, also reduced to the transverse isotropic UD material:

$$M_{11}^2 + 2M_{22}^2 - 2(2M_{11}M_{22} + M_{22}^2) < 0 \tag{2.10}$$

This restricts the variability of the axial yield stresses and has to be fulfilled in order to use the FEA approach. This criterion needs to be satisfied through all applied loads, the program itself checks it up to an equivalent plastic strain level of 20%. The $\Delta\kappa$ in plastic work is defined in Equation (2.11) with the plastic strain increment $\Delta\epsilon^{pl}$ and $\bar{\sigma}$ as the average stress over the increment. It changes the yield strengths with plastic straining to the highest applied stress, so when another load cycle is applied, the material behaves elastic until the new yield strength is reached.

$$\Delta\kappa = \{\bar{\sigma}\}\{\Delta\epsilon^{pl}\} \tag{2.11}$$

In this model, only uniaxially reinforced layers are used, where the total plastic work is simplified to Equation (2.12). Exemplary σ_0 equals σ_K for the first load step after yielding, then, as described before, σ_0 equals the updated yield stress. The stress will be calculated as shown in Equation (2.13), with E^{pl} as defined in Equation (2.14). A constant plastic modulus is introduced, which is used to update the stress response.

$$\kappa = \frac{1}{2}\epsilon^{pl}(\sigma_0 + \sigma) \tag{2.12}$$

$$\sigma = \sigma_0 + E^{pl}\epsilon^{pl} \tag{2.13}$$

$$E^{pl} = \frac{E_{ini}E_{tan}}{E_{ini} - E_{tan}} \tag{2.14}$$

E_{tan} represents the tangential elastic modulus after the yield point and E_{ini} the initial elastic modulus. The initial elastic modulus is assumed to be equal in tensile and compressive loading, while the tangential elastic modulus needs to be defined for both, tensile and compressive loading, using experimental data and considering the consistency equations. According to relevant literature, the same initial moduli in tension and compression appears to be an acceptable simplification. In [108] the difference was lower then 2 GPa in all fiber orientations of investigation. But the nonlinearity showed significantly different shapes. This was also an supportive argument for this model, as it can distinguish tensile and compressive yield points and tangent moduli. But compressive stress-strain relations were not investigated within this work.

The combination of Equation (2.12) and (2.13) with the substitution of ϵ^{pl} results in the correlation of Equation (2.15) for anisotropic stress, where j represents the respective direction. Equation (2.15) determines the updated yield stresses by calculating the amount of plastic work done on the material to an equivalent amount of plastic work in each of the directions. The entries of $[\boldsymbol{M}]$ and $\{\boldsymbol{L}\}$ can then be updated.

$$\sigma_j = \sqrt{2E_j^{pl}\kappa + \sigma_{0,j}^2} \tag{2.15}$$

For further detail on the assumed work hardening model, references [9, 159, 179, 76] are recommended.

When the model is applied to FFRP with estimated characteristics from literature, we can model the qualitative progress of stress-strain from different (cross-ply) stackings well, see Figure 2.9. The bilinear behavior of the model, the applicability on modeling different angles and the ability to model plastic deformation under shear loading could be verified. Qualitatively, the curves (Figure 2.9) show similar shapes to respective experimental results in relevant literature [115, 114, 108].

As the model implies work hardening and a plastification of the material, it can also predict a cyclic loading beyond the yield point in a more appropriate way than a purely elastic model. In the bilinear approach, the elastic modulus is assumed to be constant, which is not valid in experimental results, but slightly decreasing with increasing strains [114].

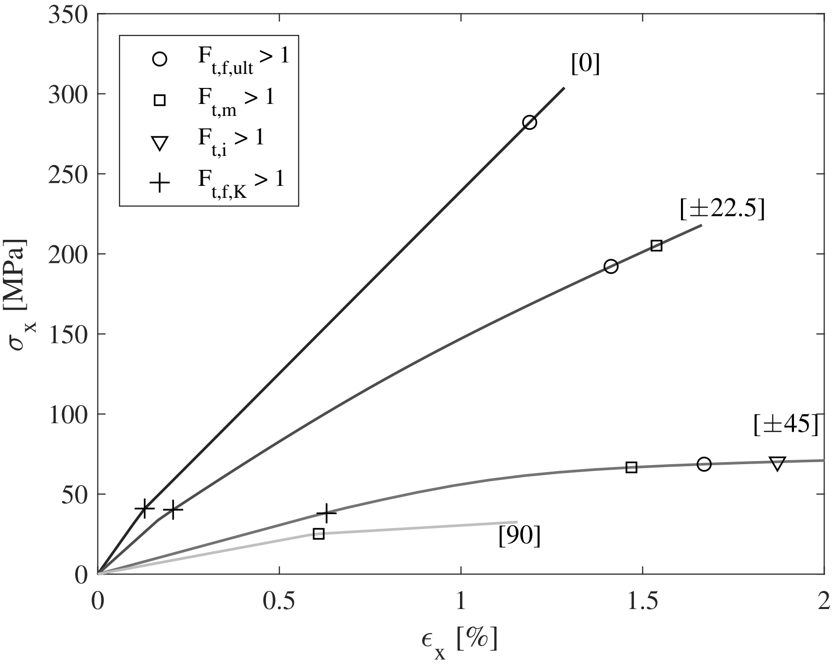

Figure 2.9: Longitudinal Stress-Strain Curves of Bilinear FEA Approach on Exemplary [0], [±22.5], [±45], and [90] UD Cross-Ply FFRP Laminates, Including Standard and Yield Tensile Failure Criteria after Hashin

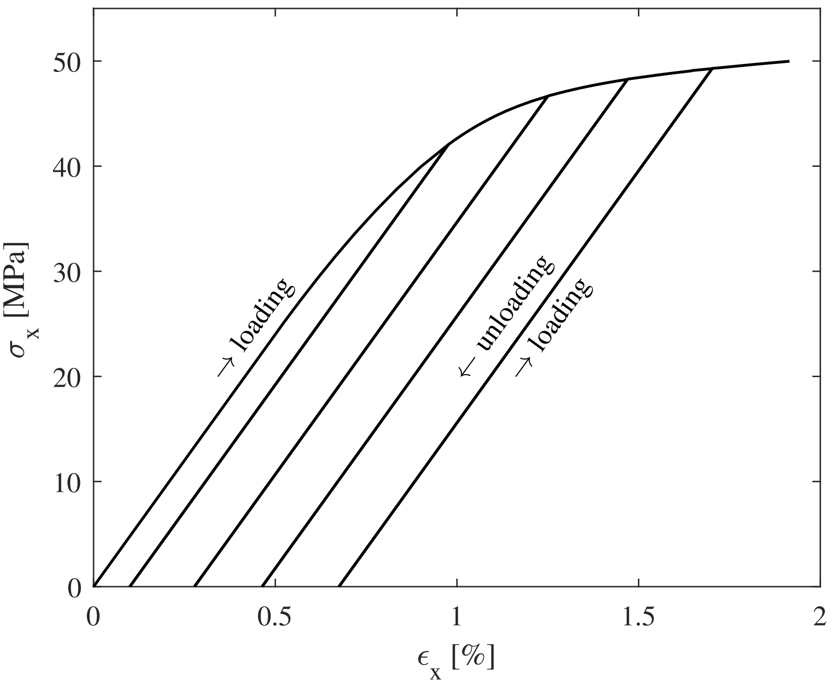

Figure 2.10: Longitudinal Stress-Strain Curve of an Uniaxially Loaded Cross-Ply Laminate of [±45] Stack-up under Force Controlled Cyclic Loading and Unloading in FEA Model with Bilinear Approach

Nevertheless, it could still be used for material behavior predictions on a macro-level, while phenomena, such as hysteresis and the strain dependent evolution of the elastic modulus, need a more detailed material modeling approach. Figure 2.10 gives the model behavior of a [±45] cross-ply laminate under force controlled loading and unloading cycles. This approach could also be beneficial for the plastic or progressive damage modeling of conventional laminates, such as cross-ply and bi-directional glass or carbon fiber reinforced polymers. These also show a nonlinear behavior under tensile loading, but were not focused within this thesis.

In order to evaluate failure, the tensile failure criterion after Hashin [193] was implemented in the user-defined results. The applied equations were the following: Equations (2.16) to (2.18), where index $()_1$ accounts for longitudinal fiber direction, $()_2$ and $()_3$ for transversal fiber directions; $()_t$ indicates tensile, $()_f$ fiber, $()_m$ matrix and $()_i$ inter-laminar failure.

$$F_{t,f} = (\frac{\sigma_{11}}{S_{11}})^2 + (\frac{\tau_{12}}{S_{12}})^2 + (\frac{\tau_{13}}{S_{13}})^2 \tag{2.16}$$

$$F_{t,m} = (\frac{\sigma_{22}}{S_{22}})^2 + (\frac{\tau_{12}}{S_{12}})^2 + (\frac{\tau_{13}}{S_{13}})^2 + (\frac{\tau_{23}}{S_{23}})^2 \tag{2.17}$$

$$F_{t,i} = (\frac{\sigma_{33}}{S_{33}})^2 + (\frac{\tau_{13}}{S_{13}})^2 + (\frac{\tau_{23}}{S_{23}})^2 \tag{2.18}$$

Implementation in ANSYS

The implementation in ANSYS was done by modeling the tensile test specimens as surface geometry, where layers were modeled using layered solid elements with one element per layer. Such layered composites have aspect ratios which are prone to locking, this should be considered when they are used on bending problems.

On the surface geometry of 150 x 15 mm, a mesh of 0.75 mm side-length, with Hex8 elements was created. In the ACP environment, a rosette was aligned with its x-axis in longitudinal fiber direction, its y-axis transversal to the fibers, and z pointing in the stack-up thickness direction. For each fiber direction, a separate rosette is needed, as angular alignments in the ACP will be overwritten by the bilinear commands in the next step. The ACP environment creates a solid element model from the surface geometry by extruding the layers in thickness direction, then, the model is imported to the transient structural analysis. Here, using command snippets in the PREP7 environment, the imported materials, layers, and coordinate systems can be reviewed. The element type is set to SOLID45.

In the analysis part (SOLUTION), the material characteristics are defined, overwriting the initial elastic moduli, Poisson's ratios, and shear moduli for each material. The materials orientation is according to the initially defined rosette. Then, the bilinear anisotropic plasticity approach needs the TB, ANISO command to define the nine yield stresses and tangential moduli. The set initial and tangential moduli are equal for tensile $()_t$ and compressive loads $()_c$.

The load was applied by a linear displacement in x-direction at one end, in 40 equally distributed time steps.

For the analysis, the elements in the middle part of the specimen with x-coordinates between 65 mm and 85 mm and y-coordinates between 5 mm and 10 mm were evaluated in order to diminish the influence of boundary conditions. The user-defined results were used to show the tensile response, SX as stress in the load direction, versus EPTOX and EPTOY to show strains in longitudinal and transversal directions. For the failure criteria, the top layer was selected and the fiber-coordinate system was used.

The EPTOX (EPTOY/EPTOZ) command, as user defined result, gives the sum of the elastic, plastic and creep strains. For more detailed analysis, the EPPL and EPEL commands can be used, referring to either plastic or elastic strains.

In the following, this approach will be applied to the experimentally tested FFRP composite materials. For the $[0]_n$-flax composites, the bilinear approach is used to describe the nonlinear behavior of the fiber itself, for the cross-ply laminates of flax the bilinear approach is used as macro scale approach for simulation of its progressive inter-laminar failure. As proposal for future work, the approach could also be applied to conventional cross-ply laminates. It is expected that also for $[\pm 45]_n$ CFRP laminates the approach could be able to model the nonlinear behavior moderately well, with low computational cost, compared to other micro-scale approaches. As this work is focusing on the structural design of hybrid FFRP parts and thereby the beginning of nonlinearity is particularly relevant, the further applicability of the model was not investigated.

Application of the Bilinear Approach to UD Flax Composites

In this section, the experimental results are described and compared to the FEA calculations using the before described bilinear approach.

In order to determine the specific material characteristics, e.g. input values for the described model, the elastic modulus was calculated for both sections. The yield-point "K" was determined to be at 0.13% strain. To see how the incremental moduli fit with this yield point, the strain was plotted versus the increment of the stress-strain relation over five measurement values. In order to reduce scatter, a range of five measurement values ($j = 5$) was chosen, while the following Equation (2.19) was used and Figure 2.11 shows the graphical comparison.

$$E = \frac{\Delta\sigma_x}{\Delta\epsilon_x} = \frac{\sigma_{i+j} - \sigma_i}{\epsilon_{i+j} - \epsilon_i} \tag{2.19}$$

It appears as if the implementation of a linear or exponentially decreasing course would be more accurate, but the assumption of cell-failure at a certain point and the fact that a range of five measurement points smooths a step decrease, this is considered the physically justifiable approach. Furthermore, in respect to the computational efficiency, we considered this approach beneficial as well.

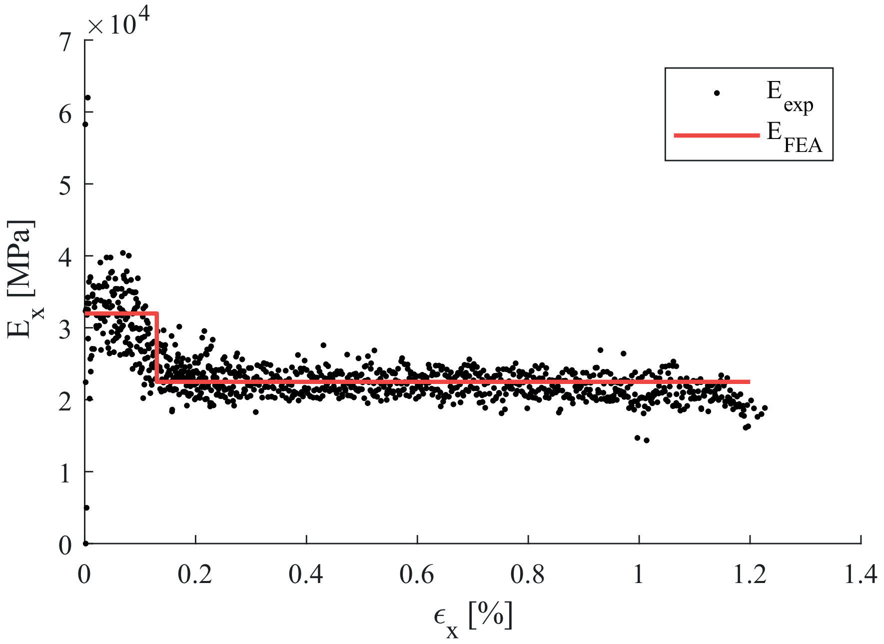

Figure 2.11: Incremental Elastic Moduli of Experimental Data (Dots) and Implemented Bilinear Moduli of FEA (Red Line) over Strain in x-Direction

The initial modulus (E_{ini}) was calculated by the stress-strain ratio with Δ between 0 and 0.1% strain, as the cumulative mean of the results of each specimen. The tangential modulus (E_{tan}) was defined by the moduli between 0.2 and 1% strain, similarly.

The Poisson's ratio was calculated by the ratio between transversal and longitudinal deformation, conventionally; for the $[90]_6$ specimens the arithmetic mean of the three transversal strain values was used. The shear modulus was calculated by means of the DIN EN 6031 [60], see also Equation (2.20), with Δ referring to the difference of respective values at 0.1% strain and 0.5% strain in x-direction.

The transversal stress-strain did not show a bilinear shape, rather a typical linear behavior. Therefore, yielding was defined at its ultimate strength, with the transversal tangent modulus ($E_{2,tan}$) of almost 0, collate Figure 2.13.

The $[45]_8$ specimens also showed a nonlinear behavior, as conventional laminates do as well. Here, shear yielding was again defined at ultimate shear stress and the tangential shear modulus $G_{12,tan}$ was fit to the experimental results by a value of almost 0.

$$G = 0.5 \frac{\Delta\sigma_x}{\Delta\epsilon_x - \Delta\epsilon_y} \tag{2.20}$$

The experimental results showed good agreement with other research, in terms of stress-strain evolutions [156, 157, 114]. In some related publications, the measured initial elastic modulus of the [0] specimens is higher than in this work, but also the fiber volume fraction [69, 17]; while the shear modulus was tested with about the same values (5 MPa lower) as in [16]. The transversal elastic modulus and strength was quite low in this study, compared to other research data [108].

The results of the FEA model are plotted in combination with the experimental results, shown in Figure 2.12, Figure 2.14, and Figure 2.13.

In all stress-strain diagrams, the blue lines show the experimental longitudinal stress-strain curves, indicated as ϵ_x, and the red lines show the transversal contraction, logically a negative strain, labeled ϵ_y. On the y-axis, the applied uniaxial stress is indicated as σ_x.

For the $[0]_7$ specimens, the bilinear FEA model shows good agreement with the experiments. Modeling the stress-strain curve in a bilinear approximation seems to represent the nonlinearity properly. In the first part of the longitudinal stress-strain curve, from 0 to the yield-point K at 41.58 MPa, the results match well. Next, the experimental data does show a smoother transition between the two stiffnesses than the discrete change implemented in the FEA model. Nevertheless, the model orders in each point well in between the range of the experimental data.

Also, the transverse contraction shows good agreement with the model. The yield-point of the experimental data is not as obviously visible as in the longitudinal direction, though the inclination rate and the range of values fit well. The positive contraction strains, right after the load initiation of some specimens', are assumed to be small unwinding processes of the specimens, interpreted wrongly by the DIC measurement technique.

The failure criterion after Hashin shows a tensile fiber failure at about 275 MPa, when us-

Table 2.5: Mean Characteristic Mechanical Values of UD-Flax Material as Experimental Results for Initial, Tangential, and Yield Point Properties

Parameter	Unit	Value
Stiffness		
$E_{1,ini}$	[GPa]	31.985
$E_{1,tan}$	[GPa]	22.482
$E_{2,ini} = E_{3,ini}$	[GPa]	2.214
$E_{2,tan} = E_{3,tan}$	[GPa]	1.500
$\nu_{12} = \nu_{13}$	[-]	0.37
ν_{23}	[-]	0.08
$G_{12,ini} = G_{13,ini}$	[GPa]	1.383
$G_{12,tan} = G_{13,tan}$	[GPa]	0.050
Strength		
$\sigma_{t,1,ult}$	[MPa]	274.5
$\sigma_{t,1,K}$	[MPa]	41.58
$\sigma_{t,2,ult} = \sigma_{t,3,ult}$	[MPa]	3.87
$\sigma_{t,2,K} = \sigma_{t,3,K}$	[MPa]	3.87
$\tau_{12,ult} = \tau_{13,ult}$	[MPa]	24.67
$\tau_{12,K} = \tau_{13,K}$	[MPa]	24.67
Strain		
$\epsilon_{1,ult}$	[%]	1.275
$\epsilon_{1,K}$	[%]	0.130
$\epsilon_{2,ult} = \epsilon_{3,ult}$	[%]	0.204
$\gamma_{12,ult} = \gamma_{13,ult}$	[%]	0.870

ing the ultimate stresses. These will be replaced by the yield stresses in the design, where failure would be apparent at the marked yield point K, see Table 2.5. The $[90]_6$-specimens showed a larger scatter in the experimental data. Especially the transversal strain could not be evaluated properly. The yield point was set to the mean ultimate stress of the experimental data and the modulus was reduced to almost 0. Since there is no sharp yield point visible in the range of the specimen, the bilinear approach is not necessary for the transversal strain behavior ($[90]_6$ specimens). Nevertheless, regarding coupling effects of multi-ply laminates with various angles, this transversal failure causes a sort of progressive damage and change of stiffness. This change is modeled by the bilinear approach. Additionally, in other research results there is a nonlinearity apparent on the transversal stress-strain relation [115]. Within this work the inclusion of this 90°-yield-point influences the $[\pm 45]_8$ curves to good agreement of their nonlinear progression as well. Epoxy itself, which is likely to dominate the transversal behavior, also shows a nonlinear stress-strain behavior.

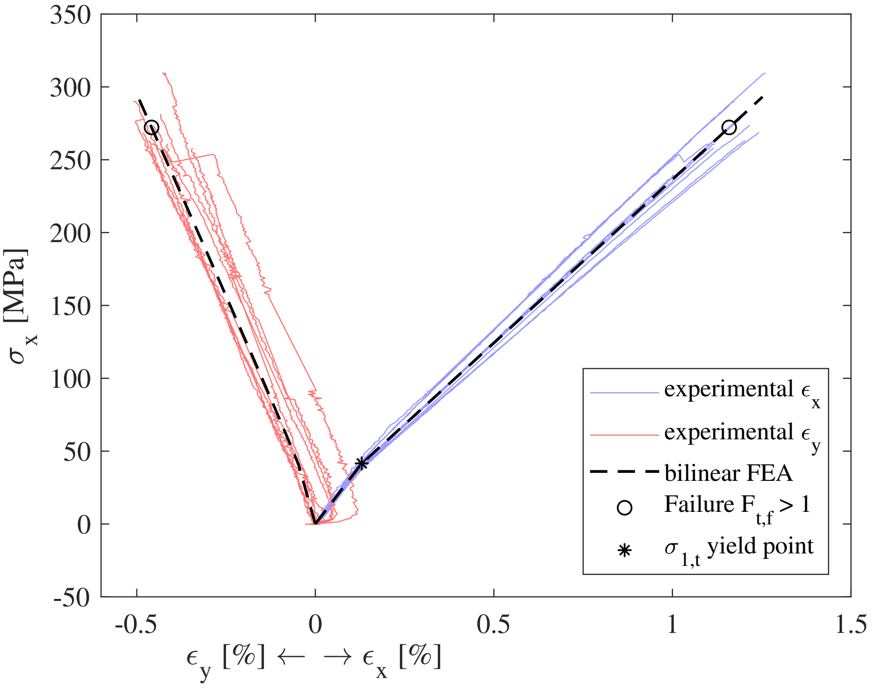

Figure 2.12: Stress-Strain Plots of the Tensile Tests of $[0]_7$-Specimens' Experimental Data and FEA Model using the Bilinear Elastic-Plastic Approach, (Precision $\sigma_x \pm 0.075\,\mathrm{MPa}$, $\epsilon_x \pm 0.02\%$)

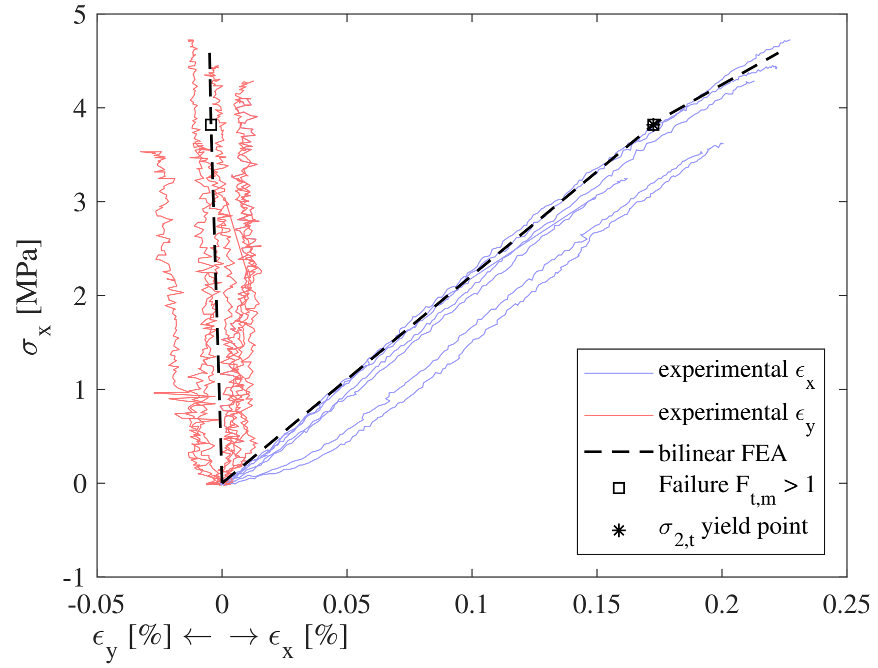

Figure 2.13: Stress-Strain Plots of the $[90]_6$-Specimens' Experimental Data and FEA Model using the Bilinear Elastic-Plastic Approach (Precision $\sigma_x \pm 0.016\,\mathrm{MPa}$, $\epsilon_x \pm 0.02\%$)

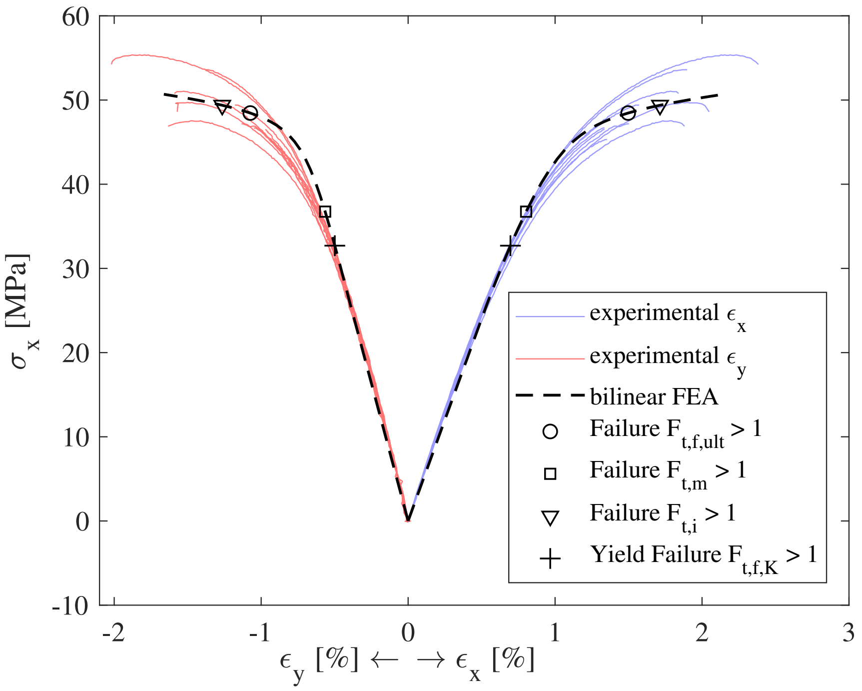

Figure 2.14: Stress-Strain Plots of the $[\pm 45]_8$-Specimens' Experimental Data and FEA Model using the Bilinear Elastic-Plastic Approach (precision $\sigma_x \pm 0.056\,\text{MPa}$, $\epsilon_x \pm 0.02\%$)

Also, in the [90] coupon model, failure after Hashin indicates tensile matrix failure, which is in this case both, ultimate and yield strength. The ultimate strength was determined by a value of $\sigma_{t,2,ult} = 3.87\,\text{MPa}$, which is below the expectations of matrix failure. Possibly the transversal strength of flax fibers is very low and due to a high fiber volume content, the matrix could not absorb the load as well as in other research studies. Another explanation is, that the contained voids in the FFRP and partially lacking epoxy lead to the low strength.

Simulation and experiment of the $[\pm 45]_8$ specimens also shows good agreement, see Figure 2.14. But, both the transversal and longitudinal strain in the experiments show a slight curvature in the first part, which is not implemented in the FEA model. Also, the curvature of the FEA approach is more severely bent than the experiments show. It should be mentioned, that the curve is plotted on the normal stress, which equals the double shear stress, so the shear-yield-point at $\tau_K = 24.67(\hat{=}\frac{\sigma_x}{2})$ MPa is plotted at around 50 MPa σ_x.

The Poisson's ratios fit well, also the failure indicators. The first conventional failure occurs at $\sigma_x = 38.57\,\text{MPa}$, which is tensile matrix failure after the Hashin criterion. At slightly lower stresses, the tensile yield failure occurs, where σ_K instead of σ_{ult} was applied as fiber tensile strength within the Hashin evaluation. This failure indicates the beginning of yielding. The inter-laminar failure and fiber tensile failure represent the total specimen failure.

For this $[\pm 45]_8$ sample we can see that the bilinear yield behavior of the flax fibers does not reduce the application range significantly, as the transversal strength is also low and would lead to failure at only 12% higher loads. We conclude that such a cross-ply laminate might be the application to envisage, as the yield strength in 0° tensile direction reduces the application range in a higher extent.

To summarize the results, the applied bilinear approach seems suitable for the three types of flax fiber reinforced laminates with the different stack-ups: $[0]_7$, $[45]_8$ and $[90]_6$. The approach, working with experimentally determined values, is able to represent the non-linear tensile response of the experimental data well. Additionally, the Hashin criterion is applied to evaluate failure, which also fits the experimental data.

This mesoscale approach does not accurately model the micro-scale damage behavior of flax fibers and their different mechanisms, which can anyways not be applied to the behavior in composites readily [74]. However, the results are rather close to other mesoscale modeling approaches and the approach is simple in terms of implementation and required input data. Additionally, it is already applicable in a public accessible the widely known FEA program, ANSYS. On the other hand the viscoelastic and viscoplastic behavior of the material is neglected. Therefore, the occurring hysteresis can not be simulated with this approach. Furthermore, a comprehensive verification of the model would need an analysis of multi-axis stress states, as the basis in this approach, the von-Mieses yield criterion is not generally valid for composites.

In the following, the applicability of the approach to weaves and conventional laminates will be investigated. Furthermore, the identified yield points will be transferred to linear shell models, which were used for the global design and part analysis.

2.6 Bidirectionally Reinforced Materials

Parts of this section were already published in VFS2019.

First, a short introduction to both BD materials is given, with a focus on the differences between flax and carbon weaves. Next, the bilinearity of weaves is analyzed as well and its yield point identified using the presented bilinear approach.

Bidirectionally reinforced materials are typically woven fibrous materials, which, depending on the weave style, reinforce the material equally in two perpendicular directions. When comparing carbon and flax fibers, it is evident that carbon fibers can be produced endlessly and flax fibers can not, as they are grown by nature. This leads to the problem in processing a weave in which fibers need to be spun into a yarn in order to process them economically. This process inevitably implies fiber angles and leads to more circular shaped bundles, which will be itemized in the following.

Figure 2.15 and 2.17 show these differences schematically in a weave segment. The geometric course of exemplary single fibers are drawn in black, whereby the additional twist

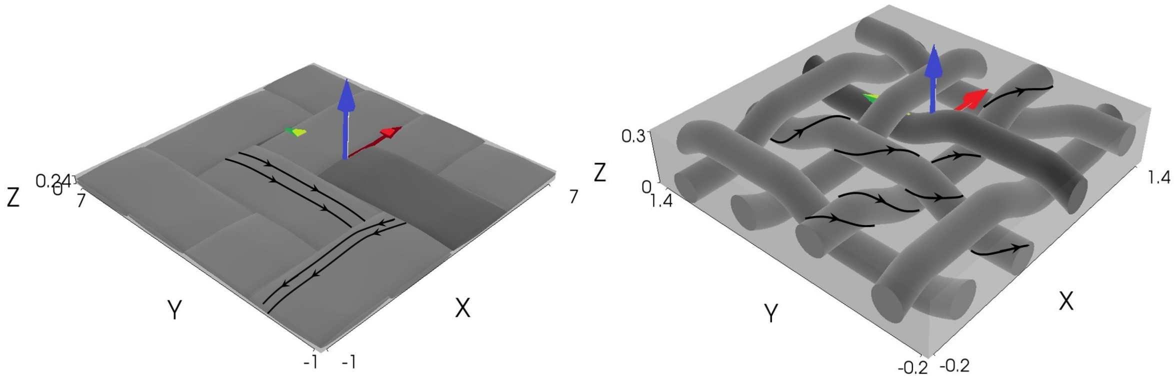

a) b)

Figure 2.15: Schematic 3D Alignment of Fibers and Fiber Bundles in a) Carbon Twill 2/2 and b) Flax Twill 2/2 Weave

angle of flax should be emphasized. Furthermore, the large spaced weave of flax should be shown compared to the neat strongly elliptic bundles in the carbon weave. It is assumed that both inherent properties of FFRP, angles and mesh-sizing, result in a low performance of the weave. When analyzing the volumetric ratios of fibers and epoxy in the schematic graphics using the tool TexGen, the φ_f result in 32% for one flax layer and in 60% for one carbon layer. The carbon values are rather high compared to the measured values of the whole laminate as interlayer spaces will be filled with epoxy. But for the flax laminates these values result in the same values as the mass-geometry related calculations. The flax weave graphic was generated by the tool TexGen using the weave wizard and the input parameters of yarn spacing 0.40 mm and yarn width of 0.16 mm, which was derived by the linear yarn density of $27.80\,\mathrm{g\,km^{-1}}$ and the fiber density of $1.45\,\mathrm{g\,cm^{-3}}$ as given in the data sheet [151]. The laminate thickness was measured on cured, 2–4 layered laminates and was generally bigger than 0.30 mm, the data sheet value of 0.17 mm could not be achieved. In combination with the calculated fiber width, we conclude to an almost circular shape and the cylindrical volume assumption of the yarn width is acceptable. As a result, the weave shows large spacings between the bundles, and undesirable fiber angles are induced by spinning and weaving.

The carbon weave graphic was generated by TexGen as well, on basis of its TDS and measured geometrical data [154]. It shows flat bundles with no induced angles which leads to a higher fiber volume content and a higher mechanical performance.

Table 2.6 summarizes the material data used in the linear FEA material models for both used weaves of flax and carbon. In comparison, a significant difference can be seen in the layer thickness t, the carbon weave is despite its higher weave grammage, thinner than the flax layers. This fact supports the assumption of nearly cylindrical fiber bundles as described before. It also leads to a higher moment of inertia, which increases the flax' specific bending stiffness.

Table 2.6: Stiffness, Strength, and Strain Values of Experimental Results and Smeared Angles Approach, Values Used for Carbon and Flax Woven Material Models in FEA

Parameter	Unit	Flax BD	Carbon BD
Stiffness			
$E_1 = E_2$	[GPa]	8.733	63.010
E_3 *	[GPa]	2.500	6.000
ν_{12}	[-]	0.14	0.14
$\nu_{13} = \nu_{23}$ *	[-]	0.30	0.30
G_{12}	[GPa]	1.371	4.710
$G_{13} = G_{23}$ *	[GPa]	0.500	0.750
Strength			
$\sigma_{t,1,ult} = \sigma_{t,2,ult}$	[MPa]	96.4	776.0
$\sigma_{t,1,K} = \sigma_{t,2,K}$ **	[MPa]	14.0	
$\sigma_{t,3,ult}$ *	[MPa]	31.0	60.0
$\sigma_{t,3,K}$ **	[MPa]	5.9	
$\tau_{12,ult}$	[MPa]	36.3	102.0
$\tau_{12,K}$ **	[MPa]	32.0	
$\tau_{13,ult} = \tau_{23,ult}$ *	[MPa]	25.0	50.0
$\tau_{13,K} = \tau_{23,K}$ *	[MPa]	25.0	
Strain			
$\epsilon_{1,ult} = \epsilon_{2,ult}$	[%]	1.530	1.170
$\epsilon_{1,K} = \epsilon_{2,K}$	[%]	0.150	
$\epsilon_{1,K,45}$	[%]	0.625	
$\epsilon_{3,ult}$ *	[%]	1.000	1.000
$\epsilon_{3,K}$ *	[%]	1.000	

* estimated values, not determined by experimental results

** values for linear BD model determined by bilinear multi-angles UD model

The next sections describe both materials in more detail, especially the methodology to the definition of the yield point K as referenced in Table 2.6 for the flax weave.

2.6.1 Bidirectional Carbon Laminate

CFRP woven materials are not explained in detail in this work. But in order to show a conventional stress-strain behavior as reference, the experimental results from tensile tests of CFRP woven coupons are plotted. A slightly nonlinear but progressively increasing curvature can be seen in 2.16 for the [0/90] samples. This is investigated in detail in [196]

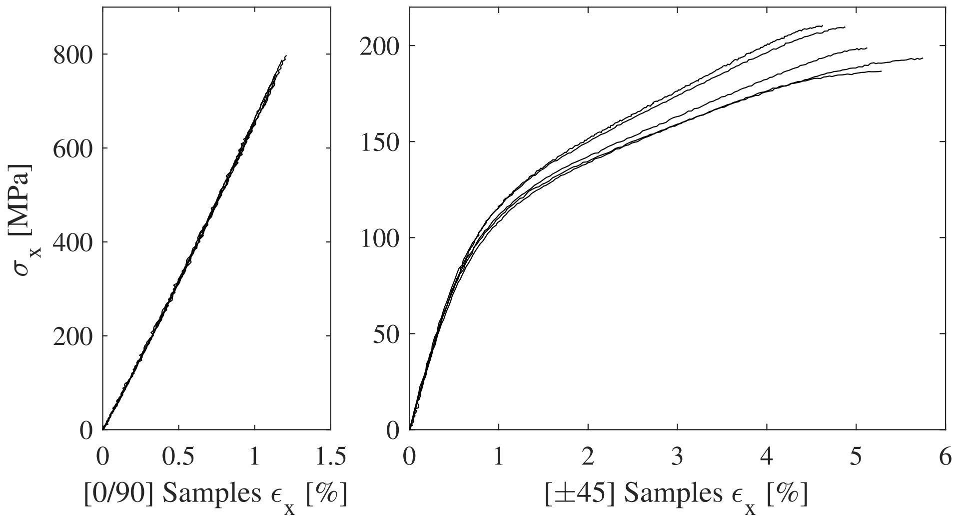

Figure 2.16: Tensile Stress-Strain Relation of Woven (Twill 2/2) CFRP-Reinforced Samples

and accounted to the out-of-plane roving ripples. Considering this behavior as woven-composite characteristic, a linear but slightly progressive stress-strain relation is expected for flax-woven composites. As the identification of the linear elastic modulus is typically derived from the beginning to middle section of the stress-strain relation, results lead to conservative designs. The nonlinear relation of the [±45] specimens is accounted to a progressive inter-laminar damage, analogically to the before described UD cross-ply behavior. For a proper design, a shear failure criterion should identify the beginning of this progressive, plastic-deformation damage.

Nevertheless, the stress-strain relation in fiber direction is considered a benchmark to the analysis of flax woven composites and is generally described as linear. The next section will pick up on the bilinearity of UD flax in combination with the BD fiber directions.

2.6.2 Bidirectional Flax Laminate

In initial attempts of processing a two-layered laminate from the flax prepreg weave (Lineo FlaxPreg BL150) problems with a proper inter-laminar bonding occurred. Parameter studies on the curing cycle, including a variation of temperature, time, and pressure, did not lead to satisfying results, see Section 2.2. Therefore, an epoxy film (Henkel Loctite EA 7000 Aero) was added in a proportion of 1:1 to the weave. As a result, a proper inter-laminar bonding was produced. On the downside, by using the additional epoxy film layers, the fiber volume content was reduced significantly to only 32%, compared to the manufacturer's given values in the TDS of 45%.

With this material combination, coupon tensile tests were performed in $[0]_8$ and $[45]_8$ fiber-orientations, which equals the BD fiber-orientations of [0/90] and [±45].

It turned out, analogically to the unidirectionally reinforced specimens, the stress-strain relations do not follow a linear correlation, but a nonlinear one. In order to identify a quantitative yield criterion for the weave, the bilinear approach, initially developed for unidirectionally reinforced laminates, was adapted. Therefore, a smeared approach of UD layers in a multi-angle lay-up was used, in combination with the φ_f-related reduced values in accordance to the Rule of Mixtures (ROM).
First, the materials' characteristic properties were reduced, in account to their lower φ_f. The initial UD material data from the previous results is again listed in Table 2.7. With the ROM upper and lower boundary equations, Equation (2.21) and (2.22), the material characteristics for the weave were calculated. The equations can generally be applied for the estimation of properties in conventional composites, while Equation (2.21) represents the upper-bound values and Equation (2.22) the lower-bound values [144].

$$E_{comp,||} = \varphi_f \cdot E_f + (1 - \varphi_f) \cdot E_m \tag{2.21}$$

$$E_{comp,\perp} = (\frac{\varphi_f}{E_f} + \frac{1 - \varphi_f}{E_m})^{-1} \tag{2.22}$$

Table 2.7: Material Characteristics Calculation with Upper-Bound and Lower-Bound ROM for Transformation of UD Data to the Multi-Angle UD Model of the BD Material

	[Unit]	UD	ROM$_{UB,f}$	ROM$_{LB,f}$	Matrix	ROM$_{UB,W}$	ROM$_{LB,W}$
(Equation)			(2.21)	(2.22)		(2.21)	(2.22)
φ_f	-	0.55				0.32	0.32
Stiffness							
$E_{1,ini}$	[GPa]	31.985	55.291	-5.652	3.500	**20.073**	7.264
$E_{2/3,ini}$	[GPa]	2.214	1.162	1.702	3.500	2.752	**2.616**
$E_{1,tan}$	[GPa]	22.482	38.013	-6.541	3.500	**14.544**	6.879
$E_{2/3,tan}$	[GPa]	1.500	-0.136	1.022	3.500	2.336	**1.971**
$\nu_{12/13}$	-	0.37	0.40	0.41	0.33	0.35	**0.35**
ν_{23}	-	0.08	-0.12	0.05	0.33	0.18	**0.12**
$G_{12/13,ini}$	[GPa]	1.383	1.492	1.515	1.250	**1.327**	1.324
$G_{23,ini}$	[GPa]	1.000	0.795	0.859	1.250	**1.105**	1.091
$G_{12/13,tan}$	[GPa]	0.050	-0.932	0.028	1.250	0.552	**0.084**
$G_{23,tan}$	[GPa]	0.050	-0.932	0.028	1.250	0.552	**0.084**
Strength							
$\sigma_{t,1,K}$	[MPa]	41.58	57.60	152.97	22.00	33.39	**30.30**
$\sigma_{t,1,ult}$	[MPa]	274.50	429.55	-333.11	45.00	**178.53**	87.62
$\sigma_{t,2/3}$	[MPa]	3.87	-10.96	2.31	22.00	11.45	**5.90**
$\tau_{12/13/23}$	[MPa]	24.67	-0.15	17.00	55.00	37.00	**32.00**

The upper-bound ROM is assuming same strains in fiber and matrix, while the lower-bound ROM or inverse ROM is assuming summarized strains for fiber and matrix. Typically, the upper-bound ROM gives proper values for elasticity in fiber direction and the lower-bound ROM for transversal directions. With this background and the exclusion of unphysical values for pure fiber or matrix characteristics, the values for the UD-stacked model were determined and are written bold in Table 2.7.

The weave itself was modeled by UD layers of half thickness and a [0/90] stacking, which means contained values in Table 2.7 are considering stacked UD material and do not represent the values used for the linear BD model and design.

Next, different angles were derived from the geometrical basics of the weave and applied in the lay-up. Figure 2.17 shows schematically the angles which are geometrically induced from spinning and weaving.

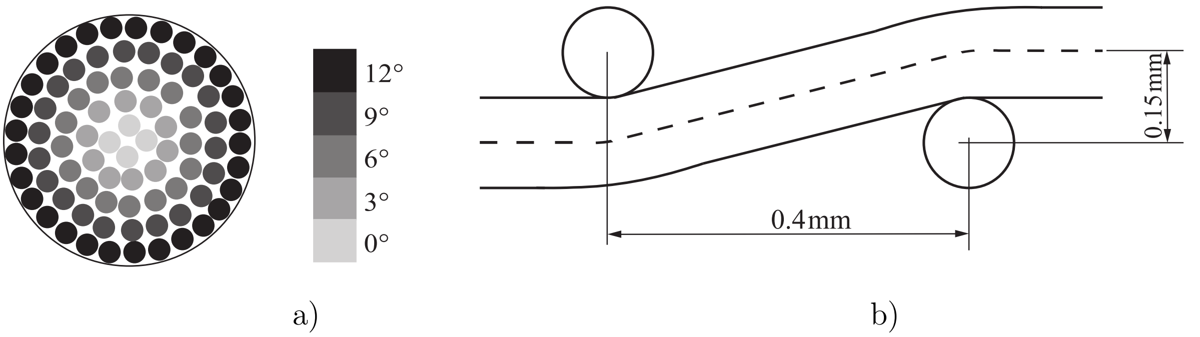

Figure 2.17: Geometrically Induced Angles by Flax Fiber Processing from Spinning and Weaving, a) Schematic Cross-Section of a Fiber Bundle, b) Weave Geometry

We assume that there is an angle induced by spinning of the fiber yarns, a) in Figure 2.17 and by weaving of the yarns, schematically in b). The angles induced by spinning of the yarns themselves range from 0 to 12° in our model. Mehmood et al. [118] showed that over a wide range of yarn diameters and weave grammages the mean twisting angle from yarn spinning is 12.1° with a standard deviation of ± 3.3°. This angle was measured on the outside of the yarns, it is assumed that the fibers in the inside of a yarn are not twisted to this extent.

The angles induced by weaving range locally from 0° to 20.5°, when assuming the given geometry as calculated in Section 2.6 and the measured thickness of approximately 0.30 mm. The used angle for the weave was calculated by the ratio of yarn length to weave length, Equation (2.23), with the yarn spacing $s_{Yarn,F} = 0.40\,\text{mm}$ for flax and $s_{Yarn,C} = 2\,\text{mm}$ for carbon as measured and given in respective data sheets [181, 155], further $t_F = 0.30\,\text{mm}$ was used for the FFRP and $t_C = 0.20\,\text{mm}$ for the CFRP. These values were approximated from measurements on respective samples.

$$\alpha_{Weave} = \arccos \frac{s_{Yarn} + \sqrt{s_{Yarn}^2 + \frac{t}{2}^2}}{2 \cdot s_{Yarn}} \tag{2.23}$$

The given values result in an overall weave-induced angle of 14.7° for the flax weave and 2° for the carbon weave. As the progressive stress-strain relation of carbon shows, the weave-induced angle reduces the stiffness of the composite, especially in the beginning. The geometries show that the induced angles are a lot higher for the flax composite than for the carbon weave, see Figure 2.15.

Combining both 3D angles in 2D, we assume a total of induced angles in a range of 14.7° to 26.8°. These angles for spinning and weaving were applied as additional fiber angles in a cross-ply setup, where the standard deviations are only included for the lower boundary as the major goal is to identify the beginning of material yielding. So the approximated lay-up was created with the stack-up $[\pm 10/\pm 14/\pm 18/\pm 22/\pm 26]$, where each direction contained half-thickness UD-layers in [0/90] fiber orientation.

With the described approach the FEA results compared to the experimental data are shown in Figure 2.18. The experimental data is plotted in light blue and red, while the modeled FEA approach is given in black; the determined failure, analogically to the UD samples are marked by a cross, a square, and a circle.

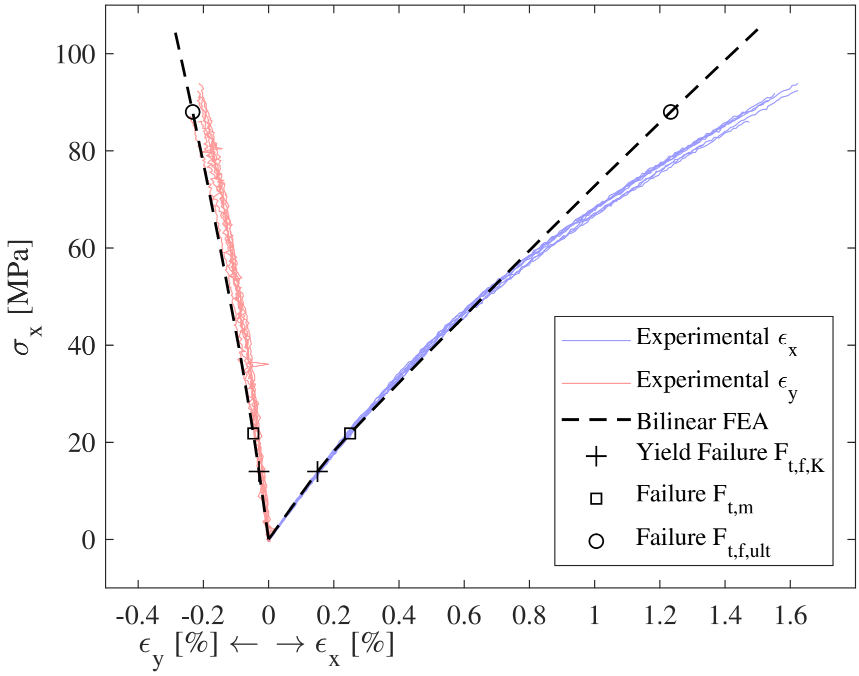

Figure 2.18: Tensile Test Data of [0/90] Specimens and Bilinear Approach with Multi-Angle UD Lay-Up Including Hashin Yield and Ultimate Failure Criteria

The bilinear approach could not perfectly match the experimental data. Nevertheless, the applied angles with the bilinear approach lead to a nonlinear stress-strain relation of a digressively decreasing shape, which was observed in the experiments. It is assumed that the load carrying fibers are changing and thereby the degressively curved shape is generated. As the approach is not modeling fiber and matrix in detail, but in a smeared material model, apparently, some phenomena of the progressive damage can not be simulated. Nevertheless, the purpose of the model, to identify a yield point, could be pursued. It can be seen that the experimental data begins to diverge from a linear behavior between 0.2 and 0.4% strain. The identified yield failure at 0.15% represents an acceptable, conservatively low yield strain.

The yield failure was determined by the Hashin criterion using the data as in Table 2.7 and by the beginning of plastic strain as the FEA predicted it. Then the yield failure was adapted to the linear model, which resulted in a yield stress of approximately $\sigma_{t,1,K} = 14\,\mathrm{MPa}$ for the weave in both reinforcement directions. The conventional failure criteria, which indicates tensile matrix failure, is probably predicting too low stresses, as the approach was pursued by UD plies in a multi-angle configuration instead of BD reinforcements. Thereby E_2 is of too low stiffness and the transversal strength too low as well. Nevertheless, as the first failure was the fiber yield failure, we consider this criterion as critical design parameter and disregard the slightly higher matrix failure. The ultimate fiber failure represents the ultimate strength of the experimental data well.

Next, [±45] specimens were tested under uniaxial loading. Here, only a [±45] stacking was sufficient for modeling. As yielding of the smallest fiber angles introduce the nonlinearity, smaller angles than 45° would yield at too low stresses, therefore, the 2D approximation is considered not suitable in this case and the real fiber orientations were used for the model.

Figure 2.19 shows the experimental results of the [±45] specimens and the bilinear approach in a purely [±45] lay-up. It can be seen, that the model matches well with the experimental data. Only in the stiffness transition, the experimental data is showing a quicker stiffness reduction than the bilinear model. Yielding starts at 0.625% strain in this model, which happens at approx. 26 MPa. This point was identified by the yield failure criterion and represents also tensile matrix failure.

Again, the tensile matrix failure is probably underestimating the real material performance, as the low transversal strength of the UD samples influence the analysis. Still, we consider the yield failure as beginning of plastic deformation. The ultimate fiber failure was predicted at too low strains, where again, the low transversal stiffness is considered accountable.

For reasons of simplification and computational efficiency, the global model used shell elements with a linear material approach with stiffness and strength properties as listed before in Table 2.6. Therefore, the herein derived yield point was adapted to the BD linear material model, this means $\sigma_{t,1,K} = 14\,\mathrm{MPa}$ is also applied to $\sigma_{t,2,K}$. Other material characteristic data was applied directly from the coupon experimental results, such as the stiffness and ultimate strength.

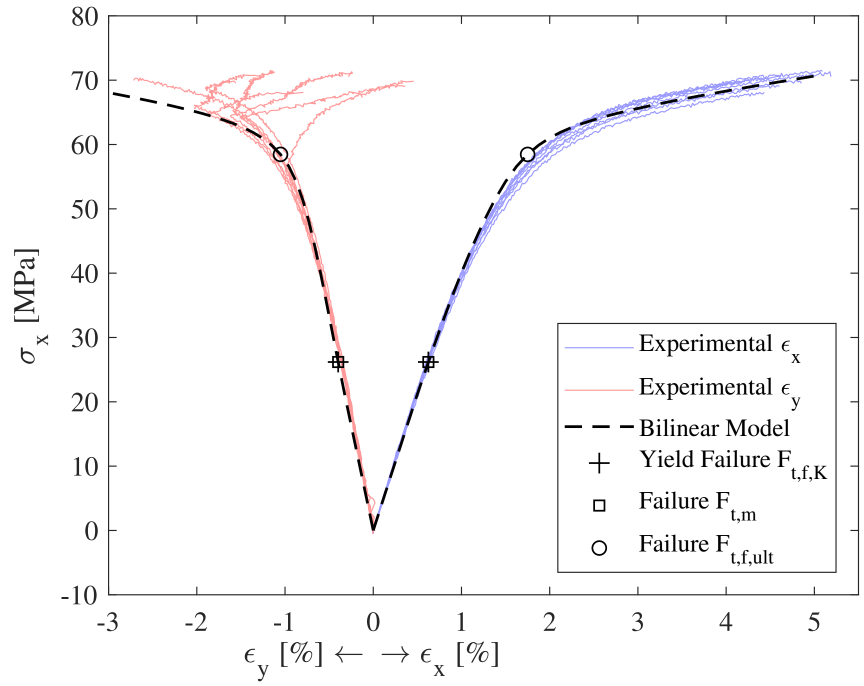

Figure 2.19: Tensile Test Data of [±45] Specimens and Bilinear FEA Approach with Multi-Angle UD Lay-Up Including Hashin Yield and Ultimate Failure Criteria

The identified yielding values at K are used in a Hashin failure analysis as defined before, in Equations (2.16) to (2.18). The derived yield criterion was applied for loads where no permanent deformation was allowed, whereas the maximum stress criterion was applied for load cases where permanent deformation was allowed, analogically to the design evaluation with UD material. The next section compares the derived values with literature data and describes the applied Hashin failure in detail.

2.7 Failure Analysis in Context to Relevant Literature

Some reviews and models of natural fiber composites, and FFRP in particular, do not regard the nonlinear behavior of the fibers themselves in tensile loading in detail [85, 128, 195]. But this behavior is considered as evident design parameter, which needs to be regarded when designing NFRP structures [134].

The change in stiffness in the stress-strain curve might appear neglectably small. But if we compare the stiffness in the beginning to the stiffness in the end, there is a difference between the moduli of approx. 30%. Furthermore, the question whether this deformation should be described as yielding or viscoplasticity is answered differently throughout the current state of science. Shah et. al. claimed the beginning of yielding at $\epsilon \approxeq 0.15\%$ and proved this using cyclic testing [158, 157]. While other research is claiming a viscoelastic and viscoplastic behavior to cause the nonlinearity, such as [97, 134, 145].

Nevertheless, both approaches agree upon the importance of the nonlinear behavior and both approaches constitute the beginning of a plastic deformation, which is not reversible and as experimental results show inherent with a stiffness degradation. The following Table 2.8 summarizes the identified "yield points" or "beginning of viscoplasticity" in available research.

Poilâne et al. [134] also divides the nonlinearity into two regions, the first region is claimed "elastic", the second region "none-elastic". This was applied by the bilinear approach within this work as well.

In order to properly include a yield point, a macro-scale approach was derived for modeling the stress-strain relation. There is also other relevant research available, presenting modeling approaches for these kinds of composites [145, 114, 8, 41, 161]. The herein presented approach is considered simpler and is readily available in the FEA software ANSYS, but does not include hysteresis or viscoelastic and -plastic behavior. Also, the herein presented model is of lower fidelity and needs further verification in multi-axis stress states, but in combination with the Hashin criterion for the application it was considered a straightforward approach for part-design needs.

For further designs, the identified yield point will be applied to the parts tailplane and cabin door in terms of a failure criterion. Major importance was put on the identification of this plastification point herein namely yield point K.

The Hashin criterion was chosen within this work, as it is a simple criterion, which is considering shear-tensile-stress correlations and does not need further empirical values. However, the identified yield points are likely to be adaptable to any other stress or strain related failure criterion.

When flax fibers are tested as single fibers, there is another nonlinearity visible. The stiffness decreases, as visible within composites, and then increases again towards the ultimate strength [15, 38]. As we could not see a significant increase when testing composites and the stiffness-constrained design was limited to the low strained area anyways, this phenomenon was neglected.

Research on short, non-oriented NFRP claim that there is no degradation in stiffness observable [182, 116]. As the investigated stresses in these references were low as well as the φ_f, these results do not apply to the herein investigated high-performance applications.

As a conclusion, we introduced a yield failure, which regards the fiber yielding under tensile load. When we include this yield stress in the failure evaluation after Hashin (Equations (2.16) to (2.18)) the failure stress reduces significantly, see Figure 2.20 and 2.21. The Figures show failure of tensile stress in fiber direction in combination with shear stress in $()_{12}$ direction.

For the UD material, the reduction in fiber tensile direction is high, the tensile strength is reduced from approx. 275 MPa to only around 40 MPa, which equals only 15% of the ultimate strength. When regarded that fiber yielding is not likely to result in catastrophic

failure, we could reduce the safety margin. In our technology demonstrator parts, the yield failure was applied to the conservatively determined loads without safety margin, while the standard approach with safety margin was evaluated with the ultimate strength, where the additional safety factor was 1.875 (standard $S_F = 1.5$ times additional 1.25 for composites). Dependant on the loading direction (compare Figures 2.12 and 2.14) the yield failure or the ultimate failure is the design-limiting constraint. Nevertheless, in a cross-ply stack-up the yield failure is reducing the laminate strength to approx. 90% of its conventional matrix failure. This reduction is not as significant as the one in 0° loading. Analogically to the UD material, this yield failure was applied to the new part design using weaves. Here the material characteristics in laminate orientations 1 and 2 are the same. Figure 2.21 shows tensile over shear failure as derived from the experimental data and by the models. The models include the multi-angle UD ROM approach as well as the applied yield failure data of the linear BD model.
It also has to be regarded that there were no tests on compression strength and multi-axis stress failure done, which would be necessary for a comprehensive failure evaluation. For the further design evaluation in the FEA models, compression strength values were estimated from relevant literature data.

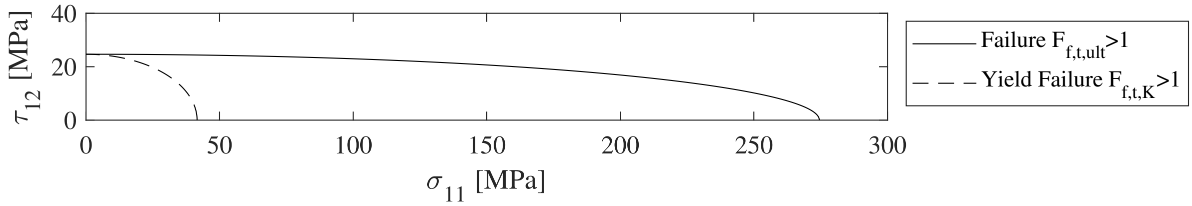

Figure 2.20: Shear and Tensile Stress Combined Failure of UD Material with Ultimate and Yield Stresses and the Hashin Criterion

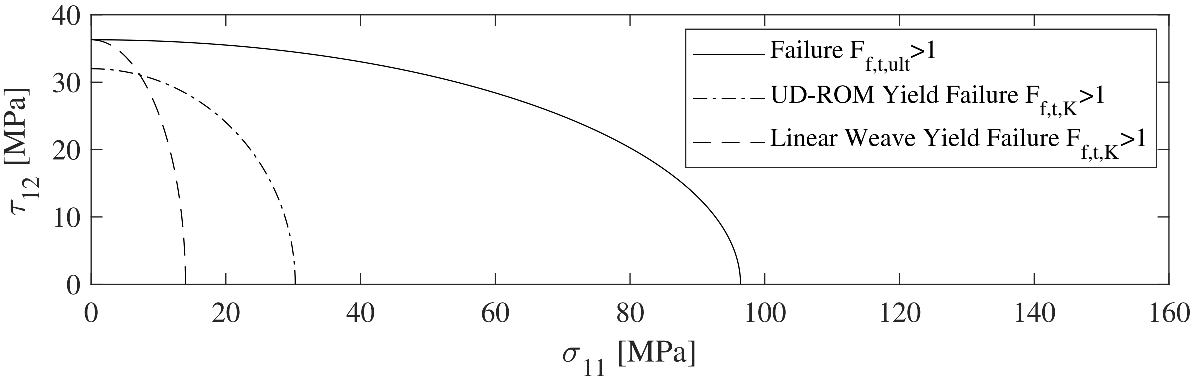

Figure 2.21: Shear and Tensile Stress Combined Failure of BD-Material with Ultimate and Yield Stresses of the Multi-Angle UD Model and the Linear Weave Model after Hashin

Table 2.8: Comparison of Yield Points as Derived by Experimental Results and Other Relevant Literature

[Unit]	Source	φ_f [%]	Yield Strain [%]	Yield Stress [MPa]	Initial $E_{\|\|}$ [GPa]
Unidirectional					
FFRP UD	exp.	55	0.13	42	32
FFRP UD	[134]	-	-	23.8	31.5
FFRP UD	[79]*	53–63	0.12–0.18	32.3–46.6	27.8–29.9
FFRP UD	[108]	44	0.2–0.3	-	22.8
FFRP UD	[157]	40	0.15	-	15
FFRP twisted	[134]	-	-	33.2	26.9
FFRP UD ROM	exp./calc.	32	0.13	30.3	32
Bi-Directional					
FFRP BD	exp.	32	0.15	14	8.7

*various modifications

2.8 Inter-Laminar Hybridization of Woven Flax-Carbon Composites

As local reinforcements by carbon-fiber weaves were envisaged, tensile tests with the symmetric lay-up $[C_{45}, F_{45,3}]_S$ of eight layers in total were performed and used to verify the composite layer modeling with derived data from pure flax and carbon specimens in the FEA model. ANSYS and other FEA-tools working with shell elements for composite modeling refer to the CLT where the in-plane properties of an element are defined by an ABD matrix. The general summarized form is shown in Equation (2.24) [176].

$$\begin{Bmatrix} n \\ m \end{Bmatrix} = \begin{bmatrix} A & B \\ B & D \end{bmatrix} \begin{Bmatrix} \epsilon^0 \\ \kappa \end{Bmatrix} \tag{2.24}$$

Each entry of the ABD matrix is representing a 3x3 matrix itself, where A is representing the in-plane stiffness, D the bending stiffness and B the bending-extension coupling. There is several relevant literature describing this widely applied procedure, therefore, it will not be explained in detail [176, 174]. This matrix can be rotated with respect to the fiber orientations. The entries in the ABD matrix for the CLT are typically determined from empirical engineering constants. In case of a symmetrical and balanced laminate, the Equations (2.25) to (2.28) show exemplary the formulaic connections of entries in A and engineering constants.

$$E_x = \frac{1}{(A^{-1})_{11} \cdot t} \tag{2.25}$$

$$E_y = \frac{1}{(A^{-1})_{22} \cdot t} \tag{2.26}$$

$$G_{xy} = \frac{1}{(A^{-1})_{66} \cdot t} \tag{2.27}$$

$$\nu_{xy} = \frac{(A^{-1})_{12}}{(A^{-1})_{22}} \tag{2.28}$$

For a hybrid material, the ABD matrix of each element is assembled by weighting the multiple stiffnesses by their ply thickness. Polar plots were derived by the described methodology, the results are shown in Figure 2.22.

The polar plots of the linear material models were based on tensile test data. The [±45] sample's stiffness was in good agreement with the CLT results. It can be seen that by the addition of only two carbon layers to the flax material, the stiffness can be enhanced by almost three times from 8.70 GPa to 21.40 GPa. It can also be emphasized, that the elastic and shear modulus of the hybrid weave is at approximately one third of the one of carbon. It is expected that with increasing weave quality, the performance of both, the pure flax and the hybrid can be significantly increased.

The described CLT is also applied within Ansys. We applied the linear material model in shell elements to tensile coupons, analogical to the later on part design, and compared the stress-strain relation to the experimental results. In Figure 2.23 we can see that the experimental results of the hybrid samples match well with the simple linear weave model and the beginning nonlinearity is predicted at the right position for the FFRP layers. The ultimate failure of the CFRP layers is predicting the global failure well, while the ultimate FFRP failure shows rather too high strength.

Concluding to the next chapter, only unloaded areas or areas of low stiffness contribution can be built using flax, while high-loaded areas need to be reinforced effectively using CFRP. The hybridization worked well and can be applied for reinforcements of the cabin door. Further tests on local reinforcements were performed, which give guidance to the analysis of discrete changes in stiffness.

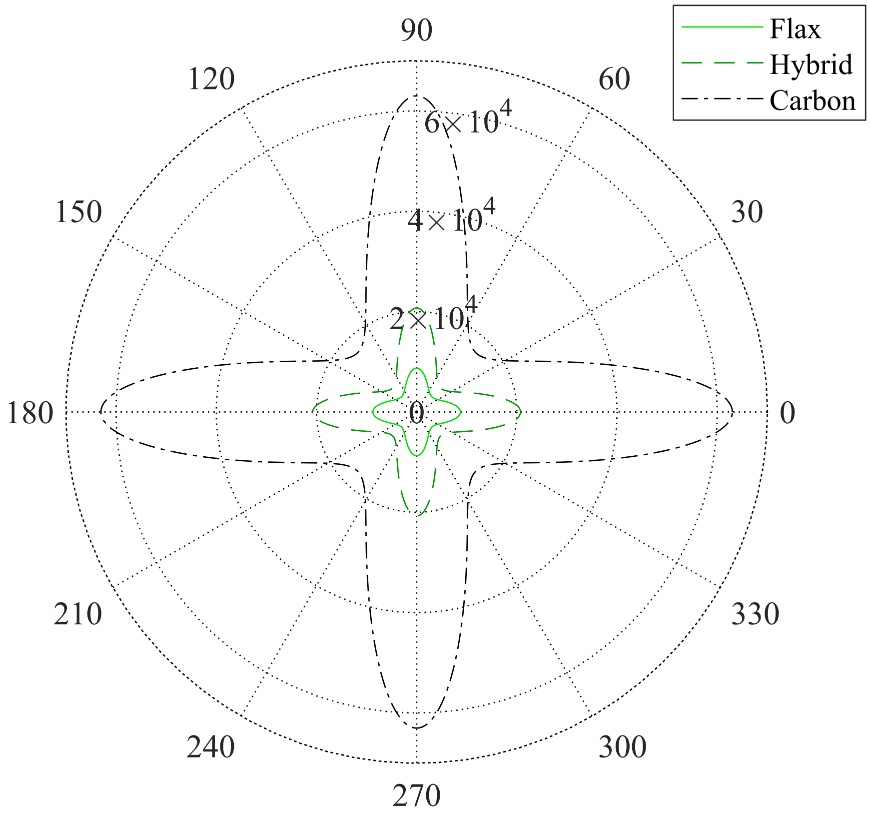

a) E-Modulus [MPa]

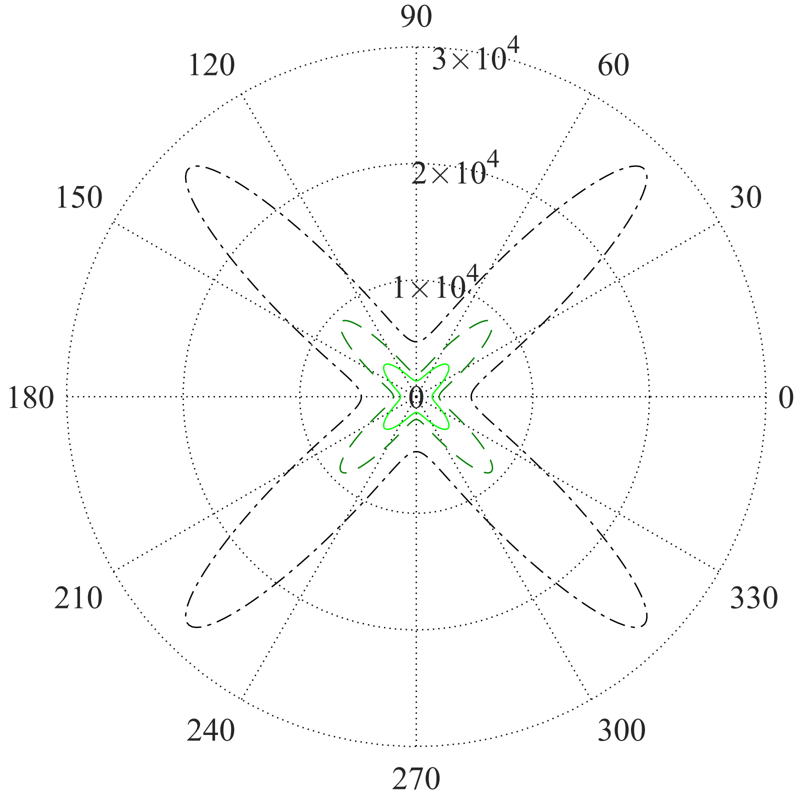

b) G-Modulus [MPa]

Figure 2.22: Tensile Elasticity Properties of Woven Flax, Carbon, and Hybrid Material Regarding their Fiber Orientation

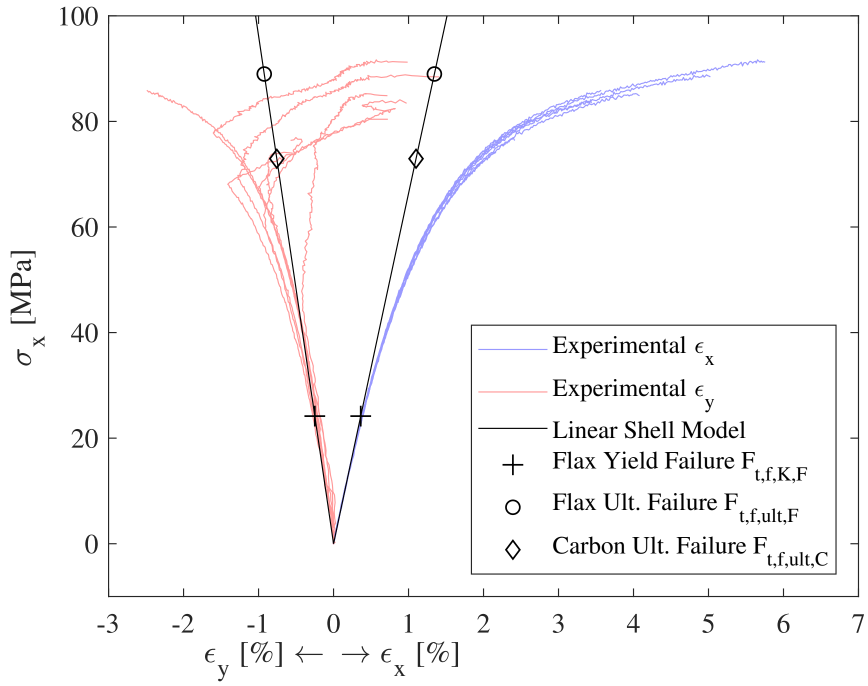

Figure 2.23: Stress-Strain Relation of Hybrid [±45] Specimens with Linear FEA Material Model and Shell Elements, Including the Derived Failure Criteria

2.9 Epoxies and Glues

A short overview on the used epoxy systems in the UD, BD, and hybrid materials should be given in this section. Generally, a composite consists of a fiber and a matrix material, where the matrix material is typically polymeric. It can be distinguished between thermosets and thermoplastics, while thermoplastic matrices are not state-of-the-art in aerospace applications. Therefore, as this work focuses on the replacement of the fiber material, the aerospace-proven thermoset-material epoxy was used.

Within epoxy materials there is a wide range of specific epoxies and only a fraction is aerospace certified. As there was no flax prepreg with an aerospace-certified epoxy available, the earlier announced material FlaxPreg by the manufacturer Lineo was used. Both, the weave and the UD material, are using an epoxy by Huntsman which is specified as "Araldite® LY 5150*/ Aradur® 1571*/ Accelerator 1573*/ Hardener XB 3471*", which is referred to by Araldite [80] in other chapters.

The used CFRP materials, unidirectional and woven, were the aerospace-certified materials by SGL Group, "CW-200-E501-45" as weave and "C UD-600-E501-53" as UD reinforced prepreg. Both are using the epoxy which is identified as SGL-E501.

Lastly, the flax weave was lacking epoxy when manufacturing only two layers with autoclave curing. This low thickness was needed for the cockpit door. A further analysis of the weave was described in Section 2.6.2. In order to diminish this problem, additional epoxy-film layers were added which were made by Henkel "Loctite Aero EA 7000". This epoxy is named epoxy-film in here.

All epoxies were cured together and resulted in a sufficient bonding of carbon and flax fibers and layers, also in the hybrids as described in the last section. For the later described impact tests, the partly bio-based epoxy SuperSap was used. The thin laminates were manufactured using VI processing, by HSH. The contained bio-based components cover 19 mass-% of the epoxy. These components typically drop-off as co-products or waste of other industrial processes, such as the bio-fuel production. Additionally, SuperSap has no color, is UV resistant and of low viscosity, which makes it suitable for VI processing.

2.10 Balsa-Wood Core

Balsa wood was used as sandwich-core material in the FFRP UD skins of the tailplane. It was considered very suitable for the sandwich core as it is 100% bio-based and has already been approved in former aviation structures by meeting the requirements of WL 6.1030 [48]. Balsa wood is also an anisotropic material. Therefore, the wood-fiber direction needs to be taken into account when using balsa wood. In this application, due the significantly lower manufacturing effort, the fiber orientation was reinforcing the bending stiffness, instead of the core crushing resistance.

The following table summarizes the used material parameters for the further on described calculations. The balsa wood's material data was not characterized itself. Only sandwich bending tests were used to show agreement with the met assumptions for the balsa material. Table 2.9 shows the material characteristics, which were applied to the FEA balsa material model.

Furthermore, as balsa is a natural material, the technical qualification sheet WL 6.1030 also defines a humidity content when the material is delivered. It specifies a humidity content of 10 ±5% and that the material should be oven dried. We expect that such a specification will also be needed for natural fibers. Also, the structural application is specified to be in combination with other covering sheet materials, such as aluminum and GFRP. The resulting limited applicability reduces the risk of fungal decay and environmental influences. Related research investigated damping and sound absorption properties of balsa, specifically as a core material, where comparable performance to synthetic foam core materials was shown [149, 194].

Table 2.9: Stiffness and Strength Values of Balsa Wood Core used for the FEA Material Model, Data from [124, 48]

Parameter	Unit	Value
ρ	[g cm^{-3}]	0.1
Stiffness		
$E_{1,ini}$	[GPa]	1.960
$E_{3,ini} = E_{2,ini}$	[GPa]	0.080
$\nu_{12} = \nu_{13}$	[-]	0.04
ν_{23}	[-]	0.40
$G_{12} = G_{13}$	[GPa]	0.300
G_{23}	[GPa]	0.050
Strength		
$\sigma_{t,1,ult}$	[MPa]	9.00
$\sigma_{t,3,ult} = \sigma_{t,2,ult}$	[MPa]	0.60
$\sigma_{c,1,ult}$	[MPa]	4.60
$\sigma_{c,3,ult} = \sigma_{t,2,ult}$	[MPa]	2.10
$\tau_{12,ult} = \tau_{13,ult}$	[MPa]	1.10
$\tau_{23,ult}$	[MPa]	1.00

As this material was not the major focus within this thesis, we will not discuss all properties in detail. Properties related to the bio-based mass which were identified for the natural fibers are expected to apply in an analogical way to balsa in a certain extent, such as humidity absorption.

3 Flax Composite Structures — Experimental and Numerical Analyses

This chapter describes the empirical investigations aiming to identify the aviation applicability of FFRP. First, the material models described in Chapter 2 will be applied to helicopter structural parts. Two parts were matter of investigation, an ultralight helicopter tailplane and a cockpit door of the CoAX 2D. For both parts the methodology of load definition, pre-design, and design phase with iterative validations of the FEA models is combined. The pre-design was based on analytical, simplified models, while the detailed design was using the more detailed FEA approach. This chapter focuses on the structural-mechanical test results of the parts' characterization, using EMA and static loading tests. With the empirical results, the material model validation on element and sub-component basis is explained in the respective part's section. First, the tailplane will be described, next, the cabin door. Both are highlighted blue in Figure 3.1.

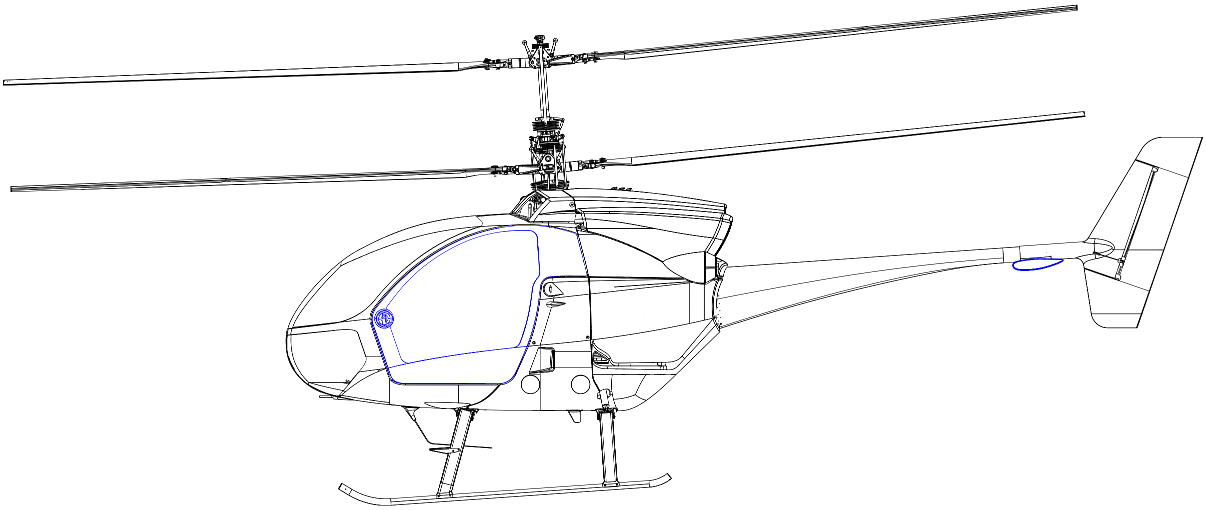

Figure 3.1: Technology Demonstrator with the Blue-Highlighted Parts Tailplane and Cabin Door in the CoAX 2D Overall Geometry

In order to further extend the holistic approach of the evaluation of FFRP for aviation structures, potentially beneficial or disadvantageous properties were analyzed. The results are sectioned by their experimental investigation. The additional experimental investigations cover impact, crash, hygroscopy, and NDI. Additionally, the statistical deviations of the performed FFRP tensile tests are compared and put in context to CFRP and relevant literature.

Empirical findings of all performed tests are extracted and perspectives for future work is given. Resulting findings will be recapitalized in Chapter 4

3.1 Design and Experimental Evaluation of the Component Tailplane

Parts of this section were previously published in AIAA2019. Also, two students' theses contributed to this section, see Kobus2016 (preliminary design studies) and Steigenb.2018 (experimental investigations on coupons and sub-components).

Within this research the tailplane was chosen as structural part and demonstrator platform to analyze the applicability of natural fibers in aviation. Therefore, this ultralight helicopter tailplane, originally made using CFRP skins and a foam core, was redesigned with the goal of using bio-based materials in a high proportion. Structural requirements were set to the national ultralight certification standards (LTF-ULH) and were also adapted from the performance of the initial design tailplane.

An FEA model was developed, fed by material data from tensile tests as described in Chapter 2, which evolved iteratively from coupon and sub-component bending tests. Finally, a 450 mm section of the resulting design was built, made using the materials FFRP, CFRP, balsa wood, and glue, where a bio-based mass content of approximately 55% could be achieved.

The new, hybrid version was analyzed experimentally in terms of weight, stiffness, strength/ failure, damping, and embodied energy. Benefits of the new design were identified in a 2–8 times higher damping ratio, 65% less embodied energy ($76.90\,\mathrm{MJ\,kg^{-1}}$), and a reduced carbon footprint ($5\,\mathrm{kg\,kg^{-1}}$), while weight, stiffness, and strength were performing in a sufficient and comparative manner as the reference. The sufficiency of applying the derived yield failure criterion could be verified.

State-of-the-art helicopter tailplanes are likely to be made out of metallic materials or of CFRP, which are not designed to be eco-efficient in their production. Furthermore, tail shake is a common but undesired phenomenon inherent with helicopters, likely to be induced by an impulse or harmonic excitation of the tailplane. The high damping ratios of NFRP (up to 5–10 times higher than CFRP [141, 119]) are considered beneficial especially in this application.

3.1.1 Identification of the Maximum Aerodynamic Load on the Tailplane

In terms of tailplane geometry, we distinguish between three versions, the initial version as the reference, the current version of the helicopter manufacturer edm aerotec GmbH and the herein used version for experimental investigations. All differ in spanwidth but not in chord length and airfoil. As the initial reference was set in the beginning of this work we did not change the reference when the manufacturer updated the design, therefore, neither version can be compared to the current design of the manufacturer.

The design load case was identified considering the helicopters maximum speed, maximum angle of attack and an additional vertical gust of 10 m s^{-1}. Regarding flight tests of the CoAX 2D [62], the maximum pitch of the helicopter, its mounting angle and the additional vertical gust would lead to flow separation, according to wind tunnel test data of the used airfoil [178]. As the flight tests were performed with a shorter span width, the new design is likely to result in a lower maximum pitch. And, as impulsively aerodynamic loads could lead to higher c_l values than laminar flows, the c_l-alpha curve was assumed linearly increasing to the calculated summarized angle of attack. This approach is considered a conservative design.

Next, the aerodynamic load was calculated using a panel method, with the tool xflr5. The input data for the calculation and the results are shown in Figure 3.2 and calculated by Equation 3.1. The input data was compared to flight test data and represents, as expected, conservative values [62].

Input

Variable	Unit	Value
chord	$[mm]$	250
span	$[mm]$	1 300
ρ	$[kg\,m^{-3}]$	1.225
ν	$[m^2\,s^{-1}]$	$1.5\,10^{-5}$
v_{NE}	$[ms^{-1}]$	55.5
Re	[-]	925 000
Elements	[-]	3 240
α	[°]	20.44

Results

Parameter	Unit	Value
C_L	[-]	1.826
C_D	[-]	0.208
C_m	[-]	-0.493
X_{CP}	[mm]	62

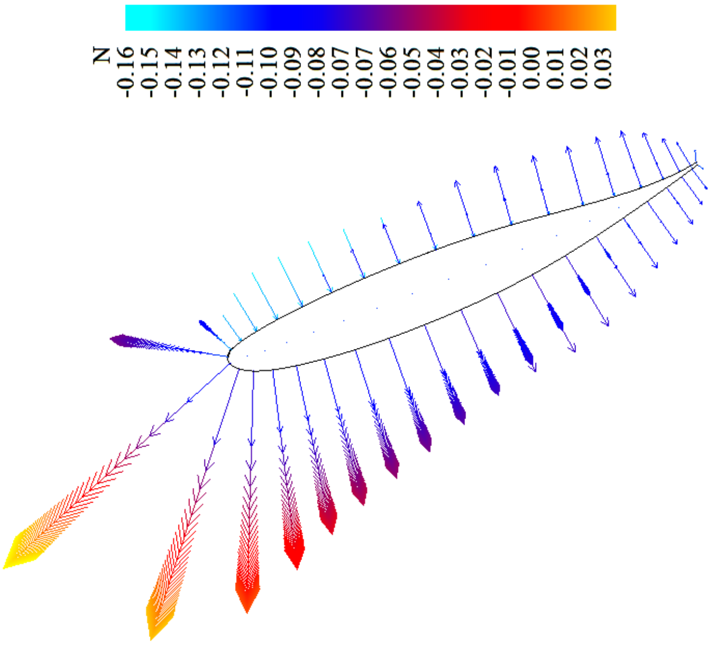

Figure 3.2: Input and Results Data for Aerodynamic Load Calculation of the Tailplane Maximum Load Distribution Using the Panel Method Based Tool xflr5

$$F = S_F \cdot c_{L,max} \cdot \frac{\rho}{2} \cdot v_{NE}^2 \cdot A \tag{3.1}$$

We assume that the tailplane clamping on the tail boom is leading to a lower aerodynamic efficiency. Still, we modeled the whole tailplane as aerodynamically efficient surface, which represents a structurally conservative design. Described assumptions resulted in a total down-thrust of about 1.10 kN, which serves as limit load to the structural design process and is applied to stiffness constraints. The additional safety factor of 1.875, using the multiplied safety margins of 1.5 (standard) and 1.25 (for composite designs), results in the ultimate load of 2 kN, which is used for strength constraints.

Figure 3.2 shows force vectors, normal on the panels, in the side view. The graphic is showing 3D-panel vectors, therefore, the panel forces are span-wise overlapping each other. For the pre-design, span wise lift data (1D) was used, while for the detailed design the 3D-C_p-values were converted into pressure values per element and imported on the FEA model, shown in Figure 3.3.

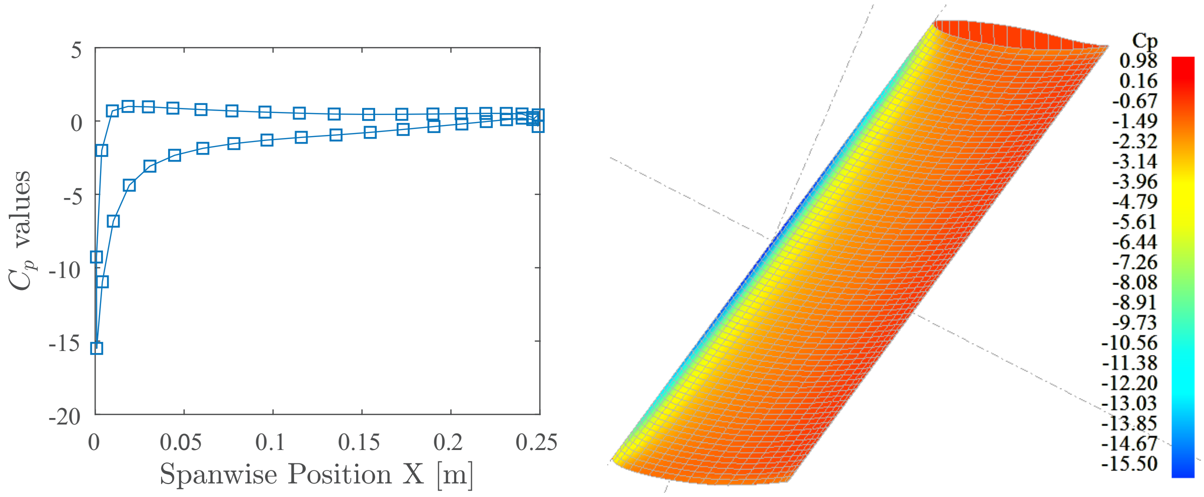

a) b)

Figure 3.3: Aerodynamic Pressure Distribution of the Tailplane with a) C_p Values on Airfoil and b) 3D-Contour Plot of C_p Distribution

3.1.2 Concept and Preliminary Design of the Tailplane

The preliminary design was examining different structural concepts suitable for a wing of this size. It turned out, that wings with respective chord length are typically more lightweight using a spar design than the ones with a core design. Therefore, a spar design was determined for this study. In the pre-design, the spar was constructed to bear bending loads, while skin and web were designed to bear shear loads.

An iterative analytical calculation of the loads per span section was developed and resulted in necessary laminate thicknesses using the materials of consideration CFRP and FFRP.

The c_l and c_m values were imported span wise per section x_i as well as the induced angle of attack α_i, which was added to the initial angle of attack. Next, the airfoil drag $c_{d,0}$ was added to the induced drag by using Equation (3.2).

$$c_{d,i} = (\frac{cl_i^2 \cdot c}{\pi \cdot S} + c_{d,0}) \cdot \frac{\rho}{2} \cdot v_{NE}^2 \cdot \Delta a \tag{3.2}$$

As the loads per span section were defined, the spar was designed to bear all bending loads in the spar caps. The bending load of each section resulted from the following equation.

$$M_{i,y} = S_F \cdot \sum_{1}^{n} \frac{\rho}{2} \cdot v_{NE}^2 \cdot (cos(\alpha) \cdot c_{l,i} + sin(\alpha) \cdot c_{d,i}) \cdot a_i \cdot x_i \tag{3.3}$$

The resulting moment was concluding to the needed bending stiffness and inertia, which was limited by the airfoil geometry, see Equations (3.4) to (3.6).

$$I_{i,y} = \sum_{1}^{n} \frac{M_{i,y} \cdot z_{max}}{\sigma_i} \tag{3.4}$$

$$\phi_i = \frac{M_{i,y} \cdot \Delta x}{E \cdot I_y} + \phi_{i-1} \tag{3.5}$$

$$w_i = \frac{M_{i,y} \cdot \Delta x^2}{2 \cdot E \cdot I_y} + tan(\phi_{i-1}) \cdot \Delta x + w_{i-1} \tag{3.6}$$

Figure 3.4 on the following page gives guidance to the calculated values and results. First, the lift is plotted, extracted from the aerodynamics calculation and transformed into a summarized moment. This yields to a certain cap thickness needed in terms of strength, which was determined for both materials, CFRP and FFRP.

As the maximum allowed stress for flax was set to 40 MPa with respect to the elastic-plastic transition point described in the previous section, it is obviously not possible to make the spar caps from FFRP material, as they would fill the whole hight of the airfoil, disregarding the increased mass.

Another constraint, besides failure, is stiffness, where the maximum deflection at the wing tip was set to 10 mm, when loaded with the limit load. In the last plot of Figure 3.4 the deflection is shown for the strength-constrained and the stiffness-constrained version. We can see that the stiffness constrained version was necessary to fulfill all demands, also the strength constraints, this version was determined as resulting design for the spar caps.

In order to design the spar web, the shear forces were summarized of three components, shear due to transverse force (I), shear due to spar cap downward forces (II), and shear due to elastic deformation of the upper and lower spar caps (III). As the components (II) and (III) were very small, the only component considered in the preliminary design was (I). The shear due to transversal load was iteratively summarized for each span-wise panel, see Equation (3.7).

Analogically to the prior steps for the spar caps design, the needed inertia resulted in a necessary thickness. For the spar web the difference between final FEA design and preliminary design was the largest. In this case, regarding the transversal shear loads, the fact of neglecting the other components such as the skin, was having a strong influence. In order to avoid repetitions, the plots for this step are not included in this thesis.

In the next step, the airfoil skin was designed to bear torsional loads. This was calculated by Equation (3.8) to (3.13). Additionally, the stiffness was designed with the constraint $\theta_n < 10^\circ$, calculated by Equation (3.13), which was later reduced to $\theta_n < 1^\circ$. As the airfoil stall angle was already close to the maximum occurring angle, this reduction was pursued.

$$\tau_i = \sum_{1}^{n} \frac{Q_i \cdot b \cdot h}{4 \cdot I_y} \tag{3.7}$$

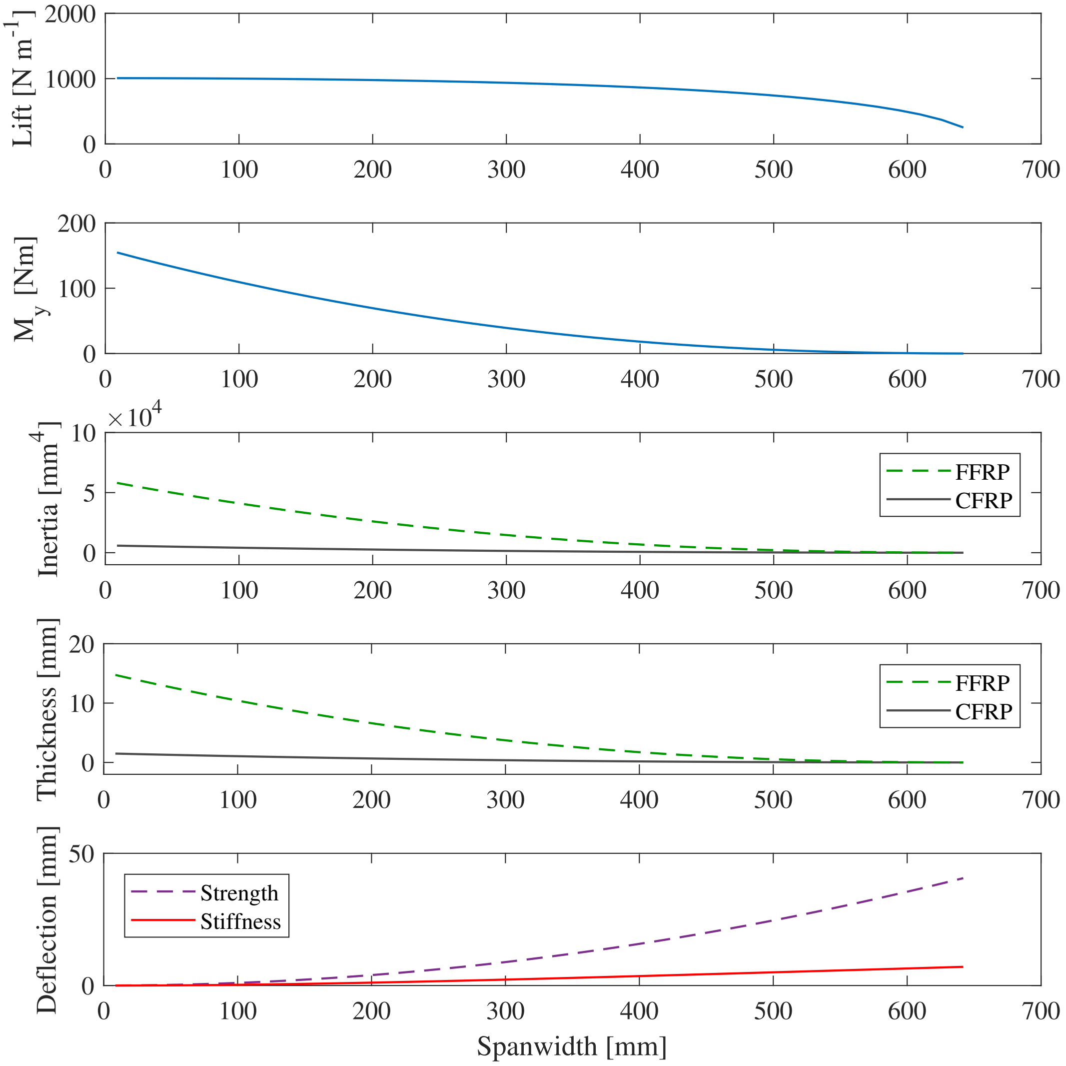

Figure 3.4: Analytical Panel-Wise Design of Spar Caps Using Bending Constraints

$$M_{i,x} = \sum_{1}^{n} \frac{\rho}{2} \cdot v_{NE}^2 \cdot c_{m,i} \tag{3.8}$$

$$A_{s,i} = r(s) \cdot \Delta s \tag{3.9}$$

$$\tau_{max} = \frac{M_T}{2 \cdot A_s \cdot t_{min}} \tag{3.10}$$

$$I_T = \frac{4 \cdot A_m^2}{\oint t(s)^{-1} ds} \tag{3.11}$$

$$I_{t,i,x} = \frac{4 \cdot A_{m,i,s}^2 \cdot t}{\Delta s} \tag{3.12}$$

$$\theta_i = \frac{M_{i,x} \cdot \Delta x}{G_{xy} \cdot I_t} + \theta_{i-1} \tag{3.13}$$

Figure 3.5 shows preliminary results of the skin design. First, the summarized torsional moment is plotted, extracted from the aerodynamics calculation. The given airfoil was divided in segments of the width Δs which were used for the calculation of τ_{max} using Equation (3.10). The parameter A_s is the included area of the segment Δs, with respect to the shear center of the closed airfoil.

By comparing the maximum shear stress with the materials' shear strength (yield and ultimate are the same), a resulting thickness is plotted. These thicknesses are very small, for both materials lower than 0.20 mm, therefore a usage of the bio-based FFRP was considered possible.

Next, the torsional-stiffness constraint was checked. Above Equations (3.11) to (3.13) were used to determine the maximum twist deformation. The plot in Figure 3.5 shows the twist deformation for the thickness designed with both, the strength and the stiffness constraint. It can be seen that the stiffness constraint is again not met by the strength-designed version, which underlines that the stiffness constraints are often the critical design constraints in aerospace engineering.

We can see in the calculations that the necessary thickness is increasing towards the clamping. For reasons of manufacturing, a thickness reduction was not performed within this work and the built section was span-wise symmetrical.

These segment-wise analytical steps concluded to the preliminary design, which was modeled in an FEA. This model further improved during the detailed design phase with each iteration of experiments, as explained in the next section. One prominent change was the integration of the carbon spars into the sandwich skin instead of having it as a separate part with the webs. This design detail increased the bending inertia and additional weight savings were possible. Another important point was the inclusion of balsa wood in the skin, which was needed in order to suppress local skin buckling.

The skin was built using a vacuum-tube manufacturing technique, which enabled a lightweight design. Additional glue was only needed for the integration of the web. The final lay-up is shown in Figure 3.6, with CFRP spar flanges for bending loads and the

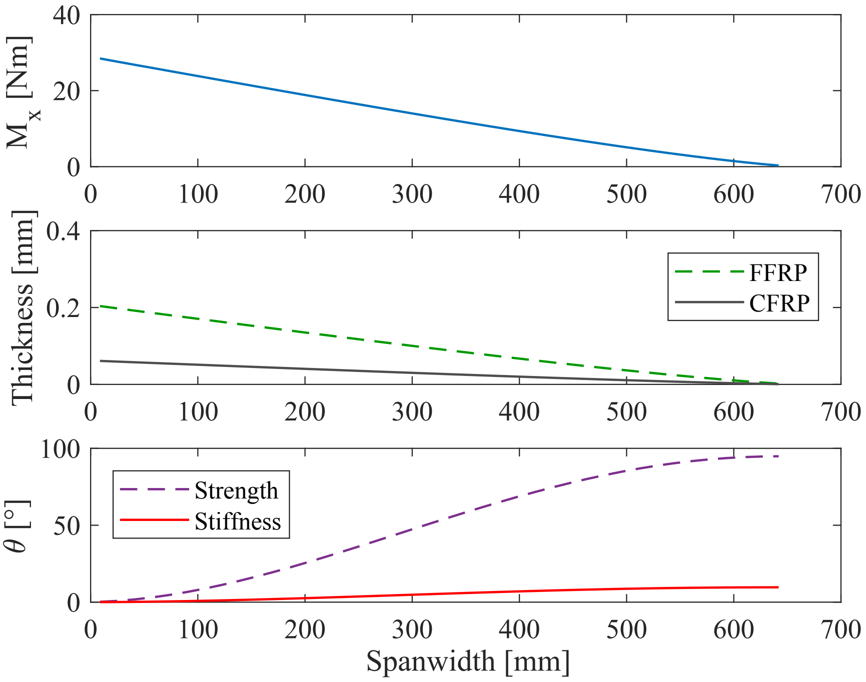

Figure 3.5: Analytical Panel-Wise Design of Airfoil Skin Using Torsional Constraints

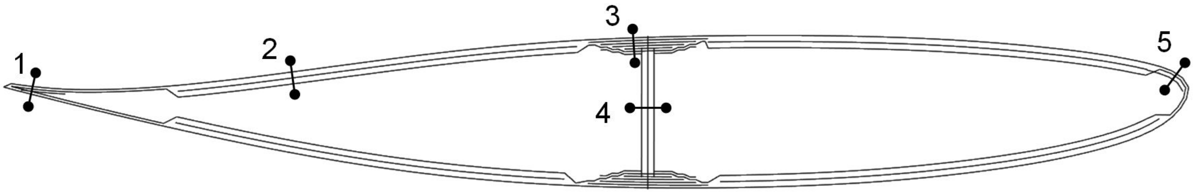

Figure 3.6: Tail Plane Cross-Section of Final Design, Lay-Up at Sampling Points is Shown in Table 3.1

FFRP balsa sandwich skin taking shear loads.

The position of the span was chosen by the shear center of the skin, at 110 mm, which was also the position of X_{CP} at 0° angle of attack. Being well aware, that the X_{CP} location is moving closer to the leading edge with increasing angles of attack, this position was considered best in order to suppress complex shear-bending couplings.

In Table 3.1 the material stack-ups are listed respectively to the shown sampling points of Figure 3.6. F is indicating unidirectionally FFRP layers of 0.13 mm thickness, with the ply-angle and the amount of layers in the suffix. B indicates a 2 mm layer of balsa wood, C stands for a CFRP of 0.58 mm thickness, also unidirectionally reinforced. Lastly, G indicates a glue (Scotch-Weld 9323), which was used to assemble shear web and airfoil skin. All contained materials are also listed with their mass-percentage in Table 4.2.

Table 3.1: Material Stack-up at Respective Sampling Points of Figure 3.6

Sampling Point	Stack-Up
1	$[F_{\pm45,4}/F_{0,3}/F_{\pm45,4}]$
2 and **4**	$[F_{\pm45,4}/B_0/F_{\pm45,4}]$
3	$[F_{\pm45,4}/C_{0,4}/F_{\pm45,4}/G/F_{\pm45,4}]$
5	$[F_{\pm45,12}]$

For the evaluation of the final design, the FEA model was loaded by the aerodynamic import itself as the limit load, and times the safety factor (1.875) as the ultimate load. The tailplane showed a maximum deformation of 6.35 mm and a maximum twist deformation of $< 1°$. No failure occurred under limit load and under the ultimate load few sporadically distributed elements showed core or tensile matrix failure. Also, the ultimate load resulted in fiber yield failure $F_{t,f,K}$ in wide ranges, see Figure 3.7, which was allowed for the ultimate load. Thereby, permanent deformations were expected after application of the ultimate load but not after the limit load.

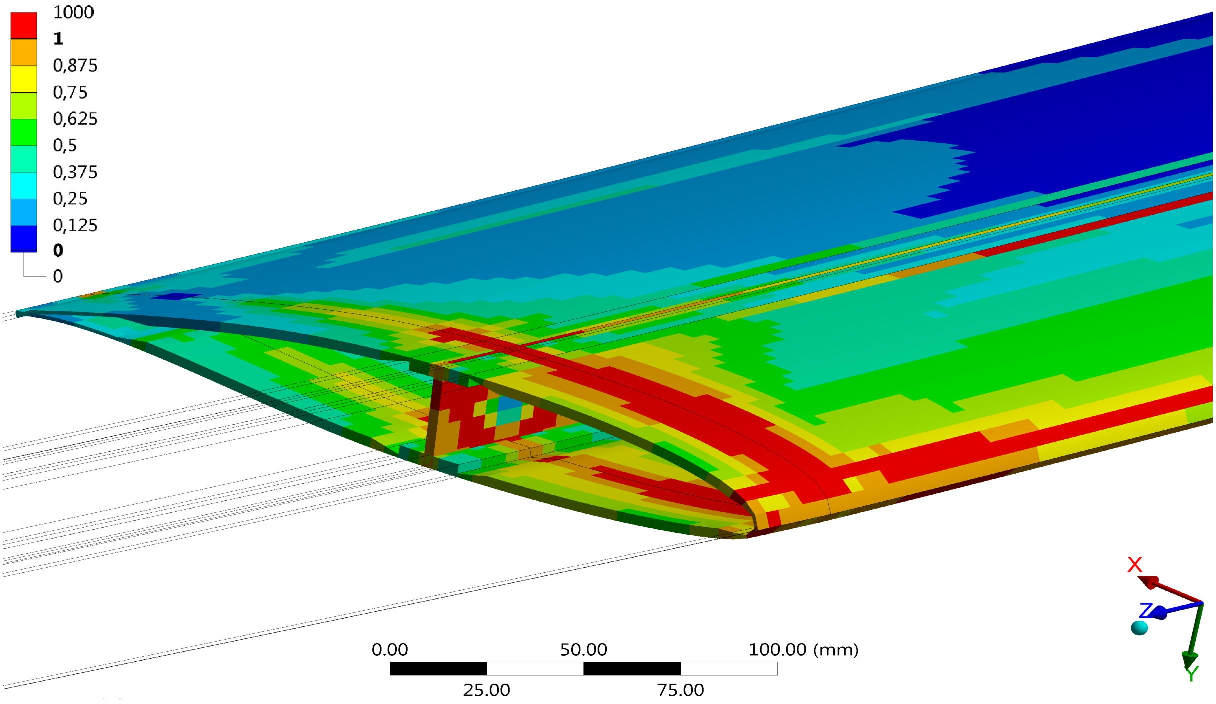

Figure 3.7: Fiber Yield Failure $F_{t,f,K}$ at Ultimate Load of the Final Design Tailplane

3.1.3 Scope of Tests to Verify and Characterize Functionality of the Tailplane

The preliminary design from analytical results was modeled with the FEA tool ANSYS and its composite environment, where intermediate results were investigated experimentally. Pictures of the manufactured elements are shown in Figure 3.8 a) to c). The calculated load of the panel method (see again Figure 3.2) was imported to the model. C_p values were transformed into pressure values, see Equation (3.14), which were mapped on the FEA mesh using a triangulation algorithm. The error due to the import was 0.98% and considered acceptable. The applied pressure was analyzed qualitatively and the sum of the imported down-force was validated with the initial lift results.

$$p_i = c_{p,i} \cdot \frac{1}{2} \cdot \rho_\infty \cdot v_{NE}^2 (+p_\infty) \tag{3.14}$$

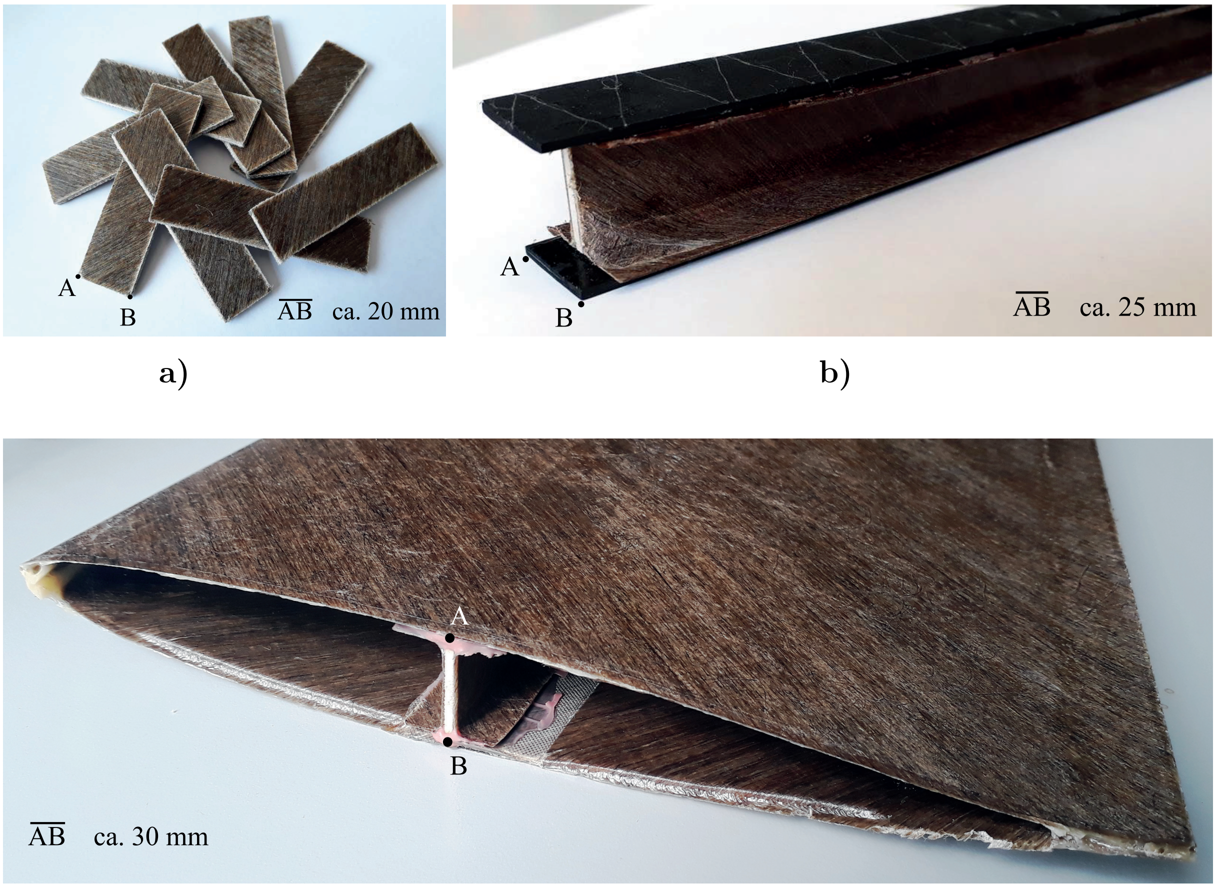

a) b)

c)

Figure 3.8: Photographs of Manufactured Parts: a) Sandwich Beams, b) Spar, c) Tailplane Section

Next, the strength and stiffness requirements were analyzed iteratively with a variation of lay-ups and materials. The critical design requirement was that the limit load should be bearable without plastic deformation. As flax fiber laminates show a sort of yielding as described in Chapter 2, the design was limited by this yield failure, which will be validated experimentally in this section. The ultimate load constraint resulted from the limit load with an 1.875 safety factor. This was combined from the 1.5 safety factor with an additional 1.25 factor for composite design. The ultimate load needed to be bearable for 1 s without rupture, while permanent deformation was allowed.

The material characteristics of the FFRP and CFRP materials were characterized with tensile tests of $[0]_n$, $[90]_n$ and $[\pm 45]_n$ samples, of which the test results are described in detail in Section 2.5.3. Then sandwich lay-ups of $[\pm 45_{F,4}/\overline{0_B}]_S$, $[\pm 45_{F,4}/\overline{90_B}]_S$ and $[\pm 45_{F,4}/0_E/\overline{45_B}]_S$ were validated in a flexural test, as well as the whole carbon-flax-balsa preliminary-design spar.

As completion of the design, the structural performance of a built tailplane section was analyzed experimentally. The experimental results include quasi-static tests where stiffness and strength of the new hybrid design were analyzed and an EMA was performed in order to determine damping ratios. All experiments concerning the tailplane are described and analyzed in detail in the following, starting with the bending tests of sandwich elements.

3.1.4 Element Bending Tests on Stiffness and Failure Evaluation

The resulting skin sandwich from the preliminary design $[F_{\pm 45,4}/\overline{B_0}]_S$ was manufactured as element sample in different configurations, in order to find out whether an additional epoxy film is necessary for a proper laminate-core bonding, between the flax laminates and the 2 mm balsa wood. Three sandwich plates were manufactured in 0°, 90°, and 45° balsa-fiber orientation and a variation of tapering and additional epoxy. Each section cut was analyzed in terms of cuttability, air voids between the two material types and a 4-point-bending test.

It turned out that the best cutting method for the FFRP cross-ply laminates was an actual cutter, while saws ripped out fibers at the cutting edges and scissor-like methods crushed the core. When we compared the experimental results of all configurations, the bonding between UD FFRP and balsa wood without additional epoxy film was good and regarding the overall weight, the epoxy film was not necessary. Furthermore, occurring voids at the core edges made tapering necessary, which was expected.

Using the material model of the flax laminates and literature data of balsa wood, all lay-ups of investigation were modeled and used for validation of the FEA. In comparison to the FEA model, it was shown that the general stiffness behavior was modeled well, whereas the scatter between different specimens was higher than the deviation between measurement and model, see Figure 3.9.

In order to identify failure in the FEA of the sandwich laminates, the described yield failure criterion, core failure, and the Hashin ultimate failure criteria were applied. Figure 3.10 shows occurring failure at the marked load levels in Figure 3.9 for each configuration. The yield failure criterion was applied in the form of a Hashin failure criterion, which showed tensile fiber failure known as $F_{t,f,K}$ starting at approximately 100 N for each configuration. The stress resistance values used in the Hashin yield approach were defined at the initiation of nonlinear behavior. Thus, a resulting stiffness reduction of the specimens was expected, which was observable in some samples of the nine tested configurations, see Figure 3.9.

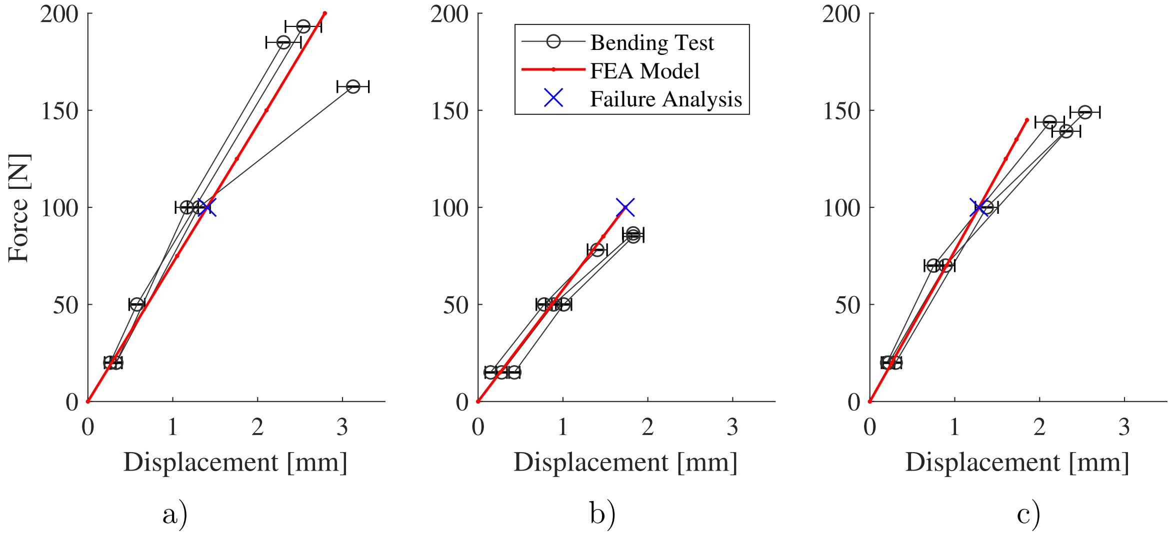

Figure 3.9: Stiffness Validation of Three Flax-Balsa Sandwich Elements in 4-Point Bending Test, Configurations are of the Following Stack-Ups a) $[F_{\pm45,4}/\overline{B_0}]_S$, b) $[F_{\pm45,4}/\overline{B_{90}}]_S$, and c) $[F_{\pm45,4}/E_{0,1}/\overline{B_{45}}]_S$

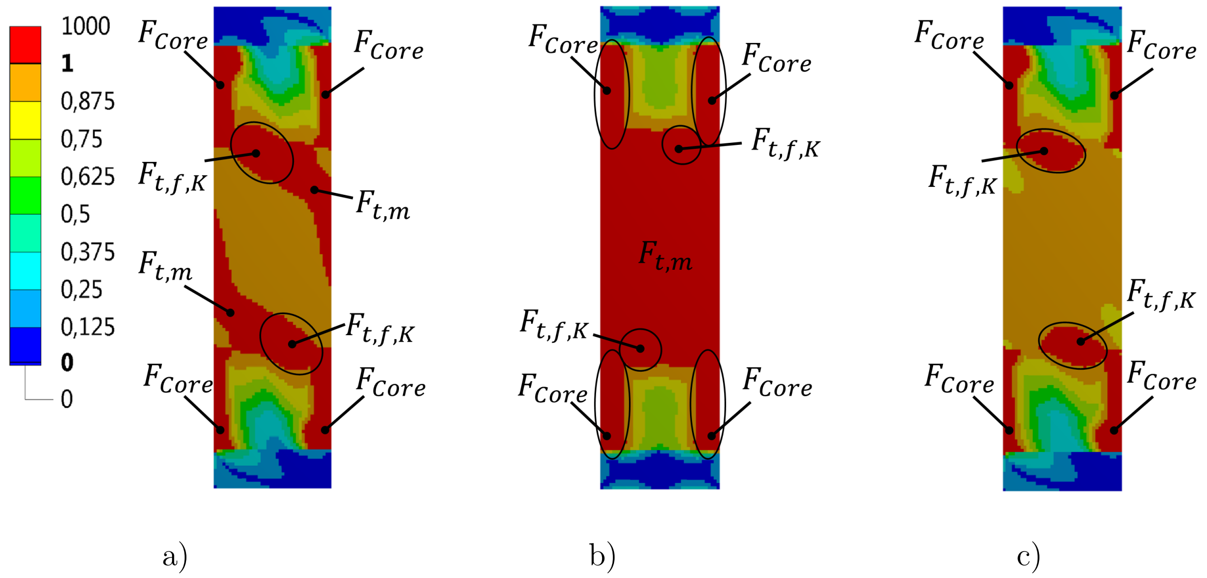

Figure 3.10: Inverse Reserve Factor of FEA when Core Failure, Hashin Ultimate and Hashin Yield Failure was applied at 100 N Load of the Three Lay-Ups a) $[F_{\pm45,4}/\overline{B_0}]_S$ at 100 N, b) $[F_{\pm45,4}/\overline{B_{90}}]_S$ at 90 N and c) $[F_{\pm45,4}/E_{0,1}/\overline{B_{45}}]_S$ at 120 N

Additionally, we can see this yield failure, tensile matrix failure, and core failure, where the latter two use the ultimate tensile strength data. The $[\mathrm{F}_{\pm 45}/\overline{B_{45}}]_S$ sample did not show $F_{t,m}$ yet. Due to the higher inertia in the model, this sample could bear slightly higher loads. As we can remember $F_{t,m}$ from the cross-ply tensile tests, see Figure 2.14, this failure mode does not lead to catastrophic failure as well. The finally observed catastrophic failure was core failure, which was predicted at the right position (between load initiation positions) but at rather too low stresses. Nevertheless, this was considered a conservative and thereby acceptable deviation.

As a result, the material models could be verified and the inclusion of the yield failure is necessary in order to prevent significant stiffness reductions. Furthermore, the core compression strength in the FEA model is probably of slightly too low values, but all in all the simulation shows good agreement with the experiments.

Additionally, the fiber orientation of the balsa wood has significant influence on stiffness and strength. The configuration chosen for the tailplane skin and web was configuration a) with the $[\mathrm{F}_{\pm 45}/\overline{B_0}]_S$ lay-up. The more advanced fiber orientation for balsa wood is probably 0° in thickness direction, but due to manufacturing issues, this was not considered economically efficient.

A similar analysis was done on failure behavior of the whole beam section of the tailplane, but will not be discussed in detail in order to avoid redundancy. This beam section was tested in a 3-point-bending test; failure occurred in the spar flanges right at the load initiation in the middle of the beam. Details can be assessed in Steigenb.2018.

3.1.5 Quasi-Static Tailplane Section Tests on Elasticity and Failure

In order to verify the final tailplane design a section of 450 mm was built. The ultralight certification standards define that under the safe load there is no plastic deformation allowed. Therefore, the Hashin failure criterion, using the yield stresses as described were applied to the design. The ultimate load is defined with plastic deformation allowed, whereas rupture or complete failure is not. In this case, the ultimate strengths were applied within the Hashin failure evaluation. The FEA calculations showed that the non-yielding constraint at the limit load is the limiting design constraint, thus the following focuses on verification of the limit load.

The limit load was defined by the maximum aerodynamic load from the initially described calculation, where in the following only one half-span is examined and thus, the loads reduce from 1.10 kN limit load and 2 kN ultimate load to 0.55 kN limit load and 1 kN ultimate load, respectively. In order to develop a simple but sufficient experimental setup, the center of lift of the aerodynamic C_p-distribution was adapted and the load initiation of the experimental set-up was defined at this point. Combined with a load initiation angle of 18.7°, the load vectors in the experiment equal the resulting forces in the clamping when the imported aerodynamic load was applied. Also, the clamping reaction moments were adapted from the aerodynamic load calculation. Table 3.2 gives a summary of the reaction forces and moments, which resulted from the aerodynamic load and the experimental setup. Coordinates are included in Figure 3.11 and defined by $x = 0$ at the clamping of the tailplane section, while y and z originate from the middle of the spar web. Figure 3.11 shows a photograph of the experimental setup for the load constraints. The reflecting marks are used for photogrammetry measurements.

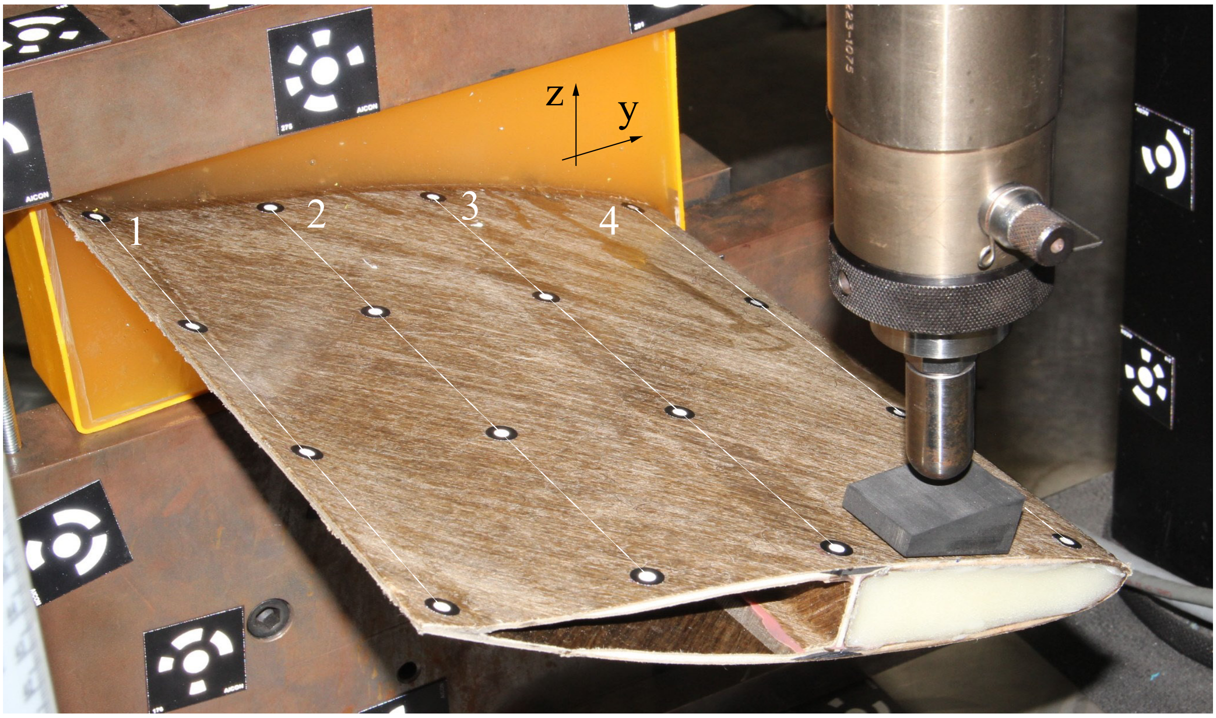

Figure 3.11: Experimental Setup of Cyclic Loading on the Tailplane Section in a Cantilever Beam Configuration, White Marks the Chord Positions 1–4

Table 3.2: Boundary Reaction Forces and Moments of Imported Aerodynamic Panel Loads Compared to those of the Experimental Setup, Both from FEA

	Unit	X	Y	Z	Total
Boundary Reaction Forces of Aerodynamics	[N]	0	531.3	-173.5	559.0
Boundary Reaction in Experimental Setup	[N]	0	532.0	-174.0	559.7
Deviation of Experiment to Import	[%]	0	0.1	0.3	0.1
Boundary Reaction Moments of Aerodynamics	[Nm]	-28.1	-47.7	-153.2	162.9
Boundary Reaction in Experimental Setup	[Nm]	-30.1	-54.5	-166.5	177.8
Deviation of Experiment to Import	[%]	7.1	14.3	8.7	9.1

The cantilever setup of the experiment was done by embedding a 50 mm section in epoxy, which was then clamped in a steel frame, see Figure 3.11. The reference coordinate system for the photogrammetric measurement was applied to the steel frame in order to diminish global deformations. At the point of load initiation, the tailplane was filled with epoxy in a section of 30 mm depth. Without the epoxy reinforcement, the skin would have failed locally at the load initiation, which would not be the case for the evenly distributed aerodynamic load, and therefore, should be avoided.

In order to validate the design calculations of the FEA model iteratively, a cyclic static loading and unloading was performed. Based on the FEA calculations the load steps were defined as in Table 3.3. The intention of applying the loads in cyclic steps with a stress release in between the load steps was to allow an analysis of a "plastic" deformation evolution. Additional intermediate load steps were added between beginning, limit, and ultimate loads. A first result comparison of experimental and FEA deflection at the measurement point at the end of chord position 3, is given as well.

Experimental results satisfied the ultimate load constraint, which was 1 kN and 288 Nm. The experimentally proven peak load was 2.50 kN and 715 Nm, at which failure appeared as buckling on the bottom side of the tailplane section. Therefore, the first design constrained of the certification specifications could be verified, even overly reached by a factor of 2.5, but as the predicted core and Hashin yield failure in the ultimate load simulation was not resulting in catastrophic failure, this was expected.

The stiffness comparison of experimental results with FEA showed a discrepancy, which could be identified to originate from the epoxy-boundary stiffness. In order to model the elasticity of the epoxy boundary, beam elements were connecting a box surface and the surface of the tailplane. Two approaches were investigated, beam elements with equal sectional areas, see Equation (3.15), and beam elements with the same moment of inertia, see Equation (3.16), where the left hand side is accounting for the rectangular elements and the right hand side for the circular beams.

$$a_{element}^2 = n_{nodes} \cdot \pi \cdot R^2 \tag{3.15}$$

$$\frac{w_{element} \cdot h_{box}^3}{12} = \frac{\pi \cdot R^4}{4} + (n_{nodes} - 1) \cdot a_{element} \cdot w_{element} \tag{3.16}$$

Table 3.3: Load Steps for Static Validation Tests of the Tailplane Section with Deformations in z-Direction at the Tip of the Beam Section (Chord Pos. 3) in Experiments' Photogrammetry Measurements and FEA Calculations

	Number	Force	$\frac{F}{F_{limit}}$	Speed	u(z) (Exp.)
Unit	-	[N]	[%]	[$\mathrm{mm\,min^{-1}}$]	[mm]
Setting Load	0	56	10	1	-
Release - 1	1	0	0	1	0.000
Intermediate Load	2	280	50	1	1.422
Release - 3	3	0	0	1	0.023
Limit Load	4	560	100	2	3.015
Release - 5	5	0	0	2	0.090
Yield Load	6	840	150	5	4.409
Release - 7	7	0	0	5	0.127
Ultimate Load (FEA)	8	1 050	188	5	5.736
Release - 9	9	0	0	5	0.273
Ultimate Load (Exp.)	10	2 510	239	5	-

Results showed that the equal area approach was the better choice. This led to the assumption, that the epoxy embedding is rather loaded in tensile and compressive manner than in bending. This adjustment was done for a better comparability of the model. Thereby, the tangential deformation angle at the boundary condition could not be met perfectly but in a reasonable range, see Figure 3.12.

The deformations in the experimental measurement and FEA simulation were compared using 3D-displacement vectors at each point of photogrammetric measurement. The view aligned with the X-direction is shown in Figure 3.12 a). It can be seen that the length of the deformation vectors and its angles fit well with the calculated values.

Additionally, the points along the spar were analyzed as a beam approximation. Figure 3.12 b) shows the deformation at the limit load and ultimate load as well as the deformation after release of the loads. The deformation under the limit load shows good agreement with the FEA results, while the model predicts too small deformations at the ultimate load. As the built design is accepting nonlinear behavior after the limit load, this would be a cause for the underestimation of the linear model. The permanent deformation after release of the ultimate load (9 in Figure 3.12 b)) is supporting this assumption. But, the first measurement point, close to the epoxy embedded clamping, is also deflecting. Therefore, deformations in the highly loaded epoxy-clamping could contribute to this discrepancy as well. In order to analyze the cause of this discrepancy we also analyzed the deformations after release of the loads at each chord-wise position, see Figure 3.13.

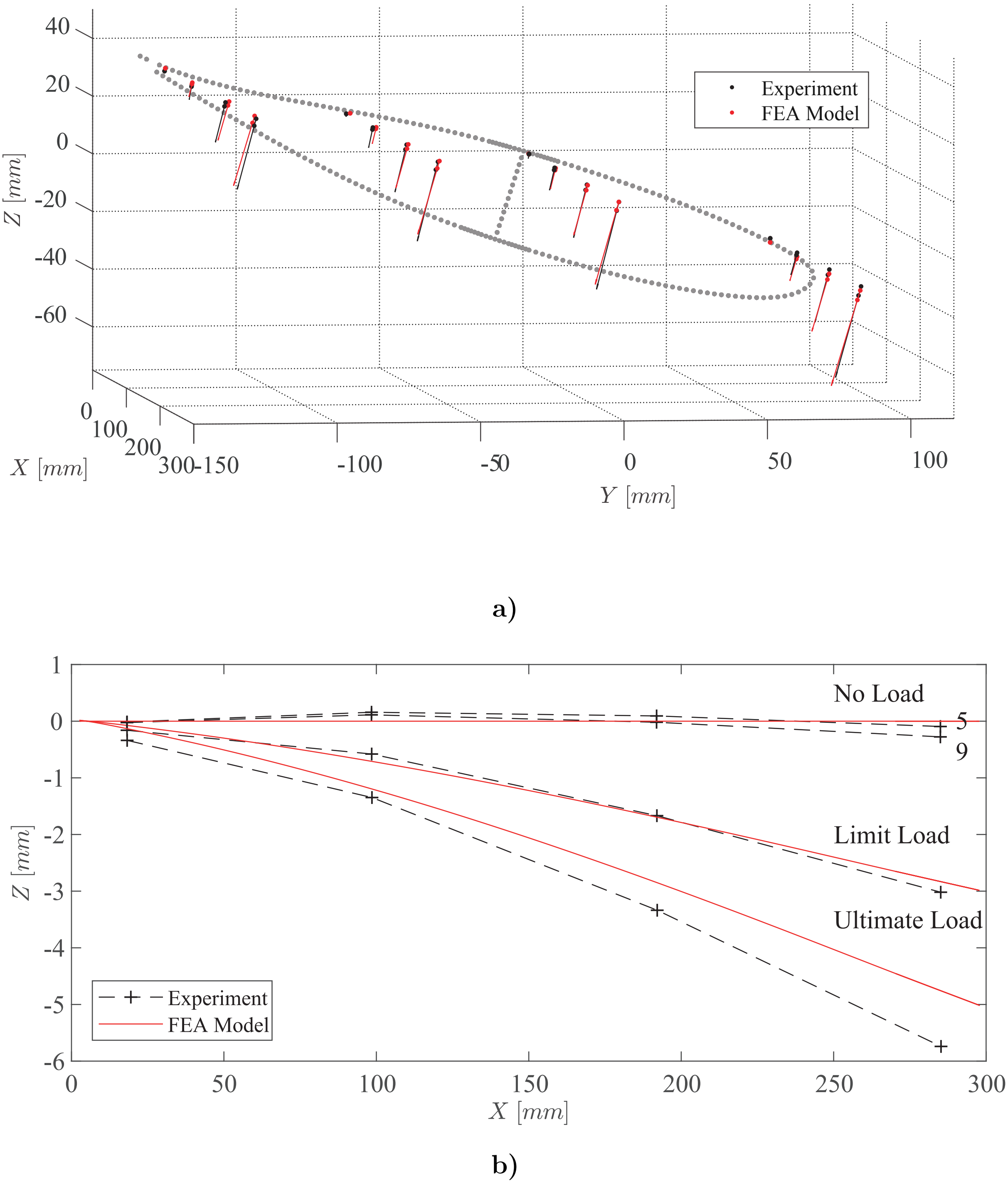

a)

b)

Figure 3.12: Experiment and FEA Deformation of Quasi-Static Loading, a) 3D Plot of Deformation Vectors at Limit Load, b) Points at Chord Position 3 of the Tailplane in the X-Z Plane with Loads According to Table 3.3

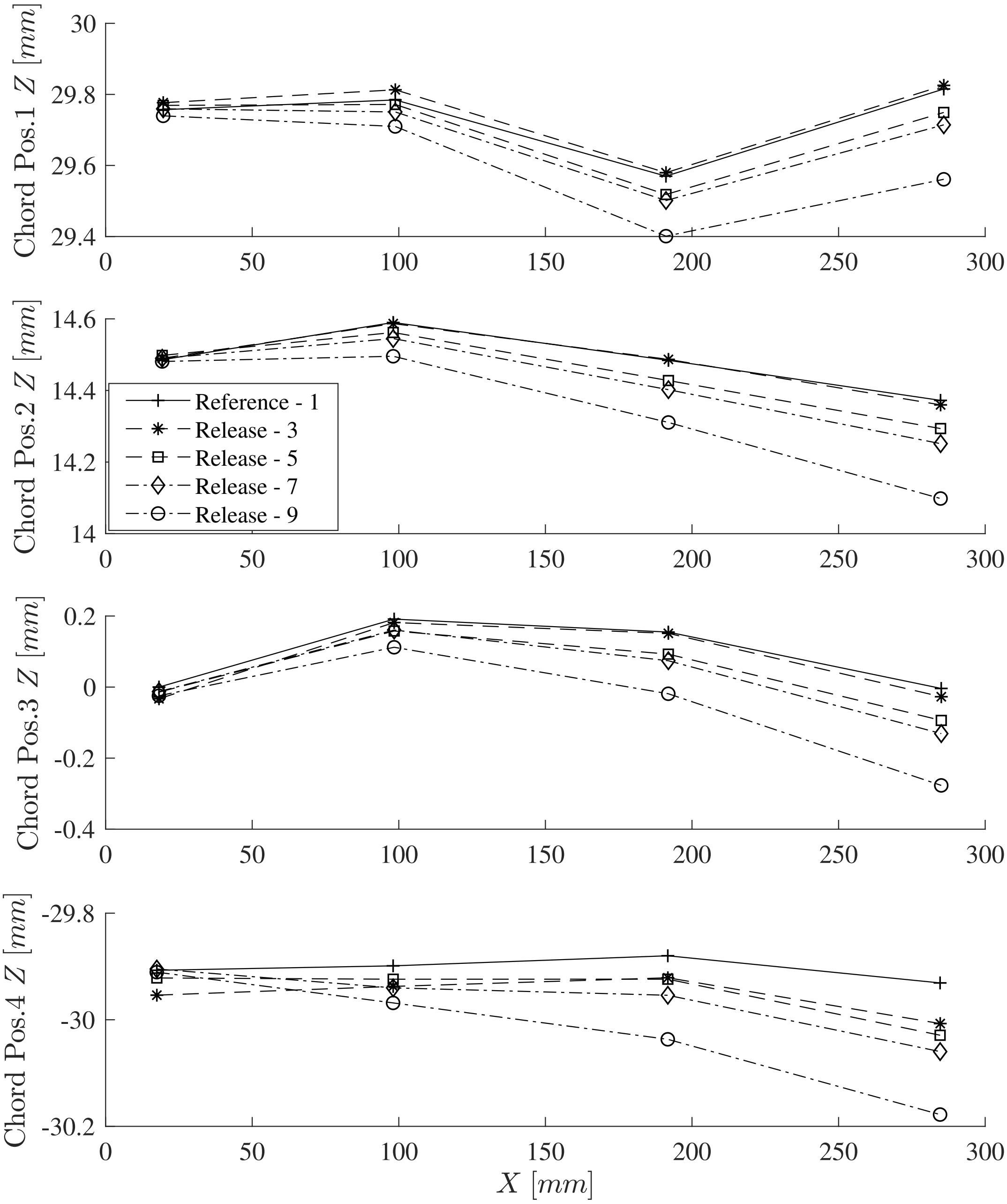

Figure 3.13: Release Load Deformations on Each Chord Position after All Load Steps, Legend Refers to Load Steps as in Table 3.3

After load application, there was permanent deformation visible in all measurements, with a maximum value of 0.28 mm. The maximum was measured after the ultimate load release (step 9 in Table 3.3). As there is a higher increase of permanent deformation after release of the ultimate load (Release 9 in Figure 3.13) we consider the yield point to be between load 6 and 8, which was also predicted for several elements in the FEA model. The deformation after the limit load release and the other load steps (3, 5, 7) were smaller than 0.10 mm and did not consecutively increase, thus it was considered an elastic deformation without yield failure. As a result, the limit-load criterion, with no permanent deformation allowed, was met as well.

In conclusion, the static stiffness deformation was considered well modeled and the elastic-plastic transition did occur at the expected load step. Still, there was an evolution of permanent deformation visible and the application of the yield failure methodology was considered sufficient. Finally, all design criteria were met and the multi-hybrid partly bio-based design was considered certification proven in terms of limit and ultimate loads.

3.1.6 Damping and Modal Analysis of the Tailplane

According to literature, flax and other NFRP show very high damping ratios compared to conventional CFRP structures [147, 12, 104]. In order to find out about the damping performance of the hybrid design tailplane, a free-free configuration EMA was performed on both, the reference CFRP tailplane section and the hybrid NFRP tailplane. Both results were compared in terms of swing-out behavior and frequency response, see Figure 3.14. It can be seen that the logarithmic decrement of the hybrid tailplane is higher, and the frequency response of the hybrid tailplane is blunter at resonance frequencies compared to the carbon reference.

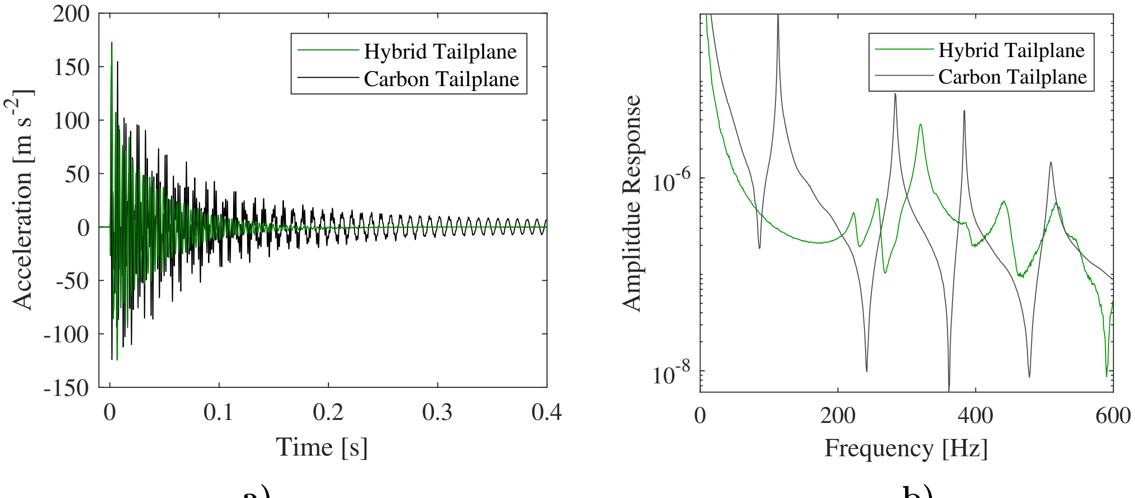

a) b)

Figure 3.14: Comparison of Hybrid Tailplane and Carbon Tailplane in Terms of Logarithmic Decrement in a) as Acceleration over Time, and b) Frequency Response

In order to quantify the better damping of the new design tailplane, the frequency dependent damping ratios were determined using the half-power-bandwidth method on the FRF, results are shown in Figure 3.17. The damping ratio ζ is defined in Equation 3.17, where ω_n is the respective eigenfrequency and ω_1 and ω_2 are defined by the FRF at the position of $2^{-\frac{1}{2}}\,a$, with a as maximum amplitude; this method is based on ASTM Standard E756 [67].

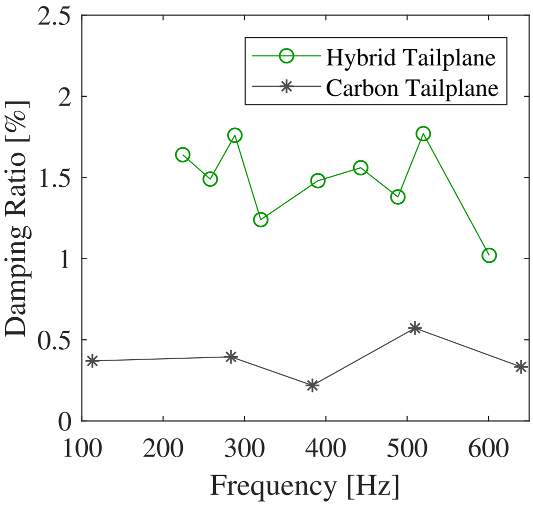

Carbon Tailplane

Mode	f [Hz]	ζ
1.	113.0	0.00370
2.	283.4	0.00395
3.	383.5	0.00219
4.	509.6	0.00572
5.	640.0	0.00333

Hybrid Tailplane

Mode	f [Hz]	ζ
1.	224.1	0.0164
2.	257.9	0.0149
3.	288.2	0.0176
4.	320.0	0.0124
5.	390.3	0.0148
6.	442.9	0.0156
8.	488.6	0.0138
9.	600.9	0.0102

Figure 3.15: Comparison of Damping Ratios Over Resonance Frequencies and Values Listed in Tables of Both Tailplane Versions

$$\zeta = \frac{\omega_2 - \omega_1}{2 \cdot \omega_n} \tag{3.17}$$

The damping ratios of the carbon, full-core version were between 0.22% and 0.57%, while the new hybrid design was damped with ratios between 1.0% and 1.8%. This results in approximately two to eight times higher damping ratios in the new FFRP design. The high variations in the damping ratios are accounted to the respective mode shapes. Material inherent damping in a composite is also dependent on the fiber orientation. Therefore, the absorbed energy by material strains is resulting from a combination of mode shape, reinforcements, and location of the strained area.

Still, structural damping is only one part of the damping mechanisms in helicopters, besides frictional, aerodynamic, and viscous damping. But in terms of cabin vibration and noise reduction, we conclude that hybrid applications with FFRP offer great potential.

Figure 3.17 shows the frequencies of the EMA versus the resonance frequencies from the

FEA calculations. Four sensors were used, with three recording accelerations each, in x, y, and z. Therefore, the compared frequencies were extracted from 12 FRFs, ergo 12 degrees of freedom. We can see that lower frequencies were rather too high in the model and higher frequencies rather too low, while in the fourth natural frequency is off the most.

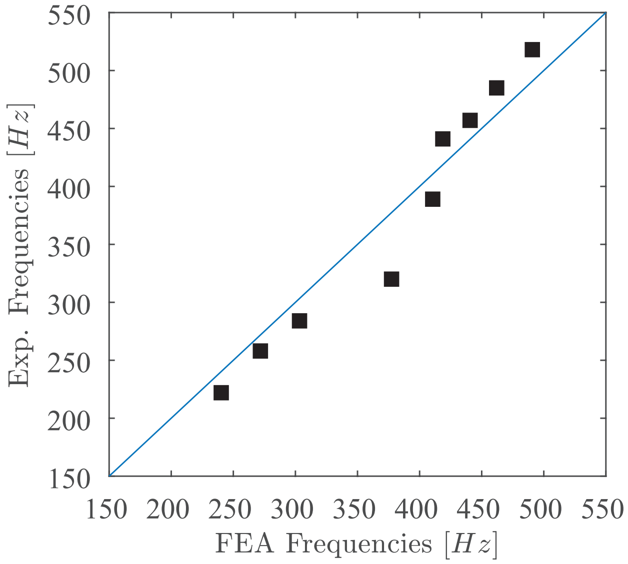

Figure 3.16: Comparison of EMA Resonance Frequencies versus FEA Resonance Frequencies, of the Hybrid Tailplane

Modes 1–3 and 5 show good agreement, but were higher in the FEA model, while the 4th mode is off by approximately 17%; modes 7–9 are in a range between 6 and 8% too low in the FEA calculations. In order to find out about the proper allocation of frequencies, the mode shapes were compared via the MAC. The criterion uses the normalized vectors of the mode shapes and compares the direction. Identical vectors result in a MAC value of 1, perpendicular vectors result in a MAC value of 0. The MAC values are calculated by Equation (3.18), with Φ_i accounting for the mode shape vectors. The results of the comparison of the first five mode shapes are plotted in a matrix in Figure 3.17.

$$MAC = \frac{|\Phi_1 \cdot \Phi_2|^2}{|\Phi_1 \cdot \Phi_1| \cdot |\Phi_2 \cdot \Phi_2|} \tag{3.18}$$

The mode shapes were calculated by Quadrature Picking, which uses the imaginary part of the frequency response function. It can be seen that the second mode of the FEA calculations matches the second and third mode of the experiment, which shows that the model was not capable of identifying all mode shapes properly. As the third mode of the FEA calculations matches the fourth mode in the FEA, the frequency comparison in Figure

3.17 a) has to be reconsidered for these modes.
This discrepancy could be explained by the perfectly symmetric FEA model, while the experiment lacks this ideal. Additionally, the free-free configuration was realized by soft rubber bands, which could also influence the results, as well as the sensors' cables. Nevertheless, this analysis was considered matching regarding to the uncertainties not included in the model. Furthermore, the four sensor positions do not describe the mode shapes entirely, which is why we can see agreements between other modes as well, e.g. 1st EMA with 5th FEA.

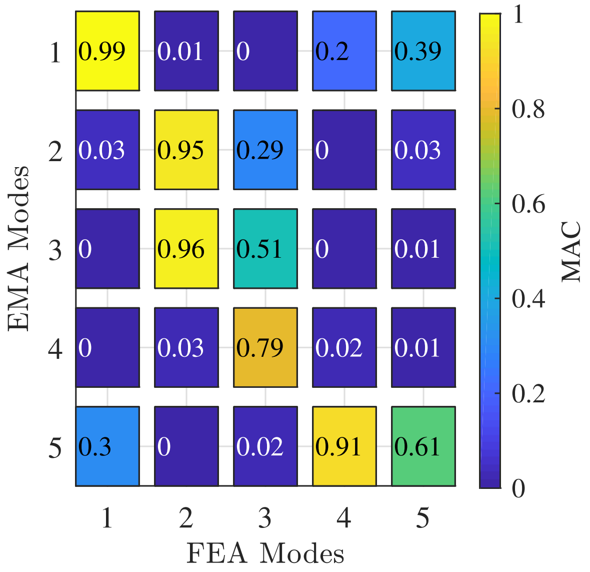

Figure 3.17: Modal Assurance Between EMA and FEA of the Flax-Carbon Hybrid Tailplane Section

As conclusion, the resonance frequencies match well with the FEA model and the high damping of FFRP could be verified, even in combination with CFRP and balsa. The high MAC values also approve the model, some mode shapes are mismatched, but due to the simple experimental set-up this was considered acceptable.

3.2 Design and Experimental Evaluation of the Component Cockpit Door

Contents of this section were also published in VFS2019. The student theses Braun2017 (manufacturing and characterization of reference door), Boesl2017 (preliminary design of hybrid door), Huber2018 (experimental investigations on coupons and beams), and

Droege2019 (manufacturing and static load tests on hybrid door) contributed to this section.

As a second technology demonstrator, the cockpit door of an ultralight helicopter was investigated, where complex curved surfaces made the use of woven composites necessary. A reference door, built from CFRP, was considered as a benchmark to the requirements in terms of mass, stiffness, damping, ecological efficiency, and costs. In this case, the CFRP benchmark door was not readily available but needed to be built and characterized.

For the new FFRP application, the geometry was redesigned with respect to the properties of FFRP, leading to an increase of the areal moment of inertia. The new geometry was then analyzed using multiple gravity loads, as specified by respective certification standards. Highly loaded areas were reinforced using woven carbon prepreg material, while the base structure was designed using woven flax layers. Tensile tests and sub-component cantilever beam tests were iteratively used for the development and advancement of an FEA model. The resulting hybrid design showed promising results, as the stiffness matched the reference door's and a mass reduction of 6% with an increase in the bio-based material mass from 0 to 43% was achieved. But, due to manufacturing issues, as explained in Section 2.6, additional epoxy layers had to be used with the FFRP weave, which significantly reduced the fiber volume content. As a result, the built hybrid door achieved a bio-based mass content of only 30%, while its weight increased by 34% in total. An LCA on the eco-efficiency regarding these facts will be itemized in Section 4.1.

3.2.1 Design and Identification of Loads on the Cockpit Door

First, a reference door was built as a structural demonstrator. It has a size of approximately 1.30 m times 1.00 m, and the reference design is made of two layers of carbon-woven prepreg with a $[\pm 45]_2$ lay-up of a 2/2 twill weave of $200\,\mathrm{g\,m^{-2}}$. This material was only used for this reference and is not used by the manufacturer as the lay-up and material type are not publicly available. The built CFRP design served as a reference in stiffness, as well as in dynamic and environmental performance.

The hard design constraints were derived from the national ultralight helicopter certifications (LTF-ULH 2016 [111]) as follows: No permanent deformation when accelerated by maneuvering loads of $+3.5$ and $-1.00\,\mathrm{g}$ in Y and Z direction and no failure when accelerated by $\pm 3\,\mathrm{g}$ in Y, by $9\,\mathrm{g}$ in X and by $\pm 4.50\,\mathrm{g}$ in Z-direction (axes as shown in Figure 3.19).

These constraints were derived in relation to the maneuvering loads, at which no permanent deformation is allowed and by emergency landing loads where no passenger should be harmed, but permanent deformations are allowed. As the doors are right besides the passengers, these should not fail completely and maintain their protective function in case of an emergency landing. Further, soft design constraints considered the aerodynamic load in a fast forward flight, the aerodynamic load of a gust when the door is open, and a handling load from a person leaning on the door. Under these loads the reference door also showed large deformations, and aerodynamic loads were not verified, conclusively, these soft constraints were substituted by an equal stiffness demand with respect to the reference door.

The design approach for the new door was as follows: First, the geometric shape of the reference cockpit door was adapted on the outside, as the aerodynamic behavior of the helicopter should not be influenced. Next, the inner geometry was redesigned in order to increase the bending and torsional moment of inertia. Comparing both designs, the cross-sectional moments of inertia could be increased in a range of 5 to 20% and in one outstanding position by 100%.

Next, critically loaded areas were identified in order to define positions for reinforcements, these locally constrained areas were split from the base-geometry in the CAD model. Next, an FEA model iteratively optimized the needed reinforcements and amounts of layers. In order to investigate methodologies of maximizing the bio-based mass content, different configurations were analyzed and five door versions were the matter of investigation using the following material combinations: 1 - pure carbon, 2 - pure flax, 3 - half-half carbon-flax hybrid, 4 - flax with flax reinforcements and 5 - flax with carbon reinforcements. The FEA material data referred to the respective TDS and were not experimentally determined at this point, therefore the masses and bio-based contents are hypothetical values. The results of the simulations are plotted in Figure 3.18.

It has to be considered that versions 2 and 3 resulted from a simple layer substitution of the materials, and these versions would not meet the requirements in terms of stiffness and strength. In the analytical comparison of all versions, the best compromise between stiffness and bio-based material content was identified as version 5 - flax with carbon reinforcements. The hybrid design (version 5) used two layers of $150\,\mathrm{g\,m^{-2}}$ flax in $[\pm45]_2$ lay-up as base material and additional carbon weave reinforcements of the type twill 2/2 with $200\,\mathrm{g\,m^{-2}}$, with fibers oriented in load-path directions. The areas of reinforcements are shown in black in Figure 3.19; the base layers of flax are plotted in gray.

The structural-mechanical design was performed using the frame structure of the door and a mass simulation of the plexiglass window. The bonding of the inner and outer shell was modeled using beam elements, as well as the foam core inserts at the load initiation and clamping points.

From the existing material model derived by coupon tests, as described in Chapter 2, the next step was a preliminary model validation using sectional beams, following the test pyramid after Rouchon [143] and a V-model approach. In doing so, the material model and the FEA simulation of the whole cabin door uses experimental results of coupons and sub-components.

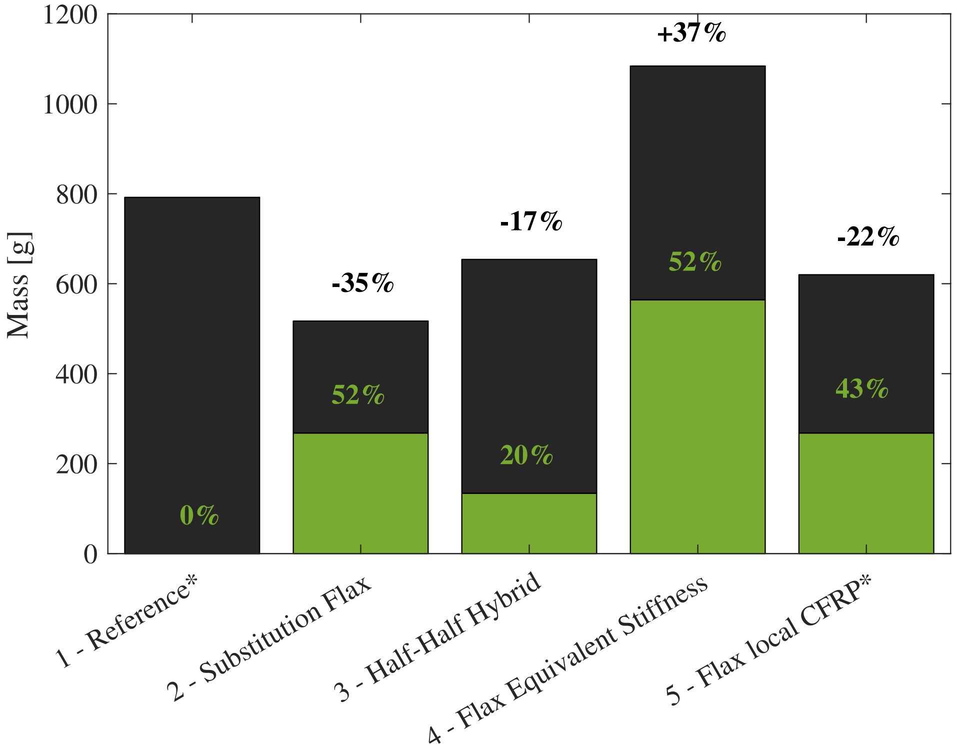

* built and characterized versions

Figure 3.18: Bio-Based Mass (green) and Total Mass Comparison to the Reference of Different Pre-Design Door Versions

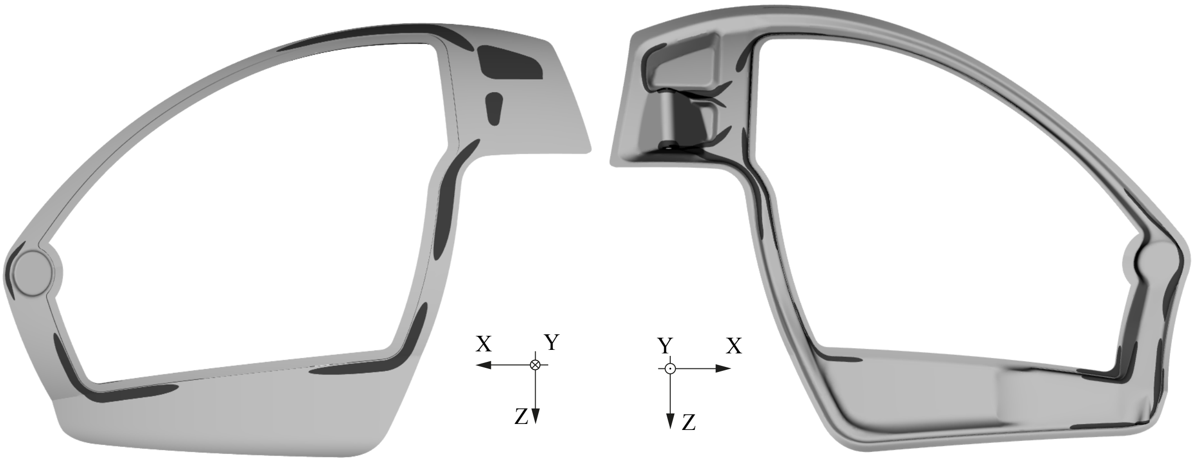

a) b)

Figure 3.19: a) Outside and b) Inside View of the Cabin Door, Gray: Flax-Fiber Material, Black: Carbon-Fiber Reinforcements

3.2.2 Sub-Component Cantilever Beam Tests

In order to validate the implemented FEA material model on a simple shape, a beam geometry of the most stressed section in the door was extracted and symmetrically balanced in its geometry. The omega-profiled cross section of the strongly curved beam structure below the hinge was chosen. Three beams were manufactured and tested, one pure flax beam, one hybrid beam, and one pure carbon beam, from left to right in Figure 3.20. These sub-component beams were analyzed preliminarily in terms of mass, bio-based content, stiffness, damping, and failure.

The pure woven CFRP beam with a fiber orientation of [±45] serves as a reference. The primarily described FFRP weave with the mentioned epoxy film layers and [±45] fiber orientations was applied in the pure flax and in the hybrid beam. The hybrid beam was built using FFRP as base material, and CFRP reinforcements with a [0/90] fiber orientation in positions of high inertia, see Pos. A in Figure 3.21 and mid-bottom reinforcement. All beams were glued in the area of Pos. B using 3M Scotch-Weld 9323. In order to imitate a completely stiff clamping, the beams were embedded in epoxy and filled with epoxy at the areas of load initiation, analogically to the tailplane experiments. The hybrid design was developed by the constraint in Equation (3.19) and a set of simplifications. The neutral axis was determined from the geometry only and the material was considered isotropic with strength and stiffness parameters from the tensile tests in the $[\pm 45]_8$ lay-up.

The built masses and bio-based contents of the beams are listed in Table 3.4. As a conclusion, the epoxy film layers reduced the fiber and thereby bio-based mass content significantly. On the other hand, it can be seen that the hybridization results in bio-based mass contents comparable to the pure FFRP beam as the CFRP material fraction was very low.

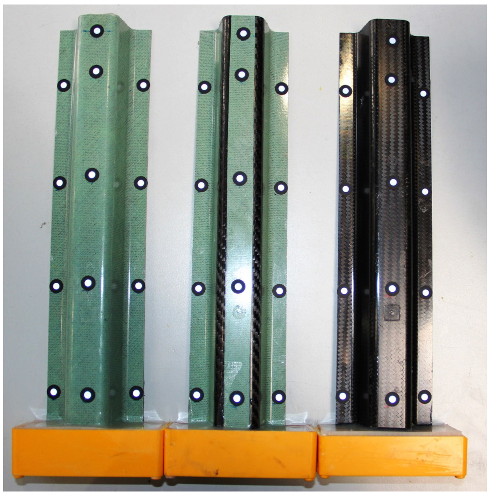

Figure 3.20: Photograph of Epoxy Embedded Beams from Left to Right: FFRP, Hybrid, CFRP

$$(E \cdot I)_{Carbon} \overset{!}{=} (E \cdot I)_{Hybrid} \tag{3.19}$$

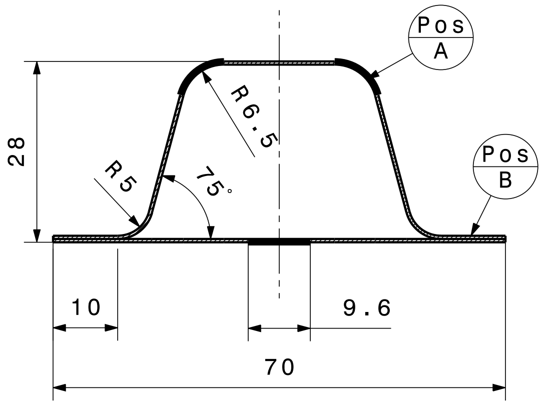

Layup-Table

	Pos A	Pos B
CFRP	$[C_{\pm45}]_S$	$[C_{\pm45}/C_{\pm45}/G]_S$
NFRP	$[E/F_{\pm45}]_S$	$[E/F_{\pm45}/F_{\pm45}/E/G]_S$
Hybrid	$[C_{0/90}]+[E/F_{\pm45}]_S$	$[E/F_{\pm45}/F_{\pm45}/E/G]_S$

Figure 3.21: Section Cut with Lay-up Definitions of all Omega-Beams, Woven Carbon, Woven Flax, and Hybrid Materials

Table 3.4: Mass Contents by Material of a 350 mm Section of All Three Omega Beams

	CFRP Beam		FFRP Beam		Hybrid Beam	
[Unit]	[g]	[%]	[g]	[%]	[g]	[%]
Carbon Fiber	20.3	50	0.0	0	2.3	5
Flax Fiber	0.0	0	15.2	32	15.2	30
Epoxy Resin	18.7	47	13.5	29	13.5	27
Epoxy Film	0.0	0	17.1	36	17.1	34
Scotch Weld 9323	1.2	3	1.2	3	2.1	4
Total	40.2	100	47.1	100	50.3	100
Total Bio-based	0.0	0	15.2	32	15.2	30

It is also noticeable that the FFRP and the hybrid beams were significantly heavier than the CFRP reference beam (17% and 25%). This drawback is expected to be reducible in the future by the availability of a neater flax prepreg weave.

Experimental investigations were done with all three beams in a cantilever beam test. The load steps were aiming to identify the elastic plastic transition as detected in the tensile tests. Therefore, the chosen load steps were right below (hybrid) and right above (pure flax) the identified yield point at $\epsilon_{45} = 0.625\%$, or $F_{t,f,K}$. Each load step was force-controlled and the deformation was measured with a static photogrammetry system (AICON 3D) and additional tracking of the machine crosshead travel. In order to determine plastic deformation, the deformations of the beams after the load application were compared to the initial positions of the beams.

The defined load steps with the resulting maximum strain in the specimens' x-direction, thus fiber orientation of [±45], as well as the FEA and experimental deformations are listed in Table 3.5.

Table 3.5: Planned and Tested Load Steps of the Three Different Beam Versions with Results of FEA and Experiment

Load Steps	Data	[Unit]	Flax	Hybrid	Carbon
1 - 1st Load	Force	[N]	50	86	86
	max. ϵ_x (FEA)	[%]	0.64	0.51	0.32
	max. R_{xyz} (FEA)	[mm]	5.591	5.188	4.332
	max. R_{xyz} (Exp.)	[mm]	6.778	6.300	4.824
	Deviation FEA/Exp	[%]	-17.5	-17.7	-10.2
2 - Release	Force	[N]	0	0	0
	max. R_{xyz} (Exp.)	[mm]	0.43	0.24	0.24
	Deformation Ratio R_2/R_1	[%]	6.3	3.8	4.9
3 - 2nd Load	Force	[N]	102*	138	138
	max. ϵ_x (FEA)	[%]	1.32	0.83	0.51
	max. R_{xyz} (FEA)	[mm]	11.784	9.047	7.029
	max. R_{xyz} (Exp.)	[mm]	18.27**	11.159	8.547
	Deviation FEA/Exp	[%]	-35.5	-18.9	-17.8
4 - Release	Force	[N]	0*	0	0
	max. R_{xyz} (Exp.)	[mm]	-	0.41	0.56
	Deformation Ratio R_4/R_3	[%]	-	3.7	6.6
5 - 3rd Load	Force	[N]	-	145	175
	max. ϵ_x (FEA)	[%]	-	0.87	0.65
	max. R_{xyz} (FEA)	[mm]	-	9.564	8.952
	max. R_{xyz} (Exp.)	[mm]	-	14.195**	13.492
	Deviation FEA/Exp	[%]	-	-32.6	-33.6

* not measured because kinking occurred before

** calculated by machine crosshead travel, not photogrammetric measurement data

In comparison, the FEA results showed lower deformations than the experiments. It is assumed that the epoxy embedded clamping is influencing the deformations and should be reconsidered for a more sophisticated verification. Nevertheless, the epoxy clamping was modeled with beam elements in order to include the inherent elasticity. Additionally, all deviations were increasing with higher loads, also the CFRP beam. Therefore, it is assumed that the geometrically nonlinear behavior, which is increasing with higher loads, is not modeled perfectly, even though the general buckling behavior is fitting well, as shown in Figure 3.22. All beams failed due to instabilities on the lower surface of the beams, described as kinking, very close to the epoxy embedded clamping. Due to this stability failure, not all load steps could be tested according to the plans. Nevertheless, the geometrical nonlinearities could be modeled qualitatively well.

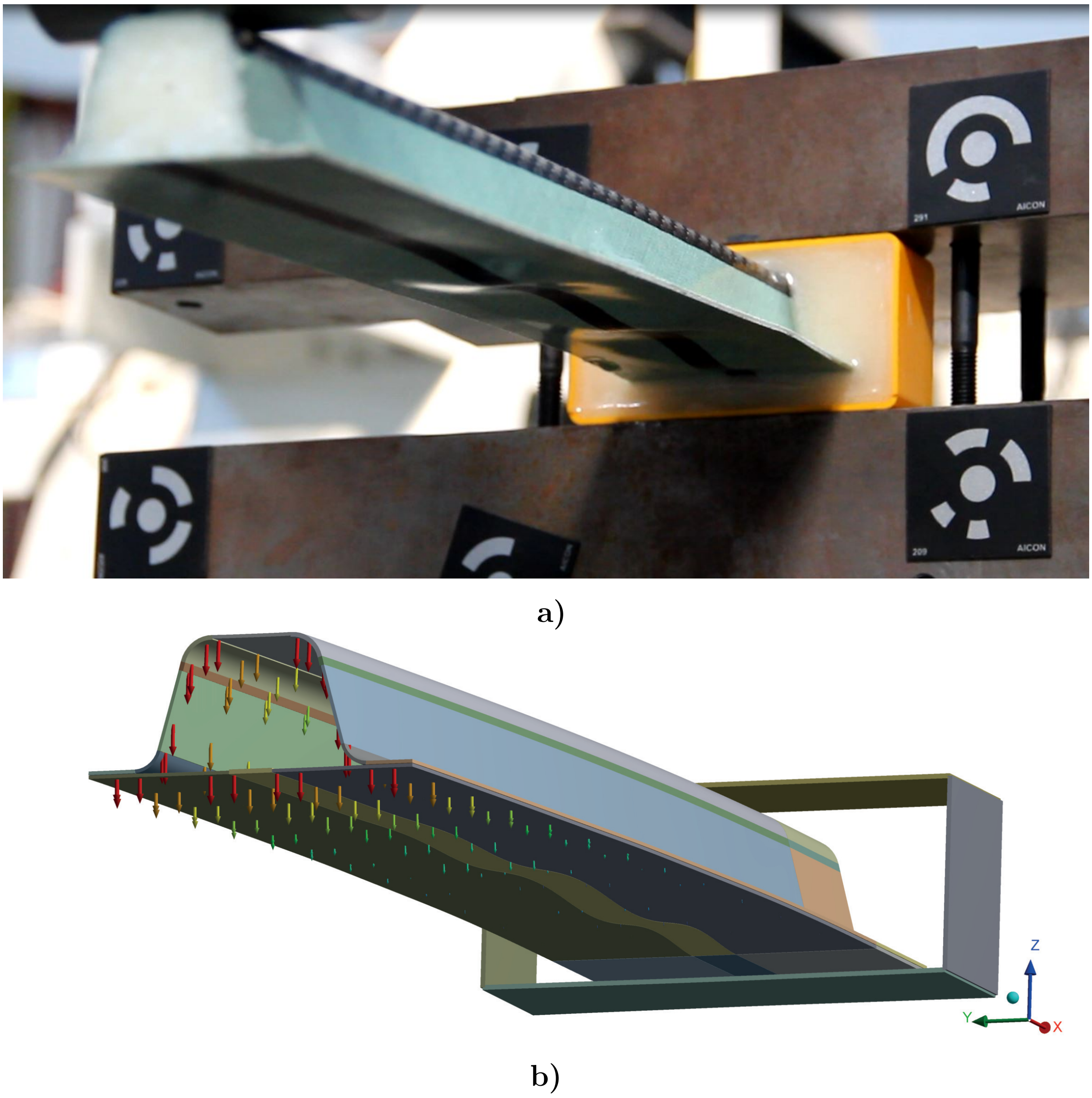

Figure 3.22: Kinking on Hybrid Beam Bottom in Comparison of a) Experiment to b) FEA Simulation at 138 N

Additionally, a geometrical compression of the omega shape could be observed and a small torsional deformation below 1°. These phenomena were not analyzed further as this was not the focus of this research, and we want to neglect the increasing deviations but use the carbon beam results as a reference.

Comparing the second load step, the pure flax beam showed the highest deviation between model and experiment, even though the loads were significantly lower. As a reminder, the FEA beam models were using linear material models. The deviations of the hybrid beam and the carbon beam were comparable.

Also, the loading led to permanent deformations in all beams, see Figure 3.23, which is likely to be induced by the epoxy clamping. Still, a significantly higher permanent deformation could be observed for the pure flax beam, despite lower loads. In both load release steps, the hybrid beam showed comparable permanent deformation to the pure carbon beam. Thus, we conclude that the CFRP reinforcements in the hybrid beam dominate the overall beam behavior and suppress the material permanent deformations by its inherent elasticity.

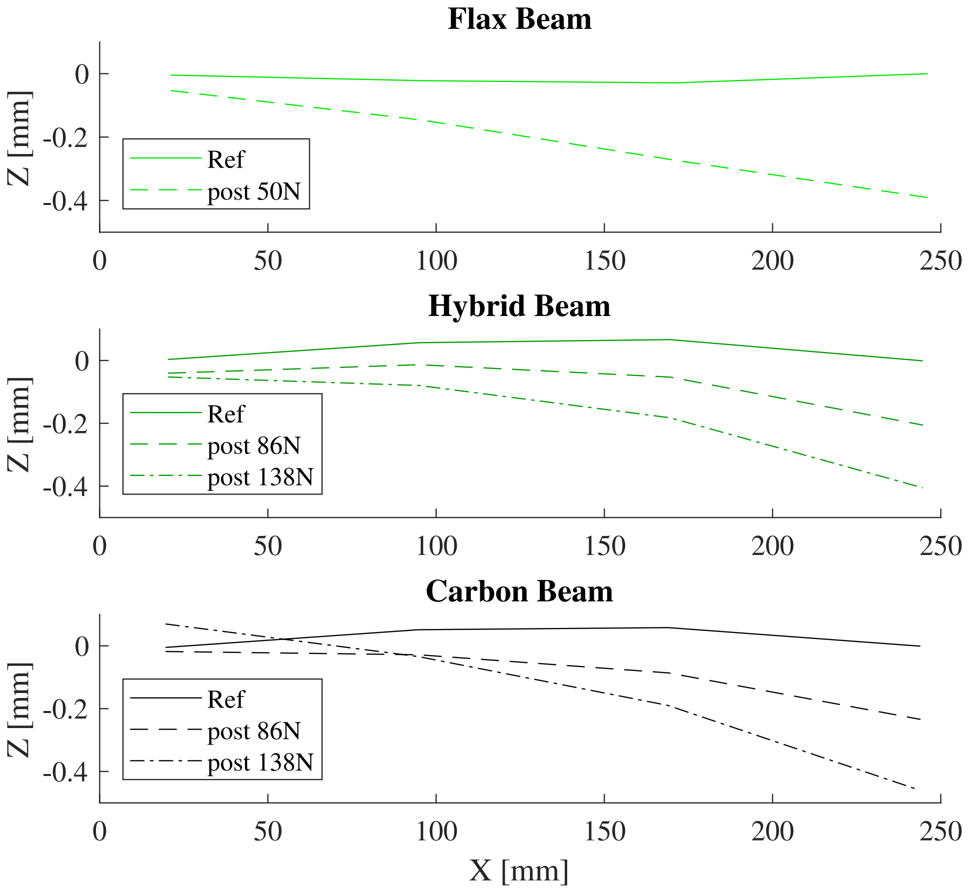

Figure 3.23: Permanent Deformations after Two to Three Different Load Applications of All Three Beams

In Figure 3.24 the stress and strain distribution in the hybrid beam simulation under the first load step is shown. We can see that the CFRP reinforcements are bearing most of the load while the flax base material is barely stressed. This observation supports the CFRP domination in the hybrid. On the other hand there is a higher strain in the middle, where only flax layers are existent. The simulations appear valid, but the values can not be verified conclusively as the overall deformation was influenced by the epoxy clamping in a significant amount which could not be validated securely.

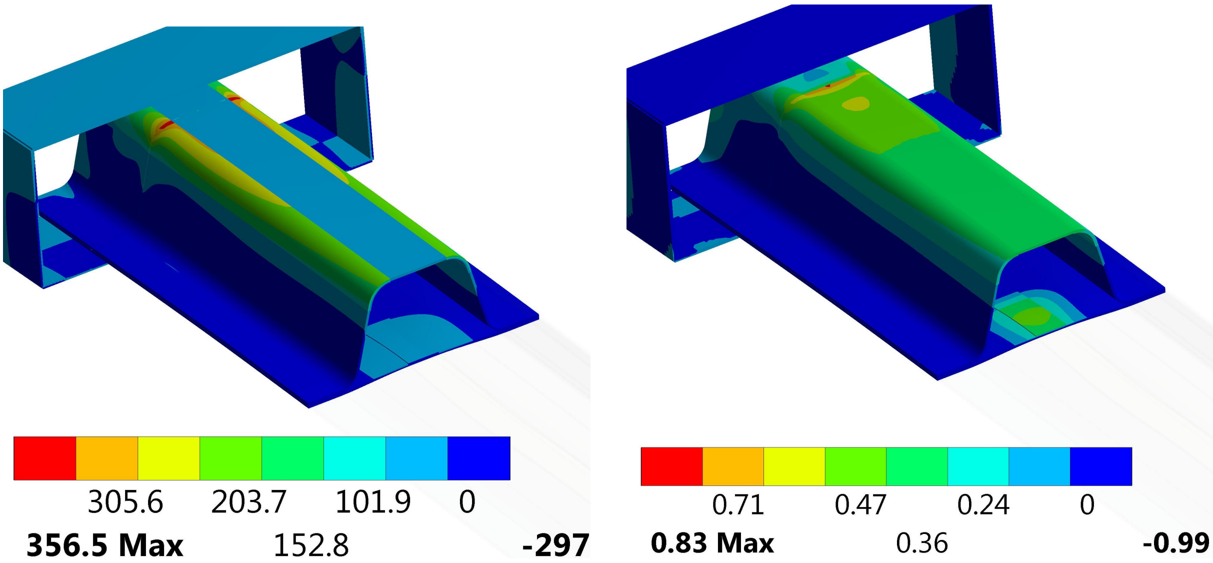

Figure 3.24: a) Stress in [MPa] and b) Strain in [%] in X-Direction of the First 100 mm Section of the Hybrid Beam Under 138 N Loading

Final conclusions drawn from the beam tests were that a stiffer clamping would be necessary in order to verify deformations reliably. Additionally, the earlier described material nonlinearities need to be taken into account and are considered a crucial property in designing cyclic or multiple loaded structures made from flax.

Finally, an EMA was done with all beams in a free-free configuration. The damping values were calculated by the half power bandwidth method from the modal FRFs. As the beams were very lightweight and acceleration responses were small, white noise was prominent in the signals. A FIR filter was applied to the frequency response functions before the damping analysis.

Results showed a mean value of 0.84% for the CFRP beam, 3.40% for the FFRP beam, and 3.19% for the hybrid beam. Results of the most prominent resonance frequencies were analyzed. It has to be mentioned that, despite the noise filter, the signal analysis was still of weak quality, the results should be reconsidered carefully. Nevertheless, the results underlined the potential of the hybridization as damping values were in the same range for the pure flax and the hybrid beam, which were approximately four times higher than the damping ratios of the pure carbon beam.

3.2.3 Built Door Masses and Bio-Based Contents

As already mentioned, the CFRP reference needed to be built itself. Its final weight was 659 g, 17% lower than the reference in the simulation. Due to the use of foam molds, the laminate was particularly dry on the mold surfaces. In order to increase the surface quality, a higher epoxy content should be aimed. Thereby, the mass would be closer to simulation results.

The simulation model of the hybrid design still resulted in benefits in weight of 6%, when compared to the built reference door. In the simulation the assumption of $\varphi_f = 45\%$ was applied, as given by the manufacturers' TDS [151]. This could not be reached by the built hybrid door, as additional epoxy layers were necessary.

For the whole hybrid door the concluding final mass was 885 g. Thus, 34% higher than the built reference instead of 6% lower. The bio-based mass content of 30% was calculated using the measured prepreg-patch masses, this ratio was also lower than expected due to the additional epoxy film.

As the tensile coupon and beam tests were performed using the additional epoxy film layers, the derived FEA model and all mechanical performance simulations are carried out on the built materials. Therefore, the built door, of low manufacturing quality and high mass, was still used for a characterization of damping and a validation of the design. The results will be explained in detail in the following. The evaluation of the eco-efficiency later on will also include the pre-design door, with the hypothetical φ_f of 45% as in the material's TDS.

3.2.4 Quasi-Static Deformation Tests of the Door Structure

Static load tests on both built door versions are described and analyzed in this section, where multiple load steps were applied in all orthogonal axis directions. The tests on the hybrid door were carried out and analyzed in respect to the FEA model and the reference door performance. Deformations were analyzed on several points using photogrammetric measurement marks, exemplary visible in Figure 3.20 and 3.25.

A stiff and variable clamping on the doors' hinge axis was designed to test both of the door structures in all 3D transversal directions. Two load steps were applied in each direction, both below the derived material yield failure. Thereby, an influence upon the experiments was aimed to be avoided. Figure 3.25 shows the experimental setup and the built door structure. The load was initiated for all load cases at the very left tip of the door.

In order to prove the design constraint of equal stiffness to the carbon reference door, the the maximum deformation in all experimental directions were compared, see Figure 3.26. In most directions, the load-deformation ratio showed comparable results in both versions and the constraint could be verified, only in the Y+ direction, the carbon reference showed significantly higher stiffness than the hybrid reference.

In order to verify the application of the derived yield criterion, which claimed no permanent deformation, the unloaded deformations of the hybrid door were also measured. An almost linear relation between the unloaded deformations and the applied load could be observed, while the unloaded deformation after the load steps were in a range of 3–5% for all directions. There was no difference in permanent deformation between the two load steps observable and the measurable permanent deformations were very low. These were accounted to the viscoplasticity of the epoxy matrix and thereby acceptable.

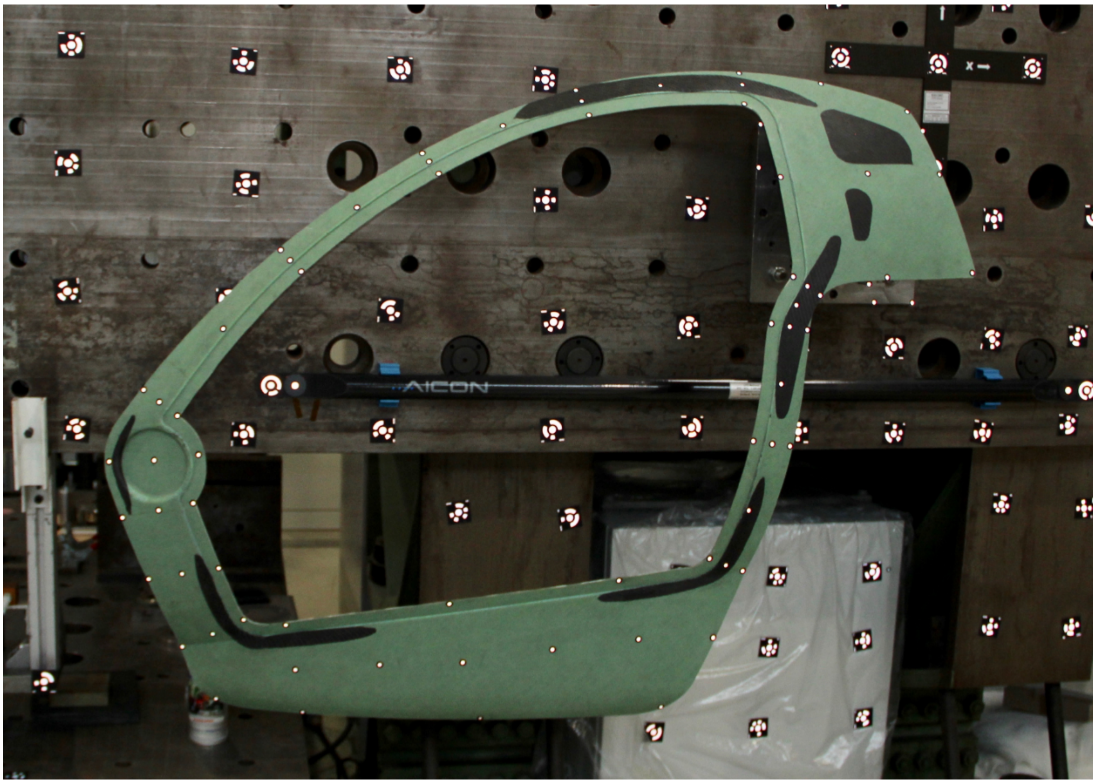

Figure 3.25: Experimental Setup of Static Load Tests in Y-Direction of the Hybrid Carbon-Flax Cabin Door

In order to further verify the design by which the certification requirements were proven, the deformation vectors were compared to the simulation in a more detailed manner. The model and experiment matched in the first load step in X and Z-directions almost perfectly by a deviation of 0–3%. In Y-directions, the agreement was between 5 and 11%, comparing the maximum deformation vector length. As a result, the design could be verified.

At the second load step, the deviations were higher comparing experiment and simulation, which was accounted to the geometrically nonlinear behavior, which is difficult itself to model. Nevertheless, as hard design constraints of the multiple gravity loads resulted in even lower deformations than the first experimental load, the model was considered suitable for proving the proper performance of the newly designed cabin door. Additionally, in the use-life application, the plexiglass window provides extra stiffness and also clamping supports the structure at three points.

For a comparison of load directions, Figure 3.27 shows the deformation vectors of all measured points in the experiment and the simulation. It can be seen that some areas match well with the experimental data while others show differences of approx. 30°. The geometrically nonlinear behavior could account for that.

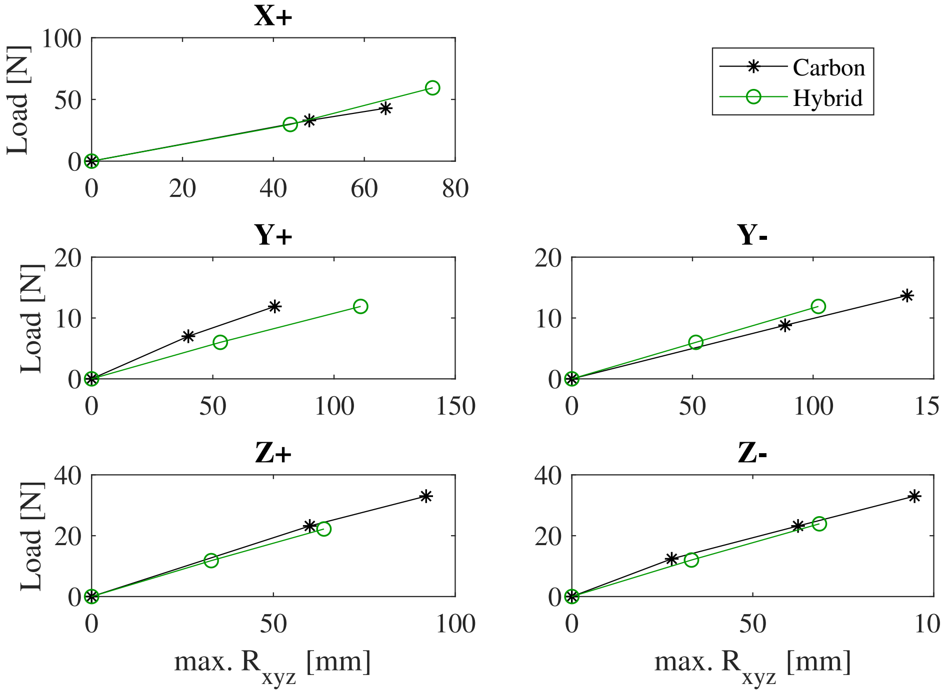

Figure 3.26: Experimental Load-Deformation Ratios of the Carbon Reference Door and the Built Hybrid Door

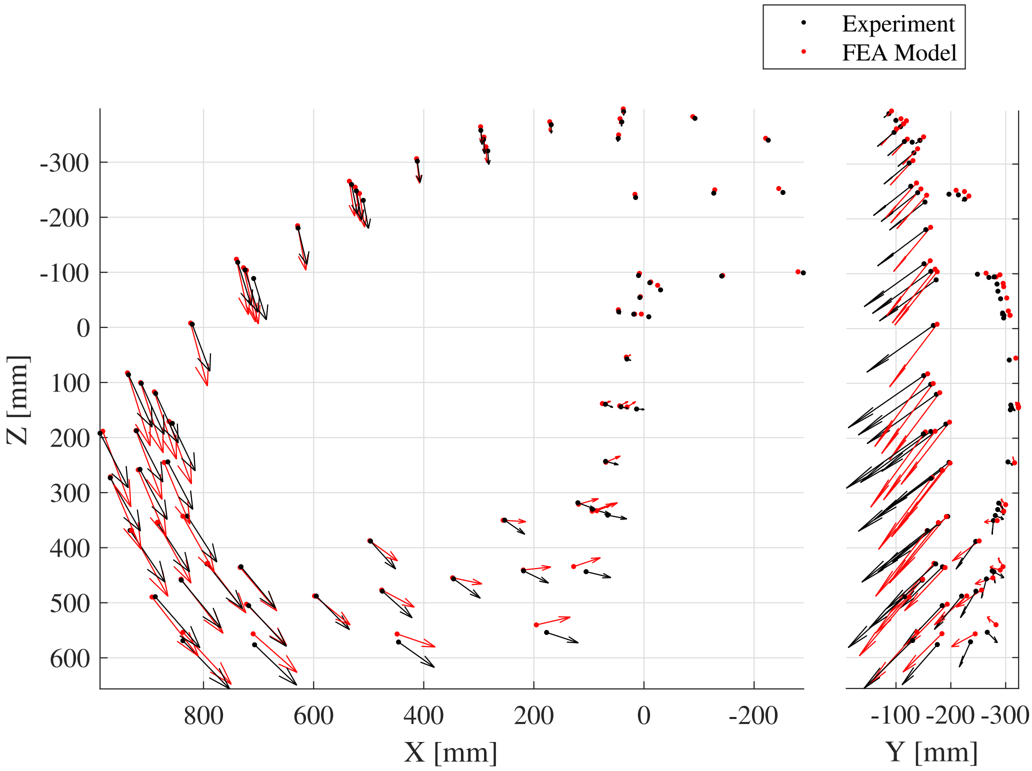

Figure 3.27: Deformation Vectors of Simulation and Experiment of the Hybrid Cabin Door at a Load of 11.80 N in positive Z-Direction

As a result, the structural performance of the cabin door could be validated and accordance to the certification specifications verified. Despite the higher weight, the design was considered successful.

3.2.5 Modal Analyses and Damping of the Cabin Door

In several references, the damping capabilities of natural fibers are emphasized [147, 136, 104, 12], as well as a high potential in noise and vibration canceling, according to relevant literature [137, 121, 95]. Therefore, damping properties of the hybrid door, with the material combination of epoxy, flax, and carbon, were determined to investigate this beneficial property.

For the EMA of the reference and the hybrid door, 12 triaxial acceleration sensors were applied in the experiment, in three configurations, with 4 sensor positions each. Thus, we have a resulting 36-degrees-of-freedom acceleration response function. All configurations were excited by an impulse hammer at the same position and direction.

With these results, the FEA simulation of the hybrid door could be validated in terms of natural frequencies. The results of the simulation and experiment matched well in the compared range of 0–150 Hz, while most of the values are in a range of ± 3 Hz and ± 5% accuracy (see Figure 3.30).

For the determination of damping properties the half-power bandwidth method was applied to the FRFs of both doors, using a least-squares complex exponential curve fitting algorithm, one per measured accelerometer degree of freedom and configuration. The median of identified natural frequencies is in a range of ±3 Hz and their respective damping ratios are plotted in Figure 3.28.

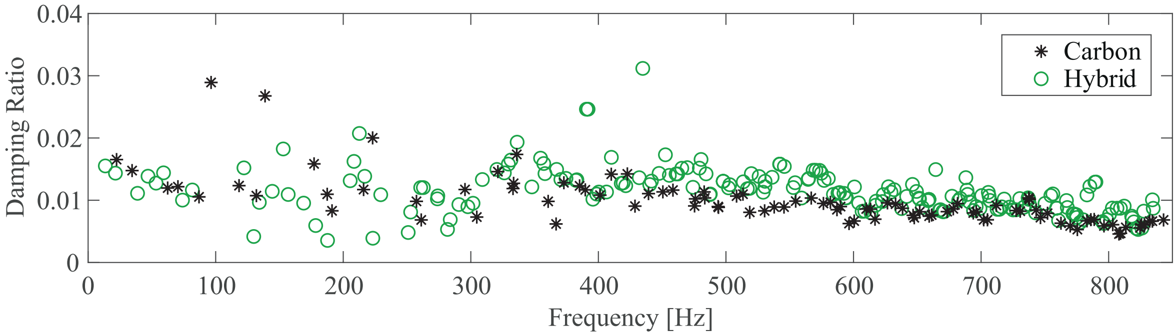

Figure 3.28: Damping Comparison of Reference and Hybrid Door

In the range of 0–400 Hz, there was no significant difference in damping observable between both door structures. In the range of 400–850 Hz, there was an offset of approximately 30% (0.003 loss factor) with higher values for the hybrid door.

In these experiments, the carbon reference door shows high damping values for CFRP structures compared to other references [11, 122], which is explained by the rather dry weave quality. The damping ratios of the hybrid flax door match other values from the data sheet and the performed measurements with unidirectionally reinforced material on the tailplane. Generally, a decrease in damping with increasing frequencies was observed for both door versions.

Again, a comparison in terms of mode shapes was performed, where we could achieve a considerably well fit between simulation and experiment for the carbon reference door, see Figure 3.29. The hybrid door did not show agreement in mode shapes with the simulation, which we could not explain satisfactorily. Possible mistakes in the results analysis were investigated and complex mode shapes were apparent for the hybrid door, therefore, the high viscoelastic and nonlinear material behavior was considered accountable for the lack of mode shape accordance.

Nevertheless, as all frequencies showed good agreement and the reference was in good agreement as could be seen in Figure 3.30, the FEA models were considered as of acceptable quality.

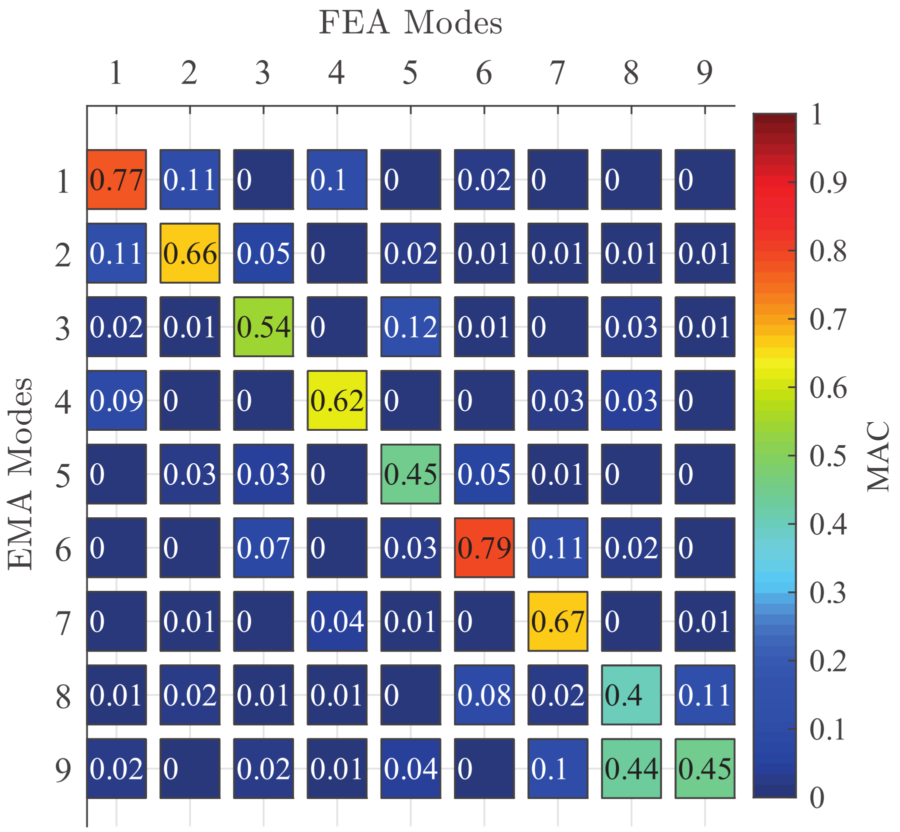

EMA \ FEA	1	2	3	4	5	6	7	8	9
1	0.77	0.11	0	0.1	0	0.02	0	0	0
2	0.11	0.66	0.05	0	0.02	0.01	0.01	0.01	0.01
3	0.02	0.01	0.54	0	0.12	0.01	0	0.03	0.01
4	0.09	0	0	0.62	0	0	0.03	0.03	0
5	0	0.03	0.03	0	0.45	0.05	0.01	0	0
6	0	0	0.07	0	0.03	0.79	0.11	0.02	0
7	0	0.01	0	0.04	0.01	0	0.67	0	0.01
8	0.01	0.02	0.01	0.01	0	0.08	0.02	0.4	0.11
9	0.02	0	0.02	0.01	0.04	0	0.1	0.44	0.45

Figure 3.29: Modal Assurance of EMA and FEA of the Carbon Reference Door

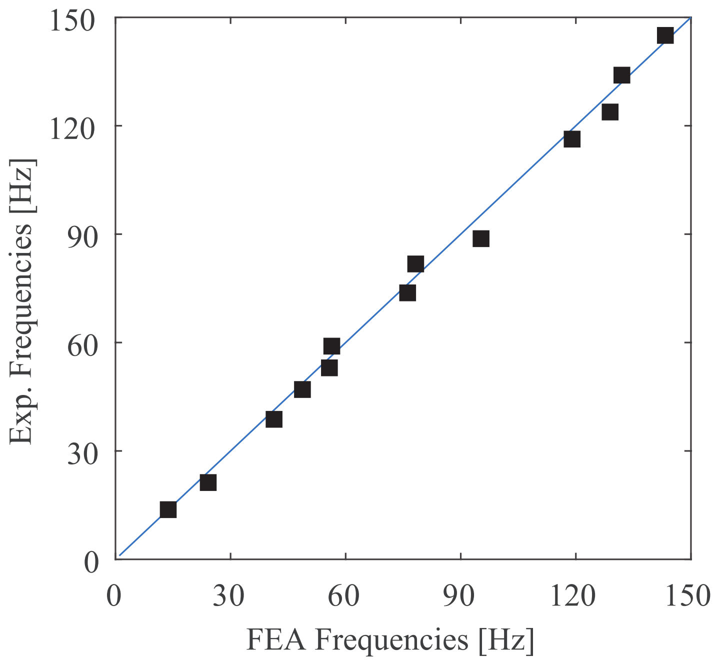

a)

Figure 3.30: Comparison of EMA and FEA results in terms of Natural Frequencies of the Hybrid Door

3.3 Moisture Uptake and Hydro-Swelling Induced Deformations

The experimental investigations of this section were performed within the student thesis Troendle2018.

The strong absorption of moisture by flax fibers is considered critical material behavior. It was observed and investigated particularly in combination with epoxy matrices by relevant literature [22, 103, 140, 160]. In order to further extend the holistic approach regarding applicability, potentials, and disadvantages of FFRP in aviation structures, this aspect was analyzed in more detail.

Humidity Induced Mass Changes in FFRP

The hygroscopic behavior of biocomposites is emphasized as a critical issue when it comes to structural usage. The bio-based fibers take up moisture and expand which leads to micro-cracks when cured in a polymeric matrix [14, 13]. This section describes the observations when moisture was applied to cured flax laminates and how undesirable swelling could be reduced.

At HSH preliminary tests for the determination of water content in flax weaves were performed. Therefore cut-outs of a $200\,\mathrm{g\,m^{-2}}$ flax weave were dried for 24 h at 100°C. Then, the laboratory conditions of 50%-rel. humidity and 23°C were influencing the weave specimens in terms of mass increase and humidity content. An infrared moisture analyzer (Sartorius MA150C) was used for determination of moisture content and an electronic scale for the gravimetric analysis of the mass. It turned out that the saturation humidity of approximately 7% was reached after 30 min. Additionally, the mass increase and thereby gravimetric analysis was giving similar results as the moisture analyzer, resulting in the simple measurement method of weighting in the hereafter described measurements. In this work, the maximum water absorption of the whole cured composite material should be identified. Therefore, samples were fully immersed in water. The MC, as ratio of total mass to dry mass, quantified the analysis. In other research, the Fickian diffusion model was used for water absorption and desorption modeling in polymeric and composite materials [65, 37]. This model was then superseded by the PEK model which was introduced by Xie et al. [187], where the MC over time t is described in a double exponential form with a fast and a slow absorption process. The sum of both is used to describe the total absorption and is defined in [187] as follows in Equations (3.20) and (3.21). Where MC is obtained from the specimens actual mass m to initial mass m_{ini} ratio.

$$MC = MC_0 + MC_1[1 - \exp(-t \cdot t_{slow})] + MC_2[1 - exp(-t \cdot t_{fast})] \tag{3.20}$$

$$MC = \frac{m - m_{ini}}{m_{ini}} \cdot 100\% \tag{3.21}$$

The absorption process was tested for three different layups in three cycles. The MC-curves' maximum value was determined in different laminates to be between 15 and 40 mass.-%. The modeling approach showed good agreement with the experimental results, all test curves could be fitted with R-squared values higher than 0.99, when parameters were determined individually. The MC_0 constant set the starting value; it is 0 for an absorption cycle and the contained MC for a desorption cycle. The parameters MC_1 and MC_2 account for the fast and slow absorption and desorption processes, respectively. An exemplary set of absorption and desorption curves is shown in Figure 3.31, where curves of the six-layers laminate are shown. Other tested laminates were four and two-layered and showed comparable but slightly steeper curves.

It should be mentioned that the mass after the first absorption cycle was about 4% below the initial mass. Therefore, the first cycle is, as a relation to the initial mass, significantly shifted to smaller values. This effect of mass reduction was explained by washing effects. It is assumed that some material contents evaporate in the water on the first contact. Distilled water was used for the tests in order to diminish other effects. The second and third cycle showed, a similar, but shifted shape.

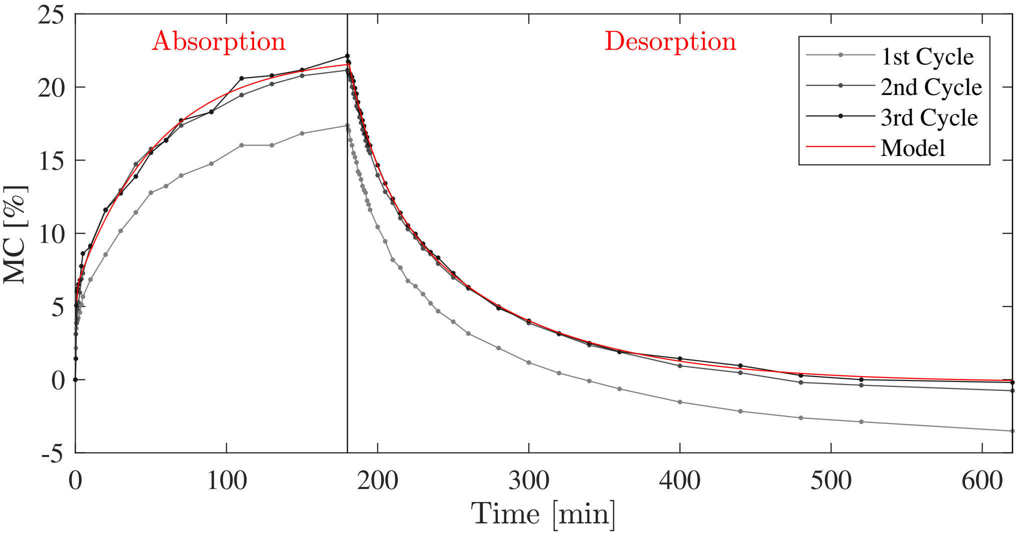

Figure 3.31: Exemplary Absorption and Desorption Measurements of Six-Layered Laminate in Three Cycles

The coefficients for the PEK model gave $MC_1 = 16$ in median, $MC_2 = 6$ and t_{slow} values of about 50, while t_{fast} was calculated to be about 0.5.

The hygroscopic swelling of the epoxy resin was also regarded, but according to the data sheets, where an ISO 62 test was performed, the water absorption of the epoxy is only 0.34–0.46% [80]. As such low values do not contribute significantly to the composite's MC behavior, flax fibers were identified as the major driver.

The different amount of layers showed that the total mass uptake is a thickness-dependent parameter, but the relative mass absorption reduced with increasing amount of layers. It led to the assumption, that the water absorption is rather a surface- than volume-driven parameter.

In order to investigate the repeatability of the water uptake, cyclic tests were done with an additional oven-drying process in between the tests, see 3.32. It can be seen that the oven could still reduce the moisture content, after the specimens were dried at laboratory conditions for two days. The water uptake in relation to the initial weight did decrease with the cycles, as already mentioned. Additionally, the six-layered laminate did not take relatively as much moisture content as the four-layered laminate; and it also reduced its mass compared to its initial mass in a higher ratio than the six-layered laminate. Again, this observation shows that the surface to volume ratio has an impact on the absorption behavior. But the batch size was small and further verification would be needed to underline this statement.

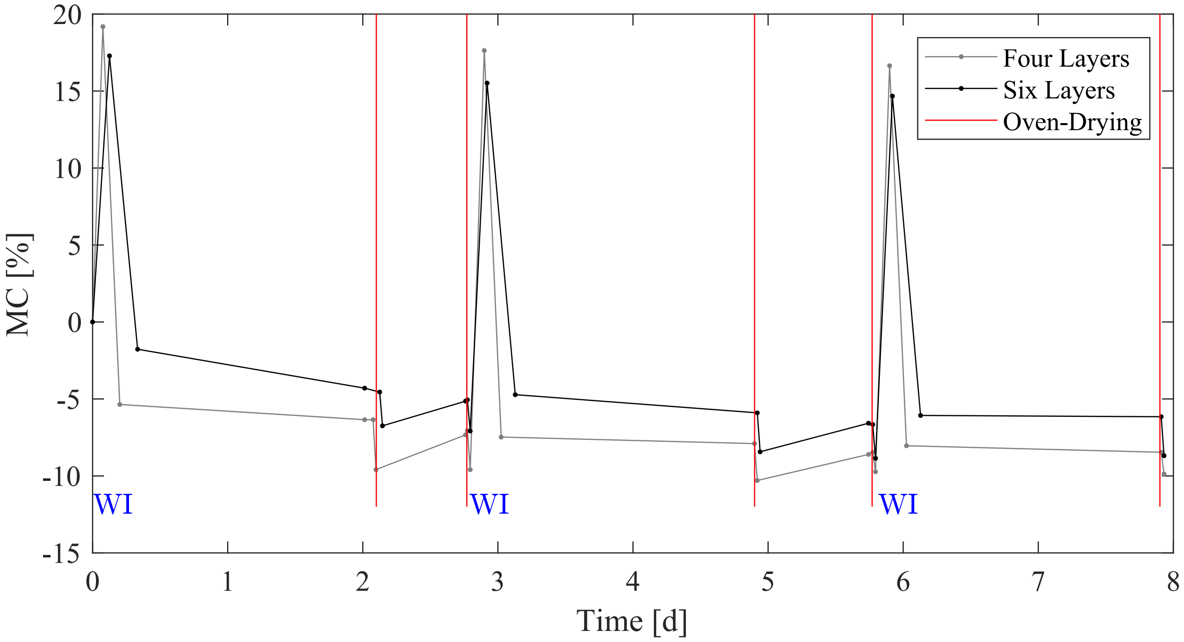

Figure 3.32: Mass over Three Moisture and Drying Cycles of Four- and Six-Layered Laminates, WI is Indicating Water Immersion and red Lines Oven Drying

Based on the assumption, that the mass uptake and the swelling behavior are mainly driven by uncovered fibers on the surfaces and cut edges, one sample was tested which was covered with an epoxy film on both surfaces. The $[E/F]_S$ lay-up was immersed in water for 24 h, the maximum mass uptake was 4.3%. This showed a significantly lower water uptake than the laminates without epoxy film, even though cut edges still showed open fibers. As a conclusion, the uptake of 4.3% may still be reduced in a fully covered part or laminate. Additionally, the laminate had the same weight after drying, than before the water immersion. Which lead to the finding that the laminate does not suffer from washing effects in the manner as the laminate without film.

Another test was done with hybrid woven laminates. They were first exposed to humid summer conditions, which were about 35°C and 80°C, and then exposed to laboratory conditions of 23°C and 40%-rel. humidity, for seven days. The hygroscopic behavior of flax could be observed in this test as well, where the specimens were again analyzed gravimetrically and results were interpreted according to their stacking order. The lay-up orders varied from pure flax to pure carbon stack-ups, with hybrid stack-ups, where either flax or carbon was on the outsides. The masses were measured after one day of conditioning and after one week. Compared with the water immersion tests, the weight reduction was low, but all samples reduced their weight. The pure flax laminates showed the highest difference, with 2.5% in average, the carbon laminates lost about 0.06% of their initial mass, in average. For the hybrids, it could be observed that the inner and outer layer of the stacking order dominated the moisture uptake, as the $[F/C]_S$ specimens showed values closer to the pure flax specimens with an average weight reduction of 0.69% and the $[C/F]_S$ samples were showing values closer to the pure carbon values, with a weight reduction of 0.08%. The values should not be compared to the water immersion tests, as the specimens were only exposed to warm-humid air and not fully immersed in water.

In summary, the fibers are still hygroscopic, even though epoxy matrix is cured around the fibers, but outer layers of conventional laminates or epoxy film layers could reduce the moisture uptake significantly. Generally, the environmental conditions need to be taken into account in all tests as the weight increase is supposing a strong influence on the laminates.

Humidity Induced Strain and Deformation

When the immersion tests were performed, water induced deformations could be observed. This led to further experiments investigating this swelling induced strain and thereby deformations. The idea for applicability was that flax composites could be used in a comparative way to bi-metals, in applications where movement should be humidity-triggered instead of temperature-induced. Therefore, bistable laminates were manufactured and tested.

Bistable laminates have two geometrically stable states in which they keep their shape when no load is applied. Typically a switch of states can be triggered by mechanical loading. Related research showed that the states can be triggered by piezo actuators or temperature influence [23]. In this research, we wanted to show that bistable laminates from flax fibers can be triggered by humidity. The general idea is pictured schematically in Figure 3.33.

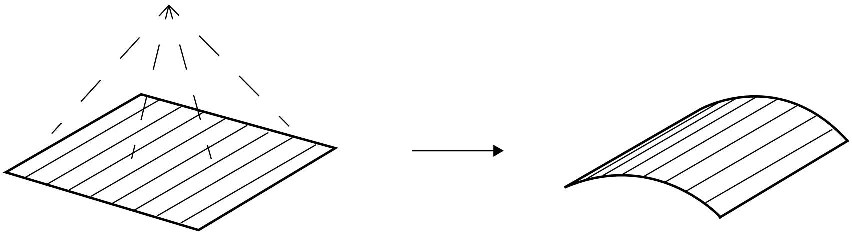

Figure 3.33: Schematic Hygroscopic Swelling with Respect to the Transversal Fiber Direction

In the experiments a water sprayer was used to immerse only one side of the laminate and thereby trigger the shape shift. The analysis with recurrently spraying water on one side of the specimen caused a curvature of about 1.85 rad over 200 mm within an hour. The shape shift was reversible by either drying or spraying water only on the other side of the bistable laminate.

Three lay-up configurations were tested in the stack-up of $[0_i/90_i]$ with i = 1,2, and 3. All in a quadratic shape of 150 mm side length. The dependencies on duration and amount of applied and absorbed water were part of the investigations. Figure 3.34 shows the test setup and proves functionality of the principal idea, the measurements showed that all lay-ups could be triggered by the use of water.

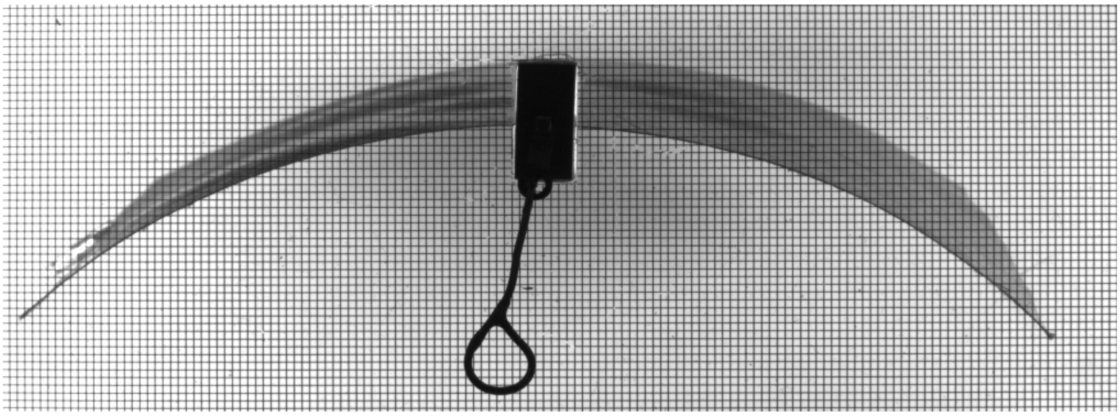

Figure 3.34: Photographic Measurement of the Deformation Induced by Hygroscopic Swelling of the Two-Layered Bistable Laminate [175]

The MC-strain relation was calculated from the optically measured deformations. Therefore, the width and hight of the curved laminate was measured. A constant curvature was assumed, which resulted in a geometrical relation between surface strain, measured height, and width of the curvature, as described in the following equations and Figure 3.35. These equations assume a pure bending deformation, which was considered suitable as the specimens fulfill the thickness to length constraint $t << l$, but some experiments showed large and more complex deformations, where a more detailed approach could result in better agreement.

$$r = \frac{h}{2} + \frac{w^2}{8h} \tag{3.22}$$

$$\frac{t}{r} = \frac{\Delta l}{l} \tag{3.23}$$

$$\epsilon_{hyg,a} = \frac{8th}{h^2 + w^2} \tag{3.24}$$

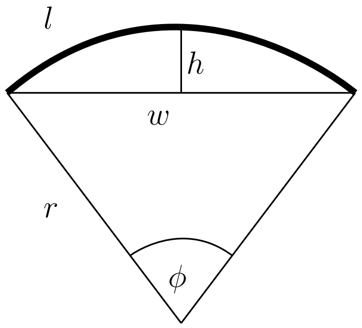

l - lenght of plate as arc length
h - hight of curved laminate
w - width of curved laminate
r - radius
ϕ - angle
t - thickness of laminate

Figure 3.35: Geometric Variables for the Quantitative Determination of the Hygroscopic Swelling Induced Strain

These assumptions led to the MC curvature relations as plotted in Figure 3.37. Furthermore, an FEA approach was modeling the humidity-triggered strain deformation from the derived expansion coefficients.

The expansion of flax under the influence of humidity was modeled analogically to thermal expansion. Equation (3.25) shows a linear dependency of hygroscopic strain to the MC, which is described similarly in [160].

$$\Delta\epsilon_{hyg} = \beta_{hyg} \cdot \Delta MC \tag{3.25}$$

With ϵ_{hyg} as the hygroscopic strain in [mm mm^{-1}], β_{hyg} as the CHS and ΔMC in [%]. The dimensionless constant CHS was only determined for the transversal fiber direction, as this was the only obvious and easy measurable expansion. The best matching parameter for the three laminates was the following, which was derived from curve fitting functions of each performed test.

$$\beta_{hyg} = 0.0004 \tag{3.26}$$

In the FEA model the square plate of the different stack-ups was modeled by solid elements of eight nodes with three degrees of freedom each. The validation was done on the calculated curvature, the inverse of the radius. Experiments and model are compared in Figure 3.37.

In the FEA model it was assumed that the upper surface was strained by the applied water in the calculated manner. Through the thickness, a linear reduction of strain within the upper layer was applied, as shown in Figure 3.36. All the other layers were not influenced by the hygroscopic strain.

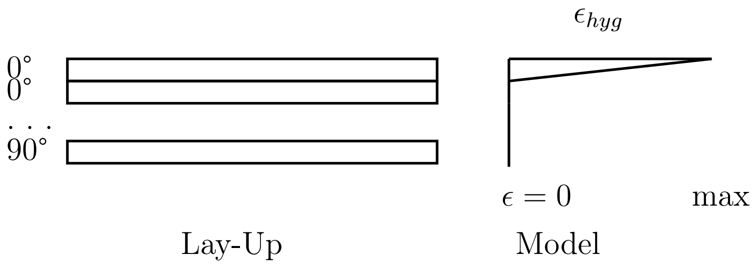

Figure 3.36: FEA Model Approach of Strain per Layer Induced by Hygroscopic Swelling

The deformation in the model was driven by the top surface expansion according to the experimental β_{hyg} in (3.26), determined from the experiment. Research of le Duigou et al. [103] is claiming a β_{hyg} coefficient of 1.14 for radial fiber expansion, but is also adding that the embedding epoxy matrix is restraining the fiber expansion. As a result, the hygroscopic swelling and water absorption is mainly driven by the fibers, the matrix is isotropic and its swelling is small according to the TDS. Therefore, it is assumed that the matrix does not contribute to the curvature of the asymmetric plates notably.

The results showed that the principal idea of the humidity-triggered bistable laminate worked well, while repeatability was scattering in a wide range. Additionally, measurement errors were prominent, as the applied water needed to be wiped away manually. Furthermore, the assumption of a constant curvature and only one surface being fully wet and strained could not be fulfilled throughout all experiments. Nevertheless, the hygroscopic strain coefficient β_{hyg} could be verified to some extent by using the described FEA model. The applicability in future technologies is considered possible, but the approach needs further verification. The elastic properties of the material were applied from the described material model derived by tensile tests, see Section 2.5.3. Le Duigou et al. published several papers addressing this effect and trying to use it in smart hygromorph structures [101, 103, 102].

As a conclusion, we could verify that water and humidity are influencing FFRP in a significant manner. For structural applications the demand of water tightness is evident and fibers need to be protected. The simple prepreg manufacturing with included epoxy is not sufficient to suppress this behavior. Additional polish or covering films are needed, where the epoxy film Henkel Loctite EA 7000 Aero could be tested as a promising material for water protection of FFRP. Furthermore, with the identified humidity-strain coefficients, the design could be analyzed in terms of weather induced deformations, but a more detailed analysis on the influences, such as micro-cracking, are necessary as well. If we think more out of the box, there are new applications possible. While bi-metals are widely applied in temperature sensors or switches, this field could be adapted to humidity, with bistable FFRP as the bi-material.

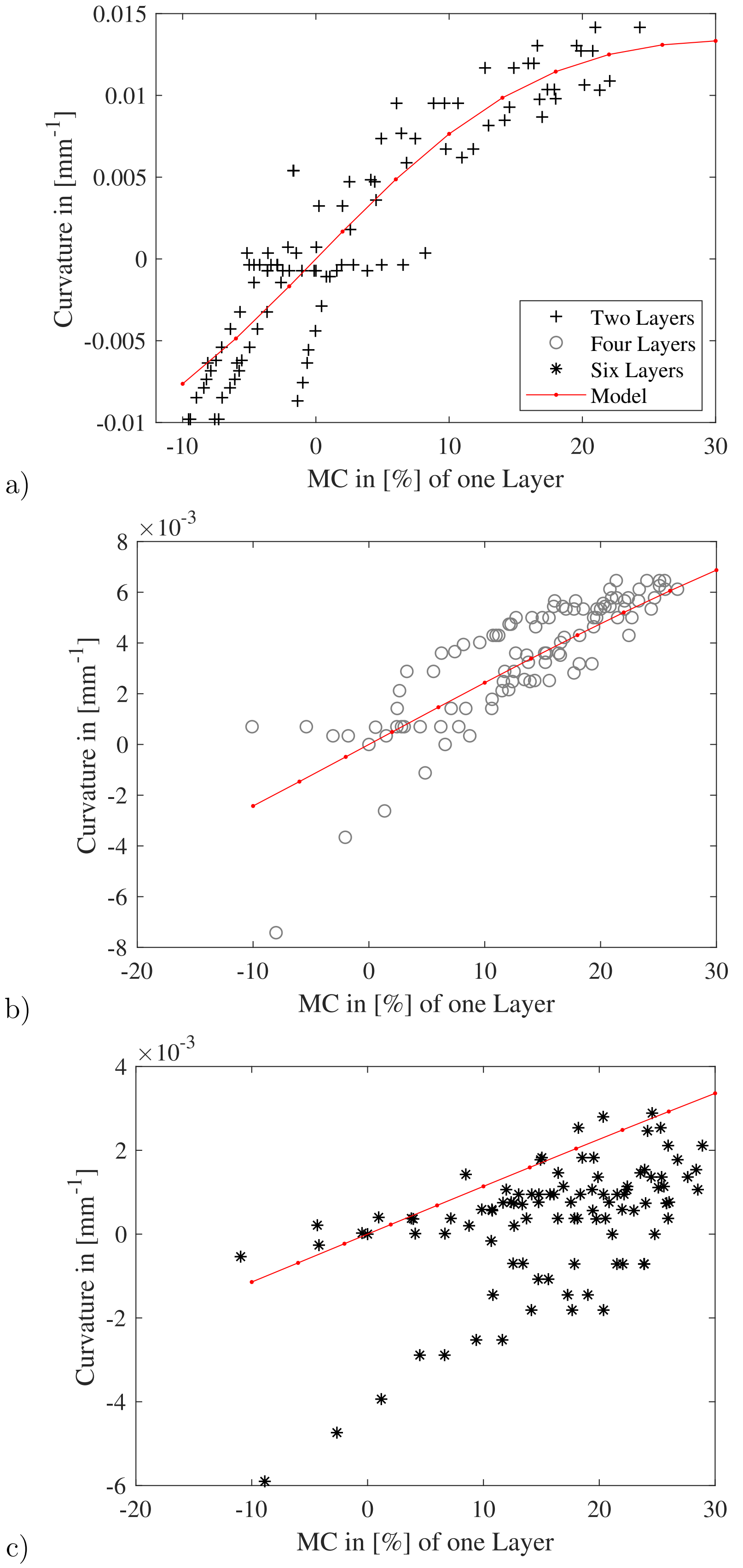

Figure 3.37: Experimental and FEA results of Bistable Laminate Compared in Curvature over Moisture Content for a) a Two-Layered Laminate, b) a Four-Layered Laminate, and c) a Six-Layered Laminate

3.4 Crashworthiness of Flax and Hybrid Tubes

Results of these experimental investigations were also published in ECCM2018.

In this section, experiments, which aim to investigate the potential of flax and carbon woven hybrid laminates in crashworthiness applications, are described. Crashworthiness in helicopter structures aim to reduce the peak loads of a crash, which would injure the occupants. Other aspects of crashworthiness are to keep the integrity of the cabin, reduce the hardware damage, and to minimize the risk of post-crash dangers, such as fire [92, 81].

Representative crash scenarios of helicopters show that the 95^{th} percentile of survivable accidents are in longitudinal direction at a velocity of $15.24\,\mathrm{m\,s^{-1}}$ and in vertical direction of $7.92\,\mathrm{m\,s^{-1}}$ [53]. Inertial load factors of crash landing conditions are, according to CS-27, between 1.50 g and 20 g, in which cases the survivability of the occupants should be proven. Survivability of the occupants can be evaluated with Eiband curves [56], which show human tolerances of multiple gravity loads over time.

Tube structures are commonly used in seats in order to absorb crash-energy. Therefore, the specific energy absorbing capabilities of composite tubes with woven flax and carbon layers were analyzed and evaluated using quasi-static and dropping-weight compression tests. The information of force-displacement curves from quasi-static pressure tests will be used to determine testing parameters of the dynamic tests, such as energy levels.

Beneficial results would be a high specific energy absorption, high crush force efficiency and stroke efficiency. These would be achieved by an initial crushing at lower force levels than most kinking structures do, with a steady-state force and little scatter, while dynamic energy is absorbed.

As flax appears to have high energy absorption properties, especially at impact or dynamic loading [141, 6, 189, 148, 119], it is only showing a compression strength of about a quarter of the strength of carbon [30]. Matter of interest is to find out whether hybrid tubes made of flax and carbon can combine the energy-absorbing properties of flax with the high strength of carbon. Thus, the hybrid tubes will be compared with pure flax and pure carbon tubes.

The flax material for this work was supplied by Lineo, with the identification: FlaxPly BL 150, the carbon weave (identification: CW200-TW2/2-E503-45%) was produced by the SGL Group. The flax material was a 2/2-twill weave of $150\,\mathrm{g\,m^{-2}}$ and the carbon material was a 2/2-twill weave of $200\,\mathrm{g\,m^{-2}}$. Both were chosen due to same thicknesses and comparable meshing sizes. Additionally, in prior studies the $150\,\mathrm{g\,m^{-2}}$ showed better mechanical behavior than the $200\,\mathrm{g\,m^{-2}}$ flax material, see Section 2.1. All specimen tubes were produced with eight woven layers and fiber orientations of [0/90] regarding the cylinder axis.

The tubes were made using prepreg materials and autoclave curing with Cycle 3 of Figure 2.1. All tubes have a cylindrical shape with both a height and a middle surface diameter of 50 mm. The wall thickness is approximately 2 mm for each tube and a

45° chamfer is applied for crack initiation at the top of each tube. In Figure 3.38 the geometrical dimensions are shown, including precision values as well as the schematic stack-up.

X and Y in the stack-up are iterated by the introduced woven flax and carbon material. Each configuration was tested in three samples. The high thickness range of 1.1–4.10 mm results from folds in the cured specimens, which appeared due to an inner mold core for the production. Nevertheless, the quality was considered feasible for the planned crash tests and the folds should have a neglectably small influence on the parameters of investigation, compared to the different materials used.

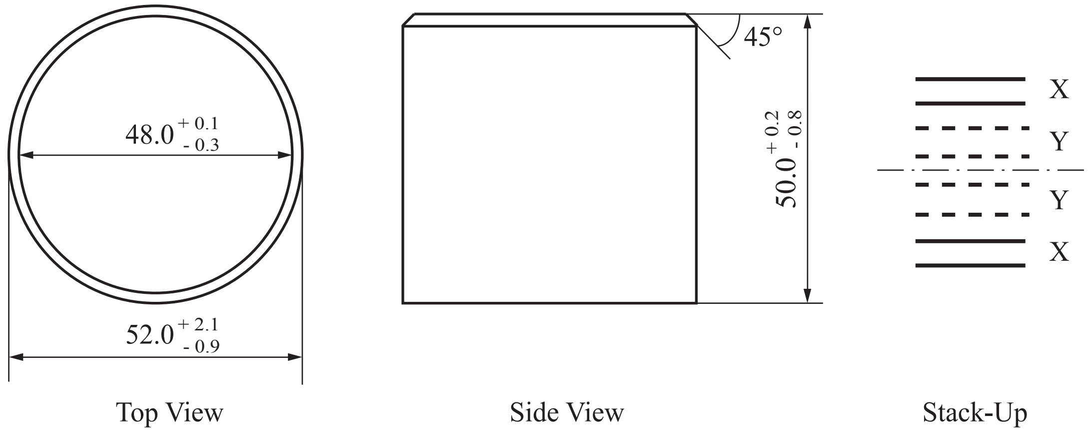

Figure 3.38: Dimensions of Test Specimens and Stack-Up of the Static and Dynamic Crashworthiness Tubes, X and Y Indicate the Alternating Materials Flax and Carbon

In order to determine dynamic crushing parameters for the experiments, one specimen of each configuration was crushed by a static pressure, with a velocity of $5\,\mathrm{mm\,min^{-1}}$. The dynamic tests were performed with a dropping weight tower at a speed of $8\,\mathrm{m\,s^{-1}}$. Equal testing conditions were attained by conditioning for a minimum of 24 h at 23°C and 40% rel. humidity before testing.

In order to analyze the crushing behavior on the basis of the different force-displacement curves, Equations (3.27)-(3.32) were used, x_1 indicates the beginning of the nearly constant force-level after the first peak force and was set to 5 mm for all specimens, see Figure 3.40. The parameter a was set to 29 mm for all specimens, as this was the lowest crushing length appearing. The results are listed in Table 3.7 for the static and dynamic tests.

$$E_{abs} = \int_0^a F(s)\,\mathrm{d}s \tag{3.27}$$

$$E_{spec} = \frac{\int_0^a F(s)\,\mathrm{d}s}{m_{destroyed}} \tag{3.28}$$

$$E_{dens} = \frac{\int_0^a F(s)\,\mathrm{d}s}{V_{destroyed}} \tag{3.29}$$

$$F_{mean,s} = \frac{\int_{x_1}^a F(s)\,\mathrm{d}s}{s_{max}} \tag{3.30}$$

$$\sigma_{mean} = \frac{F_{mean,s}}{A} \tag{3.31}$$

$$\eta_{eff} = \frac{F_{mean,s}}{F_{peak}} \cdot 100 \tag{3.32}$$

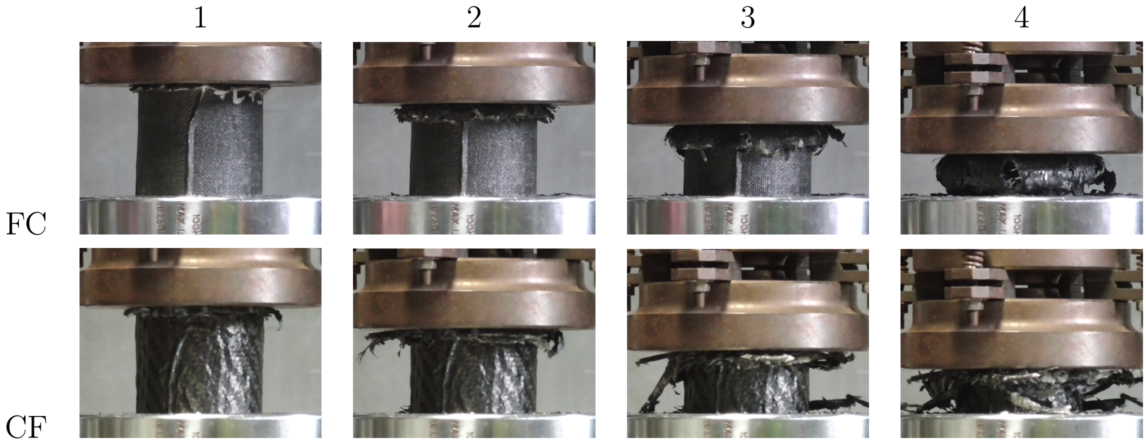

Figure 3.39: Splaying and Fragmentation Mode of $[F_2/C_2]_S$ and $[C_2/F_2]_S$ Layered Specimens during the Quasi-Static Compression Test

The static-compression testing machine was a hydraulic press used in combination with a 100 kN load cell (noise $s_{Force} = 0.82\,\mathrm{N}$). Figure 3.39 shows the quasi-static test in four different states of compression of the two hybrid stack-ups, recorded by a conventional video camera.

For the dynamic tests, a drop weight tower was used with a 400 kN load cell (scattering in the range of $s_{Force} = 94.40\,\mathrm{N}$), as well as a laser-displacement sensor, and a high-speed camera for recording the crashing behavior itself. The apparently high noise of the load cell signal resulted in a maximum measurement error of 1.9%.

The target velocity of $8\,\mathrm{m\,s^{-1}}$ was fulfilled within a range of 7.53–$8.04\,\mathrm{m\,s^{-1}}$ with a median of $7.91\,\mathrm{m\,s^{-1}}$, which is very close to the vertical crash requirement defined in MIL-STD-1209A at $7.90\,\mathrm{m\,s^{-1}}$ [81]. The resulting weights and heights were calculated with conservation of energy rules, aiming 85% of the static absorbed energy over a crushing length of 35 mm. 85% was found to be a typical ratio of dynamic and quasi-static energy absorption in conventional composites, according to relevant references [81, 188]. The experimental parameters for the dropping-weight tests are listed in the following Table 3.6. The results of both, the quasi-static and dynamic tests, are listed in Table 3.7. Also, the force-displacement curves, grouped by each lay-up configuration, are plotted in Figure 3.40.

Table 3.6: Testing Parameters of Dynamic Crushing in Drop-Weight Tower Test

	Impact Energy	Velocity	Impactor Mass	Momentum
[Unit]	[J]	[m s^{-1}]	[kg]	[Ns]
CC -2,-3	1483	8	40	589
CF -2,-3	849	8	23	340
FC -2,-3	785	8	21	314
FF -2,-3	217	8	7.5	87

Table 3.7: Summary of Results from Quasi-Static (Specimens -1) and Dynamic (Specimens -2 and -3) Compression Tests

	E_{abs}	E_{spec}	E_{dens}	F_{mean}	σ_{mean}	F_{peak}	η_{eff}	Mode
[Unit]	[J]	[J g^{-1}]	[J cm^{-3}]	[kN]	[MPa]	[kN]	[%]	-
(Equation)	(3.27)	(3.28)	(3.29)	(3.30)	(3.31)	-	(3.32)	-
CC-1	1420.2	103.6	79.5	52.0	84.4	55.81	93	Splay.
CC-2	732.5	62.0	41.02	25.6	41.5	41.42	62	Frag.
CC-3	775.2	62.3	43.4	26.8	43.6	41.69	64	Frag.
CF-1	768.2	71.2	47.9	28.0	50.7	31.30	90	Frag.
CF-2	566.6	53.9	35.3	19.7	35.6	37.31	53	Frag.
CF-3	515.1	52.9	32.1	17.8	32.2	32.61	55	Frag.
FC-1	710.0	63.5	41.9	25.1	43.0	34.31	73	Splay.
FC-2	511.6	48.3	30.2	17.7	30.4	31.13	57	Splay.
FC-3	498.8	49.7	29.4	17.5	30.0	29.75	59	Splay.
FF-1	200.8	19.3	11.2	7.3	11.8	9.43	77	Splay.
FF-2	145.2	16.0	8.1	4.9	7.9	9.39	52	Splay.
FF-3	197.8	19.9	11.1	7.1	11.5	11.38	62	Splay.

All specimens showed lower energy absorption when loaded dynamically, compared to the quasi-static compression, which is a typical phenomenon in crash-testing [188]. The peak force was comparable in static and dynamic tests, for all flax-including tubes. For the pure carbon tubes, dynamically tested specimens showed significantly lower peak forces. Also, the $[C_4]_S$ and $[C_2/F_2]_S$ specimens in static tests showed a higher scatter around the mean force while the $[F_4]_S$ and $[F_2/C_2]_S$ specimens showed a rather smooth quasi-static force-displacement curve. Additionally, the dynamic tests showed a higher scatter than the quasi-static tests, in all configurations. The 45° chamfer fulfilled its purpose, which was reducing the peak-to-mean load ratio by triggering the crushing early, to increase the crush force efficiency (η_{eff}) [190]. Within results of the hybrid specimens this effect was less apparent than with the pure material specimens. Generally, the dynamic tests showed lower η_{eff}-values, than the quasi-static results.

Pure carbon tubes showed the strongest decrease of total absorbed energy between quasi-static and dynamic tests, with the total and specific absorbed energy being reduced by almost half. The hybrid and pure flax specimens showed a lower reduction of these parameters, of only about 30%. It appears as if the flax material is less sensitive to changes in the impact velocity. Regarding the low batch sizes and strong variations in parameters, this statement needs further verification. The quasi-static carbon tube showed a high value of specific energy absorbed, compared to other research results [188], this discrepancy could also be a statistical out-lier. The pure flax tubes ordered well in between comparative research results [120, 190].

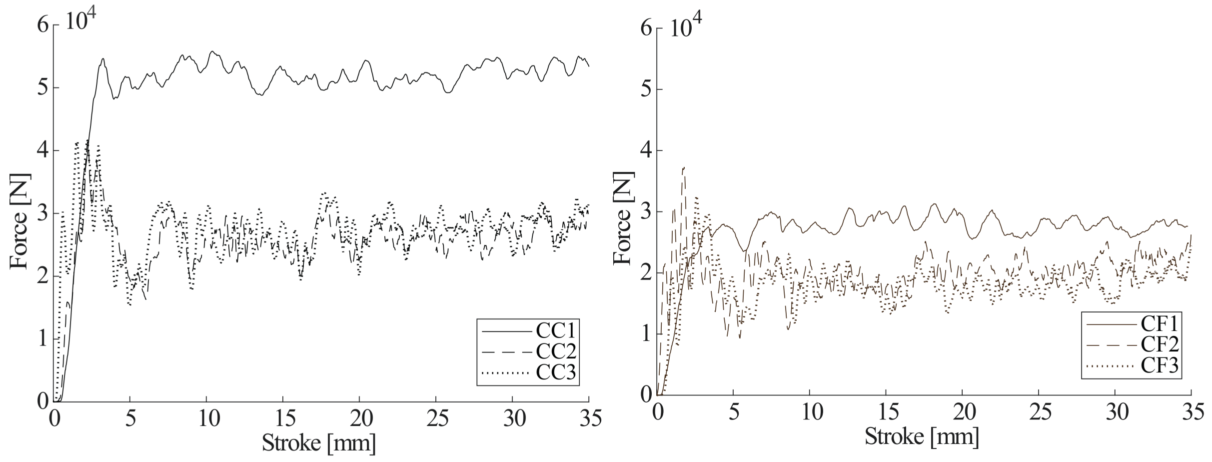

a) CC b) CF

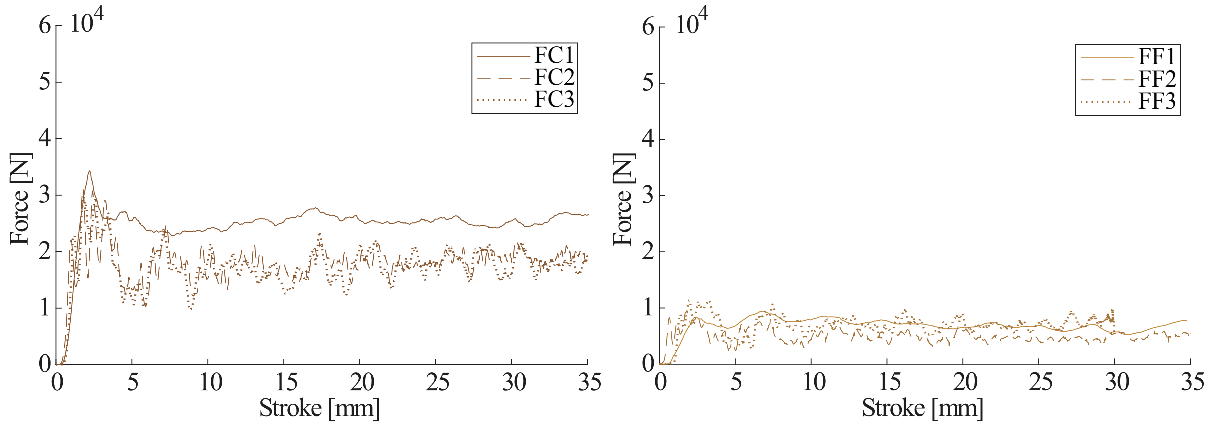

c) FC d) FF

Figure 3.40: Force over Stroke in the Quasi-Static and Dynamic Test Ordered by Configurations

In terms of energy dissipation as well as mean force and mean stress, the $[C_2/F_2]_S$ specimens were slightly better than the $[F_2/C_2]_S$ specimens, considering the same materials, the stacking order seems to influence the results. Comparing the different stack-ups, the hybrid tubes showed good performance, with down to 13% lower specific energy absorption than the pure carbon tubes, while using 24% bio-based material. The energy dissipation density E_{dens} shows similar ratios. Additionally, mean force and mean stress levels of the hybrid tubes do not order linearly between the pure carbon and flax tubes. This emphasizes potential of the hybridization.

In terms of crushing modes, we observed splaying and fragmentation mode, Figure 3.41 b) shows the fragmentation mode and a), c), and d) splaying. The splaying mode is generally the more common mode for cylindrical crash samples [189, 190, 191, 188].

In the splaying mode, the main failure mechanism is delamination, where some layers curve to the outside and others to the inside of the tube. The fragmentation mode is different, the main failure mechanism is shear failure, which makes circular parts rip off the cylinder in radial direction and form small fragments around the tube. The $[F_4]_S$ and $[F_2/C_2]_S$ tubes always crushed in splaying mode, which can be seen in Figure 3.41 c) and d), while the $[C_2/F_2]_S$ specimens always crushed in fragmentation mode, Figure 3.41 b). Surprisingly, the CC-specimens showed the splaying mode in quasi-static testing, while crushing in fragments when tested dynamically.

In [73] the effect of different failure modes is explained by the friction coefficient between the tool and the specimen surface. In the quasi-static test, the fragmentation mode only occurred on the $[C_2/F_2]_S$ specimen, the friction coefficient might be higher, with the flax layers in between the carbon layers having a less smooth fracture surface. The strong carbon layers held them upright, with the fracture surface being grated by the tool. Another possible explanation is that the flax composite is more ductile, compared to the brittle carbon composite, and the outer layers, either brittle or ductile, dominate the crushing behavior and define the crushing mode.

a) $[C_4]_S$ b) $[C_2/F_2]_S$ c) $[F_2/C_2]_S$ d) $[F_4]_S$

Figure 3.41: Photographs of Crushing Modes after Quasi-Static Compression of all Configurations

In general, the outer layers of the tubes were dominating the behavior. Either in terms of crushing modes, as outer carbon layers were rather showing the fragmentation mode, while flax always showed the splaying mode, and in terms of mass, energy absorption, and loads, where the $[C_2/F_2]_S$-specimens' results were closer to the ones of pure carbon and the $[F_2/C_2]_S$ specimens showed results closer to the $[F_4]_S$-specimens.

To sum it up, hybrid specimens showed better values than expected, in terms of mass, energy absorption, mean crushing force and mean stress. The values did not order linearly between the values of pure material specimens, but were shifted in a positive way. Thereby, potential of the hybridization could be emphasized. The $[C_2/F_2]_S$ specimens showed good potential in terms of specific energy absorption, with about 53 J g^{-1} being only 15% lower than the values of the pure carbon specimens. Additionally, the hybrid and pure flax specimens showed crushing behaviors less sensitive to the crushing speed than pure carbon specimens.

3.5 Impact Resistance of Thin Flax and Hybrid Laminates

Parts of this section were also published in DLRK2017, the tests were performed within the student thesis Blaut2017.

This section is focusing on the properties of impact energy absorption. Available research results focus on laminates with a thickness > 2 mm [138, 105, 21]. Investigations of very thin laminates, with total thicknesses between 0.45 and 1.75 mm, which are used in ultralight aviation structures, are rarely reported yet. The ultralight certification standard does not require these tests, but as flax showed promising impact resistance in related work, the benefits for this specific field were matter of investigation. In order to give a brief introduction to this topic, selected relevant literature is summarized in the following.

Y. Lebaupin et al. [105] worked on the impact behavior of different flax lay-ups and fiber orientations. They used eight layers of UD flax with an areal density of 450 g m^{-2}. The laminates were subjected to a low velocity impact of 3.60 J followed by tensile and compression tests. The results showed that the quasi-isotropic laminate was least sensible to the impact load and most of the laminates did not show a substantial loss of mechanical properties.

F. Sarasini et al. [148] analyzed hybrid laminates, as well. They investigated UD flax-carbon laminates with 14–18 layers, on which four-point-bending tests were performed, as well as an impact damage test with energies between 5–30 J. The damaged samples were also tested post-impact in tensile and bending tests. With the use of micro thermography it was shown that the pure CFRP laminates were more sensitive to the impact damage than the hybrid ones. Furthermore the [F/C/F] lay-up showed a better resistance to impact than the [C/F/C].

V. Fiore et al. [63] investigated in their work the mechanical properties of two different flax weaves with a reinforcing UD-layer of carbon. The flax weave types were 220 g m^{-2} twill weave and 150 g m^{-2} plain weave. These specimens were made of six layers. Three-point-bending tests and tensile tests were performed. It was pointed out that the pure flax specimens were not sufficient for structural demands, but the carbon reinforcement strengthened the laminates substantially.

Petrucci et al. [130] performed impact testing on hybrid laminates with glass, hemp, basalt, and flax. The performance of laminates including flax was in most cases superior to those without.

For the experiments herein, the specimens of investigation were double layered woven fabrics made of carbon and flax. The materials were carbon plain weave of $200\,\mathrm{g\,m^{-2}}$ and flax twill weave of $100\,\mathrm{g\,m^{-2}}$, $150\,\mathrm{g\,m^{-2}}$, and $200\,\mathrm{g\,m^{-2}}$. The laminates were fabricated with VI technique using the 19% partly bio-based epoxy-matrix SuperSap [61]. The impact damages were then analyzed in terms of energy dissipation, optical appearance, depth, and size. These damages were afterwards used to proof applicability of the NDI methods "Ultrasonic Echo Analysis" and "Vibration Induced Thermographic Inspection" as described in Section 3.6.

The specimen were preconditioned for 24 h at 23°C and 50% rel. humidity and the impact tower is following standards in DIN EN 6038. The tests were conducted using an hemispherical steel impactor with a diameter of 16 mm and a mass of 2.50 kg. During the impact an acceleration sensor and two light barriers were used to analyze the tests in terms of velocity and acceleration. Based on the velocities before and after the impact, the dissipated energy was calculated.

In the pretest with an energy level of 1 J the plates tended to bulge out. This effect was accounted to the clamping device. The device was set up after the guidelines of DIN EN 6038, which does not cover such thin laminates. In order to avoid this behavior, a lengthwise-strengthening fixation using frame-rails was applied in all further tests.

With respect to the variation in lay-ups, different impact energy levels were applied. In Table 3.8 an overview of the different impact energy levels and the damage appearance of all specimens is given. The applied energy levels were determined from pretest results. To clarify the different clamping method at the pretest, a (pre) was added to the specification of these results, which showed generally less damage than the tests with improved fixations.

Table 3.8: Overview of Impact Energy Levels and Damage Characterization with Exemplary Photographs of the Legend Entries

Lay-Up	*am* [g m^{-2}]	1 J(pre)	0.5 J	1 J	1.5 J	2 J	3 J
$[F]_3$	200	+ /+				+	
$[F]_2$	100	|	*	*		*	
$[F]_2$	150	+	+	+		*	
$[F]_2$-A	200	*	+	+		+	
$[F]_2$-B	200	+	+	+		+	
[F/C]	200	nF		o	o	o	
[C/F]	200	•		•	•	*	
[F/C]	150	nF		nF		nF	*
$[C]_2$-A	200	nF		nF		•	*
$[C]_2$-B	200	nF		nF		•	–

Legend:

+	cross-shaped failure
*	antisymmetric failure
–	horizontal failure
|	transversal failure
•	dot-shaped failure
o	round failure
nF	no failure
	(empty) not specified

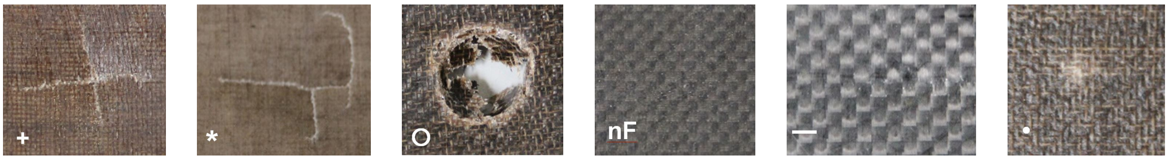

In all tests the aimed impact energy was verified with the kinetic energy assessed through the light barrier signal shortly before impact. A maximum deviation of ±0.15 J was achieved. The damages were characterized by visual inspection, where the failure modes of the specimens are provided in Table 3.8. The carbon specimens showed failure starting at impact energies of 2 J. The damage of the carbon material was small and barley visible. On the pure flax specimens, damage occurred at all impact energy levels. The specimens of lower areal density were largely disrupted by the impactor and showed anti-symmetric failure modes.

Tests of the hybrid specimens, with an areal density of 200 g m^{-2}, showed that the stack-up had an influence on the failure mode and the severity of damage. For an [F/C] stack-up no failure did occur at 1 J impact energy. The mirrored stack-up ([C/F]), showed a small dot-shaped failure at an energy level of 1 J. At higher loads, the [C/F] lay-up showed less fracture damage than the [F/C] lay-up and up to 1.50 J only a small fracture in the flax layer was detected. This was explained by the bending stress during the impact, which stresses the lower layer in a higher order than to the top layer. Increased energy levels caused large rupture in both layers.

The $[F]_3$ layered material was used for the setup and pretests, therefore two specimens were tested at 1 J, both showing a cross-shaped failure. The [F/C] 150 g m^{-2} laminate showed good impact resistance results, as di not show failure as than the pure carbon specimens did when 2 J impact energy was applied. A possible explanation was the lower stiffness resulting in a rather elastic behavior of the material. But, due to the small thickness, the friction in the clamping might also have absorbed additional energy.

Next, the damage relaxation over one week was analyzed, as relaxation processes are matter of interest for BVID identification in aviation maintenance. With a dial gauge (precision of ±0.01 mm) the penetration depth directly after the impact is averaged (depth in [mm] in Figure 3.42). In order to identify the relaxation of the damage within a week after the impact test, the penetration depth is measured a second time. In general, the relaxation after one week resulted in a decrease of damage depth, in average 12%.

In Figure 3.42 the damage depth right after testing is compared to the depth seven days after the impact. The difference is averaged in Figure 3.42 as relaxation in [mm], and the percentage of the relaxation to the initial depth is also graphed as relaxation in [%]. All values are averaged per laminate type. The characterized modes "no failure", "disruptive failure", and relaxation values higher than 100% were excluded.

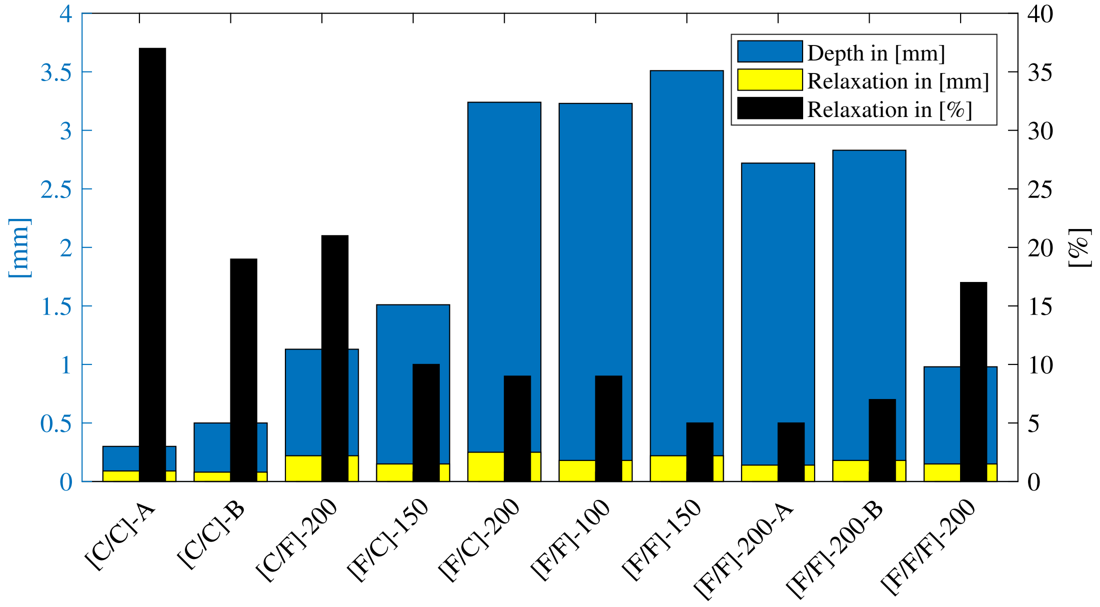

Figure 3.42: Average Weight Reduction by Conditioning at 40% rel. Humidity and 20°C After 1 Day and 1 Week

It can be seen that all specimens are showing relaxation processes. In general the damage depth and the absolute relaxation increased with the amount of flax in the laminate, while the relative relaxation decreased. But, considering the small batch size, the different energy levels, and excluded values, these findings can not be stated significant.

As a result, very thin partly FFRP laminates were tested, and one hybrid specimen showed a comparable impact resistance to pure carbon layers, including a bio-based content of over 30%, the 150 g m^{-2} flax weave [F/C] hybrid. Furthermore, the stack-up order [C/F] (both 200 g m^{-2}), with flax in the lower layer, showed smaller damage on impact loads than the [F/C] stack-up (excluding the pretest). Finally, no significant difference due to fiber material could be observed regarding relaxation processes over one week.

3.6 Non-Destructive Material Inspections

The experiments of both NDI methods were performed within the scope of Blaut2017. Some results were already published in DLRK2017.

In aviation, there are further material inspection methods applied than the initial, destructive, and detailed material analysis, which was already described in Section 2.3. Further material inspections are motivated by maintenance or quality assurance, used for failure or void inspections. For these applications, non-destructive methods are necessary, as the parts should not be harmed.

In this section, two NDI methods are described, the ultrasonic echo analysis and the vibration induced thermographic inspection. Matter of interest was to investigate the applicability of these aerospace methods on the new flax and hybrid materials. Therefore, the methods were used on the impact-damaged specimens, where the damage was well-known in position and size. These NDI methods are commonly used in the aviation sector, specifically for the detection of BVID, voids, or other manufacturing errors.

3.6.1 Ultrasonic Echo Analysis

The ultrasonic echo analysis is exemplary applied in the quality assurance of CFRP helicopter cabin doors. As there is little knowledge about ultrasonic reflection and echo performance of NFRP yet, this was matter of investigation within this work. El-Sabbagh et al. [58] tested flax-PP laminates with not-oriented fibers, they stated a relation between the reflected waves and the fiber volume content, but also proved that glass fiber composites show more attenuation in comparison to natural fiber composites. Furthermore, Jawaid et al. [85] are giving a brief overview about other NDI methods on natural fiber composites, but these did not cover the same area of interest as the tests herein did.

Within this work, the ultrasonic echo analysis was performed by a 3-axis-scanner using 3 MHz and the software HILLGUS. The investigated area is 70 mm x 100 mm and a grid of 0.25 mm steps in X and Y-direction was used. A volume scan of each specimen was performed, which was used to derive a C- and D-scan of the specimen.

The C-scan shows the amplitude of the echo signal, the ultrasonic waves are reflected at a significant change in speed of sound of the conducting medium. In a healthy material, this happens at the specimen's front- and backside. The different media within the composite (i.e. fibers and matrix), show only a small-amplitude echo, distinguishable from defects and the backside of the material. In case of delamination, voids, or fracture the signal is reflected at the air-material interface, where the profound difference is resulting in a high-amplitude echo.

Some selected results are shown in Figure 3.43–3.44. The strength of the echo signal in dB is shown gray-scaled in the pixel pattern. The higher the echo, the less was transmitted through the laminate. An inspection of a conventional carbon-woven laminate is shown in Figure 3.43. In CFRP it is often hard to see impact damages, especially when they are of low depth ($< 0.3\,\mathrm{mm}$, BVID). The graphics on the left show photographs of the laminates. In the CFRP, the ultrasonic echo analysis makes the damage clearly visible, approximately in the middle of the image. Further, the weave pattern is visible in the undamaged areas, rather light gray, which can be evaluated as a good material quality.

Figure 3.44 shows the same test with a pure flax laminate. We can still detect the damage in the ultrasonic scan, but also in the photograph. Flax appears to be white friable, like GFRP, where impact damages can be detected easily. The weave pattern of the material is well visible too, but rather dark. We account this to air inclusions in the flax fiber bundles. The irregularities in the healthy area of the specimen are due to folds in manufacturing sheets and resulting variations in thickness. These should be neglected for the damage characterization and technology applicability analysis. Still, ultrasonic inspection is applicable as an NDI-method for flax laminates.

The ultrasonic inspection was also performed with hybrid carbon-flax specimens. In Figure 3.45 the damage of a [C/F] laminate, impacted with 1 J, can be seen. The damage was only on the backside optically visible, where it showed a dot-shaped damage. Using a hybrid structure, where the backside might not be accessible, maintenance would again rely on NDI methods.

The small black dots in the figure are indicating either air inclusions in the laminate, likely in the flax layers, or inter-laminar imperfections. The white dots are likely to be measurement errors, as white means there was no signal echo detected.

It could be shown that also for hybrid flax carbon materials, with an inter-laminar hybridization, the ultrasonic inspection can be applied. Also, voids and uneven thicknesses of pure FFRP can be detected by the ultrasonic scan. Therefore, the application of this NDI method is considered possible for quality assurance and maintenance of FFRP and its hybrid structures, but not constantly necessary for impact damaged laminates, as the material is white friable.

In combination with the strong hygroscopic behavior of flax, described in detail in Section 3.3, we need to consider that a distilled water bath is often used for ultrasonic inspection. This might have had an influence on the measurement [47], but in the optical inspection there were no difficulties or influences detected.

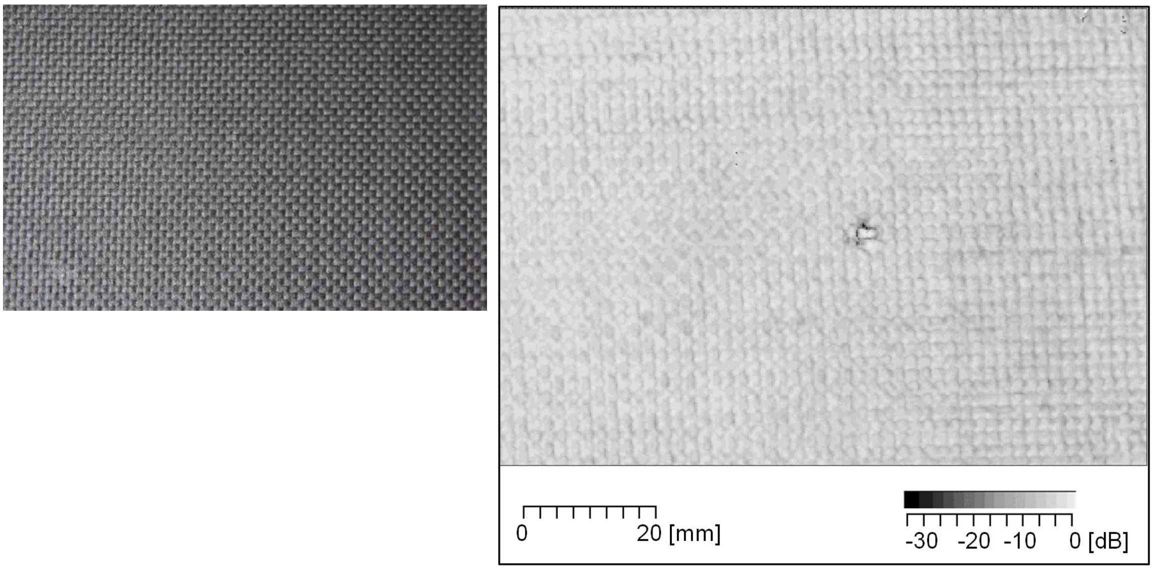

Figure 3.43: Backside Photography and C-Scan of Damaged $[C]_2$ with $200\,\mathrm{g\,m^{-2}}$ Carbon Weave

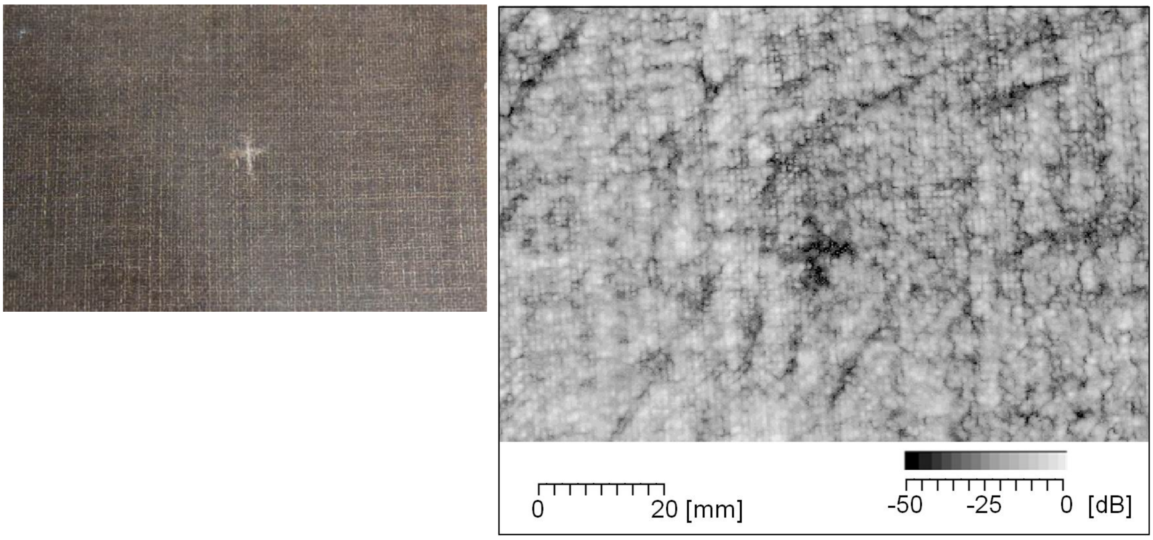

Figure 3.44: Frontside Photography and C-Scan of Damaged $[F]_3$ with $200\,\mathrm{g\,m^{-2}}$ Flax

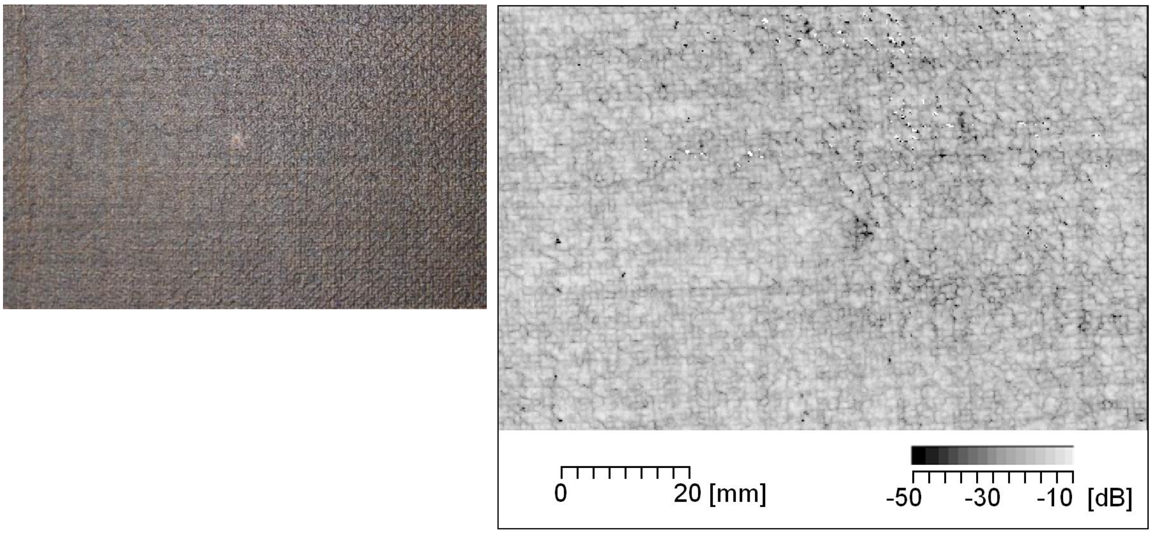

Figure 3.45: Backside Photography and C-Scan of Damaged [C/F] with $200\,\mathrm{g\,m^{-2}}$ Carbon-Flax Hybrid Laminate

3.6.2 Ultrasonic-Vibration Induced Thermography

Another NDI method in aviation structures is thermographic imaging. The benefit of this method is that it can be applied during maintenance more easily than ultrasonic inspection and to a larger area at a time. There are several thermography technologies available, such as lock-in thermography. As natural fibers show high energy absorption rates and damping, the herein investigated method was the vibration induced thermography. A special interest on this experiments was whether the fibers would absorb the induced energy before it could be transmitted to the damaged area, or if this NDI damage detection would work similarly to conventional laminates.

For the vibration induced thermographic inspection, the specimens were stimulated by ultrasonic vibration with 40.80 kHz for 0.60 ms. This vibration is dynamically transmitted through the material and open fractures or de-bonded layers are heated due to the resulting friction. This friction heat can be detected when compared to the surrounding material. An infrared video camera in combination with the software IRControl V4.53 was used for video imaging of a duration of 3 s. Afterwards, the most significant pictures in the video were interpreted and analyzed. The thermographic image of the pure carbon specimen $[C]_2$ of $200\,\mathrm{g\,m^{-2}}$ weave, impacted with 3 J, is shown in Figure 3.46. The lower bright point was caused by the stimulation with ultrasonic vibration. In the middle of the figure a horizontal fracture is visible. The shown graphic is imaging an expected result of this inspection method. Figure 3.47 shows the infrared picture of a $[F]_2$ laminate with a $200\,\mathrm{g\,m^{-2}}$ weave, impacted with 0.50 J. The stimulation point is clearly visible, the cross-shaped damage is hardly detectable, only the horizontal crack can be seen slightly. Additionally, the whole laminate heated more than the carbon laminate, approx. 24°C vs. 23°C. This supports the hypothesis that the good damping properties of flax absorb energy by internal friction in the yarns and fibers. Thereby, the temperature contrast on the open crack surface is less visible.

Furthermore, there is a circular pattern around the stimulation visible. This phenomenon also appears in CFRP laminates, occasionally, and is explained by vibrating standing waves causing heat in the pattern of the resonance mode shape.

Next, Figure 3.48 shows the infrared picture of the [C/F] $200\,\mathrm{g\,m^{-2}}$ weave specimen, impacted with 1.50 J. The damage in the flax layer is clearly visible. But for the same materials in a [F/C] stack-up sequence the results were hardly interpretable. This is associated to the layer where the stimulation is coupled into the material. The infrared imaging worked better on the carbon side of the hybrid laminate than on the flax side, which is again explained by the higher damping and internal friction in the flax layer. The blurry larger dots on all specimens are assumed to be hand-warmed finger prints, due to handling the specimen shortly before testing.

To sum it up, vibration-induced thermography is hardly interpretable for thin flax laminates, while hybrid laminates worked better with inducing the vibrations on the carbon side of the inter-laminar hybrid.

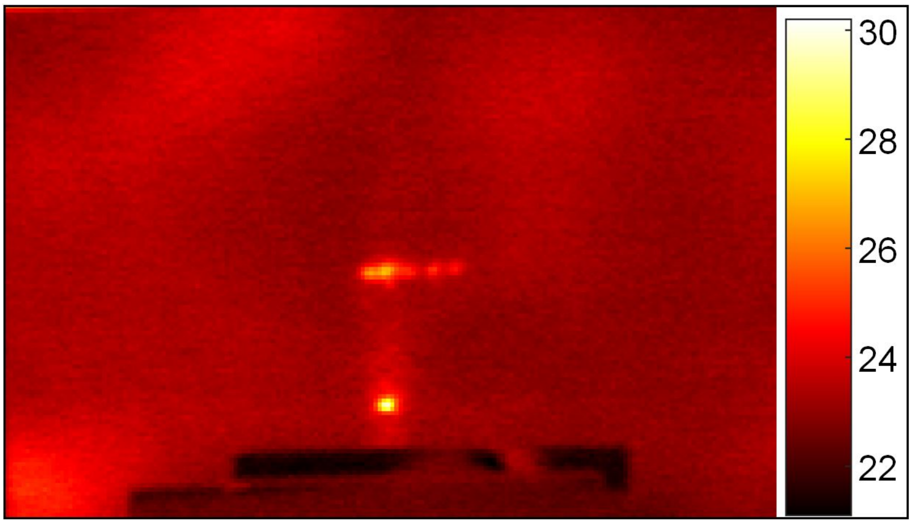

Figure 3.46: Thermographic Image of a $[C]_2$ Laminate, Damaged by an Impact of 3 J, Temperature Scale in [°C]

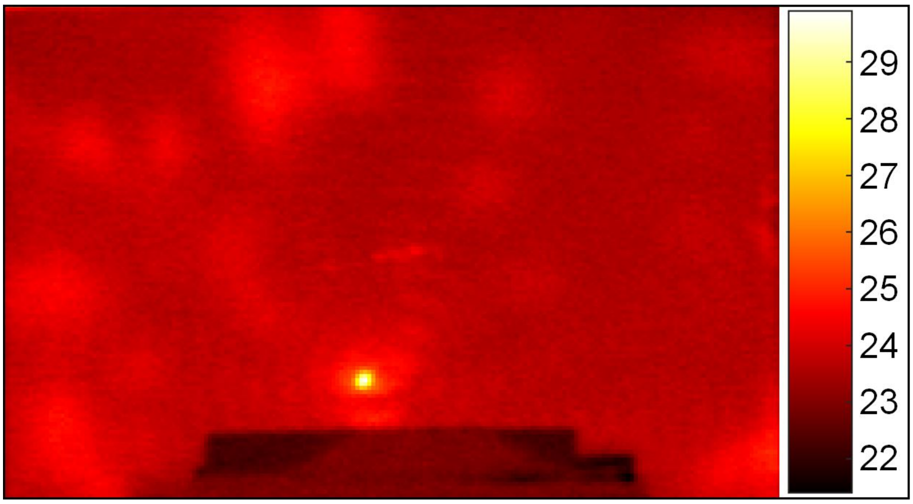

Figure 3.47: Thermographic Image of a $[F]_2$ Laminate, Damaged by an Impact of 1 J, Temperature Scale in [°C]

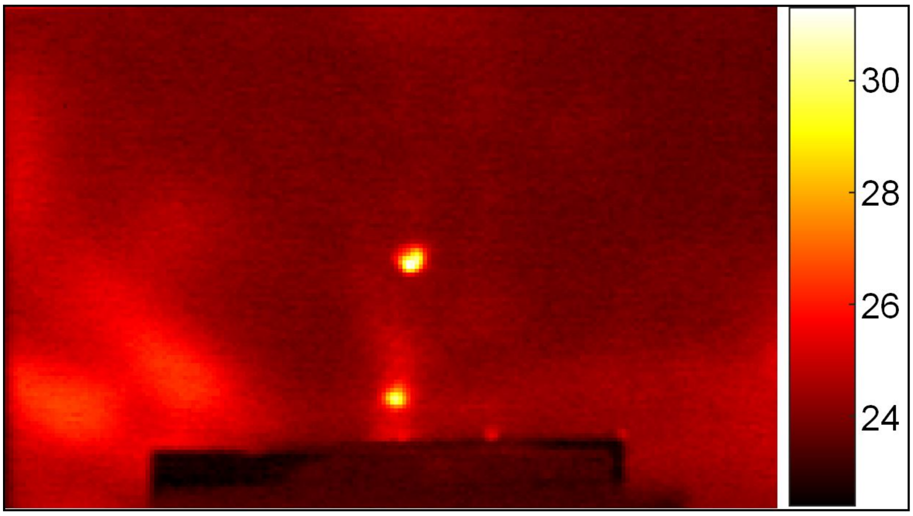

Figure 3.48: Thermographic Image of a [C/F] Laminate, Damaged by an Impact of 1.50 J, Temperature Scale in [°C]

3.7 Statistical Deviations

In this section we want to give a brief overview on the statistical deviations of structural-mechanical properties fo flax laminates. First, a literature review is given, next, the herein performed tensile tests are evaluated with respect to findings of other researchers.

Generally, it is assumed that the statistical variability of mechanical properties in natural fibers is greater than that one of conventional fibers [71, 40]. Which is, with regard to its natural growth, comprehensible. Specifically, the tensile strength and tensile stiffness, when single fibers are tested is extremely high, the values vary in a range of $\sigma_{ult,0} = 343$–2000 MPa and $E_0 = 27.6$–103 GPa [16, 51, 98]. According to Bos et al. [30], this strong variation in fiber properties is influenced by the used clamping length, which could be explained by the apparent failure mechanism, switching from the weaker pectin interphase to the stronger cellulosic cell wall as soon as the clamping length is below a limit of approx. 25 mm. The referred literature shows an asymptotic decrease of strength with increasing clamping lengths to a value of about 500 MPa.

Charlet et al. [40] investigated morphological and mechanical property scattering of single fibers, where inter-fiber and intra-fiber scattering were distinguished. "Intra-fiber" addresses the variations of a single fiber in thickness along its length, "inter-fiber" between different fibers. Furthermore, it is stated that the variety in mechanical properties is not due to the morphological characteristics, but due to the variation in its cellulose content and randomness of its local defects in position and size.

Haag et al. [71] investigated scatter in fiber bundles using the calculation method of the cross-sectional area, claiming that the method itself is introducing high variation in tensile strength data. Additionally, Lefeuvre et al. showed that elementary flax fibers scatter in the same range as glass fibers do [106], where fibers grown over 4 years and different climatic conditions were regarded.

Nevertheless, we assume that the high variation in properties of single fibers and fiber bundles even out by the application of multiple parallel fibers in a composite. This hypothesis is also supported by Liang et al. [108], who showed that the coefficient of variation (CoV) (standard deviation divided by mean value) is significantly smaller for composites ($< 5\%$) than for elementary fibers (between 21% and 57%).

Within this work we want to compare the scattering between the performed tensile tests at HSH (VI processed) and the herein performed tensile tests (prepreg processing) and their CoV to literature. There were no significance tests done and sample sizes were too small (between 6 and 10) for statistically valid statements. Nevertheless, when standard deviations are evaluated and Gauss distributions are assumed, we can estimate tendencies and draw first conclusions.

For this evaluation, the results of each batch were normalized to 100, which means the integral of each respective Gauss curve is 100. The width of the Gauss distribution is defined by the measured standard deviations. Thereby, we can compare statistics without the influence of the actual mean values. All distributions which were evaluated are plotted in Figure 3.49 and 3.50.

Results were obtained using the statistics software "R", we compare tensile tests of two manufacturing techniques, VI and prepreg as well as woven BD and UD material of carbon and flax. But, there were no tests performed with UD carbon material in VI processing.

The carbon UD composites showed lower CoV values than the flax composites. In ultimate strength, the CoV of the carbon batch was calculated as 3.0%, compared to the FFRP batches with 5.9% and 7.6%. The elastic moduli were scattering a bit lower, with 0.9% for the carbon batch and 4.3% and 7.0% for the flax batches. While the elastic moduli are showing higher variations for the prepreg FFRP samples, the ultimate strength was showing higher variations for the VI samples. For the woven coupons, the CoVs of elastic moduli were in the range of 1.8% and 3.4% for all batches, while the CFRP batches were showing the lowest and the highest values. We conclude that in this case the variation was rather dependent on the manufacturing technique than on the reinforcing fiber.

The CoVs of the ultimate strength were higher in general. The CoVs ranged from 3.1% to 15.4% while the flax batches were showing higher variations than the carbon batches, when compared by manufacturing technique. Still, the prepreg flax batches showed lower CoVs than the VI carbon batches.

Summarized, the variety of the woven batches was in a comparable range for both materials, CFRP and FFRP, also the scattering was lower than in elementary fibers and fit well to relevant literature [108]. For UD composites the CFRP showed always lower variations than the flax batches, but here the only manufacturing method of investigation was prepreg which also showed lower variations in the weaves. The moduli were of lower variation than the ultimate strengths, for all batches. All in all, the composites showed CoV values in a comparable range to the conventional composite CFRP, but sample sizes were small and there was no quality assurance applied to manufacturing and testing, for a significant statement further tests are needed. Table 3.9 summarizes the results.

In aerospace applications, the standard "DIN V 65 352 Aerospace; Methods for statistical evaluation of test results for qualification and acceptance testing of fiber-reinforced composites" can be used for statistical evaluations. It describes that the material characteristic values shall be specified in a qualification test, with more than two production batches and a confidence level of α=95% with scatter comparison and a probability of 90% (CS 27.613(b)(2)). This means that material characteristic values must be selected in such a way that a test specimen has a 95% confidence level and a 90% probability of achieving this characteristic value.

If this methodology should be applied to the mechanical characteristics in the part design, a larger batch size is necessary.

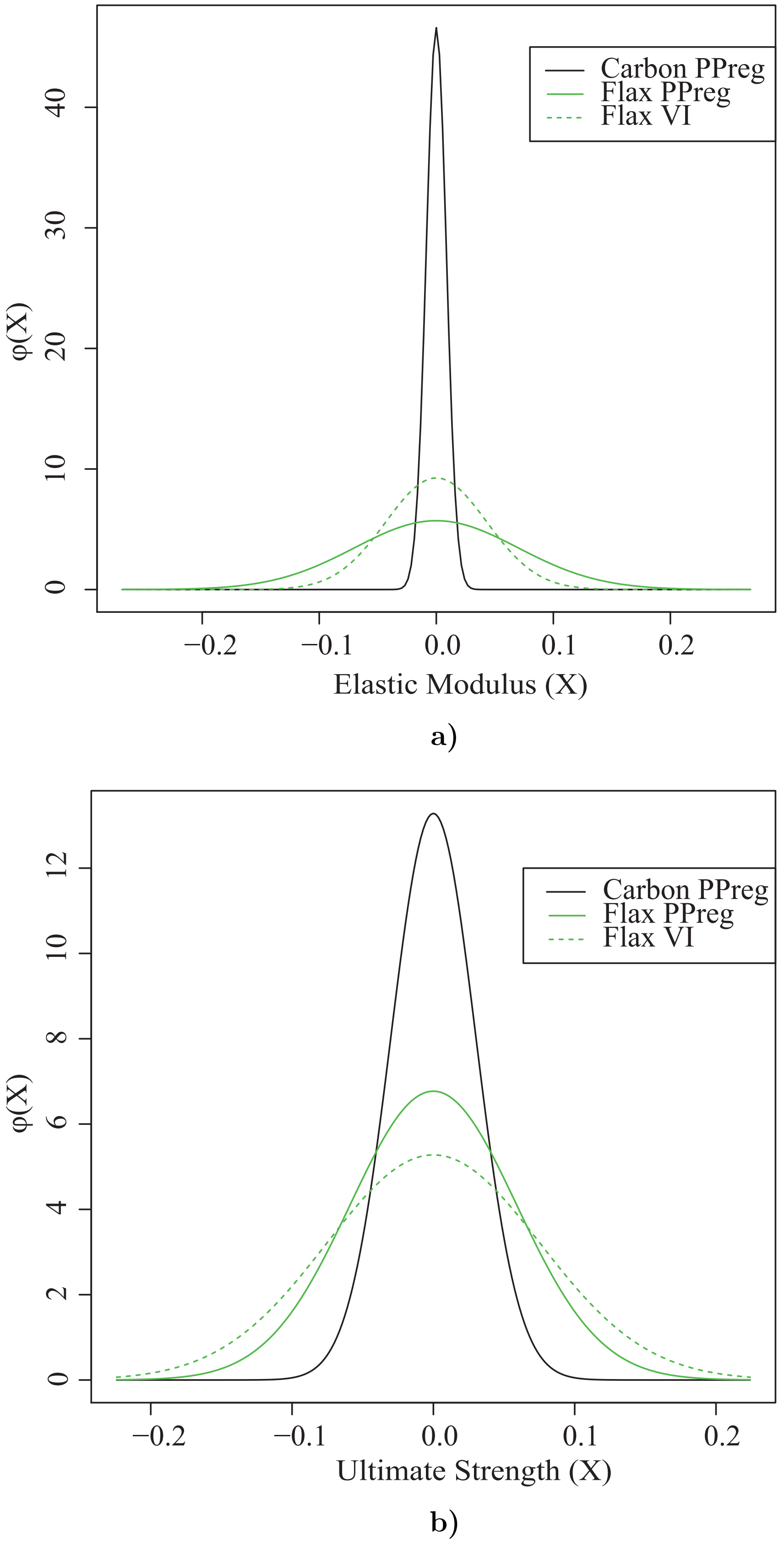

a)

b)

Figure 3.49: Normalized Gauss Distribution of a) Elastic Moduli and b) Ultimate Strength from Unidirectional Flax and Carbon Materials, either Processed from Prepregs or using Vacuum Infusion

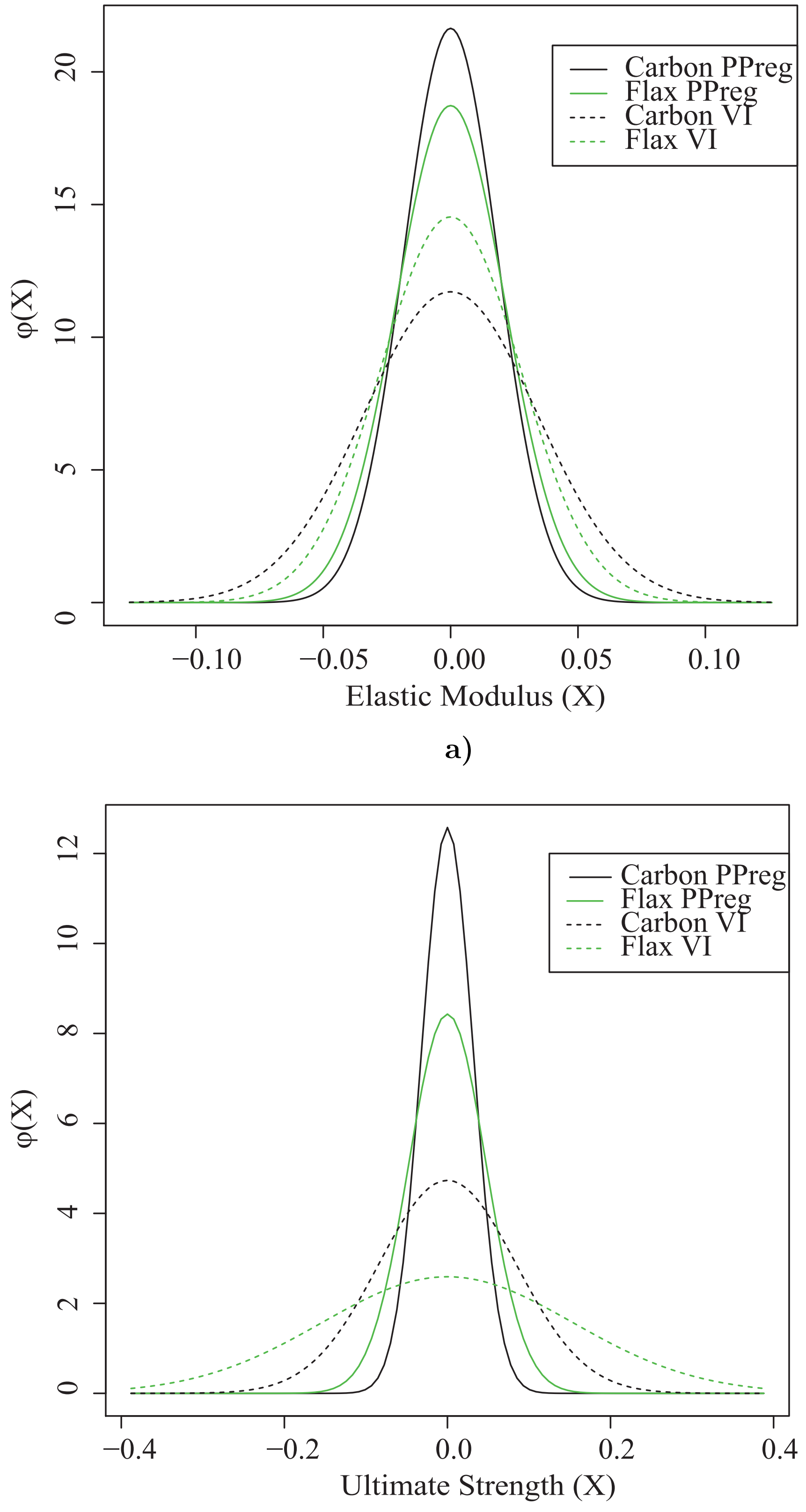

a)

b)

Figure 3.50: Normalized Gauss Distribution of a) Elastic Moduli and b) Ultimate Strength from Woven Flax and Carbon Materials, either Processed from Prepregs or using Vacuum Infusion

Table 3.9: Statistical Evaluation of Tensile Test Coupon Sets by Standard Deviation "s" and Coefficients of Variation (CoV)

	Stiffness			Strength		
	mean	s	CoV	mean	s	CoV
[Unit]	[GPa]	[GPa]	[%]	[MPa]	[MPa]	[%]
CFRP prepreg UD	13.4	1.1	0.86	1 793	54	3.00
FFRP prepreg UD	31.9	2.2	6.99	275	16	5.89
FFRP VI UD	21.9	0.9	4.31	207	16	7.56
CFRP prepreg weave	63.0	1.2	1.84	776	25	3.17
FFRP prepreg weave	8.7	0.2	2.13	91	4	4.73
CFRP VI weave	38.5	1.3	3.41	580	49	8.43
FFRP VI weave	8.7	0.2	2.75	104	16	15.39

4 Application of Flax in Aviation — Discussion and Outlook

In this chapter an evaluation on the eco-efficient performance regarding the whole life-cycle is performed with respect to the initially described motivation. Additionally, all findings on the investigated FFRP properties are summarized and discussed in context to aviation applications. Properties which are considered relevant for aviation structures, but were not investigated empirically within this work, are briefly reviewed in relevant literature.

4.1 Ecological and Economical Life-Cycle-Assessment

First, we want to evaluate the major motivational driver of this work, the beneficial eco-efficiency when using FFRP in a high proportion. Thereby, we consider the two structural demonstrators tailplane and cabin door regarding their bio-based mass content, of which the results were also published in AIAA2019 and VFS2019. Further analysis is done on the embodied energy in primary production of the used material masses and the embodied CO_2 consumption. Both are analyzed over the whole life-cycle, but only regarding material masses and literature data. The benchmark mass is the mass of their respective reference CFRP part.

4.1.1 Input Data and Assumptions

First, we want to elaborate the input data and assumptions, which were made in order to assess the LCA in terms of economic and ecologic efficiency. The herein applied eco-efficiency quantification factors embodied energy in $[\mathrm{MJ\,kg^{-1}}]$ and consumed CO_2 in $[\mathrm{CO_2\text{-}kg\,kg^{-1}}]$ are listed in Table 4.1 for the used materials. As we can see, values for flax fiber are significantly lower than values for carbon fiber in primary production. In order to show the high benefits of the fiber, we split the constitutive materials of the composites for comparison, fibers and matrix. Also, the price of flax fibers is lower than the price for carbon fibers, which might still reduce further when the overall FFRP application and thereby production increases.

Several papers claim different values for embodied energy of the materials [96, 50, 173, 163, 185, 70, 45]. In this work, we assumed values given by Ashby [10], as his data ordered well in between other sources and values of each material are given, which supports comparability. The end-of-life is considered by combustion of the materials were the given negative values indicate the heat release of the material combustion, which can be used for power generation. But, combustion also releases CO_2, therefore, these values are also positive and lead to an increase in CO_2 penalty.

In order to find out about life-cycle proportions in energy consumption, especially weight increase vs. material related energy savings, both tailplane and door versions were compared. The three life-cycle phases "primary production," "operational life," and "end-of-life" were considered.

In terms of production, we did not consider all manufacturing steps, only the material-mass based values of primary production, where differences are significant for the used fibers. Certainly, the production process of the parts consume additional energy, which is claimed by [10] with $40\,\mathrm{MJ\,kg^{-1}}$ for prepreg production and with $100\text{–}300\,\mathrm{MJ\,kg^{-1}}$ for autoclave molding. But as both materials were manufactured with the same process, these steps should not influence the fiber-inherent differences and were neglected. Analogically, the economic evaluation was performed.

Table 4.1: Evaluation Data for Ecological and Economical Assessment of the Technology Demonstrators, Data Basis from [10]

	Primary Production			End-of-Life	
	Energy	CO_2	Price	Energy	CO_2
[Unit]	$[\frac{\mathrm{MJ}}{\mathrm{kg}}]$	$[\frac{\mathrm{kg\text{-}CO_2}}{\mathrm{kg}}]$	$[\frac{USD}{kg}]$	$[\frac{\mathrm{MJ}}{\mathrm{kg}}]$	$[\frac{\mathrm{kg\text{-}CO_2}}{\mathrm{kg}}]$
Carbon Fiber	400	25.2	145.00	-33	3.7
Flax Fiber	11	0.4	3.15	-18	1.4
Epoxy Resin	134	7.2	9.00	-31	2.5
Balsa Core	10	0.9	7.00	-22	1.8
Foam Core	59	2.5	1.43	-18	1.4

Of course, we also have to consider the operational life of the helicopter, as the major fraction of the overall energy is consumed in a helicopter's operational life. Both tailplane versions were compared in terms of weight, even though the spar design accounts for weight savings and due to different span widths, the requirements were not the same. But the weight was scaled respective to its span width. For the cabin door a higher weight was accompanied by the new material as the flax weave was of low meshing density, see Section 2.6. Concluding to the statement that a proper design is more important than the material choice, in terms of weight.

Regarding the end-of-life, CFRP lack proper reuse or recyclability possibilities, which are matter of investigation in other research, but not state of the art yet [77, 19, 152]. It is assumed that the high bio-based mass content in the new version tail plane supports recyclability, as flax fibers could rot or be used in bio-gas energy production, but sufficient segmentation of the composite materials is needed. A bio-based matrix would further sup-

port recyclability, but was not taken into account in this study.
Also, as no studies on recycling were included, we assumed combustion with energy release and CO_2 demands respective to the material-mass proportions for the end-of-life. Therefore, the values are negative and indicate an energetic recovery. Values were assessed from [10] and are also included in Table 4.1.

4.1.2 Mass-Based Consumption in the Production of the Tailplane

Regarding the tailplane, Table 4.2 summarizes the mass contents by materials of the manufactured tailplane and Figure 4.1 visualizes the mass fractions of the materials contained in the respective tailplane version. A total mass of 505 g was measured for the new design, while a 450 mm section of the reference tailplane weighs 528 g. Thus, the masses were almost the same, but a benefit of 4.3% in weight savings could be achieved. Additionally, the new design contains a bio-based mass fraction of 55%. For the LCA comparison in the next section the parts' masses were multiplied by a factor of 1.5 in order to model additional scrap material in production or maintenance replacements during the life-cycle. Table 4.2 lists the contained material masses, as well as the mass-based values for embodied energy (E-E), embodied CO_2 (E-CO_2), and the costs.

Table 4.2: Eco-Efficiency and Prices of Primary Production by Material Masses of a 450 mm Section of Both Tailplane Versions, Material Data as in Table 4.1

	Hybrid Tailplane				Carbon Tailplane			
	Mass	E-E	E-CO_2	Price	Mass	E-E	E-CO_2	Price
[Unit]	[g]	$[\frac{MJ}{Part}]$	$[CO_2 \frac{kg}{Part}]$	[USD]	[g]	$[\frac{MJ}{Part}]$	$[CO_2 \frac{kg}{Part}]$	[USD]
Carbon Fiber	36.7	14.7	0.93	5.32	233.1	93.2	5.87	33.80
Flax Fiber*	247.2	2.7	0.10	0.78	0.0	0.0	0.00	0.00
Epoxy	189.3	25.4	1.36	1.70	125.5	16.8	0.90	1.13
Balsa Core*	31.5	0.3	0.22	0.03	0.0	0.0	0.00	0.00
Foam Core	0.0	0.0	0.00	7.84	169.0	10.0	0.42	0.24
Total	504.7	43.1	2.61	8.02	527.6	120.0	7.20	35.17

* 100% bio-based materials

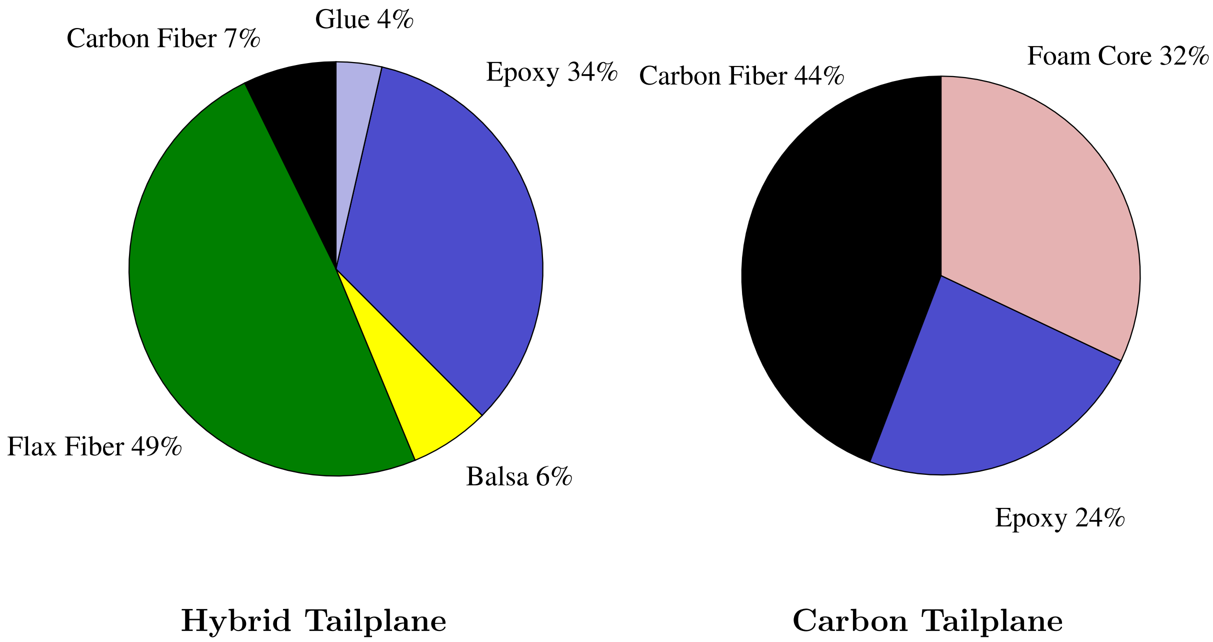

Figure 4.1: Mass Fractions of Materials in Hybrid and Carbon Tailplane Versions in [%]

The potential of reduced energy consumption is driven by the use of bio-based flax fibers. When we apply data as written in Table 4.2 for the inherent masses of both tailplane sections, a reduction, purely based on primary production, of 76.90 MJ of embodied energy is possible, as well as a reduction of 4.80 kg of carbon dioxide. The section is approximately a third of the whole tailplane. So the absolute values triple and the embodied energy in the material's primary production could be reduced by approximately 64%, while in terms of carbon emissions a reduction of 67% is possible.

We can also see that the total embodied energy is mainly driven by the carbon fiber in the conventional tailplane, but considering the low energy consumption of flax, the epoxy resin has a relevant contribution to the total embodied energy in the new design. In order to further reduce the environmental impact, there would be a substitution of the matrix by partly bio-based epoxy necessary [146].

For the economic evaluation, when only material prices are assumed, we could achieve savings of 77% for the materials in the hybrid tailplane section, according to data from [10]. The relation of these savings in comparison to the demands in the use life will be described in Section 4.1.4.

4.1.3 Mass-Based Consumption in the Production of the Cabin Door

The mass contents of both door versions are listed in Table 4.3. As outlined in Section 3.2, these are the built versions "CFRP reference" and the new "hybrid FFRP" version with carbon reinforcements. Besides the total mass of each door version, Table 4.3 provides the embodied energy, the CO_2 consumption, and the material price per door.

The values indicate that the built pure carbon door is 223 g lighter than the built hybrid door, which is attributed to the described low meshing density of the flax weave. Still, the hybrid door requires less energy (98.60 MJ) and leads to less carbon emissions (6.70 kg CO_2) in primary material production. Again, a factor of 1.5 is regarded in the overall LCA in Section 4.1.4 with respect to waste and maintenance, but not applied in this table.

Table 4.3: Eco-Efficiency and Prices of Primary Production by Material Masses of both Cabin Door Versions, Material Data as in Table 4.1

	Hybrid Cabin Door				Carbon Reference Door			
	Mass	E-E	E-CO_2	Price	Mass	E-E	E-CO_2	Price
[Unit]	[g]	$[\frac{MJ}{Part}]$	$[CO_2\frac{kg}{Part}]$	[USD]	[g]	$[\frac{MJ}{Part}]$	$[CO_2\frac{kg}{Part}]$	[USD]
Carbon Fiber	19.2	7.7	0.50	2.79	379.8	151.9	9.60	55.07
Flax Fiber	267.6	2.9	0.10	0.84	0.0	0.0	0.00	0.00
Epoxy	581.3	77.9	4.20	5.09	262.2	35.1	1.90	2.25
Foam Core	16.7	1.0	0.00	0.02	17.0	1.0	0.00	0.02
Total	884.8	89.5	4.80	8.74	659.0	188.1	11.50	57.34

When we compare the prices which are based on the used material masses and values given by [10], a saving of 85% would be achievable with the hybrid door. Due to the high cost of the additional epoxy film layers and the low batch size, this benefit was not apparent within this work. But when assuming the paid material costs without the additional epoxy film, a cost reduction of 45% per door would be inherent. This benefit ist not as high as the ideal, purely mass based benefit according to [10], but as suppliers of flax prepregs are limited and manufacturing steps of the prepreg processing reduce the offset, the 45% benefit is considered reasonable.

4.1.4 Ecologic and Economic LCA of Both Components

In order to include the changes in fuel consumption due to the new masses in the operational life, we compare the savings in energy consumption, carbon emissions, and costs, as before described. Figure 4.2 shows the development of the three quantities over the operational lifetime, depicted in flight hours, for both technology demonstrators. For both, zero is the benchmark, which would be implied by the overall life-cycle of each reference part.

For the operational life an energy-weight-penalty of the helicopter of 1.48 MJ kg^{-1} was calculated from assumptions as in Section 1.3. The 4.3% lower weight of the new design tailplane results in energy savings in the 10 000 h operational life of almost 1000 MJ and CO_2 savings of approx. 75 kg. Costs behave analogically, but with a higher off-set and a lower gradient than the other consumptions. Material-mass based cost savings are approx. 150 USD. As all calculations are scaled by the part masses, the tendencies are very similar for all, energy, CO_2, and costs.

For the cabin door we can see that savings of embodied energy and carbon emissions cancel out before 300 flight hours already, while costs break even after 4000 hours. However, the tailplane, which was lighter than the reference, shows a reduced power demand and resulting fuel consumption decrease. Thus, initial savings in energy consumption and carbon emissions grow steadily during operation. With a better and neater weave it is assumed that the modeled cabin door mass can be achieved, which was 6% more lightweight than the built reference door. Thereby, the overall LCA would result in a similar development as the tailplane evaluation.

Two conclusions can be drawn at this stage: First, the energy saved with the built hybrid door resides for only a small share of the operational life. It is expected to reside longer with potentially lighter hybrid door configurations, with less epoxy, which was achieved for the tailplane. Second, and as expected, weight is the major driver of eco-efficiency. Reducing the part's mass in hybrid FFRP designs will lead to a significant shift of the described break evens to later stages of the operational life. As FFRP are of lower density but also lower specific strength and stiffness, this can only be achieved with a tailored high-performance design.

These results need to be considered as estimations, and only two aspects of environmental impacts were included. Further co-products, such as named in [82], and demands in area or water are not considered. Also, additional processing steps for laminate curing, frozen storage, or transportation were disregarded.

Still, we conclude that if a tailored design can lead to weight savings despite the lower weight-specific characteristics, economic and ecologic superiority is expected. If a weight increase is inherent with the use of FFRP, further considerations need to be done and ecological and economical benefits to the reference are not guaranteed.

Curves in Figure 4.2 are similar for the evolution of costs during the life-time of both parts, while the costs of the more lightweight tailplane reduce further during the operational hours and the ones of the door increase. Again, if the prepreg quality of flax weave increases and no additional epoxy is needed, the economic assessment can be expected to be beneficial for the cabin door as well.

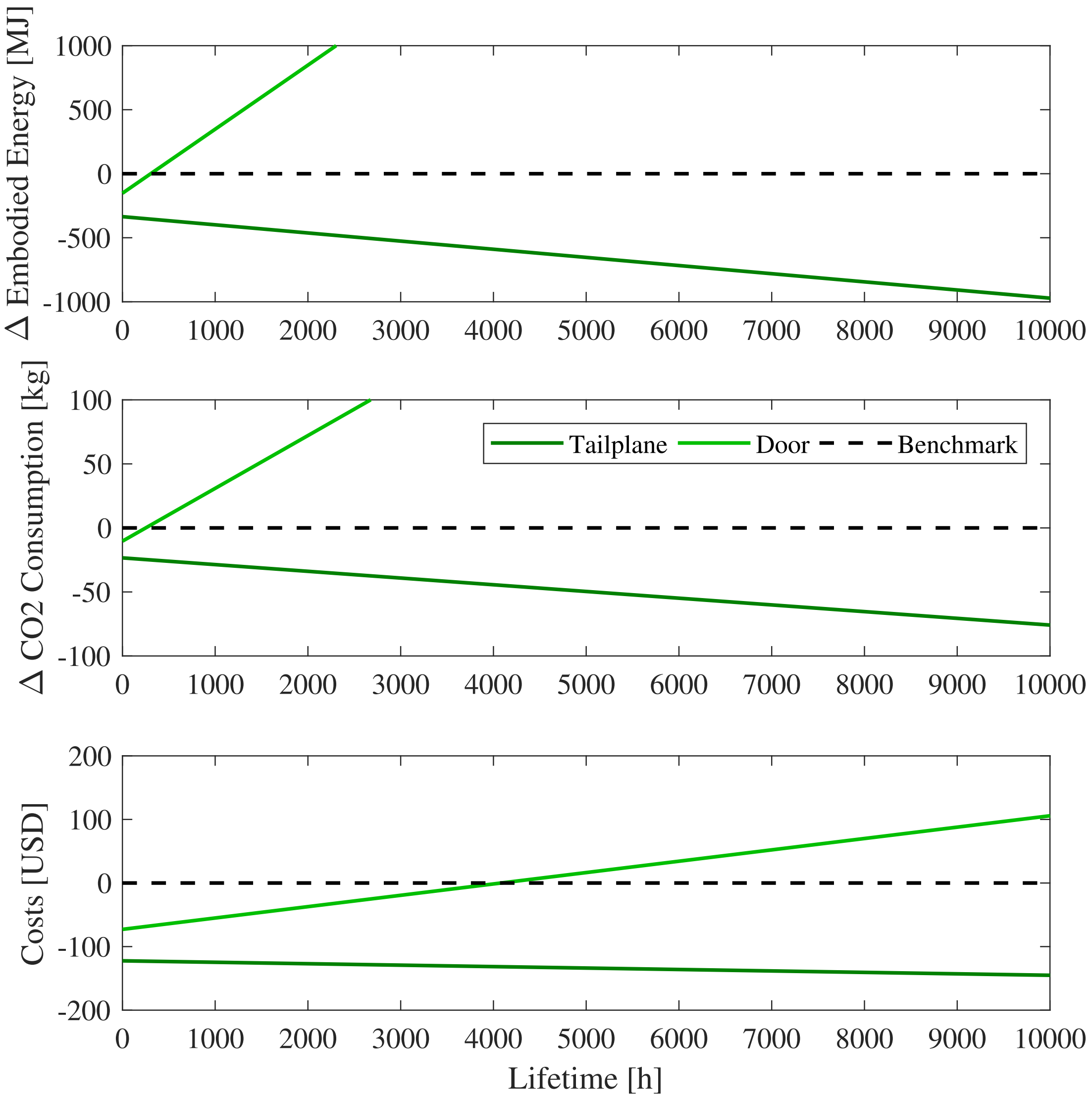

Figure 4.2: Ecologic and Economic LCA of Cabin Door and Tailplane over Flight Hours

All in all, it is clear that in helicopter applications, the operational life is the major driver of the overall energy, CO_2 consumption, and costs. As a conclusion, a weight reduction will typically be superior to energy savings in the primary production and recycling. But if equal weight can be achieved, the natural fiber hybrid design is preferable in terms of economic and ecological efficiency, regarding CO_2 and energy consumption.

4.2 Discussion of Derived Material Characteristics and Applicability

In this section the investigated properties of FFRP in respect to conventional fiber reinforced polymers are summarized. Additionally, concluding recommendations for the use of FFRP in the aviation sector are given, based on the herein gained findings. The recommendations resulted of the performed work and can vary from other related work and findings. Nevertheless, they should give guidance to industry and future research.

4.2.1 Physical Properties

The physical properties of FFRP, which are considered relevant for the use as reinforcing fibers in aviation structures, include density, fiber geometry, fiber mass, and volume content. These properties are important for manufacturing and have an influence on the structural performance. In particular, discrepancies between measured and given data in the TDS are itemized. Furthermore, the differences found in correlation to the manufacturing techniques are listed.

The low density of FFRP offers potential for low loaded structural applications. But, as the specific strength and stiffness is significantly lower to CFRP, the beneficial replacement is only possible in combination with a smart design.

Density

The manufacturer of the used materials specifies a density of $1.45\,\mathrm{g\,cm^{-3}}$ for the fiber material, while the resin system has a density of $1.10\,\mathrm{g\,cm^{-3}}$ according to both TDS [80]. In combination, Lineo is giving a density of $1.29\,\mathrm{g\,cm^{-3}}$ and $1.33\,\mathrm{g\,cm^{-3}}$ for the composites [181, 151].

The experimentally determined values in the pretests were 1.24–$1.26\,\mathrm{g\ cm^{-3}}$ for the VI composites. The composite made by prepreg processing were of a density between $1.17\,\mathrm{g\,cm^{-3}}$ and $1.18\,\mathrm{g\,cm^{-3}}$.

At the same time, the prepreg material showed better mechanical properties, which implied that the lower density does not result of a lower φ_f. Therefore, we conclude to possible air inclusions that contributed to the low density. As a result, φ_f was calculated in different ways and a proportion of air inclusions of 3–4% was determined. The VI process leads to lower φ_f but also less voids, whereas in a prepreg systems there is only a limited amount of resin available.

We conclude that all measured densities were lower than those indicated by the manufacturer. Additionally, the tendency to lower densities was identified when using higher areal weights, and the tendency to lower densities when the materials were prepreg processed, which was due to both, the additional epoxy layers in the woven laminates and probable air inclusions.

As the mechanical performance was still high, as described in the next section, this drawback was accepted for this work. But still, there is further research on quality needed and further detailed analysis of voids in order to identify particular influences and risks. Demands in quality and consistency are particularly high in aviation applications and the number of voids and the low φ_f need to be improved for the industrial application of this material.

Fiber diameters and lengths

Technical flax fibers, such as used in composites, have a limited length of 25–120 cm according to [192]. Since the fibers are not synthesized endlessly like conventional fibers, but grow, each extracted fiber has a different size. For UD processing, this fact did not influence the fiber alignment in the layers, but for the weave, the fibers need to be spun into a yarn before being processed into a fabric. With this step an additional fiber angle is introduced into the fabric, which ultimately leads to lower characteristic values than assumed by classical methods such as ROM, described in detail in Section 2.6. The resulting reduced mechanical performance of the weaves, due to additional angles and a low φ_f, is particularly low and hinders introduction to the aviation market. If a process could be developed in which the fibers do not need to be spun, but could be woven as an non-spun bundle, better fabric properties are likely to be achieved.

In CT-scans and microscopic imaging it could be found that the scattering of the flax fiber diameters is much greater than that of the carbon fibers and flax fibers are multiple times thicker than carbon fibers. For this reason, we recommend to define a minimum thickness for FFRP composites in order to ensure compensation of local variation of fiber diameters. This results in a limitation in the design, due to both, the thicker fibers themselves and the necessary thickness to constrain scatter.

Fiber volume and fiber mass fraction

In the production of prepreg materials, the flax fiber composite generally achieved lower fiber volumes and mass contents than comparable carbon fiber materials. In the case of unidirectional materials, this was 53–56 vol.-% for flax laminates and 59–62 vol.-% for carbon laminates. The difference was even more significant in the case of woven materials, where a fiber volume content of 32% was calculated for the flax fiber weaves, and carbon weaves showed 53–54%. This is explained by the additional epoxy film layers and the coarse-meshed fabric as already described in Section 2.6.

The fiber mass contents show higher differences since carbon fibers have a higher density than flax fibers. As the fiber mass content has inferior influence on the mechanical properties, this aspect is not examined further. The same tendencies can be seen when processing the laminates by VI. Furthermore, φ_f differed by about 5–10% between the prepreg and the VI samples. This is a typical difference inherent with the processing technique, but concomitant with the lower density also suggests a high void content in the flax prepreg material.

It can be summarized that flax fiber composites do not achieve as high φ_f as CFRP. This can be attributed to variations in the geometry, length, and diameter inherent in flax fibers, which are as a result locally not as neatly packed as carbon fibers are.

As a recommendation for the envisaged use in aviation, the most promising material was UD FFRP prepreg. UDs are only applicable in one-dimensionally curved structures, as the draping capabilities are limited. For the application of weaves the VI technique showed more promising results, which were still inferior to conventional weaves, due to the necessary weave processing steps.

4.2.2 Structural-Mechanical Properties

In this section the structural-mechanical findings of FFRP are summarized and put in context to conventional laminates. Tensile tests were carried out to determine the structural-mechanical characteristics. In doing so, and also by literature review, it was recognized that the majority of natural fibers exhibit a nonlinear stress-strain behavior, see Section 2.5.3. This property cannot be seen in conventional laminates loaded only in the direction of the fibers. The findings regarding this behavior are influencing stiffness and strength evaluations significantly.

Further, findings on impact, crash, and damping are itemized. Fatigue behavior is also considered relevant for aviation structures, therefore, a brief literature review is included on this topic.

Tensile Stiffness

The mentioned nonlinearity is expressed in a bilinearly approached shape with a significant stiffness reduction from about 32 GPa to only 23 GPa (in UD prepreg tensile tests). This occurs at an elongation of about 0.13% or a stress of about 42 MPa in the investigated UD reinforced material. This behavior is also evident in tensile tests with pure fiber bundles and is therefore very probably due to the fiber behavior. It is described in literature as well, see [30, 74, 63]. Cyclic loads were also applied in relevant literature, which showed that further loading, beyond the claimed yield point, results in a permanent deformation. Which is verified as the material does not return completely to the strain state before loading [115, 114, 79, 42, 133].

Since this behavior has not been fully investigated yet, we recommend to avoid loading beyond this yield point in the design of aviation structures. This can be fulfilled by the application of the described Hashin yield criterion, but other stress or strain related failure criteria are probably sufficient as well.

The design recommendation that multiply or cyclic loaded structures with a demand on geometrical integrity should be designed below this yield point, was applied on two demonstrators successfully; while the actual maximum stress or elongation can be used for breaking loads at which plastic deformations are permitted. As the ultimate stress is 6.5 times as high as the yield stress, a re-evaluation of the safety factors could be considered. Exceeding the yield stress would most likely not result in a catastrophic failure, but rather a slight permanent deformation. This could be detected easily in maintenance and the higher safety factors for the use of composites (1.875 in LTF-ULH) compared to metallic materials (1.5 in LTF-ULH) is not considered necessary.

This nonlinear behavior can also be shown with woven materials where the division into two moduli of elasticity is not as clearly separable as it was in UD material. However, an elastic region was identified and the following region shows a degressive curvature, probably due to a combination of epoxy nonlinearity and the reduction of stiffness in the fibers. Still, when using weaves, it is also recommended to consider the beginning of nonlinearity by application of a yield failure criterion when designing structures with FFRP.

As already explained in the last section, the woven FFRP showed a much lower stiffness than the UD material (about 8.70 GPa in prepreg tensile tests). Whereas conventional laminates show moderately well matching characteristics by use of the ROM, this did not apply to the investigated flax fiber composites. Here, the measured stiffness was even lower, which in turn can be explained by the additional twisting angle of the spun yarns. With an additional angle of about 18° the initial stiffness of the UD samples could be brought in correlation to the BD results, see Section 2.6.2.

Strength

The strength of pure flax fibers varies in a wide range from 343–2000 MPa, as does the stiffness with values between 27.6–103 GPa. Bos et al. [30] showed that this correlates with the clamping length of the fibers. If the clamping length is low, the strength and stiffness is strongly fluctuating and sporadically very high. From a clamping length higher than about 25 mm the strength remains on a more constant level at about 500 MPa, this is justified by a change of the failure mechanism from inter-cell failure to cell wall failure. A detailed description of these investigations can be found in the primary source.

As a result, the scatter for use in components and laminates is much smaller than the scatter of individual fibers, since the length of 25 mm, is generally exceeded. Experiments with UD prepreg materials have shown a strength of about 275 MPa, while the yield strength is about 42 MPa. Depending on the manufacturing process, fiber volume fraction, etc., these parameters vary, but this is also the case with conventional materials and therefore no flax-specific behavior. Regarding the statistics evaluations in Section 3.7, the CoV of the composites is significantly lower than the ones of pure fibers, which was also observed by other relevant research [108].

The bi-directional fabric shows a much lower ultimate strength of about 100 MPa, where again this is attributed to the additional fiber angles caused by the spinning and weaving processes, analogically to the influence on its stiffness. Also, the yield strength is only 14 MPa, which results from approximately the same yield strain but significantly lower tensile stiffness.

For the use in aviation structures the yield strength should be regarded in failure evaluation, as already explained, compare Section 2.5.3, Section 2.6.2 and in the parts design, Chapter 3.

Poission's Ratios

The transverse contraction, namely the Poisson's Ratio, was measured for the VI tensile specimens as approximately 0.23 for the 150 g weave, 0.12 for the 200 g weave and 0.29 for the UD material. Prepreg processing also showed greater transverse contraction for the UD reinforced laminates. This can be explained by the second reinforcing direction in the BD laminates transversal to the direction of tension, in which UD laminates are of low stiffness. This is not a FFRP-specific behavior and was expected.

The transverse contraction is thus rather influenced by the used resin, reinforced fiber directions, and fiber volume content and did not differ significantly from experienced data of conventional laminates.

Shear Stiffness

While the mechanical performance in the tensile direction shows a strong decrease between UD and fabrics, the shear modulus is about the same for both types. For the 150 $\mathrm{g\,m^{-2}}$ fabric of the VI process, the shear modulus is highest with 1.60 GPa. The shear modulus is an important feature in thin-walled aviation structures where (torsional) rigidity is often a limiting criterion. If we compare CFRP and FFRP fabric values, the shear modulus of the flax fabric is about 0.3–0.5 times the modulus of the CFRP material, which is not in the same order of magnitude as the tensile stiffness (0.1–0.25 times the CFRP values). In conclusion, it can be said that the substitution of CFRP by FFRP makes more sense for components subject to shear loads than for those subjected to in-axis tensile loads, especially woven laminates. Other related research comes to similar conclusions, where the off-axis tensile properties of BD composites are better than UD composites when the applied axis is $> 30°$ [157].

We conclude for the design of aviation structures, that a shear loaded structure can be designed with BD laminates, but still, the low φ_f of the weaves should be improved. For the UD laminates, the shear modulus is slightly better compared to the tensile stiffness as well, both evaluated as ratio compared to the CFRP characteristics.

Damping and Absorption

In general, NFRP are considered to incorporate good damping properties, vibration and acoustic absorption, these attributes are emphasized in various sources [147, 186, 104, 136, 137]. The damping and acoustic absorption properties were investigated on hybrid compounds, the results were presented in a joint publication [141], where hybrids showed highest acoustic absorption properties.

The damping ratio was compared for the hybrid structures tailplane and cabin door with the CFRP reference structures, within this work. According to the TDS, the damping ratios of carbon and glass composites are in the range of 0.15–0.8%, while for FFRPs between 1.1–1.75%. The measured values from EMAs showed values of 0.3–0.6% for the rather stiff and thick-walled structure of the horizontal tailplane reference (CFRP fabric and solid core), while 1.0–1.8% were measured for the FFRP hybrid carbon-flax tailplane made of prepreg materials. Results showed that these characteristic values correspond very well to the specifications in the data sheet and a significant gain in damping properties could be achieved, see Section 3.1.

The cabin door, on the other hand, was a rather soft, very thin-walled structure. The carbon reference damped better than in relevant literature and a difference could only be detected in the frequency range of $f > 400\,\mathrm{Hz}$ whereby the difference was only about 0.3% and the values of both versions were in the range of $1 \pm 0.5\%$, see Section 3.2.

In general, the higher damping of FFRP compared to CFRP as claimed in literature could be confirmed and is considered beneficial for aviation and in particular helicopter applications. Again, the UD material performed better than the weave, which might be due to higher φ_f.

Other composites of high-damping are aramid reinforced, but the energy penalty of its primary production is even higher than the energy needed for CFRP, [10] is giving approximately $1200\,\mathrm{MJ\,kg^{-1}}$, which is 100 times as much as flax fibers need. Therefore, aramid fiber composites might be technologically similar, but with respect to ecologic aspects, multiply inferior to flax.

Impact

Impact resistance was investigated on generic samples, see Section 3.5. In the impact tests the hybrid laminates with $150\,\mathrm{g\,m^{-2}}$ flax showed a comparable mass and impact resistance as the very thin carbon laminates. But the slightly better performance compared to pure carbon laminates could also be liable to the test setup. Furthermore, the arrangement of the hybrid laminates proved to be an important influencing factor. Here, hybrid laminates with a [C/F] arrangement showed a higher resistance to impact stress than corresponding laminates with a [F/C] arrangement.

As the samples were very thin and no demand of impact resistance is contained in the certification specifications, this can only be evaluated as tendency and needs further evaluation for other applications. Another aspect that should be analyzed is, if impact damaged structures suffer from contact with water. Hygroscopic tests showed that open flax fibers are prone to increase weight and probably micro-cracking. Therefore, an investigation on how fractures from impact damages suffer from water and how this influences the structural integrity should be performed.

Crash

With regard to crash, cylindrical test specimens produced by prepreg processing were investigated, see Section 3.4. The samples were made of pure CFRP, pure FFRP, or hybrid composites. Despite the "half-half" composition, the hybrid samples showed better resistance to crash than the mean value of the two measurements. The $[C_2/F_2]_S$ samples showed a good specific energy absorption of about $53\,\mathrm{J\,g^{-1}}$, which was only 15% less than the characteristic values of the pure CFRP specimens. Furthermore, the hybrid and pure FFRP specimens were less sensitive to the crushing speed compared to pure CFRP specimens, which showed significantly lower strength with increased crushing speed. [86] showed that FFRP ultimate tensile strengths increased with increasing test speed, which supports the applicability of FFRP in highly dynamic loaded structures. Flax also showed a less brittle failure behavior and failed more in delamination than in fragmentation, in the performed crash tests.

All in all, the potential of hybridization could be enhanced, however, the quantities were low and the manufacturing quality varied, so the listed findings have to be verified further. Nevertheless, in crashworthiness applications, a hybridization with FFRP and CFRP is expected to be beneficial in order to increase variability to occurring crushing speeds.

Another beneficial aspect is health-driven, studies found carbon fiber particles to be in conjunction with lung cancer when breathed in [117, 135]. During a crash, the crashworthy structures are breaking into small fragments, which are small enough to evaporate in the air. For the occupants in the crash itself there might be a small risk, as they are impaired only a short amount of time. But testing facilities or manufacturing facilities need protection devices when CFRP are used in these applications, which might not be the case for manufacturing FFRP. But, there are also studies claiming a relation between flax textile industry work and breathing diseases as well as an increased cancer risk for the employees [99, 84].

Fatigue

Fatigue properties were not matter of investigation within this thesis. In order to complete the holistic approach of the evaluation of aviation applicability, literature is summarized and referenced for an overview.
Jeannin et al. [86] investigated flax-epoxy composites' fatigue behavior and claimed that fatigue damage continues to evolve and the maximum stress continues to decrease as a function of increasing number of cycles, which underlines the herein claimed material yielding. The fatigue evolution is following a power-law trend. Mahboob et al. [113] reviewed several NFRP laminates and found them to be superior or similar to GFRP in fatigue endurance, but also claims that existing knowledge of fatigue damage evolution in NFRP is contradictory and can not be used for design consideration. Other related work, less recent than the described above, can be found in [20, 107, 162]. As a result, we recommend further fatigue testing with a special regard on the two stiffness stages, where it is assumed that there is no fatigue limit in the identified elastic region, below the yield point. Furthermore, the testing speed appears to have a significant influence on the fatigue, failure, and stiffness evolution.

4.2.3 Environmentally Influenced Properties

Flax fibers are reported to be strongly influenced by the environment. For aviation structures the demands in terms of temperature, fluids, humidity, fire, and fungal decay differ from other industries. Unfortunately, we could not cover all environmental aspects within this work. Nevertheless, we summarize demands concerning the specific aviation application and review related work in the following.

Water and Hygroscopy

In Section 3.3 the water absorption capacity of the material was evaluated by immersion in distilled water. The weight increase in the UD prepreg was between 17% and 40%, depending on the thickness of the material. Since thicker laminates showed a lower relative mass absorption, a proportionality between the surface and the mass increase was concluded. The duration of saturation moisture was also proportional to the laminate thickness, with the six-layer laminate reaching saturation moisture after about 200 min and the two-layer laminate already after 15 min. Furthermore, the measurements were repeated three times each, which showed a degressive evolution of the saturation moisture. This is explained by wash-out effects.

An attempt has been made to limit this behavior, additional resin film layers were laminated on both outside surfaces. A significant reduction of the mass increase could be achieved when immersed in water. In order to develop a reliable lightweight coating to protect against water absorption this is considered a viable approach, but should be brought in synergy with paints or other necessary coatings. When the material can be protected from water reliably, the resistance against aerospace fluids, such as de-icing, kerosene, cleaning agents, etc. should be investigated. Furthermore, long-term studies and cyclical immersion and additional mechanical performance should be investigated.

Temperature

In this work, all tests were performed under norm climate conditions in the laboratory, as significant environmental influences were avoided. The relevant range of temperature in aviation structures is beginning, depending on the specific area of application, at -55°C and ending at +135°C (see DIN EN ISO 844 and DIN 53 294).

While Gassan et al. [66] studied the thermal degradation of jute and flax fibers under temperatures between 170°C and 210°C, a significant influence due to temperatures below 170°C was not detected. Temperatures above 170°C significantly dropped the fiber's tenacity. In composites, Habibi et al. [72] showed that a temperature of 75°C reduces the tensile modulus significantly, by more than 50%. Campana et al. [36] tested post-curing temperatures on flax-epoxy composites, and found that ultimate stress and strain decreased drastically at 150°C, while the tangent modulus increased slightly. Further investigations, also covering hydrothermal influences, can be found in [123, 153, 180].

As a result, we consider the range between 150–170°C to be critical for flax fibers. In order to investigate this range of temperatures, certain high-temperature resistant epoxy matrices need to be chosen, exemplary aerospace certified epoxies. This temperature limit is considered acceptable for some aviation applications.

Theres is only limited literature available about the lower boundary of temperature. Research on freezing temperatures was done by Khanlou et al. [91], where the flax composites were less influenced by the freezing temperatures than by humidity and wetting. For aviation structures this is still considered an area that needs to be investigated further.

Fire Resistance

According to literature, flax fibers are considered to be more flammable than conventional materials [51, 139]. The fire behavior with additional flame retardants in the matrix was investigated by the cooperating partner HSH, a detailed description of the procedure and results can be found in the project report of the HSH and the Fraunhofer WKI, see [52]. In the following sections, the achieved results and the gained findings are summarized.

According to the specifications there are the classifications "flash resistant", "flame resistant", "fireproof", and "self-extinguishing", which are defined in AC 23-2A. Furthermore, heat radiation, flue gas seals, and flue gas components need to be identified. This requires extensive testing, which was not performed within this work. Only flammability tests were analyzed in terms of burning time and fire rate in [mm min^{-1}].

All in all, it can be summarized that a liquid flame retardant is preferable to a powdery one, since processing by means of VI was performed. Furthermore, a modification of the fiber was not effective and thereby a modification of the matrix is recommended in order to meet the fire requirements. A proportion of 20–30% flame retardant Luvogard FC-2050 in hybrid samples with SuperSap matrix leads to a fulfillment of the fire requirements without reduction of the mechanical properties, whereby the additive-mass proportion should be adapted to the specific fire requirements.

Another, rather commercial publication, was an announcement by the flax manufacturer Lineo, who claimed to have reached the "self-extinguishing" constraints of CS-25 [150]. Other investigations [88], regarding flax-balsa sandwich laminates, showed that an additional GFRP layer impregnated with ammonium polyphosphate reduced the heat release rates and thermal damage through-thickness significantly.

To sum it up, fire or flame retardants are needed to meet the high fire resistance requirements of aerospace standards. Nevertheless, also CFRP laminates only pass these tests with certain epoxy systems. For FFRP, there are additives available that increase the fire resistance to an acceptable level, but these are often inherent with a reduction of mechanical performance. For specific demands of certain aviation structures, there is tailored design regarding this trade-off necessary.

Fungal Decay Resistance

For aviation structures the demand of biological resistance is considered critical when plant based fibers are used. The specification RTCA DO-160 13.0 is describing experiments on fungal decay and applicable fungi specifications.

Research showed that NFRP decays when being exposed to fungi. Cooper et al. [110] investigated the decay of several NFRP when exposed to fungi, resulting weight losses of the composites were up to 11%. The decay is also considered to be correlating with the moisture swelling of the fibers. Therefore, several research is addressing chemical fiber treatments in order to reduce swelling, hygroscopy, and thereby fungi [87]. Bledzki et al. [27] modified the fibers by acetylation in the presence of perchloric acid. They found that the hygroscopy was reduced significantly and the fungi resistance was increased by the acetylation while the biocide had less effect on biological resistance. On the other hand, the superiority of flax in terms of embodied energy as a natural fiber is reduced when non-bio-based chemical treatments and co-products are necessary.

We conclude that this requirement is still considered critical and can either be addressed by a protective coating in synergy with paint, analogically to the hygroscopic protection, or by additional fiber treatments. When fiber treatments are necessary, the eco-efficiency in production and the overall life-cycle should be re-evaluated.

4.2.4 Other Properties and Non-Destructive Inspection Methods

Further properties, which were not covered within this work, are dielectric, electromagnetic, and thermal conductivity, just to name a few. The holistic description of material properties is very extensive and some are only relevant to certain aviation structures but not generally necessary. Therefore, we focused on the mechanical-structural characteristics and aviation specific demands. Other research covers automotive demands, as the application of NFRP is already brought to serial production in the automotive industry. There, NFRP are not applied as high-performance structural parts, but rather as acoustical isolation material, where the fibers are not oriented and the structures are barely loaded.

Another investigated aspect of specific aerospace demands are NDI methods, as quality assurance and maintenance is done extensively compared to other industries. Two methods were covered within this work and the findings are briefly summarized in the following.

Non-Destructive Inspection Methods

Two non-destructive test methods were applied to thin-walled CFRP, FFRP, and hybrid laminates. The detailed description of the tests is described in Section 3.6. The applied NDI methods were ultrasonic inspection and ultrasonically induced thermography.

It was shown that ultrasonic inspections can be applied to pure flax and hybrid carbon flax laminates and lead to satisfactory results. In contrast, ultrasonically induced thermography could not be utilized for inspection of pure flax laminates, i.e. the damage could not be localized. In the case of hybrid laminates, an evaluation could be carried out, with a tendency towards better evaluation if the ultrasonic induction was carried out on the carbon side of the two-layered laminate. This was explained by the fact that in flax material, due to the high inherent damping and the air inclusions, the energy introduced is absorbed within the material and thus, not carried to the damaged area.

For the use in aerospace applications, damages in FFRP are easier to detect visibly due to their white friability than damages in CFRP. Therefore, impact damage detection is simpler with these laminates. Additionally, quality assurance can be done by ultrasonic inspection. For the damage evaluation in hybrids, there is further analysis on NDI methods necessary as the inter-laminar hybrid reacted differently on the performed investigations.

4.3 Summary

In summary, we wanted to introduce NFRP, and FFRP in particular, into structural aviation applications. Thereby, various material characteristics were derived empirically, which concluded to an FEA model. Based on these data, a tailplane and a cockpit door were designed and finally built. Further experiments on element, sub-component, and component level were used for verification of the design.

Critical and beneficial properties were extracted from literature and investigated empirically, with a focus on aviation demands and diverging properties compared to conventional composites. It was determined, that the "attractive" idea of simply replacing conventional laminates by NFRP needs further material-characteristic evaluation.

First of all, and a very significant difference to CFRP and GFRP was the nonlinear stress-strain relation. This was described as bilinear, with an elastic region up to a yield point, inherent with a stiffness reduction of about 30%. The application of the Generalized Hill Potential Theory in the FEA model was showing good agreement with the nonlinear stress-strain relation in the performed tensile, uniaxially loaded tests. For further verification, multi-axially loaded samples should be matter of investigation. The determined yield point from the UD coupons could be adapted to the woven laminates by using the Rule of Mixtures and a multi-angled approach. The yield point was included as a Hashin failure criterion in the design of all structural samples. This failure analysis was then verified in terms of stiffness reduction and post-load permanent deformations. As a result, it is recommended to include this yield point in failure analyses when multiply or cyclic loaded structures are designed. Furthermore, fatigue tests should be performed with a special consideration on this yield point, where high fatigue strength is expected for loads below this point, and material deterioration is expected for loads above this point.

Another recommendation results from the manufacturing. Natural fibers need to be spun into a yarn for weave fabrication, and therefore, show a considerable circular shape of the fiber bundles and a low fiber volume content. As a result, the use of UD reinforced laminates was considered in many ways superior to woven materials.

Next, in order to balance statistical scattering, a minimum laminate thickness should be regarded. A high variety is inherent in flax fiber diameters and shape, according to literature, which also results in variable mechanical performance. FFRP tensile coupon tests of approx. 1 mm thickness, showed acceptably low CoV.

Another critical property is the highly hygroscopic behavior of flax and other natural fibers. Despite the surrounding epoxy matrix, the laminates' masses swell up to 40%. As a result, the laminates need to be protected when used in environmentally influenced surroundings. A promising approach of laminate protection was conducted with additional aerospace certified epoxy film. Additionally, the swelling behavior induces strain which can be predicted moderately well, an innovative beneficial application could make use of that behavior. It is expected that the the influence of fungal decay can be prevented analogically, but was not matter of investigation herein. A brief summary of fire resistance tests showed that the aviation regulations could be met with certain fluid additives, which are often inherent with reductions of mechanical performance.

Overall, the goal of applying FFRP in aviation and in particular helicopter structures was pursued successfully. Bio-based mass contents of up to 55% could be achieved. Flax fibers are, regarding their primary production, superior to carbon fibers, in respect to their ecological and economical effort. But, there is only a benefit possible in combination with smart, tailored designs, as the lower density itself can not replace the lower specific strength and stiffness.

Furthermore, a high performance in dynamic behavior could be verified. Therefore, vibratory or dynamically loaded structures can be virtuously built using FFRP. Specifically, high damping ratios, a high potential in carbon-flax inter-layer hybridization for crash and impact applications could be identified, where the lower sensitivity to crushing speeds was considered beneficial.

Also, the applicability of the non-destructive testing methods ultrasonic inspection and ultrasonically induced thermography on FFRP were evaluated. It turned out that ultrasonic inspection can be applied conventionally, and leads to evaluable results. The application of the ultrasonically induced thermography did not work for several specimens and was only evaluable for thin hybrid laminates where the ultrasonic induction was carried out on the carbon side of the laminate.

As a conclusion, with respect to the low TRL of 2–4 of this applications and the recent introduction of flax prepregs to the market, FFRP offer various potentials. New design methods, an improvement in weave manufacturing, and a larger market would be supportive next steps for the introduction of flax to the aviation industrial market. Furthermore, combinatorial design of experiments is needed for a final material configuration, which should meet the various requirements in a holistic approach.

Bibliography

[1] F Abbassi, A Gherissi, A Zghal, S Mistou, and J Alexis. Micro-scale modeling of carbon-fiber reinforced thermoplastic materials. *Applied Mechanics and Materials*, 146:1–11, 2012.

[2] Airbus Helicopters. Airbus Helicopters, Inc. - H135 (formerly known as EC135) specifications. URL: https://www.airbushelicoptersinc.com/products/H135-specifications.asp, Date accessed: 2018-10-18.

[3] Airbus SAS. Airport and Maintenance Planning Code Descriptions of Change-A380. Technical report, Airbus S.A.S., 2016.

[4] Airbus S.A.S. Airbus A320 Aircraft Characteristics - Aiport and Maintenance Planning, Rev. No 32. Technical report, Airbus S.A.S, 2017.

[5] Airbus SAS. Family Figures July 2017 Edition. Technical report, Airbus S.A.S., 2017.

[6] M F M Alkbir, S M Sapuan, A A Nuraini, and M R Ishak. Fibre properties and crashworthiness parameters of natural fibre-reinforced composite structure: A literature review. *Composite Structures*, 148:59–73, 2016.

[7] J Andersons, J. Modniks, and E. Spārniņš. Modeling the nonlinear deformation of flax-fiber-reinforced polymer matrix laminates in active loading. *Journal of Reinforced Plastics and Composites*, 34(3):248–256, 2015.

[8] J. Andersons, E. Spārniņš, and J. Modniks. Scale Effect of the Tensile Strength of Aligned-Flax-Fiber Reinforced Composite. In *13th International Conference on Fracture*, Bejing, China, 2013.

[9] ANSYS. Theory Reference for the Mechanical APDL and Mechanical Applications. Technical report, 2009.

[10] M.F. Ashby. *Materials and the Environment: an eco-informed material choice.* Butterworth-Heinemann/Elsevier, 2nd edition, 2013.

[11] Sam Ashworth, Jem Rongong, Peter Wilson, and James Meredith. Mechanical and damping properties of resin transfer moulded jute-carbon hybrid composites.

Composites Part B, 105:60–66, 2016.

[12] Mustapha Assarar, Wajdi Zouari, Hamid Sabhi, Rezak Ayad, and Jean Marie Berthelot. Evaluation of the damping of hybrid carbon-flax reinforced composites. *Composite Structures*, 132:148–154, 2015.

[13] A. Athijayamani, M. Thiruchitrambalam, U. Natarajan, and B. Pazhanivel. Effect of moisture absorption on the mechanical properties of randomly oriented natural fibers/polyester hybrid composite. *Materials Science and Engineering: A*, 517(1-2):344–353, 2009.

[14] Z.N. Azwa, Belal Yousif, A.C. Manalo, and W. Karunasena. A Review on the Degradability of Polymeric Composites Based on Natural Fibres. *Materials and Design*, 47:424–442, 2013.

[15] C Baley. Analysis of the flax fibres tensile behaviour and analysis of the tensile stiffness increase. *Composites: Part A*, 33:939–948, 2002.

[16] Christophe Baley and Alain Bourmaud. Average tensile properties of French elementary flax fibers. *Materials Letters*, 122(Supplement C):159–161, 2014.

[17] Christophe Baley, Yves Perrot, Frederic Busnel, Herve Guezenoc, and Peter Davies. Transverse tensile behaviour of unidirectional plies reinforced with flax fibres. *Material Letters*, 60:2984–2987, 2006.

[18] Bandhini Homeware Design. More facts about our linens ∼ Bandhini Homewear Design. URL: http://bandhinihomeweardesign.blogspot.com/2012/06/more-facts-about-our-linens.html, Date accessed: 2018-10-24.

[19] S Baz, L Ausheyks, O Reichert, A Dinkelmann, H Finckh, J Hehl, A Poeppel, and G T Gresser. Recycling of long carbon fibers, part 1: Development of a high aligned RCF-sliver for a binder tape manufacturing process. In *ECCM18 - 18th European Conference on Composite Materials*, Athens, Greece, 2018.

[20] F. Bensadoun, K.A.M. Vallons, L.B. Lessard, I. Verpoest, and A.W. Van Vuure. Fatigue behaviour assessment of flax–epoxy composites. *Composites Part A*, 82:253–266, 2016.

[21] F Bensadoun, I Verpoest, and A W Van Vuure. Are flax-epoxy composites tough? In *ECCM17 - 17th European Conference on Composite Materials*, Munich, Germany,

2016.

[22] M Bergès, R Leger, V Person, V Placet, E Ramasso, J Rousseau, X Gabrion, S Corn, S Fontaine, and P Ienny. Effect of moisture uptake on flax fiber-reinforced composite laminates: Influence on dynamic and quasi-static properties. In *ECCM17 - 17th European Conference on Composite Materials*, Munich, Germany, 2016.

[23] David N. Betts, H. Alicia Kim, and Christopher R. Bowen. Modeling and optimization of bistable composite laminates for piezoelectric actuation. *Journal of Intelligent Material Systems and Structures*, 22(18):2181–2191, 2011.

[24] Alexander Bismarck, Supriya Mishra, and Thomas Lampke. Plant Fibers as Reinforcement for Green Composites, 2005.

[25] Julia Blaut. *Bewertung der Widerstandsfähigkeit von hybriden Kohle-Flachs Faserverbundlaminaten gegen Schlagbeanspruchung*. Semester thesis, Technical Univsersity of Munich, 2017.

[26] Andrzej K. Błedzki, Adam Jaszkiewicz, Magdalena Urbaniak, and Dobrosława Stankowska-Walczak. Biocomposites in the past and in the future. *Fibres and Textiles in Eastern Europe*, 96(6 B):15–22, 2012.

[27] Andrzej Korneliusz Bledzki, Marta Lucka, Abdullah Al Mamun, and Janusz Michalski. Biological and electrical resistance of acetylated flax fiber reinforced propylene composites. *BioResources*, 4(1):111–125, 2009.

[28] Christian Bonten. *Kunststofftechnik - Einführung und Grundlagen*. Carl Hanser Verlag & Co. KG, München, 2nd edition, 2016.

[29] H L Bos. *The potential of flax fibres as reinforcement for composite materials*. PhD thesis, Technische Universiteit Eindhoven, 2004.

[30] H L Bos, M J A Van Den Oever, and O C J J Peters. Tensile and compressive properties of flax fibres for natural fibre reinforced composites. *Journal of Materials Science*, 37:1683–1692, 2002.

[31] Michael Bösl. *Dimensionierung und Auslegung einer Kabinentür aus Naturfaserverbundwerkstoffen*. Master's thesis, Technical University of Munich, 2017.

[32] Mark Braun. *Berechnung, Fertigung und experimentelle Validierung einer Cockpit-*

tür aus Kohlefaserverbundwerkstoff. Master's thesis, Technical University of Munich, 2017.

[33] BS 3F54 : 1975. *Specification for heavy duty linen (flax) sewing thread for aerospace purposes*. British Standards Institution, 1985.

[34] BS 5F34 : 1975. *Specification for light and medium duty linen (flax) sewing thread for aerospace purposes*. British Standards Institution, 1984.

[35] BS 6F35 : 1975. *Specification for braided linen (flax) lacing cord for aerospace purposes*. British Standards Institution, 1985.

[36] Charlotte Campana, Romain Leger, Rodolphe Sonnier, Laurent Ferry, and Patrick Ienny. Effect of post curing temperature on mechanical properties of a flax fiber reinforced epoxy composite. *Composites Part A: Applied Science and Manufacturing*, 107:171–179, 2018.

[37] Amandine Celino, Sylvain Fréour, Frédéric Jacquemin, Pascal Casari, Amandine Celino, Sylvain Fréour, Frédéric Jacquemin, and Pascal Casari. Study of the diffusion behavior of natural fibers. In *ECCM15 - 15th European Conference on Composite Materials*, Venice, Italy, 2012.

[38] K Charlet, S Eve, J P Jernot, M Gomina, and J Breard. Tensile deformation of a flax fiber. *Procedia Engineering*, 1:233–236, 2009.

[39] K Charlet, J P Jernot, M Gomina, L Bizet, and J Bréard. Mechanical properties of flax fibers and of the derived unidirectional composites. *Journal of Composite Materials*, 44(24):2887–2896, 2010.

[40] Karine Charlet, Jean-Paul Jernot, Joël Breard, and Moussa Gomina. Scattering of morphological and mechanical properties of flax fibres. *Industrial Crops & Products*, 32:220–224, 2010.

[41] Abderrazak Chilali, Wajdi Zouari, Mustapha Assarar, Hocine Kebir, and Rezak Ayad. Analysis of the mechanical behaviour of flax and glass fabrics-reinforced thermoplastic and thermoset resins. *Journal of Reinforced Plastics & Composites*, 35(16):1217–1232, 2016.

[42] Abderrazak Chilali, Wajdi Zouari, Mustapha Assarar, Hocine Kebir, and Rezak Ayad. Effect of water ageing on the load-unload cyclic behaviour of flax fibre-

reinforced thermoplastic and thermosetting composites. *Composite Structures*, 183(1):309–319, 2017.

[43] Composites Evolution Ltd. Biotex Flax 100 g/m2 2x2 Twill. Technical Report 442031, Composites Evolution Ltd., 2018.

[44] D-Motor. D-motor dmotor LF39 specifiactions. URL: https://www.d-motor.eu/nl/specifications-64.htm, Date accessed: 2018-10-18.

[45] Sujit Das. Life cycle assessment of carbon fiber-reinforced polymer composites. *The International Journal of Life Cycle Assessment*, 16(3):268—-282, 2011.

[46] Delphine Depuydt, Kevin Hendrickx, Wouter Biesmans, Jan Ivens, and Aart Willem Van Vuure. Digital image correlation as a strain measurement technique for fibre tensile tests. *Composites: Part A*, 99:76–83, 2017.

[47] H. N. Dhakal, Z. Y. Zhang, R. Guthrie, J. MacMullen, and N. Bennett. Development of flax/carbon fibre hybrid composites for enhanced properties. *Carbohydrate Polymers*, 96(1):1–8, 2013.

[48] DIN - Deutsches Institut für Normung. WL6.1030 - Werkstoffleistungsblatt Balsaholz (BAL) niedrige Dichte. In *Werkstoffhandbuch der deutschen Luftfahrt*. Beuth Verlag GmbH, 1987.

[49] DIN EN ISO 527-4 - 1997-07. Plastics - Determination of tensile properties - Part 4: Test conditions for isotropic and anisotropic fibre-reinforced plastic composites (ISO 527-4:1997); German version EN ISO 527-4:1997. Technical report, CEN - European Committee for Standardization, 1997.

[50] Nilmini P.J. Dissanayake, J. Summerscales, S. M. Grove, and M. M. Singh. Energy use in the production of flax fiber for the reinforcement of composites. *Journal of Natural Fibers*, 6(4):331–346, 2009.

[51] David B Dittenber and Hota V S Gangarao. Critical review of recent publications on use of natural composites in infrastructure. *Composites Part A*, 43:1419–1429, 2012.

[52] Anna Dörgens. Abschlussbericht der HSH Arbeitspakete im LUFO V2 geförderten Projekt InteReSt (FKZ: 20E1501C). Technical report, University of Applied Sciences Hannover, Garching, 2019.

[53] DOT/FAA/CT-91/7 FAA. Rotorcraft Crashworthy Airframe and Fuel System Technology Development Program. Technical report, FAA Technical Center, US Department of Transportation, Federal Aviation Administration, Atlantic City International Airport, 1994.

[54] Christian Dröge. *Fertigung und experimentelle Charakterisierung einer Hubschraubertür aus hybriden Flachs-Kohlefaser- Verbundwerkstoffen*. Semester thesis, Technical University of Munich, 2019.

[55] Edm aerotec GmbH. edm aerotec GmbH website: Home. URL: https://www.edm-aerotec.de/index.php?id=2, Date accessed: 2018-10-18.

[56] A. Martin Eiband. Human Tolerance to Rapidly Applied Accelerations - A Summary of the Literature. Technical Report June 1959, National Aeronautics and Space Administration, Washington, USA, 1959.

[57] Rani F El-Hajjar and Issam I. Qamhia. Modeling and characterization of the moisture-dependent bilinear behavior of regenerated cellulose composites. *Journal of Wood Science*, 59(4):331–336, 2013.

[58] A. El-Sabbagh, L. Steuernagel, and G. Ziegmann. Characterisation of flax polypropylene composites using ultrasonic longitudinal sound wave technique. *Composites Part B: Engineering*, 45(1):1164–1172, 2013.

[59] Emmanuel.boutet. Stem histology cross section tag, 2007. URL: https://commons.wikimedia.org/wiki/File:Stem-histology-cross-section-tag.svg, Date accessed: 2018-06-20.

[60] EN 6031:2015. Aerospace series – Fibre reinforced plastics – Test method – Determination of in-plane shear properties (± 45° tensile test); German and English version EN 6031:2015. Technical report, CEN - European Committee for Standardization, 2016.

[61] Entropy Resins. Technical Data Sheet SUPER SAP ® INR Epoxy System. Technical report, Entropy Resins, Hayward, CA, USA, 2015.

[62] Roland Feil, Markus Rinker, and Manfred Hajek. Flight Testing of a Coaxial Ultralight Rotorcraft. In *AHS International 73rd Annual Forum Proceedings*. American Helicopter Society Forum, 2017.

[63] V. Fiore, A. Valenza, and G. Di Bella. Mechanical behavior of carbon/flax hybrid composites for structural applications. *Journal of Composite Materials*, 46(17):2089–2096, 2012.

[64] R. R. Franck, editor. *Bast and Other Plant Fibres*. Woodhead Publishing, 2005.

[65] L Freund, V Bouchart, H Perrin, and P Chevrier. Hydrothermal Aging of Natural Fibers Composite: Determination of Diffusivity Parameters. In *ECCM17 - 17th European Conference on Composite Materials*, Munich, germany, 2016.

[66] Jochen Gassan and Andrzej K Bledzki. Thermal Degradation of Flax and Jute Fibers. *Journal of Applied Polymer Science*, 82:1417–1422, 2001.

[67] Maria Virginia Gelfuso, Daniel Thomazini, Júlio César, Silva De Souza, and José Juliano De Lima Junior. Vibrational Analysis of Coconut Fiber-PP Composites. *Materials Research*, 17(2):367–372, 2014.

[68] Garip Genc, Ali El Hafidi, and Papa Birame Gning. Comparison of the mechanical properties of flax and glass fiber composite materials. *Journal of Vibroengineering*, 14(2):572–581, 2012.

[69] L. B. Gning, S. Liang, L. Guillaumat, and W. J. Pui. Influence of process and test parameters on the mechanical properties of flax/epoxy composites using response surface methodology. *J Mater Sci*, 46:6801–6811, 2011.

[70] S. González-García, A. Hospido, G. Feijoo, and M.T. Moreira. Life cycle assessment of raw materials for non-wood pulp mills: Hemp and flax. *Resources, Conservation and Recycling*, 54(11):923–930, 2010.

[71] Katharina Haag, Jö Rg, and Mü Ssig. Scatter in tensile properties of flax fibre bundles: influence of determination and calculation of the cross- sectional area. *Journal of Materials Science*, 51:7907–7917, 2016.

[72] Mohamed Habibi, Luc Laperrière, and Hojjat Mahi Hassanabadi. Effect of moisture absorption and temperature on quasi-static and fatigue behavior of nonwoven flax epoxy composite. *Composites Part B*, 166:31–40, 2018.

[73] H. Hamada, J.C. Coppola, and D. Hull. Effect of surface treatment on crushing behaviour of glass cloth/epoxy composite tubes. *Composites*, 23(2):93–99, 1992.

[74] K Hendrickx, D Depuydt, A W Van Vuure, and J Ivens. The relationship between the tensile properties of natural fibers and their UD composites. In *ECCM 17 - 17th European Conference on Composite Materials*, 2016.

[75] Henkel Corporation Aerospace. LOCTITE EA 7000 AERO Epoxy Film Adhesive (KNOWN AS Hysol PL7000). Technical report, LOCTITE Technical Process Bulletin, Henkel Corporation Aerospace, Bay Point, CA, USA, 2013.

[76] Rodney Hill. *The Mathematical Theory of Plasticity.* Cleardon Press, 1998.

[77] Jack Howarth, Sada S R Mareddy, and Paul T Mativenga. Energy intensity and environmental analysis of mechanical recycling of carbon fibre composite. *Journal of Cleaner Production*, 81:46–50, 2014.

[78] Thomas Huber. *Strukturmechanik hybrider Flach-Kohlefaserlaminate in Omega-Profil Balken und im Zugversuch.* Bachelor's thesis, Technical University of Munich, 2018.

[79] Mark Hughes, James Carpenter, and Callum Hill. Deformation and fracture behaviour of flax fibre reinforced thermosetting polymer matrix composites. *Journal of Materials Science*, 42:2499–2511, 2007.

[80] Huntsman. TDS - Araldite® LY 5150 * / Aradur® 1571* / Accelerator 1573* / Hardener XB 3471* Prepreg System. Technical Report June, Huntsman, 2012.

[81] P. E. Irving and C. Soutis, editors. *Polymer composites in the aerospace industry.* Woodhead Publishing, 2015.

[82] J. Summerscales and N. P. J. Dissanayake. Allocation in the Life Cycle Assessment (LCA) of Flax Fibres for the Reinforcement of Composites. In Raul Fangueiro and Sohel Rana, editors, *Advances in Natural Fibre Composites - Raw Materials, Processing and Analysis*, pages 223–235. Springer International Publishing AG, 2018.

[83] Maya Jacob John, R D Anandjiwala, and Sabu Thomas. Hybrid Composites. In Sabu Thomas and L. A. Pothan, editors, *Natural Fibre Reinforced Composites — From Macro to Nanoscale*, pages 315–328. Old City Publishing, Paris, 2009.

[84] J. P. Jamison, J. H. M. Langlands, and C. C. Bodel. Ventilatory Responses of Normal Subjects to Flax Dust Inhalation: The Protective Effect of Autoclaving the Flax. *British Journal of Industrial Medicine*, 42(3):196–201, 1985.

[85] Mohammad Jawaid and Mohamed Thariq, editors. *Sustainable Composites for Aerospace Applications*. Woodhead Publishing, 1st editio edition, 2018.

[86] Thomas Jeannin, Xavier Gabrion, Emmanuel Ramasso, and Vincent Placet. About the fatigue endurance of unidirectional flax-epoxy composite laminates. *Composites Part B*, 165:690–701, 2019.

[87] M M Kabir, H Wang, K T Lau, and F Cardona. Composites : Part B Chemical treatments on plant-based natural fibre reinforced polymer composites : An overview. *Composites Part B*, 43(7):2883–2892, 2012.

[88] Everson Kandare, Piyanuch Luangtriratana, and Baljinder K. Kandola. Fire reaction properties of flax/epoxy laminates and their balsa-core sandwich composites with or without fire protection. *Composites Part B: Engineering*, 56:602–610, 2014.

[89] Michael Karus, Markus Kaup, and Daike Lohmeyer. Study On Markets and Prices for Natural Fibres (Germany and EU). Technical Report March, nova Institute, Hürth, Germany, 2000.

[90] Malika Kersani, Stepan V Lomov, Aart Willem, Van Vuure, Ahcè Ne Bouabdallah, and Ignaas Verpoest. Damage in flax/epoxy quasi-unidirectional woven laminates under quasi-static tension. *Journal of Composite Materials*, 49(4):403–413, 2015.

[91] Hossein Mohammad Khanlou, Wayne Hall, Peter Woodfield, John Summerscales, and Gaston Francucci. The mechanical properties of flax fibre reinforced poly (lactic acid) bio-composites exposed to wet, freezing and humid environments. *Journal of Composite Materials*, 52(6):835–850, 2018.

[92] Christof Kindervater. Untersuchungen zur Crashsicherheit von Hubschraubern. Technical report, Deutsches Zentrum für Luft- und Raumfahrt e.V., Institut für Bauweisen und Konstruktionsforschung, Stuttgart, 2006.

[93] U Kling, D Empl, O Boegler, and A T Isikveren. Future Aircraft Wing Structures Using Renewable Materials. In *Deutscher Luft- und Raumfahrtkongress 2015*, 2015.

[94] Dawid Kobus. *Auslegung und Dimensionierung eines Höhenleitwerks aus Naturfaserverbundwerkstoffen.* Semester thesis, Technical University of Munich, 2016.

[95] Christian R Koenig, Dieter H Müller, and K.-D. Thoben. Acoustical Parameters of Automotive Interiors using Hybrid Fleeces basing on natural fibres. *The Journal of*

the Acoustical Society of America, 123(5), 2008.

[96] A. Koezjakov, D. Urge-Vorsatz, W. Crijns-Graus, and M. van den Broek. The relationship between operational energy demand and embodied energy in Dutch residential buildings. *Energy and Buildings*, 165:233–245, 2018.

[97] E. Kontou, G. Spathis, and P. Georgiopoulos. Modeling of nonlinear viscoelasticity-viscoplasticity of bio-based polymer composites. *Polymer Degradation and Stability*, 110:203–207, 2014.

[98] H Ku, H Wang, N Pattarachaiyakoop, and M Trada. A review on the tensile properties of natural fiber reinforced polymer composites. *Composites Part B*, 42(4):856–873, 2011.

[99] Irena Kuzmickiene and Mecys Stukonis. Cancer incidence among women flax textile manufacturing workers in Lithuania. *Occupational and environmental medicine*, 67(7):500–2, 2010.

[100] Dennis Lam, Omar Faruque, James Cheng, Saeed Barbat, Guowei Zhou, Xuming Su, Alex Akkerman, and Steve Schaller. 5 th International LS-DYNA ® Users Conference Meso-scale Modeling of Carbon Fiber Composites for Crash Simulation. In *15th International LS-DYNA Users Conference*, 2018.

[101] A. Le Duigou and M. Castro. Evaluation of force generation mechanisms in natural, passive hydraulic actuators. *Scientific Reports*, 6(1):18105, 2016.

[102] Antoine Le Duigou, Vincent Keryvin, Johnny Beaugrand, Miguel Pernes, Fabrizio Scarpa, and Mickael Castro. Humidity responsive actuation of bioinspired hygromorph biocomposites (HBC) for adaptive structures. *Composites Part A*, 116:36–45, 2019.

[103] Antoine le Duigou, Justin Merotte, Alain Bourmaud, Peter Davies, Karim Belhouli, and Christophe Baley. Hygroscopic expansion: A key point to describe natural fibre/polymer matrix interface bond strength. *Composites Science and Technology*, 151:228–233, 2017.

[104] Marie Joo Le Guen, Roger H. Newman, Alan Fernyhough, and Mark P. Staiger. Tailoring the vibration damping behaviour of flax fibre-reinforced epoxy composite laminates via polyol additions. *Composites Part A*, 67:37–43, 2014.

[105] Y Lebaupin, M Chauvin, Tq Truong Hoang, and F Touchard. Effect of Stacking Sequence on Low Velocity Impact and Post-Impact Behavior of Flax/Polyamide 11 Composites. In *ECCM17 - 17th European Conference on Composite Materials*, Munich, Germany, 2016.

[106] Anaële Lefeuvre, Alain Bourmaud, Claudine Morvana, and Christophe Baley. Tensile properties of elementary fibres of flax and glass: Analysis of reproducibility and scattering. *Materials Letters*, 130:289–291, 2014.

[107] Larry Lessard, Soroush Asgarinia, Chanvit Viriyasuthee, Steven Phillips, and Martine Dubé. Fatigue Behavior of Woven Flax / Epoxy Composites. In *20th International Conference on Composite Materials Copenhagen, 19-24th July 2015*, Copenhagen, 2015.

[108] Shaoxiong Liang, Papa Birame Gning, and Laurent Guillaumat. Quasi-static behaviour and damage assessment of flax/epoxy composites. *Materials and Design*, 67:344–353, 2015.

[109] Justin D Littell, Charles R Ruggeri, Robert K Goldberg, Gary D Roberts, William A Arnold, and Wieslaw K Binienda. Measurement of Epoxy Resin Tension, Compression, and Shear Stress–Strain Curves over a Wide Range of Strain Rates Using Small Test Specimens. *Journal of Aerospace Engineering*, 21(3), 2008.

[110] J. L. Lopez, Paul A Cooper, and Mohini Sain. Evaluation of Proposed Standard Test Method to Determine Decay Resistance of Natural Fiber Plastic Composites. *Forest Products Journal*, 55(12):95–99, 2005.

[111] Luftfahrt-Bundesamt. LTF-ULH - Lufttüchtigkeitsforderungen für Ultraleichte Hubschrauber. *ID 2-312-16*, 2016.

[112] Bo Madsen and Hans Lilholt. Guidelines for mechanical design with biocomposites: properties, weight and cost. *JEC Magazine*, 37, 2007.

[113] Zia Mahboob and Habiba Bougherara. Fatigue of flax-epoxy and other plant fibre composites: Critical review and analysis. *Composites Part A: Applied Science and Manufacturing*, 109:440–462, 2018.

[114] Zia Mahboob, Yves Chemisky, Fodil Meraghni, and Habiba Bougherara. Mesoscale modelling of tensile response and damage evolution in natural fibre reinforced laminates. *Composites Part B*, 119:168–183, 2017.

[115] Zia Mahboob, Ihab El Sawi, Radovan Zdero, Zouheir Fawaz, and Habiba Bougherara. Tensile and compressive damaged response in Flax fibre reinforced epoxy composites. *Composites: Part A*, 92:118–13, 2017.

[116] Erik Marklund, Janis Varna, and Lennart Wallström. Nonlinear Viscoelasticity and Viscoplasticity of Flax/Polypropylene Composites. *Journal of Engineering Materials and Technology*, 128(4):527, 2006.

[117] Thomas R. Martin, Stephen W. Meyer, and Daniel R. Luchtel. An evaluation of the toxicity of carbon fiber composites for lung cells in vitro and in vivo. *Environmental Research*, 49(2):246–261, 1989.

[118] Shahid Mehmood and Bo Madsen. Properties and performance of flax yarn / thermoplastic polyester composites. *Journal of Reinforced Plastics and Composites*, 31(24):1746–1757, 2012.

[119] James Meredith, Stuart R. Coles, Richard Powe, Ed Collings, Sophie Cozien-Cazuc, Brendon Weager, Jorg Müssig, and Kerry Kirwan. On the static and dynamic properties of flax and Cordenka epoxy composites. *Composites Science and Technology*, 80:31–38, 2013.

[120] James Meredith, Richard Ebsworth, Stuart R. Coles, Benjamin M. Wood, and Kerry Kirwan. Natural fibre composite energy absorption structures. *Composites Science and Technology*, 72(2):211–217, 2012.

[121] Justin Merotte, Antoine Le Duigou, Alain Bourmaud, Karim Behlouli, and Christophe Baley. Mechanical and acoustic behaviour of porosity controlled randomly dispersed flax/PP biocomposite. *Polymer Testing*, 2016.

[122] D. Montalvão, A.M.R. Ribeiro, N.M.M. Maia, J. Duarte Silva, and R.A. Cláudio. Damping measurements on a carbon fibre reinforced laminate. *Proceedings of ISMA2006: International Conference on Noise and Vibration Engineering*, 1, 2006.

[123] B A Muralidhar. Viscoelastic and thermal behaviour of flax preforms reinforced epoxy composites. *Journal of Industrial Textiles*, 44(4), 2013.

[124] Peter Niemz. Physik des Holzes. Technical report, ETH Zürich, Institut für Baustoffe, 2005.

[125] Normenstelle Luftfahrt. Aerospace series - Carbon fibre reinforced plastics - Unidi-

rectional laminates, Tensile test parallel to the fibre direction; German Version EN 2561 : 1995. Technical Report 3113, Deutsches Institut für Normung, Berlin, 1995.

[126] Normenstelle Luftfahrt. Aerospace series - Carbon fibre reinforced plastics, unidirectional laminates - Tensile test perpendicular to the fibre direction; German version EN 2597 : 1998. Technical Report 3113, Deutsches Institut für Normung, Berlin, 1998.

[127] Tim Palucka and Bernadette Bensaude-Vincent. Materials Research Activities, History of composites - overview, 2002. URL: https://authors.library.caltech.edu/5456/1/hrst.mit.edu/hrs/materials/public/composites/Composites Overview.htm, Date accessed: 2018-09-07.

[128] Shyam M. Panamoottil, Raj Das, and Krishnan Jayaraman. Anisotropic continuum damage model for prediction of failure in flax/polypropylene fabric composites. *Polymer Composites*, 37(8):2588–2597, 2016.

[129] B V Perov and I P Khoroshilova. *Hybrid composite materials*, chapter 6, pages 269–304. Springer Netherlands, Dordrecht, 1995.

[130] R. Petrucci, C. Santulli, D. Puglia, E. Nisini, F. Sarasini, J. Tirillò, L. Torre, G. Minak, and J. M. Kenny. Impact and post-impact damage characterisation of hybrid composite laminates based on basalt fibres in combination with flax, hemp and glass fibres manufactured by vacuum infusion. *Composites Part B*, 69:507–515, 2015.

[131] Emmanuel Piet. *Structural Evaluation and Optimization of the AREA Rotor Blade.* Semester thesis, Technical University of Munich, 2018.

[132] Giuseppe Pitarresi, Davide Tumino, and Antonio Mancuso. Thermo-mechanical behaviour of flax-fibre reinforced epoxy laminates for industrial applications. *Materials*, 8(11):7371–7388, 2015.

[133] Vincent Placet, Frédérique Trivaudey, Ousseynou Cissé, and M. Lamine Boubakar. What are the possible origins of the nonlinear tensile behaviour of hemp fibres? *International conference on composite materials*, 2014.

[134] Christophe Poilâne, Florian Gehring, Haomiao Yang, and Fabrice Richard. About Nonlinear Behavior of Unidirectional Plant Fibre Composite. In Raul Fangueiro and Sohel Rana, editors, *Advances in Natural Fibre Composites - Raw Materials, Processing and Analysis*, pages 69–79. Springer International Publishing AG, 2018.

[135] Craig A. Poland, Rodger Duffin, Ian Kinloch, Andrew Maynard, William A. H. Wallace, Anthony Seaton, Vicki Stone, Simon Brown, William MacNee, and Ken Donaldson. Carbon nanotubes introduced into the abdominal cavity of mice show asbestos-like pathogenicity in a pilot study. *Nature Nanotechnology*, 3(7):423–428, 2008.

[136] S. Prabhakaran, V. Krishnaraj, M. Senthil Kumar, and R. Zitoune. Sound and vibration damping properties of flax fiber reinforced composites. *Procedia Engineering*, 97:573–581, 2014.

[137] Le Quan, Ngoc Tran, Kede Huang, Abhishek Vishwanath Rammohan, Wern Sze Teo, and Heow Pueh Lee. Investigation of sound absorption and vibration damping of flax fibre composites. In *ECCM 17 - 17th European Conference on Composite Materials*, 2016.

[138] Karthik-Ram Ramakrishnan, Nicolas Le Moigne, Pierre Slangen, and Anne Bergeret. Experimental Characterisation of the Impact Resistance of Flax Fibre Reinforced Composite. In *ECCM17 - 17th European Conference on Composite Materials*, Munich, Germany, 2016.

[139] S Rao, A Bhardwaj, A Beehag, and D Bhattacharyya. Fire performance of flax laminates and their hybrids. *Advanced Materials Research*, 410:114–117, 2012.

[140] S Requile, A Le Duigou, A Bourmaud, and C Baley. Moisture induced hygroscopic and mechanical properties of hemp reinforced biocomposite . In *ECCM18 -18th European Conference on Composite Materials*, Athens, Greece, 2018.

[141] R Rinberg, R Svidler, M Klärner, L Kroll, K Strohrmann, M Hajek, and H-J Endres. Anwendungspotenzial von naturbasierten hybriden Leichtbaustrukturen in der Luftfahrt. In *Deutscher Luft- und Raumfahrtkongress 2016*, page ID: 420092, Braunschweig, 2016.

[142] William G. Roeseler, Branko Sarh, and Max U. Kismarton. Composite Structures: The First 100 Years. In *16th International Conference on Composite Materials*, Kyoto, Japan, 2006.

[143] Jean Rouchon. Certification of Large Aircraft Composite Structures, Recent Progress and New Trends in Compliance Philosophy. In *17th ICAS Congress*, volume 2, pages 1439–1447, Stockholm, Sweden, 1990. 17th ICAS Congress.

[144] David Roylance. Introduction to Composite Materials. Technical report, Department of Materials Science and Engineering, Massachusetts Institute of Technology, Cambridge, MA, 2000.

[145] A. Rubio-López, T. Hoang, and C. Santiuste. Constitutive model to predict the viscoplastic behaviour of natural fibres based composites. *Composite Structures*, 115:8–18, 2016.

[146] Alfred Rudin and Phillip Choi. Biopolymers. In *The Elements of Polymer Science and Engineering*, chapter 13, pages 521–535. Woodhead Publishing, third edition, 2013.

[147] M Rueppel, J Rion, C Dransfeld, and K Masania. Damping of Carbon Fibre and Flax Fibre Reinforced Angle Ply Polymers. In *ECCM 17 - 17th European Conference on Composite Materials*, Munich, Germany, 2016.

[148] Fabrizio Sarasini, Jacopo Tirillò, Simone D'Altilia, Teodoro Valente, Carlo Santulli, Fabienne Touchard, Laurence Chocinski-Arnault, David Mellier, Luca Lampani, and Paolo Gaudenzi. Damage tolerance of carbon/flax hybrid composites subjected to low velocity impact. *Composites Part B: Engineering*, 91:144–153, 2016.

[149] James J. Sargianis, Hyung-Ick Kim, Erik Andres, and Jonghwan Suhr. Sound and vibration damping characteristics in natural material based sandwich composites. *Composite Structures*, 96:538–544, 2013.

[150] SAS LINEO. SAS LINEO developed a flax prepreg satisfying the self-extinguishing constraints of Aeronautics. Technical report, Lineo SAS, Saint Martin Du Tilleul, France, 2015.

[151] SAS LINEO. Technical Datasheet 2016 - FLAXPREG BL150. Technical report, SAS LINEO, Saint Martin du Tilleul, France, 2016.

[152] Jan Schueppel, Denny, Stockschlaeder and Tjark von Reden. END-OF-LIFE CFRP AS A RAW MATERIAL IN STEEL AND OF CALCIUM CARBIDE PRODUCTION. In *ECCM18 - 18th European Conference on Composite Materials*, Athens, Greece, 2018.

[153] Daniel Scida, Mustapha Assarar, Christophe Poilâne, and Rezak Ayad. Influence of hygrothermal ageing on the damage mechanisms of flax-fibre reinforced epoxy composite. *Composites Part B: Engineering*, 48:51–58, 2013.

[154] SGL Group The Carbon Company. Technical Data Sheet Sigrapreg® c w200-tw2/2-e501/48%, 2016.

[155] SGL Group The Carbon Company. Technical Data Sheet Sigrapreg® c w200-tw2/2-e503/45%, 2016.

[156] Darshil U Shah. Damage in biocomposites: Stiffness evolution of aligned plant fibre composites during monotonic and cyclic fatigue loading. *Composites Part A*, 83:160–168, 2016.

[157] Darshil U. Shah, Peter J. Schubel, Mike J. Clifford, and Peter Licence. The tensile behavior of off-axis loaded plant fiber composites: An insight on the nonlinear stress-strain response. *Polymer Composites*, 33(9):1494–1504, 2012.

[158] Darshil U Shah, Bhavna Sharma, and Michael H Ramage. Processing bamboo for structural composites: Influence of preservative treatments on surface and interface properties. *International Journal of Adhesion and Adhesives*, 85:15–22, 2018.

[159] C. F. Shih and D. Lee. Further Developments in Anisotropic Plasticity. *Journal of Engineering Materials and Technology*, 100:294–302, 1978.

[160] M.H. Shirangi and B Michel. Mechanism of Moisture Diffusion, Hygroscopic Swelling, and Adhesion Degradation in Epoxy Molding Compounds. In X.J. Fan and E Suhir, editors, *Moisture Sensitivity of Plastic Packages of IC Devices, Micro- and Opto-Electronic Materials, Structures, and Systems*, pages 29–69. Springer, Boston, MA, 2010.

[161] Janis Sliseris, Libo Yan, and Bohumil Kasal. Numerical modelling of flax short fibre reinforced and flax fibre fabric reinforced polymer composites. *Composites Part B: Engineering*, 89:143–154, 2016.

[162] F.K. Sodoke, L. Toubal, and L. Laperrière. Hygrothermal effects on fatigue behavior of quasi-isotropic flax/epoxy composites using principal component analysis. *Journal of Materials Science*, 51(24):10793–10805, 2016.

[163] Young S. Song, Jae R. Youn, and Timothy G. Gutowski. Life cycle energy analysis of fiber-reinforced composites. *Composites Part A*, 40(8):1257–1265, 2009.

[164] C. Soutis. Fibre reinforced composites in aircraft construction. *Progress in Aerospace Sciences*, 41(2):143–151, 2005.

[165] Josef Steigenberger. *Fertigung, Charakterisierung und Validierung von Subkomponenten eines Höhenleitwerks aus flachsfaserverstärkten Kunststoffen.* Master's thesis, Technical University of Munich, 2018.

[166] K Strohrmann, J Blaut, C Panescu, H.-J. Endres, R. Svidler, and M. Hajek. Impact Damage Behavior and Non-Destructive Inspection Methods of Thin Hybrid Carbon-Flax Laminates. In *Deutscher Luft- und Raumfahrtkongress 2017*, Munich, Germany, 2017. DGLR. ID: 450143.

[167] K Strohrmann and M Hajek. An Eco-Efficient Helicopter Tailplane Hybridized from Flax, Balsa and Carbon. In *AIAA SciTech 2019 Forum, San Diego, CA, USA*, San Diego, CA, USA, 2019.

[168] K Strohrmann, S Schmeer, G Fortin, H Hamada, and M Hajek. Crashworthiness Characteristics of Carbon-Flax Composite Tubes for Aerospace Applications. In *ECCM18 -18th European Conference on Composite Materials*, Athens, Greece, 2018.

[169] Katharina Strohrmann. Abschlussbericht der TUM Arbeitspakete im LUFO V2 geförderten Projekt InteReSt (FKZ: 20E1501C). Technical report, Technichal University of Munich, Garching, 2019.

[170] Katharina Strohrmann, Nicolas André, and Manfred Hajek. Hybrid Natural Fiber Composites in a Helicopter Cabin Door – Mechanical Properties and Ecological Efficiency. In *VFS International 75th Annual Forum & Technology Display*, Philadelphia, 2019.

[171] Katharina Strohrmann and Manfred Hajek. Bilinear Approach to Tensile Properties of Flax Composites in Finite Element Analyses. *Journal of Materials Science*, 54:1409–1421, 2019.

[172] Deborah A. Sunter, William R. Morrow, Joseph W. Cresko, and Heather P.H. Liddell. The Manufacturing Energy Intensity of Carbon Fiber Reinforced Polymer Composites and its Effect on Life Cycle Energy use for Vehicle Door Lightweighting. In *20th International Conference on Composite Materials*, Copenhagen, 2015.

[173] Tetsuya Suzuki and Jun Takahashi. Prediction of Energy Intensity of Carbon Fiber Reinforced Plastics for Mass-Produced Passenger Cars. In *9th Japan International SAMPE Symposium*. 9th Japan International SAMPE Symposium, 2005.

[174] Gyaneshwar Tandon, editor. *Composite, Hybrid, and Multifunctional Materials,*

Volume 4: Proceedings of the 2014 Annual Conference on Experimental and Applied Mechanics. Springer, 2014.

[175] Martin Tröndle. *Untersuchung von bistabilen Flachslaminaten mittels Feuchtigkeitstrigger*. Bachelor's thesis, Technical University of Munich, 2018.

[176] M. E. Tuttle. *Structural analysis of polymeric composite materials*. CRC Press, 2nd edition, 2012.

[177] S. Ucsnik, M. Scheerer, S. Zaremba, and D.H. Pahr. Experimental investigation of a novel hybrid metal–composite joining technology. *Composites Part A*, 41(3):369–374, 2010.

[178] U.S. Department of Commerce - National Technical Information Service. WIND TUNNEL TESTS OF THE GA (W)-2 AIRFOIL WIH 20% AILERON, 25% SLOTTED FLAP, 30% FOWLER FLAP, AND 10% SLOT-LIP SPOILER. Technical report, Wichita State University, Wichita, KS, 1976.

[179] S. Valliappan, P. Boonlaulohr, and I. K. Lee. Non-linear analysis for anisotropic materials. *International Journal for Numerical Methods in Engineering*, 10(3):597–606, 1976.

[180] K van de Velde and P Kiekens. Thermal Degradation of Flax : The Determination of Kinetic Parameters with Thermogravimetric Analysis. *Journal of Applied Polymer Science*, 83(12):2634–2643, 2002.

[181] Francois Vanfleteren. Technical Data Sheet - FLAXPREG T-UD. Technical report, LINEO S.A.S., 2015.

[182] J Varna, L Rozite, R Joffe, and A Pupurs. Non-linear behaviour of PLA based flax composites. *Plastics, Rubber and Composites*, 41(2):49–60, 2012.

[183] Verein Deutscher Ingenieure. VDI 2206 - Entwicklungsmethodik für mechatronische Systeme. Technical report, Beuth Verlag GmbH, 2004.

[184] Volkswagen AG. VW Golf | Volkswagen Deutschland. URL: https://www.volkswagen.de/de/models/golf.html, Date accessed: 2018-10-18.

[185] Gregor Wernet, Christian Bauer, Bernhard Steubing, Jürgen Reinhard, Emilia Moreno-Ruiz, and Bo Weidema. The ecoinvent database version 3 (part I): overview

and methodology. *The International Journal of Life Cycle Assessment*, 21(9):1218–1230, 2016.

[186] Wilhelm Woigk, Alex Heusi, Kunal Masania, and André R. Studart. Damping behaviour of hierarchical natural fibre composites. In *ECCM18 -18th European Conference on Composite Materials*, Athens, Greece, 2017.

[187] Yanjun Xie, Callum A.S. Hill, Zaihan Jalaludin, Simon F. Curling, Rajesh D. Anandjiwala, Andrew J. Norton, and Gary Newman. The dynamic water vapour sorption behaviour of natural fibres and kinetic analysis using the parallel exponential kinetics model. *Journal of Materials Science*, 46(2):479–489, 2010.

[188] Jing Xu, Yan Ma, Qianjin Zhang, Toshi Sugahara, Yuqiu Yang, and Hiroyuki Hamada. Crashworthiness of carbon fiber hybrid composite tubes molded by filament winding. *Composite Structures*, 139:130–140, 2016.

[189] L Yan and N Chouw. Crashworthiness characteristics of flax fibre reinforced epoxy tubes for energy absorption application. *Materials and Design*, 51:629–640, 2013.

[190] L Yan, N Chouw, and K Jayaraman. Effect of triggering and polyurethane foam-filler on axial crushing of natural flax/epoxy composite tubes. *Materials and Design*, 56:528–541, 2014.

[191] L Yan, N Chouw, and K Jayaraman. Lateral crushing of empty and polyurethane-foam filled natural flax fabric reinforced epoxy composite tubes. *Composites Part B*, 63:15–26, 2014.

[192] Libo Yan, Nawawi Chouw, and Krishnan Jayaraman. Flax fibre and its composites - A review. *Composites Part B*, 56:296–317, 2014.

[193] Hashin Z. Failure Criteria for Unidirectional Fiber Composites. *Journal of Applied Mechanics*, 47:329–334, 1980.

[194] Jichun Zhang, Yiou Shen, Bing Jiang, and Yan Li. Sound Absorption Characterization of Natural Materials and Sandwich Structure Composites. *Aerospace*, 5(3):75, 2018.

[195] Yucheng Zhong, Le Quan Ngoc Tran, Umeyr Kureemun, and Heow Pueh Lee. Prediction of the mechanical behavior of flax polypropylene composites based on multi-scale finite element analysis. *Journal of Materials Science*, 52(9):4957–4967, 2017.

[196] Maik Ziermaier. *Nichtlineare Versagensanalyse von dünnwandigen Faser-Kunststoff Verbund-Bauteilen unter besonderer Berücksichtigung von out-of-plane Roving-welligkeiten.* PhD thesis, Technische Universität Kaiserslautern, 2014.

Prior Publications by the Author

DLRK2016	R. Rinberg, R. Svidler, M. Klaerner, L. Kroll, K. Strohrmann, M. Hajek, H.J. Endres, "Anwendungspotenzial von naturbasierten hybriden Leichtbaustrukturen in der Luftfahrt", *Deutscher Luft- und Raumfahrtkongress 2016*, Braunschweig, Germany, 2016. Reference: [141]
DLRK2017	K. Strohrmann, J. Blaut, C. Panescu, H.-J. Endres, R. Svidler, M. Hajek, "Impact Damage Behavior and Non-Destructive Inspection Methods of Thin Hybrid Carbon-Flax Laminates", *Deutscher Luft- und Raumfahrtkongress 2017*, Munich, Germany, 2017. Reference: [166]
ECCM2018	K. Strohrmann, S. Schmeer, G.Fortin, H. Hamada, M. Hajek, "Crashworthiness Characteristics of Carbon-Flax Composite Tubes for Aerospace Applications", *ECCM18 - 18th European Conference on Composite Materials*, Athens, Greece, 2018. Reference: [168]
JMSC2018	K. Strohrmann, M. Hajek, "Bilinear approach to tensile properties of flax composites in finite element analyses", *Journal of Materials Science*, 54:1409–1421, 2019. https://doi.org/10.1007/s10853-018-2912-1, Reference: [171]
AIAA2019	K. Strohrmann, Hajek, M., "An Eco-Efficient Helicopter Tailplane Hybridized from Flax, Balsa and Carbon", *AIAA SciTech Forum 2019*, San Diego, USA, 2019. Reference: [167]
VFS2019	K. Strohrmann, N. André, M. Hajek, "Hybrid Natural Fiber Composites in a Helicopter Cabin Door – Mechanical Properties and Ecological Efficiency", *75th Annual Forum of the Vertical Flight Society*, Philadelphia, USA, 2019, Reference: [170]
InteReSt2019	K. Strohrmann, "Abschlussbericht der TUM Arbeitspakete im LUFO V2 geförderten Projekt InteReSt (FKZ: 20E1501C)", Technical University of Munich, *TiB Hannover*, Germany, 2019. Reference: [169]

Students Theses Guided by the Author

Kobus2016 Kobus, D., "Auslegung und Dimensionierung eines Höhenleitwerks aus Naturfaserverbundwerkstoffen", *Semester thesis*, Institute of Helicopter Technology, Technical University of Munich, December 2016. Reference: [94]

Boesl2017 Bösl, M., "Dimensionierung und Auslegung einer Kabinentür aus Naturfaserverbundwerkstoffen", *Master's thesis*, Institute of Helicopter Technology, Technical University of Munich, June 2017. Reference: [31]

Blaut2017 Blaut, J., "Bewertung der Widerstandsfähigkeit von hybriden Kohle-Flachs Faserverbundlaminaten gegen Schlagbeanspruchung", *Semester thesis*, Institute of Helicopter Technology, Technical University of Munich, July 2017. Reference: [25]

Braun2017 Braun, M., "Berechnung, Fertigung und experimentelle Validierung einer Cockpittür aus Kohlefaserverbundwerkstoff", *Master's thesis*, Institute of Helicopter Technology, Technical University of Munich, July 2017. Reference: [32]

Steigenb.2018 Steigenberger, J.,"Fertigung, Charakterisierung und Validierung von Subkomponenten eines Höhenleitwerks aus flachsfaserverstärkten Kunststoffen", *Master's thesis*, Institute of Helicopter Technology, Technical University of Munich, April 2018. Reference: [165]

Troendle2018 Tröndle, M., "Untersuchung von bistabilen Flachslaminaten mittels Feuchtigkeitstrigger", *Bachelor's thesis*, Institute of Helicopter Technology, Technical University of Munich, June 2018. Reference: [175]

Huber2018 Huber, T., "Strukturmechanik hybrider Flachs-Kohlefaserlaminate im Zugversuch und in Omega-Profil Balken", *Bachelor's thesis*, Institute of Helicopter Technology, Technical University of Munich, September 2018. Reference: [78]

Droege2019 Dröge, C., "Fertigung und experimentelle Validierung einer Cockpittür aus hybriden Kohle-Flachs-Faserverbundwerkstoffen", *Semester thesis*, Institute of Helicopter Technology, Technical University of Munich, Feburary 2019. Reference: [54]

Acknowledgments

This work was conducted within a LUFO V2 funded project, namely InteReSt (FKZ: 20E1501C). Thereby, contents overlap partly with the final report of the project see InteReSt2019. So firstly, I would like to thank the funding of this work, which was based on a decision by the German Bundestag.

Further, I want to acknowledge the support and given opportunity to work self-determined and independently, based on the trust, confidence, and latitude Prof. Dr.-Ing. Manfred Hajek placed in me. Thank you!

I want to thank the second examiner, Prof. Dr.-Ing. Horst Baier as well as the examination presidency Prof. Dr. Ing. Hartmut Spliethoff for their work. Farther, I want to thank Karl-Ludwig Krämer, Manfred Bauer, and all personnel of the lightweight structures workshop who supported my experiments and test set-up continuously in a technical and highly satisfactory manner. Thank you for the support and commitment.

Additionally, I want to acknowledge the work of my students and co-authors, who contributed to this achievement by the dedication they put into their own theses and papers, but also, secondarily contributed to this work by their motivation and discussion.

My colleagues at the Institute of Helicopter Technology shall be mentioned as well, who made the working days pass quickly and discussed technological issues extensively on a very high level with me. Additionally, I want to point out Martina Thieme who is the soul of the Institute and was always there for a good laugh. Her positive way of working and support in all dimensions of management helped a lot. Thank you.

My family was a great support as my sister and role model Christina Strohrmann gave detailed and high-level feedback on my thesis. Also, my father Martin Strohrmann and his wife Heike Karbstein gave helpful annotations, together with mentoring and advice during my whole academic progress, thank you for this support. In my family, I would also like to acknowledge social support and confidence, which also includes my family in-lay. I want to point out my mother Gabriele Strohrmann and my sister Lisa Holschuh, where I can feel contiunously love and trust in me, even while being miles apart. Thank you!

Last but not least, I want to thank my beloved husband Johannes Henschel who supported me privately and technically. I would not have pursued my personal and career goals in the way I did without him. I love you.